Progress in Energy and Combustion Science 82 (2021) 100877

Contents lists available at ScienceDirect

Progress in Energy and Combustion Science

journal homepage: www.elsevier.com/locate/pecs

Transcritical diffuse-interface hydrodynamics of propellants in high-pressure combustors of chemical propulsion systems

Lluís Jofre, Javier Urzay*

Center for Turbulence Research, Stanford University, Stanford, CA 94305, USA

ARTICLE INFO

Article history:
Received 30 September 2019
Accepted 10 August 2020

Keywords:
Fuel sprays
Transcritical flows
Phase change
High-pressure thermodynamics

ABSTRACT

Rocket engines and high-power new generations of gas-turbine jet engines and diesel engines oftentimes involve the injection of one or more reactants at subcritical temperatures into combustor environments at high pressures, and more particularly at pressures higher than those corresponding to the critical points of the individual components of the mixture, which typically range from 13 to 50 bars for most propellants. This class of trajectories in the thermodynamic space has been traditionally referred to as transcritical. However, the fundamental understanding of fuel atomization, vaporization, mixing, and combustion processes at such high pressures remains elusive. In particular, whereas fuel sprays are relatively well characterized at normal pressures, analyses of dispersion of fuel in high-pressure combustors are hindered by the limited experimental diagnostics and theoretical formulations available. The description of the thermodynamics of hydrocarbon-fueled mixtures employed in chemical propulsion systems is complex and involves mixing-induced phenomena, including an elevation of the critical point whereby the coexistence region of the mixture extends up to pressures much larger than the critical pressures of the individual components. As a result, interfaces subject to surface-tension forces may persist in multicomponent systems despite the high pressures, and may give rise to unexpected spray-like atomization dynamics that are otherwise absent in monocomponent systems above their critical point. In this article, the current understanding of this phenomenon is reviewed within the context of propulsion systems fueled by heavy hydrocarbons. Emphasis is made on analytical descriptions at mesoscopic scales of interest for computational fluid dynamics. In particular, a set of modifications of the constitutive laws in the Navier–Stokes equations for multicomponent flows, supplemented with a high-pressure equation of state and appropriate redefinitions of the thermodynamic potentials, are introduced in this work based on an extended version of the diffuse-interface theory of van der Waals. The resulting formulation involves revisited forms of the stress tensor and transport fluxes of heat and species, and enables a description of the mesoscopic volumetric effects induced by transcritical interfaces consistently with the thermodynamic phase diagram of the mixture at high pressures. Applications of the theory are illustrated in canonical problems, including dodecane/nitrogen transcritical interfaces in non-isothermal systems. The results indicate that a transcritical interface is formed between the propellant streams that persists downstream of the injection orifice over distances of the same order as the characteristic thermal-entrance length of the fuel stream. The transcritical interface vanishes at an edge that gives rise to a fully supercritical mixing layer.

© 2020 Elsevier Ltd. All rights reserved.

Contents

1. Introduction . . . 3
   1.1. Transcritical conditions in combustors fueled by heavy hydrocarbons . . . 3
   1.2. Objectives and outline of the present review . . . 8
2. High-pressure transcritical flow phenomena . . . 8
   2.1. Transcriticality in monocomponent systems . . . 8

* Corresponding author.
E-mail address: jurzay@stanford.edu (J. Urzay).

https://doi.org/10.1016/j.pecs.2020.100877
0360-1285/© 2020 Elsevier Ltd. All rights reserved.

2.2. Transcriticality in bicomponent systems ... 11
2.3. Transcriticality in aerospace propulsion systems ... 11
2.4. Additional research aspects of transcritical systems ... 13
3. Thermodynamic phase diagrams of mixtures fueled by heavy hydrocarbons ... 14
3.1. Equation of state ... 14
3.2. Critical-point elevation in hydrocarbon-fueled mixtures ... 14
3.3. Conditions suppressing transcritical behavior ... 18
4. Theoretical foundations of the diffuse-interface theory for transcritical flows ... 18
4.1. Gradient-dependent thermodynamic potentials ... 19
4.2. Gradient-energy coefficients ... 19
4.3. Open issues of experimentally calibrated models for gradient-energy coefficients ... 20
4.4. Characteristic scales in the diffuse-interface theory ... 21
4.5. The interface-continuum hypothesis ... 22
4.6. The role of antidiffusion in transcritical flows ... 23
4.7. Conservation equations for transcritical flows ... 23
5. The structure of transcritical interfaces ... 24
5.1. Entropy-production sources ... 24
5.2. Closure for the interfacial stress tensor ... 25
5.3. Mechanical equilibrium conditions ... 25
5.3.1. Mechanical equilibrium normal to the interface ... 26
5.3.2. Mechanical equilibrium tangential to the interface ... 28
5.3.3. The thermodynamic pressure near the interface ... 28
5.3.4. Generalizations to multicomponent systems ... 29
5.4. Closures for the interfacial transport fluxes of heat and species ... 30
5.5. The Onsager coefficients in transcritical conditions ... 31
5.6. Transport equilibrium condition ... 32
5.6.1. The transport equilibrium condition in terms of a balance of species fluxes ... 32
5.6.2. The transport equilibrium condition in terms of a balance of heat fluxes ... 35
5.6.3. Combination of mechanical and transport equilibrium conditions in terms of chemical potentials ... 35
5.6.4. Generalizations to multicomponent systems ... 36
5.7. Remarks on transcritical interfaces in equilibrium and near-equilibrium conditions ... 36
6. Transcritical interfaces in isothermal bicomponent systems ... 37
6.1. Formulation ... 37
6.2. Results: the steady transcritical interface ... 37
6.3. The generalized Cahn-Hilliard equation ... 40
7. Transcritical interfaces in non-isothermal bicomponent systems ... 42
7.1. Formulation ... 42
7.2. Results: The evolution of a transcritical interface downstream of the injection orifice ... 45
8. Concluding remarks ... 47
Declaration of Competing Interest ... 51
Acknowledgments ... 51
Appendix A. Basic aspects of thermodynamic stability and phase equilibrium for transcritical systems ... 51
A1. Thermodynamic-stability considerations ... 51
A2. Phase equilibrium ... 53
Appendix B. Transcritical behavior of thermophysical properties and molecular transport coefficients ... 53
B1. Molar enthalpy ... 53
B2. Constant-pressure molar heat ... 55
B3. Chemical potentials ... 55
B4. Molecular transport coefficients ... 56
Appendix C. Supplementary thermodynamic expressions applicable to multicomponent systems at high pressures ... 58
C1. Local thermodynamic relations ... 58
C2. Coefficients of the Peng-Robinson equation of state ... 58
C3. Parameters of the model for the gradient-energy coefficient ... 58
C4. Molar Helmholtz free energy and chemical potential ... 58
C5. Volume expansivity ... 59
C6. Enthalpy departure function ... 59
C7. Molar heats, adiabatic coefficient, and isentropic compressibility ... 59
C8. Partial molar enthalpies and partial-enthalpy departure functions ... 60
C9. Internal-energy departure function ... 60
C10. Partial molar internal energies ... 60
C11. Partial molar volume and isothermal compressibility ... 60
C12. Ideal-gas Gibbs free energies ... 60
C13. Fugacity coefficients ... 61
C14. Speed of sound ... 61
Appendix D. High-pressure interfaces in subcritical monocomponent systems ... 61
D1. Formulation ... 61

D2. Results . . . 62
Appendix E. Transcritical bicomponent systems approaching mechanically unstable conditions . . . 63
E1. Singularities of the theory at the limit of mechanical stability . . . 63
E2. Negative thermodynamic pressures . . . 66
Appendix F. Supplementary expressions for molecular transport coefficients at high pressures . . . 66
F1. Dynamic viscosity . . . 66
F2. Thermal conductivity . . . 67
F3. Stefan-Maxwell forms of the standard fluxes of heat and species . . . 68
F4. Fickian diffusion coefficients . . . 68
F5. Binary diffusion coefficients . . . 69
F6. Thermal-diffusion ratios . . . 69
Appendix G. Numerical methods for the calculation of transcritical interfaces . . . 69
G1. Spatial and temporal discretizations . . . 70
G2. Numerical considerations for cases involving equilibrium isothermal bicomponent systems . . . 70
G3. Numerical considerations for cases involving non-isothermal bicomponent systems . . . 71
References . . . 71

1. Introduction

The utilization of high pressures for burning fuel and oxidizer is a necessary requirement for the generation of thrust in chemical propulsion systems for ground, air, and space engineering applications. In modern designs, the characteristic pressures in the combustor range from 40 to 560 bars in rocket engines, to 20–60 bars in gas-turbine jet engines at takeoff, and 10–30 bars in diesel engines. However, great difficulties arise when attempting to model the dynamics of chemically reacting flows at high pressures. One of them, which influences the dispersion of fuel in the combustor and represents the focus of the present work, is related to the occurrence of transcritical conditions.

Challenges associated with transcritical conditions have been known since the development of high-pressure thrust chambers for liquid-fueled rocket engines [1–4]. A number of controlled experiments have been undertaken over the years to study flows at high pressures [5–14], and many have revealed the presence of interfaces separating the propellants [15–23]. The high pressures, however, limit the amount of information that can be obtained from state-of-the-art experimental diagnostics. Numerical simulations have accompanied these endeavors [24–31], but most of these computations have been limited to high-pressure conditions that did not warrant the existence of interfaces. Major reviews in the field have also focused on those conditions [32–34]. The field has evolved rapidly in recent years spurred by a number of publications, including (a) the thermodynamic analysis of Qiu and Reitz [35], which has provided detailed information about the thermodynamic space transited by homogeneous hydrocarbon-fueled mixtures at high pressures; (b) the molecular-dynamics simulations by Mo and Qiao [36], which have described the structure of transcritical interfaces albeit limited to very small length and time scales imposed by the high computational cost of molecular methods; and (c) the continuum-level theoretical work of Dahms and Oefelein [37], and Gaillard et al. [38,39], which have provided insight into the problem of transcriticality by using the diffuse-interface theory of van der Waals. The work by Dahms and Oefelein [37] was limited to the analysis of mean thermodynamic states in the combustor and stationary interfaces in absence of flow effects. In contrast, Gaillard et al. [38,39] made significant progress in coupling extensions of the diffuse-interface theory of van der Waals with the Navier-Stokes equations to describe, for instance, steady counterflow hydrogen diffusion flames in transcritical conditions.

This review article shows that fluid-mechanical effects are central to the description of transcritical phenomena, and that the problem cannot be treated solely by mean thermodynamic states in the combustor or isolated stationary interfaces, as previously attempted [37]. This review article fulfills the following objectives: (a) it summarizes relevant operating conditions leading to transcriticality; (b) it describes the state-of-the-art in the theoretical and computational understanding of transcritical interfaces at the continuum level; (c) it provides a comprehensive diffuse-interface theory of the hydrodynamics of propellants under transcritical conditions; and (d) it employs that theory to describe, for the first time, the downstream evolution of a transcritical interface separating the propellant streams. This review article also provides an analysis of the terminal structure of the transcritical interface at an edge located at a supercriticalization distance downstream of the orifice that is calculated as part of the solution. The diffusional critical point of the mixture of the propellants is shown to play a crucial role in the description of the interface edge. Downstream of the interface edge, the flow becomes fully supercritical, the interface disappears, and the propellants mix by molecular diffusion across a growing compositional mixing layer.

1.1. Transcritical conditions in combustors fueled by heavy hydrocarbons

Although there may be several definitions of the character of transcritical conditions in the literature [1–4,6,7,9–14,19,22,24,25,30,32,33,35–37], one that is of practical relevance for chemical propulsion systems corresponds to the thermodynamic conditions attained in the injection configuration sketched in Fig. 1. There, two streams of different propellants, denoted by the subindexes F (for the fuel stream) and O (for the coflow stream), are injected in such a way that the temperature of the coflow stream T_O is higher than that of the fuel stream T_F. In this configuration, transcriticality is attained when at least one of the propellant streams, often the fuel stream in practical applications, enters the combustor at a subcritical temperature, but the combustor pressure P_∞ is larger than the critical pressures of the two separate components, denoted here by $P_{c,F}$ and $P_{c,O}$.

The configuration depicted in Fig. 1 drives the discussion throughout the remainder of this manuscript. It is shown in Section 7 that the main characteristics of the flow field sketched in Fig. 1, including the interface separating the propellant streams, can be described by the diffuse-interface theory presented in Sections 4 and 5 even in a simpler canonical configuration where complex but inessential factors such as turbulence, shear, and interface corrugation are not considered. This section provides a qualitative summary of the main physical processes and the associated characteristic scales.

The possible number of combinations of thermodynamic conditions in the propellant streams that may lead to transcritical phenomena are large and cannot be addressed in a single study. Their particularities depend on the propulsion system and the mixture

Nomenclature

Latin letters

a, b	coefficients of the Peng-Robinson equation of state
A_P / A_μ	characteristic oscillation amplitudes of the pressure / chemical potential across the interface
$\mathcal{A}, \mathcal{B}$	parameters of the gradient-energy coefficient model
$\mathfrak{b}$	volume expansivity divided by the corresponding ideal-gas value
c	speed of sound
$\hat{\mathrm{c}}$	ratio between real and ideal specific heats at constant pressure
c_p / $\bar{c}_p$	constant-pressure specific / molar heat
c_v / $\bar{c}_v$	constant-volume specific / molar heat
d	equivalent hard-sphere diameter
$D_{i,j}$	Fickian diffusion coefficient
$\mathcal{D}_{i,j}$	binary diffusion coefficient
D_T	thermal diffusivity
e / $\bar{e}$	specific / molar internal energy
E	total energy
$\mathscr{E}_m$ / $\mathscr{E}_s$	mechanical- / transport-equilibrium parameters
f / $\bar{f}$	specific / molar Helmholtz free energy
F	Helmholtz free energy of the system
$\boldsymbol{F}$	vector of thermodynamic forces
f	fugacity
g / $\bar{g}$	specific / molar partial Gibbs free energy
G	Gibbs free energy of the system
h / $\bar{h}$	specific / molar enthalpy
H	enthalpy of the system
$\boldsymbol{J_i}$	species diffusion flux
$\boldsymbol{\mathcal{J}_i}$	interfacial species flux
k_T	thermal-diffusion ratio
$\mathrm{K_I}$	local curvature of the interface
$\boldsymbol{\mathcal{K}}$	interfacial stress tensor
Kn_I	Knudsen number
ℓ_{ca}	capillary length
$L_{i,j}$	Onsager coefficients
$\boldsymbol{\mathcal{L}}$	Onsager matrix
$\mathrm{L_{TR}}$	supercriticalization length
Le	Lewis number
M	momentum-flux ratio
Ma	Mach number
n	number of moles
$\hat{n}$	spatial coordinate normal to the interface
N	number of components
$\mathcal{N}$	nondimensional curvature
N_A	Avogadro's number
Oh	Ohnesorge number
OPR	overall pressure ratio
P	pressure
P_a	air pressure at a given altitude
$P_{c,\mathrm{F}}/P_{c,\mathrm{O}}$	critical pressures of the propellants
P_∞	combustor pressure
$\mathcal{P}$	ratio between the characteristic oscillation amplitude of the pressure through the interface and the combustor pressure
Pe	Péclet number
$\boldsymbol{q}$	heat flux
$\boldsymbol{q_t}$	heat flux (excluding heat transport by interdiffusion of species)
$\boldsymbol{\mathcal{Q}}$	interfacial heat flux
R_F	radius of the orifice
$\mathrm{R^0}$	universal gas constant
$\mathcal{R}$	ratio between fuel and oxidizer densities
Re	Reynolds number
s / $\bar{s}/\tilde{s}$	specific / molar / generalized entropy
$\dot{s}_\mathrm{prod}$	entropy production rate
t	time
T	temperature
$T_{c,\mathrm{diff}}$	temperature of the diffusional critical point
$T_{c,\mathrm{F}}/T_{c,\mathrm{O}}$	critical temperatures of the propellants
$T_{c,\mathrm{mix}}$	critical mixing temperature
T_{pb}	pseudo-boiling temperature
T_TR	supercriticalization temperature
U_F / U_O	injection velocities of the propellants
$\mathbf{v}$	velocity vector
v	molar volume
V	volume of the system
VLE	vapor-liquid equilibrium
$\bar{\mathcal{V}}$	partial molar volume
W / $\overline{\mathrm{W}}$	molecular weight / mean molecular weight of the mixture
$\mathcal{W}$	ratio between fuel and coflow molecular weights
We	Weber number
x	streamwise spatial coordinate
X	molar fraction
y	transversal spatial coordinate
Y	mass fraction
Z	compressibility factor

Greek symbols

α	thermal-expansion ratio
β_s	isentropic compressibility
β_T	isothermal compressibility
β_v	volume expansivity
γ	adiabatic coefficient
δ_I	interface thickness
δ_T / δ_Y	thermal / compositional mixing-layer thickness
$\Delta_d e$ / $\Delta_d h$	internal energy / enthalpy departure function
ϵ_R / ϵ_T	large-scale / thermal Cahn number
η	dynamic viscosity
θ	reduced temperature
ϑ	binary-interaction parameter
ι	model parameter for calculation of thermal-diffusion ratio
κ	gradient-energy coefficient
λ	thermal conductivity
Λ	molecular mean free path
μ / $\bar{\mu}$ / $\tilde{\mu}$	specific / molar / generalized chemical potential
ρ	density
σ	surface-tension coefficient
σ_0	characteristic value of the surface-tension coefficient
τ	ratio between interface and fuel-stream temperatures
$\boldsymbol{\tau}$	viscous stress tensor
φ	fugacity coefficient
$\boldsymbol{\phi}$	vector of thermodynamic currents
χ	auxiliary variable
Ω	Landau potential
$\boldsymbol{\psi}$	auxiliary vector

Main subscripts

c	critical thermodynamic state
diff	diffusional critical point
e	vapor-liquid equilibrium conditions
f	formation value
F	fuel stream

FF, O	employed to denote the value of the binary diffusivity in the fuel stream
F, OO	employed to denote the value of the binary diffusivity in the coflow stream
GD	gradient-dependent thermodynamic potential or pressure
I	interface-related quantity
mix	critical mixing conditions
O	coflow stream
pb	pseudo-boiling conditions
∞	conditions in the combustor environment

Main superscripts

g	gas-like state
IG	ideal-gas conditions
ℓ	liquid-like state
ΔT	species or heat flux components dependent on temperature gradients
$'$	species or heat flux components independent of temperature gradients
$\star$	nondimensional variable
0	reference or initial value

of propellants considered, as discussed in Sections 2 and 3. However, the transcritical conditions illustrated in Fig. 1 are of general relevance in combustors fueled by heavy hydrocarbons because of two factors:

(a) As observed in Table 1, heavy hydrocarbons have relatively high critical temperatures, and therefore require significant temperature increments of order unity relative to their injection temperature to become fully supercritical, namely

$$\frac{T_{c,\mathrm{F}} - T_\mathrm{F}}{T_\mathrm{F}} = O(1). \tag{1}$$

Specifically, $T_{c,\mathrm{F}} - T_\mathrm{F} \sim$ 200–400 K for heavy hydrocarbon fuels of interest (e.g., C_6H_{14}, C_7H_{16}, $C_{10}H_{22}$, $C_{12}H_{26}$, Jet-A, and RP-1), where $T_\mathrm{F} \sim$ 300–450 K and $T_{c,\mathrm{F}} \sim$ 500–700 K are the typical ranges of the fuel injection temperature and the fuel critical temperature, respectively.

(b) As discussed in Section 3, mixtures of heavy hydrocarbons with molecular nitrogen (N_2), molecular oxygen (O_2), or air have much higher critical pressures than their separate components.

Under the aforementioned transcritical conditions, which are often found in practice as discussed in Section 2, and despite the prevailing high pressures, the flow field contains a region immediately downstream of the injector orifice where a thin transcritical interface is formed between the fuel and coflow streams because of diffusion processes essential to the mixing that necessarily precedes combustion. Specifically, as described in Section 5, the theory presented here indicates that surface tension survives the high pressures because of the intrinsic diffusional instability of the fluid resulting from mixing the two propellant streams. This diffusional instability, whose basic foundations are discussed in Appendix A, leads to separation of the propellants by a transcritical interface that bears large composition gradients across and is accompanied by surface tension.

Both thermal and compositional mixing layers sketched in Fig. 1 are slender, since the characteristic Reynolds number

$$Re_\mathrm{F} = \rho_\mathrm{F} U_\mathrm{F} R_\mathrm{F} / \eta_\mathrm{F} \tag{2}$$

is typically much larger than unity in practical applications. In Eq. (2), U_F, ρ_F, and η_F are the velocity, density, and dynamic viscosity of the fuel stream, respectively, and R_F is the fuel orifice radius, which is typically of order 0.1–1 mm in chemical propulsion systems of interest [19,43–45].

The magnitude of U_F relative to the coflow-stream velocity U_O is represented by the momentum-flux ratio

$$\mathrm{M} = \frac{\rho_\mathrm{O} U_\mathrm{O}^2}{\rho_\mathrm{F} U_\mathrm{F}^2}, \tag{3}$$

with ρ_O being the density of the coflow stream. The momentum-flux ratio is of order M $\sim$ 1–10 in rocket engines and gas-turbine jet engines [43,46–48], whereas M = 0 for diesel engines. In the high-pressure operating conditions investigated herein, the density ratio

$$\mathcal{R} = \rho_\mathrm{F} / \rho_\mathrm{O} \tag{4}$$

is within the range $\mathcal{R}$ = 5–40, as opposed to $\mathcal{R}$ = 500–1000 at atmospheric pressure. The corresponding velocity ratios are of order $U_\mathrm{O}/U_\mathrm{F} = \sqrt{\mathrm{M}\mathcal{R}} \sim$ 1–10.

In the model problem depicted in Fig. 1, the coflow temperature T_O is large enough to heat up the fuel to its critical temperature downstream of the injection orifice. For coflows comprised of N_2, O_2, or air, the prevailing condition implies that T_O must be larger than the critical temperature of the coflow, $T_\mathrm{O} > T_{c,\mathrm{O}}$, since $T_{c,\mathrm{O}} \sim$ 120–150 K is in the range of cryogenic temperatures for those components (see Table 1). As a result, the relative temperature difference between the propellant streams, defined as the thermal-expansion ratio

$$\alpha = \frac{T_\mathrm{O} - T_\mathrm{F}}{T_\mathrm{F}}, \tag{5}$$

is an order-unity parameter. Additionally, the coflow is cooled down by the fuel stream and, to a much lesser extent, the fuel stream is heated by the coflow. This discrepancy is driven by the much higher thermal diffusivity of the coflow. The thickness of the resulting thermal mixing layer, δ_T, grows with distance downstream from small values compared to R_F near the orifice (a good assumption for thin orifice rings), to values of order R_F far from the orifice where the interface vanishes. Since the Prandtl number remains close to that of air at normal conditions, only δ_T may be considered, for simplicity, as the length scale representative of both momentum and thermal transport.

The transcritical interface extends from the orifice ring to an edge at a supercriticalization distance $x = \mathrm{L_{TR}}$, where the fuel stream has been heated up to a supercriticalization temperature $T = T_\mathrm{TR}$. The latter depends on the combination of propellants and is a solution of the thermodynamic phase diagram of the mixture. For mixtures of heavy hydrocarbons with N_2, O_2, or air, it will be shown that

$$T_\mathrm{TR} \simeq T_{c,\mathrm{diff}}, \tag{6}$$

where $T_{c,\mathrm{diff}}$ is the temperature of the diffusional critical point of the mixture at the combustor pressure P_∞ (see Appendix A for a formal definition of the diffusional critical point). The temperature of the diffusional critical point $T_{c,\mathrm{diff}}$ is smaller than the fuel critical temperature $T_{c,\mathrm{F}}$ by small amounts,

$$\frac{T_{c,\mathrm{F}} - T_{c,\mathrm{diff}}}{T_{c,\mathrm{F}}} \ll 1. \tag{7}$$

For instance, $T_{c,\mathrm{F}} - T_{c,\mathrm{diff}} \sim$ 10–40 K at pressures $P_\infty \sim$ 50–200 bar in $C_{12}H_{26}/N_2$ mixtures, thereby yielding $(T_{c,\mathrm{F}} - T_{c,\mathrm{diff}})/T_{c,\mathrm{F}}$ = 0.02–0.06. The value of $T_{c,\mathrm{diff}}$ is also similar to the critical mixing temperature $T_{c,\mathrm{mix}}$ defined as the maximum temperature that can be attained by the mixture under conditions of phase coexistence at P_∞, with $T_{c,\mathrm{mix}} - T_{c,\mathrm{diff}}$ being at most 5 K in $C_{12}H_{26}/N_2$ mixtures at P_∞=50–200 bar. As a consequence, T_TR is also larger than the fuel injection temperature T_F by relative amounts of order unity,

$$\frac{T_\mathrm{TR} - T_\mathrm{F}}{T_\mathrm{F}} = O(1). \tag{8}$$

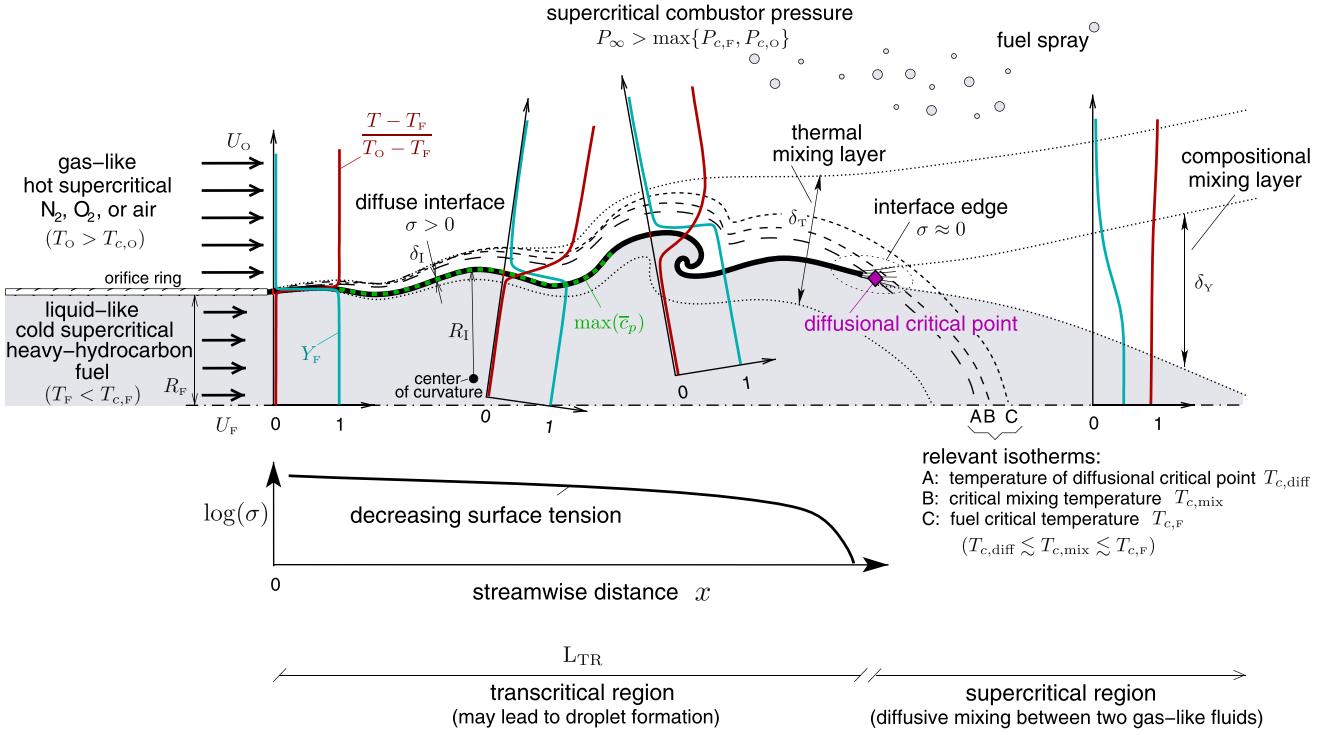

Fig. 1. Schematics of a transcritical flow near an injector orifice delivering a cold supercritical heavy-hydrocarbon fuel into a hot supercritical coflow in a combustor at a pressure higher than the critical pressures of the two separate components. The symbol R_F denotes the radius of the orifice, and U_F and U_O are the characteristic injection velocities of the fuel and oxidizer streams, respectively. Additionally, σ is the surface-tension coefficient, P_∞ is the combustor pressure, Y_F is the fuel mass fraction, and T_F and T_O correspond to the temperatures of the fuel and coflow streams, respectively. The critical temperatures and pressures of the fuel and oxidizer streams are denoted, respectively, by $T_{c,\mathrm{F}}$ and $P_{c,\mathrm{F}}$, and by $T_{c,\mathrm{O}}$ and $P_{c,\mathrm{O}}$. The rest of the symbols are defined in the main text.

Table 1
Critical temperatures and pressures for selected species [40–42].

	N_2	O_2	air	H_2O	CO_2	H_2	CH_4	C_6H_{14}	C_7H_{16}	$C_{10}H_{22}$	$C_{12}H_{26}$	Jet-A	RP-1
T_c [K]	126	155	131	647	304	33	191	508	540	618	658	671	677
P_c [bar]	34	50	36	220	74	13	46	30	27	21	18	24	22

The transcritical interface terminates at an edge crossed by the supercriticalization isotherm, where a fundamental change in the diffusional characteristics of the mixture occurs. The structure of the edge can be previewed in terms of spatial contours of the fuel mass fraction Y_F in Fig. 2 for a system consisting of $C_{12}H_{26}$ injected at $T_\mathrm{F} = 450$ K into a coflowing N_2 stream at $T_\mathrm{O} = 1000$ K. The system is at $P_\infty = 100$ bar, which represents a supercritical pressure with respect to both components. The resulting distribution of surface tension along the transcritical interface with distance downstream of the injection orifice is shown in Fig. 3. The results in both of those figures are obtained by using the diffuse-interface theory presented in Sections 4 and 5. The resulting formulation describes high-pressure flows with interfaces whose strength can vary in space and vanish altogether. The results obtained by using this theory indicate that the interface thickness δ_I remains small along a large portion of the interface despite the high pressures involved. Consequently, the integration of the formulation is hindered by the large disparity between the interface thickness δ_I and other length scales, including δ_T, R_F, $\mathrm{L_{TR}}$, and the interface radius of curvature R_I. In particular, it will be shown, in conditions of practical relevance, that the large-scale Cahn number

$$\epsilon_R = \delta_\mathrm{I}/R_\mathrm{F} \tag{9}$$

and the thermal Cahn number

$$\epsilon_\mathrm{T} = \delta_\mathrm{I}/\delta_\mathrm{T}, \tag{10}$$

are both much smaller than unity in the transcritical region, where the interface survives. These represent fundamental characteristics that simplify the theoretical description of the interface structure. Further details and additional explanations of the results in Figs. 2 and 3 are deferred to Section 7.

In the transcritical region $0 < x < \mathrm{L_{TR}}$, the interface survives along with the surface-tension force it engenders. In general, the quantification of $\mathrm{L_{TR}}$ requires numerical integration of the diffuse-interface formulation presented here. In laminar flows at moderately large values of the Reynolds number (2), an estimate of $\mathrm{L_{TR}}$ can be obtained by an integral balance between the streamwise variation of the enthalpy flux in the fuel stream and the total amount of heat conduction received across the interface from the hot coflow,

$$\rho_\mathrm{F} c_{p,\mathrm{F}} U_\mathrm{F} R_\mathrm{F}^2 \frac{(T_\mathrm{TR} - T_\mathrm{F})}{\mathrm{L_{TR}}} \sim \lambda_\mathrm{O} R_\mathrm{F} \frac{(T_\mathrm{O} - T_\mathrm{F})}{\delta_\mathrm{T}}, \tag{11}$$

where λ_O is the thermal conductivity in the coflow stream. For axisymmetric jets, the approximation $\delta_\mathrm{T} \sim R_\mathrm{F}$ can be made in Eq. (11) in analogy to cold round jets at downstream distances approaching thermal-entrance conditions [49]. It follows that $\mathrm{L_{TR}}$ depends quadratically on the orifice radius R_F as

$$\mathrm{L_{TR}} \sim \left(\frac{R_\mathrm{F}^2 U_\mathrm{F} \mathcal{R}}{D_{\mathrm{T,O}}}\right)\left(\frac{c_{p,\mathrm{F}}}{c_{p,\mathrm{O}}}\right)\left(\frac{T_{c,\mathrm{F}} - T_\mathrm{F}}{T_\mathrm{O} - T_\mathrm{F}}\right), \tag{12}$$

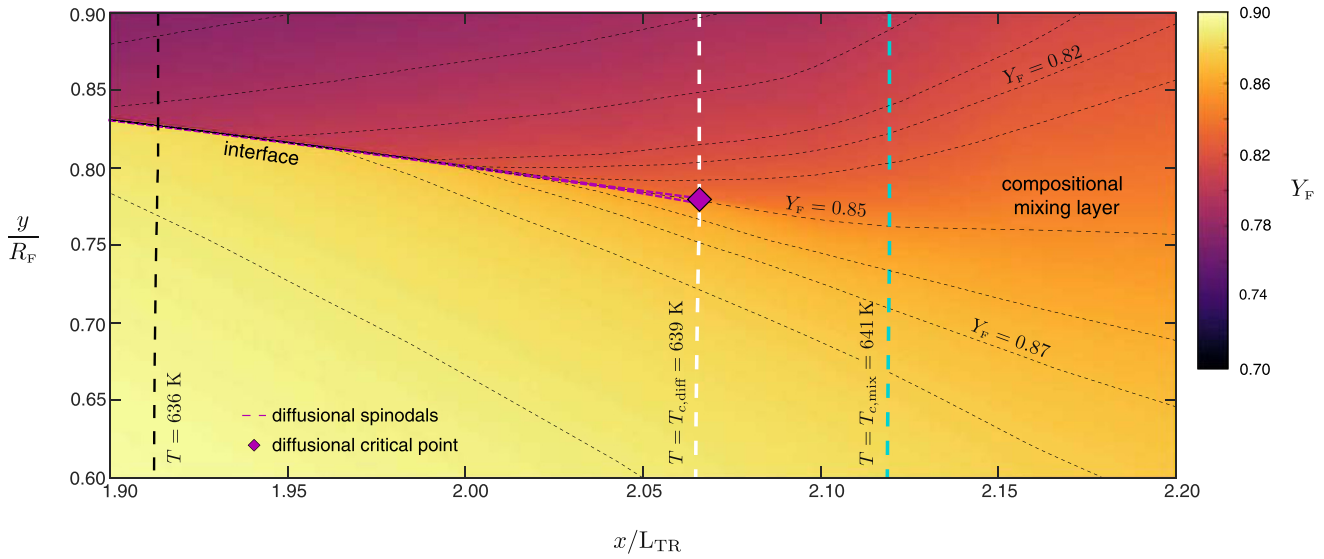

Fig. 2. Numerical results of the present theory showing a zoomed view of the terminal structure of a transcritical interface at an edge. The interface separates two planar laminar streams at high Péclet numbers: one of dodecane ($C_{12}H_{26}$) injected at $T_F = 450$ K (below the interface), and one of molecular nitrogen (N_2) injected at $T_O = 1000$ K (above the interface). The system is at a supercritical pressure $P_\infty = 100$ bar with respect to both components. The figure shows the fuel mass fraction Y_F (solid contours and dark thin dashed lines), temperature (colored thick dashed-line contours), diffusional critical point (purple diamond symbol), and diffusional spinodal (thick purple dashed lines). The vertical axis is the transversal distance from the jet axis y normalized with the orifice radius R_F, whereas the horizontal axis is the streamwise distance x normalized with the estimate (13) for the supercriticalization length. The flow attains fully supercritical conditions downstream of the interface edge. There, both propellants resemble gas-like supercritical fluids and mix by molecular diffusion across a compositional mixing layer that emanates from the interface edge. Details about the calculations are provided in Section 7. (For interpretation of the references to color in this figure legend, the reader is referred to the web version of this article.)

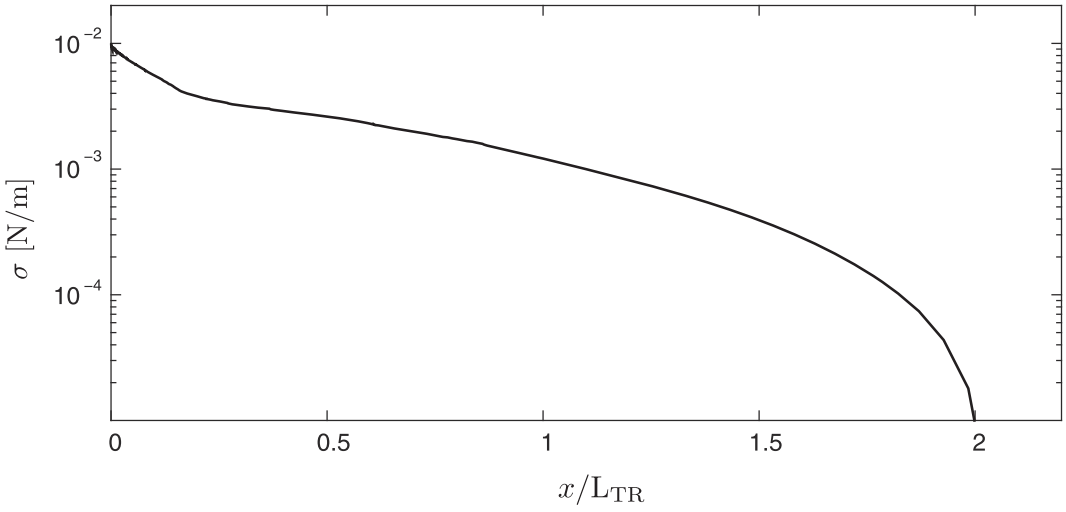

Fig. 3. Evolution of the surface-tension coefficient along the transcritical interface in Fig. 2 obtained from the present theory. Further details about these calculations are provided in Section 7.

where the approximation $T_{TR} \approx T_{c,\mathrm{diff}} \approx T_{c,F}$ has been made in accordance with Eqs. (6) and (7). In Eq. (12), $D_{T,O}$ is the thermal diffusivity of the coflow stream, and $c_{p,F}/c_{p,O}$ is the ratio of fuel and coflow specific heats, which is of order unity in the conditions analyzed here, as discussed in Appendix B. Additionally, $(T_{c,F} - T_F)/(T_O - T_F)$ is an order-unity temperature-difference ratio, as prescribed by Eqs. (1) and (5). In contrast, two-dimensional laminar jets are known to have much longer thermal-entrance lengths than their round counterparts because the outer region, where streamwise convection and transverse diffusion balance, grows indefinitely with the square root of x, thereby yielding comparatively smaller heat fluxes into the cold stream [49]. In this case, a more appropriate approximation to utilize in Eq. (11) is $\delta_T \sim (D_{T,O} L_{TR}/U_F)^{1/2}$. This leads to the estimate

$$L_{TR} \sim \left(\frac{R_F^2 U_F \mathcal{R}^2}{D_{T,O}}\right)\left(\frac{c_{p,F}}{c_{p,O}}\right)^2\left(\frac{T_{c,F} - T_F}{T_O - T_F}\right)^2, \tag{13}$$

which is used for normalizing x in Figs. 2 and 3.

The estimates (12) or (13) predict that the supercriticalization length increases with decreasing values of the fuel injection temperature T_F, coflow injection temperature T_O, and combustor pressure P_∞. Among these three quantities, the maximum sensitivity is to variations of T_O. For instance, a decrease of 300 K in T_O leads to a four-fold increment in L_{TR} in the conditions analyzed in Figs. 2 and 3.

The considerations above suggest that the injection orifice radius R_F has a decisive influence on the size of the transcritical region. In practice, L_{TR} is a fraction of the thermal-entrance length, the latter delimiting the condition for which the hot coflow temperature T_O (rather than $T_{c,F}$) is attained in the bulk of the fuel stream. However, it will be shown that the transfer of heat from the coflow to the fuel stream is hindered in transcritical conditions because of two factors:

(a) High pressures lead to small values of the thermal diffusivity in the coflow stream.
(b) For a significant portion of the interface length, the specific heat attains a global maximum in the vicinity of the interface, thereby leading to a decrease in the local thermal diffusivity there.

These factors should be taken into account when interpreting molecular-dynamics simulations of transcritical systems, since those techniques are typically limited to microscopic length scales that may be too small compared to the supercriticalization length required to describe the macroscopic evolution of the interface with distance downstream of the injection orifice.

Additional complexities arise in realistic scenarios that are beyond the scope of this study. For instance, in turbulent transcritical flows at large values of the Reynolds number (2), the molecular thermal diffusivity $D_{T,O}$ in Eq. (12) should be replaced by a turbulent eddy diffusivity of order $D_{turb} \sim U_F R_F$, which is lager than $D_{T,O}$ by a factor of order $Re_F \gg 1$. Consequently, the ratio of the supercriticalization length to the orifice radius decreases from $L_{TR}/R_F \sim Re_F \mathcal{R}$ in laminar flows to $L_{TR}/R_F \sim \mathcal{R}$ in turbulent flows. There is however little work to date that have addressed closures in high-pressure turbulent flows [50], and therefore the effects of turbulence will not be further pursued here. Similarly, hydrodynamic instabilities may develop as a result of the competition between aerodynamic stresses and the interface-restoring surface-tension force in the transcritical region. These force imbalances may roll the interface leading to a finite local radius of interface curvature R_I, and eventually to the formation of ligaments and droplets, as sketched in Fig. 1. Configurations different from that in Fig. 1 may therefore exist in which the supercriticalization isotherm never crosses the interface before it breaks up, but instead crosses the ensuing fuel spray cloud.

1.2. Objectives and outline of the present review

This review focuses on theoretical aspects of transcritical phenomena at a continuum level and in a manner amenable to computational fluid dynamics (CFD). The key question to be explored is whether transcritical systems can be computed by integrating the Navier-Stokes equations uniformly over the entire flow field while subject to high-pressure equations of state along with the standard transport theory for multicomponent mixtures. The key concern that impedes that approach is related to the antidiffusive character of the mass transport predicted by the standard theory in transcritical conditions, which renders the problem ill-posed. To address that, a formulation of the Navier-Stokes equations with revisited constitutive laws, supplemented with (a) proper redefinitions of thermodynamic potentials, (b) a high-pressure equation of state, and (c) high-pressure thermophysical and multicomponent transport properties, is introduced that regularizes the problem and enables the description of volumetric effects of transcritical interfaces in multicomponent flows. The formulation is based on extensions of the diffuse-interface theory of van der Waals [108] – a useful formalism originally designed for monocomponent isothermal systems at high pressures, when the interface broadens significantly relative to intermolecular distances.

The theory outlined here provides a description of the structure of stationary transcritical interfaces in equilibrium, as well as the downstream evolution of non-equilibrium transcritical interfaces separating propellant streams with different temperatures. In the latter case, this theory predicts that the interface ends at an edge, whose structure elicits the central role played by the diffusional critical point of the mixture in supercriticalizing the system, as shown in Fig. 2. Emphasis is made on transcritical interfaces in $C_{12}H_{26}/N_2$ mixtures, but supplementary thermodynamic analyses are provided for several other mixtures of interest that identify pressure and temperature conditions inducing transcritical interfaces in the flow field. A discussion is also included about operating conditions in combustors of aerospace propulsion systems leading to transcriticality.

The remainder of this manuscript is structured as follows. A qualitative description of transcritical phenomena is provided in Section 2 for monocomponent and bicomponent systems, along with a short survey of characteristic injection conditions in aerospace propulsion systems. Phase diagrams for hydrocarbon-fueled binary mixtures are discussed in Section 3. Using the diffuse-interface theory, a formulation of the Navier-Stokes equations that incorporates high-pressure effects and volumetric terms representing embedded interfaces is outlined in Section 4. Entropy-based closures of interface-related terms in the augmented Navier-Stokes equations, which enable the description of the structure of transcritical interfaces, are derived in Section 5. Readers who are not interested in the development of the formulation can skip Sections 4 and 5 and move directly to Sections 6 and 7, in which calculations of simplified canonical problems are provided. In Section 6, transcritical interfaces in equilibrium isothermal systems are analyzed. Section 7 is devoted to non-equilibrium transcritical interfaces in non-isothermal systems and their evolution downstream of the injection orifice. Lastly, concluding remarks are given in Section 8. Additionally, seven appendices are included that contain supplementary details and fundamental concepts closely connected with the formulation. In particular, Appendix A reviews basic concepts of thermodynamic stability and phase equilibrium. Appendix B provides a description of thermophysical properties and transport coefficients at high pressures. Appendix C outlines supplementary thermodynamic expressions for systems at high pressures. Appendix D focuses on numerical results obtained for near-critical interfaces in monocomponent systems. Appendix E discusses the behavior of the present theory near mechanically unstable conditions. Appendix F lists supplementary expressions for transport coefficients at high pressures, and Appendix G provides methods for the numerical integration of the formulation presented here.

2. High-pressure transcritical flow phenomena

A significant challenge for the predictive calculation of transcritical flows lies in the complexity of the transitional and composition-dependent character of the interface formation and breakup, and of the subsequent dispersion and mixing of fuel in the combustor. To address these aspects, this section begins by introducing the main problems associated with transcriticality in monocomponent flows, followed by a description of more complex phenomena in bicomponent flows. In addition, a survey of characteristic injection conditions in aerospace chemical propulsion systems is provided at the end of this section that serves to familiarize the reader with practical configurations.

2.1. Transcriticality in monocomponent systems

Consider a closed vessel filled with a monocomponent liquid in phase equilibrium with its own vapor. The pressure and temper-

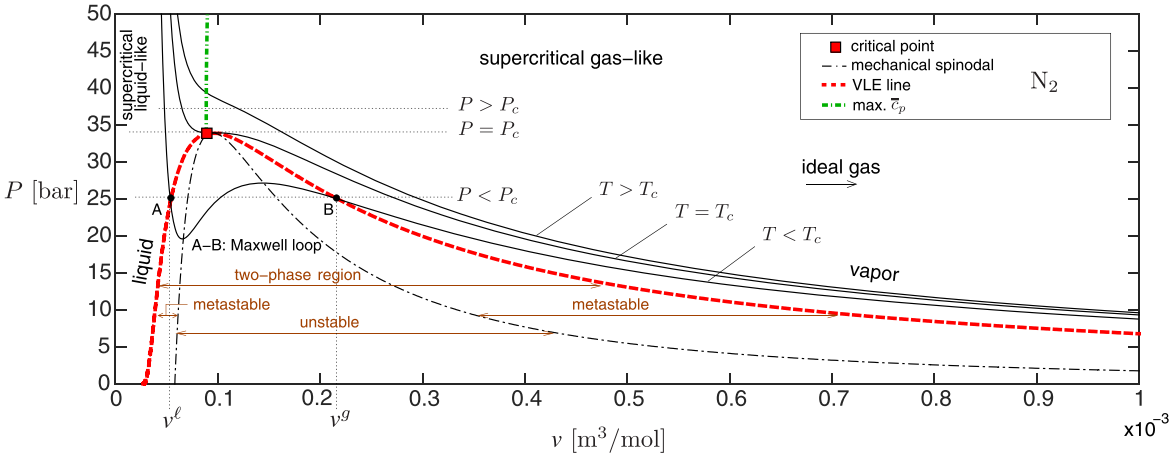

Fig. 4. Thermodynamic phase diagram for pure N_2 calculated with the Peng-Robinson equation of state introduced in Section 3.1. Included in the plot are the mechanical spinodals (dot-dashed lines), vapor-liquid equilibrium lines (thick red dashed lines), the pseudo-boiling line (thick green dot-dashed line), and the critical point (square symbol). (For interpretation of the references to color in this figure legend, the reader is referred to the web version of this article.)

ature in the vessel are denoted by P and T, respectively. At normal pressure, the liquid and vapor are separated by an interface whose thickness is clearly not in the continuum range, and which is subject to a surface-tension force. Below the critical pressure P_c, the presence of such interface is warranted since each thermodynamic state (P, T) is associated with two densities [51] corresponding to the phase-equilibrium values for vapor, ρ_e^g, and liquid, ρ_e^ℓ. This is illustrated in the $P-v$ thermodynamic phase diagram in Fig. 4 for N_2, where $v = W_{N_2}/\rho$ is the molar volume and W_{N_2} is the molecular weight. The resulting ratio of densities of the phases, $\mathcal{R} = \rho_e^\ell/\rho_e^g$, is typically of order 10^3 at normal conditions.

As the temperature of the vessel is increased, the liquid evaporates and a new phase-equilibrium condition is attained in which the pressure increases as well in accordance with the Clausius–Clapeyron relation. During this process, the interface thickens and the density ratio decreases to a value close to unity near the critical pressure P_c, at which the two phases become visually indistinguishable. Above the critical pressure, $P > P_c$, the fluid is supercritical with a uniquely defined density ρ for each thermodynamic state (P, T), thereby preventing the existence of an interface. Meanwhile, the surface tension necessarily vanishes at $P \geq P_c$; the limit $P \to P_c$ is taken here in combination with $T \to T_c$ [53,54].

The transition from subcritical to supercritical conditions described above can be visualized in laboratory experiments involving the thermodynamic characterization of pure substances by using equilibrium cells [52,55]. A sequence of photographs that illustrates the vanishing distinction between the two phases in a system approaching and crossing the critical point of propane is provided in Fig. 5(a).

In contrast with closed systems, combustors involve continuous flows of propellants. Consider a cold liquid jet injected at temperature T_F and atmospheric pressure into its own hot vapor at temperature T_O, where $T_F \leq T_e \leq T_O$, with T_e being the vapor-liquid equilibrium (VLE) or boiling temperature at the corresponding pressure. The resulting liquid-to-gas density ratio ρ_F/ρ_O is of order 10^3. The liquid jet breaks up due to unbalances between aerodynamic and surface-tension forces [45,56–60] as illustrated in Fig. 5(b). A relatively large amount of energy, comparable to the thermal enthalpy of the hot environment, must be transferred to the spray to heat it up and vaporize it [61].

Similarly to the closed vessel operating at normal pressure, the thickness of the liquid-gas interface in the jet flow mentioned above is several orders of magnitude smaller than any of the relevant hydrodynamic scales involved. Nonetheless, predictive simulation capabilities have been developed in recent years using interface-capturing methods such as the volume-of-fluid or level-set formulations, both of which volumetrically incorporate the surface-tension force in the momentum equation through a surface-tension coefficient σ multiplied by the interface curvature and by a Dirac-delta function localized at the interface [62–66]. As the ambient pressure P_∞ increases, the liquid-to-gas density ratio decreases. In particular, the interface becomes thicker as the critical pressure is approached, both surface tension and vaporization enthalpy decrease, and the atomization process becomes a mixing between gas-like fluids without any breakup.

Entering the supercritical region, it is important to distinguish between supercritical gas-like and supercritical liquid-like fluids as depicted in Fig. 4. As discussed in Appendix B.4, the factors that separate the behavior of liquid-like from gas-like supercritical fluids are:

(a) A supercritical liquid-like fluid is one whose density is large, whose isothermal compressibility is small, and whose transport coefficients behave in a manner that is reminiscent of a liquid, with decreasing viscosities and thermal conductivities found at increasingly larger values of temperature, whereas the mass diffusivity remains mostly constant or increases slowly with temperature.

(b) In contrast, the density of supercritical gas-like fluids is relatively smaller, their isothermal compressibility is larger, and their viscosity, thermal conductivity, and mass diffusivity increase with temperature, thus resembling the behavior observed in gases. At high temperatures, $T \gg T_c$, and despite the high pressures, the intermolecular distances are sufficiently large for the supercritical gas-like fluid to behave like an ideal gas.

At pressures not too large compared to P_c, a clear transition from liquid-like to gas-like supercritical behavior occurs at the pseudo-boiling, or Widom, temperature T_{pb} denoted by the thick green dot-dashed line in Fig. 4 (see Refs. [67,68] and Appendix B.4 for related discussions). This temperature depends on pressure and is not too different from T_c (e.g., $T_{pb} \sim 130$ K at 40 bar and $T_{pb} \sim 150$ K at 60 bar, both for N_2, for which $T_c = 126$ K). In particular, T_{pb} corresponds approximately to the temperature where a second-order phase transition occurs, with the density, viscosity and thermal conductivity plunging as transition from a liquid-like to a gas-like state occurs, and with the specific heat at constant pressure displaying a characteristic finite-amplitude spike [69,70]. As the pressure becomes increasingly larger than P_c, the distinction

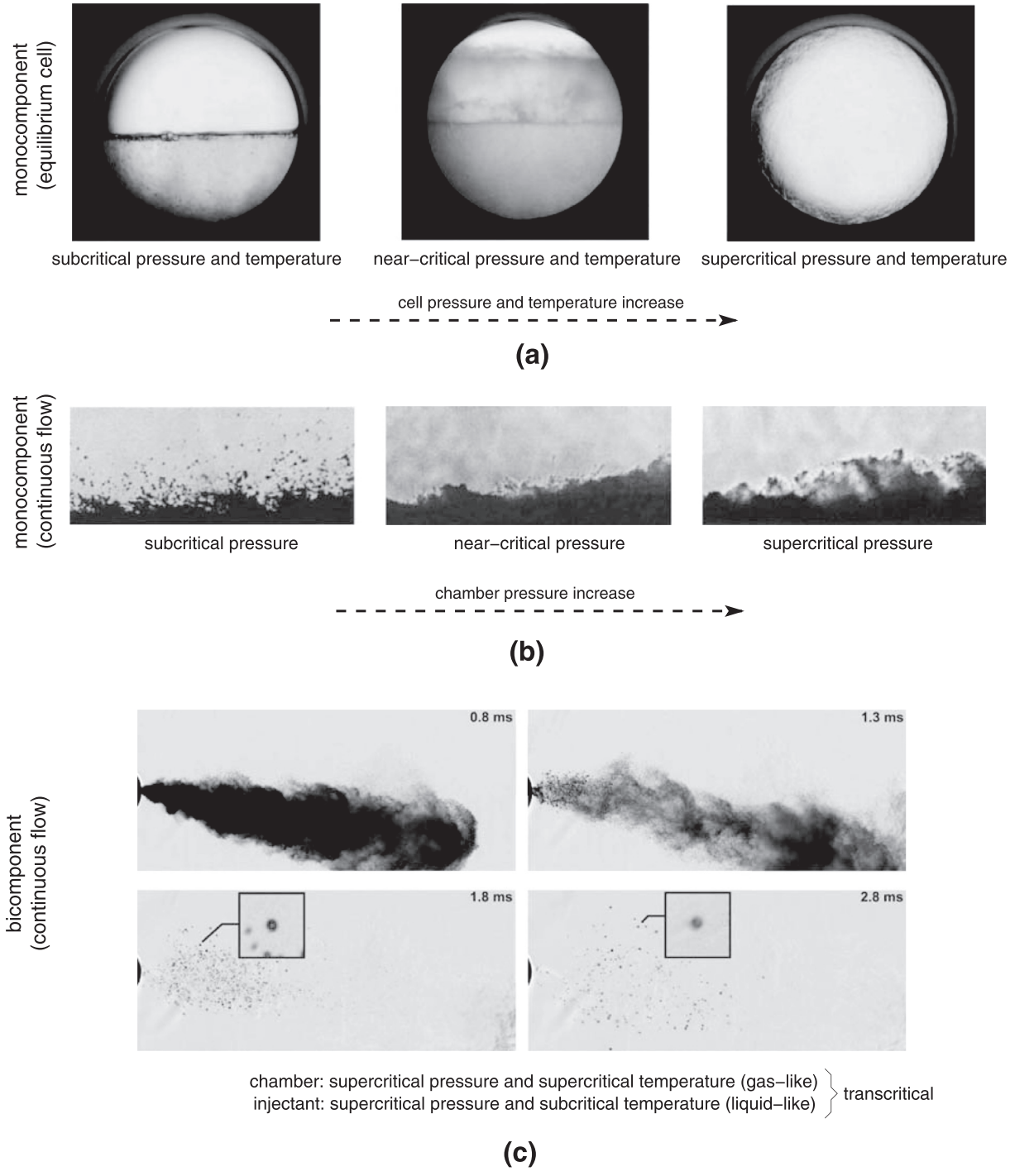

Fig. 5. Experimental visualizations of high-pressure flow systems. (a) Equilibrium cell filled with pure propane at pressure and temperature below the critical point (left panel), at pressure and temperature near the critical point (center panel), and at pressure and temperature above the critical point (right panel) (adapted from Ref. [52]). (b) Cold nitrogen at 105 K (dark stream) injected into a hot nitrogen environment at 300 K at subcritical pressure 10 bar (left panel), near-critical pressure 30 bar (center panel), and supercritical pressure 40 bar (right panel) (adapted from Ref. [6]). (c) N-hexadecane injected at subcritical temperature 300 K (dark stream) into a hot supercritical nitrogen environment at temperature 907 K and pressure 79 bar (i.e., higher than the critical pressures of the individual components). The different panels in (c) correspond to different instants of time after injection cutoff, with insets showing magnified views of fuel droplets (reprinted from Ref. [19] with permission from Elsevier).

between liquid-like and gas-like supercritical behavior is increasingly more difficult to ascertain. Consequently, the dynamical relevance of the pseudo-boiling line diminishes away from the critical point.

The chamber pressure in the jet flow shown in the right panel in Fig. 5(b) is supercritical, but the jet and ambient temperatures are, respectively, smaller and larger than T_{pb}. Many studies have characterized those conditions as transcritical [5,8,26–29,31]. However, surface-tension effects are irrelevant in monocomponent systems above the critical point [53,71–74] as corroborated, for instance, by the absence of a spray in the right panel in Fig. 5(b). Furthermore, the decrease of surface tension with pressure and temperature is continuous, and as a result its value is always of little to no dynamical relevance even at subcritical conditions nearing the critical point in monocomponent systems. As a result, the liquid-like supercritical N_2 jet in the right panel in Fig. 5(b) mixes with

the gas-like supercritical N_2 environment similarly to pure gaseous mixing.

2.2. Transcriticality in bicomponent systems

Bicomponent systems behave fundamentally different from monocomponent ones and can lead to spray formation at combustor pressures that are supercritical with respect to the separate components, $P_\infty > \max\{P_{c,\mathrm{F}}, P_{c,\mathrm{O}}\}$ [15–19,22,23]. As shown in Section 3.2, an important physical characteristic enabling the formation of the spray is that binary mixtures of heavy hydrocarbons with typical oxidizers, including pure oxygen (for rockets) and air (for gas-turbine jet engines and diesel engines), have much higher critical pressures than those of the individual components. For mixtures of n-alkanes with O_2, this effect is easily recognizable as a promontory in the coexistence region of the phase diagram along the pressure axis. For mixtures of n-alkanes with N_2 or air, the maximum pressure of the coexistence region diverges [21,75,76]. Consequently, even at supercritical pressures with respect to both components, the system can traverse the coexistence region when the injection temperatures of the two propellant streams are oppositely placed on either side of it. These incursions in the coexistence region, which engender transcritical behavior in combustors, are particularly likely when the injection temperature of at least one of the propellant streams (typically the heavy hydrocarbon fuel stream) is smaller than its critical temperature.

An innermost zone is encountered within the coexistence region of the thermodynamic phase diagram that is bounded by the spinodal lines similarly to Fig. 4 for a pure component. In binary systems, this zone can exist above the critical pressures of the separate components due to the elevation of the critical pressure of the mixture, as mentioned above. This zone is thermodynamically unstable, in that no stable thermodynamic state exists that describes a spatially homogeneous mixture there. On the contrary, in those conditions, the components tend to stay separated into two fluids bounded by an interface where capillary forces become important. This phenomenon is observed in experiments (e.g., see Refs. [15–23]), but not necessarily in computations unless an appropriate formulation of the problem, such as the diffuse-interface theory developed in this review article, is employed that accounts for interfaces consistently with the thermodynamic stability of the mixture.

In bicomponent systems at high pressures, the fluids on each side of the interface, or on each side of the coexistence region of the thermodynamic phase diagram, cease to be different ordinary phases such as liquid and vapor, and instead become distinct supercritical fluids whose composition depends on the particular configuration. For instance, in the problem depicted in Fig. 1, the two participating fluids are a liquid-like supercritical mixture rich in a heavy hydrocarbon on the fuel side of the interface, and a gas-like supercritical mixture rich in coflow species (e.g., O_2, N_2, or air) on the coflow side of the interface. Fundamental differences between gas-like and liquid-like supercritical $C_{12}H_{26}/N_2$ mixtures are analyzed in Appendix B.4.

In the present theory, the transcritical interface is a physical-space representation of the coexistence region. References to VLE lines at high pressures should therefore be understood as the loci of points where gas-like and liquid-like supercritical fluids – rather than classic vapor and liquid states – coexist. Pseudo-boiling conditions are attained within the transcritical interface, these being understood in multicomponent systems as approximately the conditions where the constant-pressure molar heat of the mixture attains a local maximum, and where transition between liquid-like and gas-like supercritical behavior takes place, as discussed in Appendices B.2 and B.4.

As noted in Section 1.1, the disparity between the critical ($T_{c,\mathrm{F}}$) and injection (T_F) temperatures of the fuel stream plays an important role in the onset of transcriticality in combustors fueled by heavy hydrocarbons. The larger this disparity, the larger the supercriticalization length L_{TR}, and the more favored are transcritical thermodynamic trajectories across the elevated coexistence dome. As indicated in Table 1, $T_{c,\mathrm{F}}$ is typically 200–400 K larger than T_F, since the latter is typically limited to 300–450 K in order to minimize carbon deposition by thermal decomposition of the fuel in feeding systems and engine wall-cooling channels [77]. At those injection temperatures, heavy-hydrocarbon fuels resemble supercritical liquid-like fluids. That tendency increases with the number of carbon atoms due to the corresponding increase in the fuel critical temperature: $T_{c,\mathrm{F}} = 191$ K for CH_4, 508 K for C_6H_{14}, 540 K for C_7H_{16}, 618 K for $C_{10}H_{22}$, and 658 K for $C_{12}H_{26}$. However, this is counterbalanced by an increasing supercriticality in pressure with increasing number of carbon atoms: $P_{c,\mathrm{F}} = 46$ bar for CH_4, 30 bar for C_6H_{14}, 27 bar for C_7H_{16}, 21 bar for $C_{10}H_{22}$, and 18 bar for $C_{12}H_{26}$.

In contradistinction, the critical temperature of the coflow stream is much smaller: $T_c = 155$ K for O_2, 126 K for N_2, and 131 K for air. As a result, the coflow stream often resembles a gas-like supercritical fluid in propulsion systems operating at high pressures, including (a) gas-turbine jet engines, where the air coflow entering the combustor is at $T_\mathrm{O} \sim 700$–1000 K; (b) diesel engines, where the enclosed air near the top-dead center attains similar temperatures; and (c) thrust chambers of O_2-rich staged-combustion rocket engines, where the oxidizer stream is preheated to $T_\mathrm{O} \sim 600$–700 K in a preburner. All these systems operate in the transcritical conditions discussed in Section 1.1.

2.3. Transcriticality in aerospace propulsion systems

Developments in aviation jet-propulsion technologies have been characterized over the last five decades by ever-growing overall pressure ratios (OPR) as a means of increasing thermal efficiency and reducing emissions of CO, CO_2, and unburnt hydrocarbons. This trend is illustrated in Fig. 6(a). The overall pressure ratio of a jet engine can be approximated as $\mathrm{OPR} \approx P_\infty/P_a$, where P_∞ is the combustor pressure and P_a is the ambient pressure at the corresponding flight altitude. At sea level, $P_a = 1$ bar and OPR is approximately equal to P_∞ in bars. Modern engine designs reach $\mathrm{OPR} \sim 50$–60, which translate into fully supercritical combustor pressures $P_\infty \sim 50$–60 bar at takeoff. At these pressures, the fuel is injected as a supercritical liquid-like fluid into a supercritical gas-like air coflow, thereby leading to the transcritical conditions depicted in Fig. 1. Transcriticality in the combustor may persist up to flight altitudes of 2.7 km for OPR=50, and 4.2 km for OPR=60, above which the combustor pressure P_∞ becomes smaller than the critical pressure of air, $P_c = 36$ bar.

Whereas diesel and gas-turbine jet engines are now mature technologies that operate with air and derivatives of kerosene at standardized injection temperatures, the propellant combinations and injection conditions are much more numerous in rocket engines due to big leaps in designs over the last 80 years, as summarized in Table 2. Early developments in rocket propulsion during the V-2 program involved the utilization of a steam-catalyst-generator cycle at subcritical pressure $P_\infty \sim 15$ bar [79]. Motivated by the need of higher thrust to lift heavier payloads to orbit and accomplish longer-range mission profiles in space exploration and military applications, the operating pressures in rocket engines have increased significantly over recent decades, as indicated in Fig. 6(b), and they have reached values much larger than the critical pressures of the propellants. Typical pressures range from $P_\infty \sim 70$ bar in the F-1 gas-generator rocket engine employed during the Apollo program, to $P_\infty \sim 250$–350 bars in thrust cham-

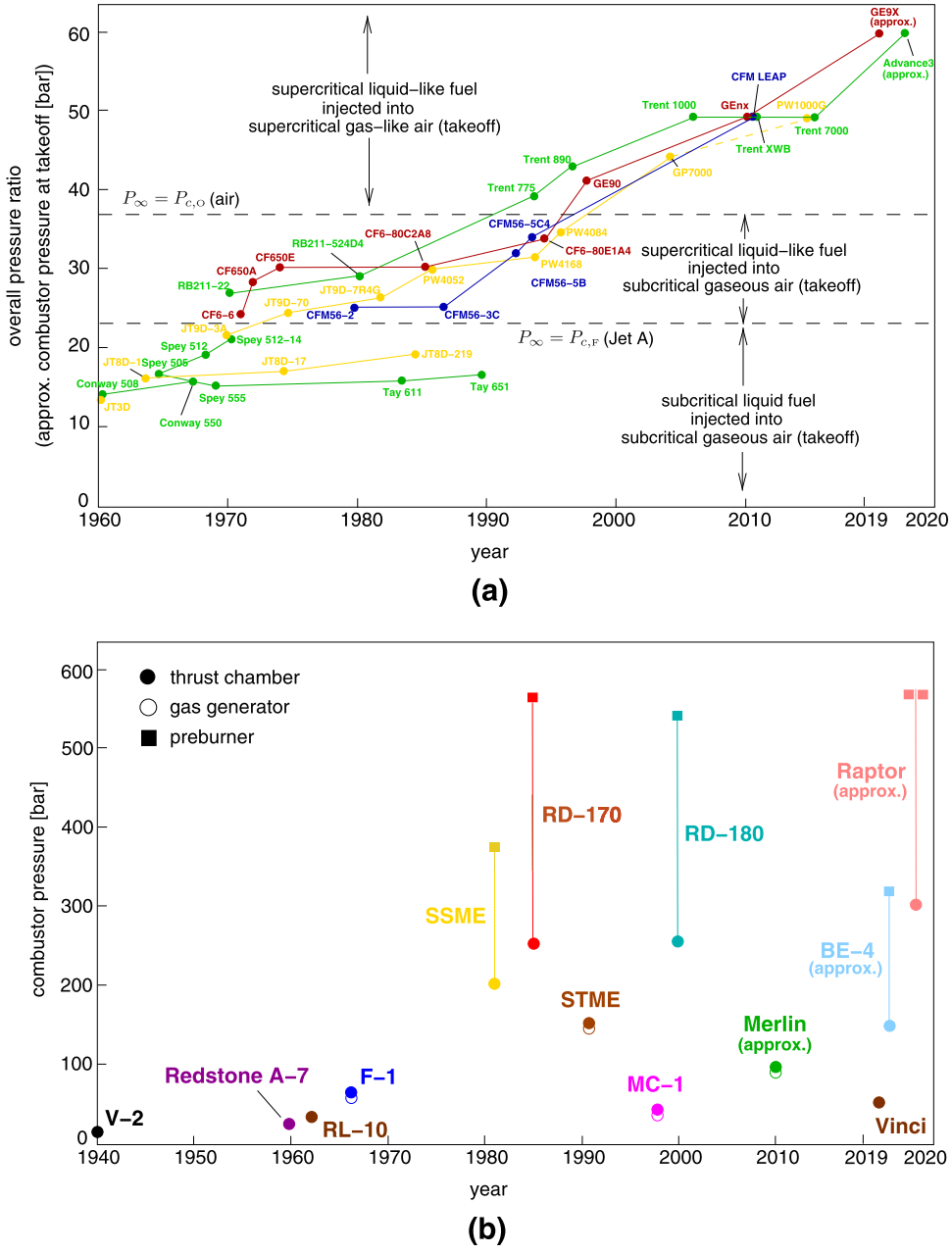

Fig. 6. (a) Overall pressure ratio (or equivalently, combustor pressure P_∞ in bars at sea-level takeoff) for gas-turbine jet engines as a function of time (adapted and extended with data beyond year 2000 from the original version in Ref. [78]). The different colors indicate manufacturers, including Rolls Royce (green), General Electric (red), CFM (blue), and Pratt & Whitney (yellow). The upper and lower dashed horizontal lines mark the OPRs required to reach supercritical combustor pressure with respect to both air ($P_{c,O} = 36$ bar) and Jet-A ($P_{c,F} = 24$ bar [41]) during takeoff at sea level. (b) Pressures in gas generators, preburners, and main thrust chambers of rocket engines as a function of the production year. (For interpretation of the references to color in this figure legend, the reader is referred to the web version of this article.)

bers of modern staged-combustion-based rocket engines such as the RD-180 and Raptor, whose preburners operate at much higher pressures of about 500–600 bar.

In rockets fueled by RP-1 (a highly refined kerosene whose critical point can be approximated as $P_c = 22$ bar and $T_c = 677$ K [42]), the fuel is injected at temperatures ranging from near-storage values $T_F \sim 280$ K in gas generators and preburners, to $T_F \sim 320$ K in thrust chambers after passing through the wall cooling channels. In RP-1-fueled open-cycle systems such as the F-1 and Merlin engines, whose gas generators and thrust chambers operate at 60–100 bar, the liquid oxidizer (LOX) is injected at near-storage cryogenic temperatures $T_O \sim 90$–100 K. As a result, the RP-1 and LOX resemble liquid-like supercritical fluids at injection in the gas generator and thrust chamber. Much higher pressures are achieved in RP-1-fueled closed cycles such as the RD-170 and RD-180 engines. The preburners of these engines operate with RP-1 and LOX injected at very high combustor pressures $P_\infty > 500$ bar but at cold near-storage temperatures, thereby resembling supercritical liquid-like fluids. The O_2-rich hot combustion products from the preburner are expanded in the turbine and injected at temperatures $T_O \sim 600$–700 K along with the cold RP-1 stream into the thrust chamber at pressures larger than 200 bar. The resulting transcritical conditions in the thrust chamber are analogous to those depicted in Fig. 1, with RP-1 and oxidizer entering as liquid-like and gas-like supercritical fluids, respectively.

Table 2
Characteristic propellant injection conditions in rocket engines.

	Gas-generator rocket-engine cycles	
	Gas Generator	Thrust Chamber
F-1 (Saturn-V first stage) [80,81]	$P_\infty = 62$ bar O_2: $T_O = 94$ K (supercritical liquid-like) RP-1: $T_F = 305$ K (supercritical liquid-like)	$P_\infty = 66$ bar O_2: $T_O = 94$ K (supercritical liquid-like) RP-1: $T_F = 315$ K (supercritical liquid-like)
MC-1 [82]	$P_\infty = 40$ bar O_2: $T_O = 94$ K (subcritical liquid) RP-1: $T_F = 300$ K (supercritical liquid-like)	$P_\infty = 44$ bar O_2: $T_O = 94$ K (subcritical liquid) RP-1: $T_F = 300$ K (supercritical liquid-like)
STME (Space Transportation Main Engine) [81]	$P_\infty = 152$ bar O_2: $T_O = 101$ K (supercritical liquid-like) H_2: $T_F = 43$ K (supercritical gas-like)	$P_\infty = 153$ bar O_2: $T_O = 100$ K (supercritical liquid-like) H_2: $T_F = 110$ K (supercritical gas-like)
Merlin (Falcon-9 first stage, approx.) [83]	$P_\infty = 89$ bar O_2: $T_O = 105$ K (supercritical liquid-like) RP-1: $T_F = 303$ K (supercritical liquid-like)	$P_\infty = 100$ bar O_2: $T_O = 105$ K (supercritical liquid-like) RP-1: $T_F = 313$ K (supercritical liquid-like)
	Fuel-rich staged-combustion rocket-engine cycles	
	Preburner	Thrust Chamber
SSME (Space Shuttle Main Engines) [84,85]	$P_\infty = 382$ bar O_2: $T_O = 118$ K (supercritical liquid-like) H_2: $T_F = 154$ K (supercritical gas-like)	$P_\infty = 208$ bar O_2: $T_O = 104$K (supercritical liquid-like) H_2-rich products: $T_F = 810$ K (supercritical gas-like)
	Oxidizer-rich staged-combustion rocket-engine cycles	
	Preburner	Thrust Chamber
RD-170 (Energia-Buran first stage) [81]	$P_\infty = 563$ bar O_2: $T_O = 101$ K (supercritical liquid-like) RP-1: $T_F = 288$ K (supercritical liquid-like)	$P_\infty = 244$ bar O_2-rich products: $T_O = 703$ K (supercritical gas-like) RP-1: $T_F = 414$ K (supercritical liquid-like)
RD-180 (Atlas-V first stage) [86]	$P_\infty = 537$ bar O_2: $T_O = 118$ K (supercritical liquid-like) RP-1: $T_F = 318$ K (supercritical liquid-like)	$P_\infty = 256$ bar O_2-rich products: $T_O = 689$ K (supercritical gas-like) RP-1: $T_F = 480$ K (supercritical liquid-like)
	Expander rocket-engine cycles	
RL-10 (upper stages of Atlas-V and Delta-IV) [87]	$P_\infty = 33$ bar O_2: $T_O = 100$ K (subcritical liquid) H_2: $T_F = 200$ K (supercritical gas-like)	
Vinci (Ariane-6 upper stage) [88]	$P_\infty = 61$ bar O_2: $T_O = 94$ K (supercritical liquid-like) H_2: $T_F = 225$ K (supercritical gas-like)	
	Steam-catalyst-generator rocket engines	
V-2 [79]	$P_\infty = 15$ bar (subcritical) O_2: T_O = unavailable Water/alcohol mixture: T_F = unavailable	
A-7 (Mercury-Redstone) [89]	$P_\infty = 21$ bar (subcritical) O_2: T_O = unavailable Water/alcohol mixture: T_F = unavailable	

In H_2-fueled rocket engines, the role of the fuel and coflow streams is opposite to that shown in Fig. 1, in that the LOX stream occupies the center core, whereas the H_2 stream is the coflow [43,84,85,89]. As discussed in Section 3.2, the thermodynamic phase diagram of H_2/O_2 mixtures is qualitatively similar to those of mixtures of n-alkanes with N_2 or air. Since the H_2 is typically recirculated through the wall cooling channels, or is injected via fuel-rich combustion products exhausted from the preburner, its temperature is always much larger than the critical value $T_c = 33$ K, and often larger than the critical temperature of oxygen. Correspondingly, the H_2 and LOX streams resemble, respectively, gas-like and liquid-like supercritical fluids at injection in thrust chambers of rocket engines such as the SSME or Vinci. The resulting transcritical conditions may involve supercriticalization of the oxidizer stream upon undergoing relatively small temperature increments of order $T_{c,O} - T_O \sim 50$ K by heat transfer from the hot hydrogen stream. However, at elevated pressures, when the combustor is ignited and the orifice ring is thick, results from existing numerical simulations suggest that the ensuing diffusion flame may be anchored so close to the orifice that it would rapidly supercriticalize the oxidizer, thereby diminishing the practical relevance of the transcritical region [25].

Some of the most recent rocket engines currently under design or testing, such as BE4 (oxidizer-rich staged-combustion cycle, $P_\infty \sim 134$ bar in thrust chamber) and Raptor (full-flow staged-combustion cycle, $P_\infty \sim 300$ bar in thrust chamber) operate with CH_4 fuel instead of RP-1. As shown in Section 3.2, CH_4/O_2 mixtures behave differently from mixtures of heavy hydrocarbons with O_2, in that the coexistence region in CH_4/O_2 mixtures does not display a significant elevation above the critical pressures of the separate components. As a result, the diffuse-interface theory presented here predicts no interface formation in CH_4/O_2 systems at supercritical pressures with respect to both propellants above $P_\infty \gtrsim 50$ bar.

2.4. Additional research aspects of transcritical systems

There exist several other aspects that may be of technological and scientific relevance that have been intentionally left out of the remainder of this paper because of their complexity:

(a) The autoxidation and pyrolysis of the heavy-hydrocarbon fuel as it progressively heats up flowing downstream of the injection orifice in transcritical configurations similar to that depicted in Fig. 1. The breakdown of the fuel may cause variations in its physical properties (including surface tension) that could influence atomization [90].
(b) The release of chemical heat as a result of combustion reactions between fuel and oxidizer, which may contribute through conduction and radiation to prompt supercriticalization of the flow upstream and around flames [10,25,32].
(c) The role of the complex thermodynamic-state spaces of tertiary and higher-degree mixtures of heavy hydrocarbons with oxygen, nitrogen, and combustion products at high pressures, the

understanding of which remains mostly incomplete in the literature.

(d) The transition from subcritical to supercritical combustor pressures during ignition sequences, including in-space ignition of upper stages of rocket space launchers or spacecraft reaction-control thrusters [91]. In particular, as observed in the phase diagrams introduced in Section 3, hydrocarbon fuels such as CH_4 injected in subcritical gaseous state at $T_F < T_{c,F}$ early during engine ignition may undergo complex processes until fully supercritical pressures are attained in the combustor, including retrograde condensation when the combustor pressure becomes similar to the phase-equilibrium pressure at T_F.

3. Thermodynamic phase diagrams of mixtures fueled by heavy hydrocarbons

The physical-space solution of the diffuse-interface formulation developed in this review article has a direct correspondence to thermodynamic states in the phase diagram. In this section, quantitative descriptions of phase diagrams of relevant mixtures are provided.

3.1. Equation of state

The thermodynamic space of solutions for the state variables $\{P, \rho, T, \text{and } Y_1, Y_2 ... Y_{N-1}\}$ of a single substance or a mixture of N components is described by its phase diagram. In this notation, Y_i is the mass fraction of species i, with $Y_N = 1 - \sum_{i=1}^{N-1} Y_i$. A first constraint on the state variables that narrows down all of their possible combinations is provided by an equation of state. One popular choice for systems at high pressures, which is used in this study, is the Peng-Robinson equation of state [92]

$$P = \frac{\mathrm{R}^0 T}{v - b} - \frac{a}{v^2 + 2bv - b^2}, \tag{14}$$

where R^0 is the universal gas constant, $v = \overline{W}/\rho$ is the molar volume of the mixture, ρ is the density of the mixture, and $\overline{W} = (\sum_{i=1} Y_i/W_i)^{-1} = \sum_{i=1}^{N} X_i W_i$ is the mean molecular weight, with W_i and $X_i = \overline{W} Y_i / W_i$ the corresponding values of the molecular weight and molar fraction of species i, respectively. The coefficients a and b take into account real-gas effects related to attractive forces and finite packing volume, respectively, and depend on the critical temperatures, critical pressures, and acentric factors of the individual mixture components, as well as on the local temperature and mixture composition. In particular, a and b are obtained by first computing the individual values of the coefficients for each species, a_i and b_i, as specified in Ref. [92] and also provided in Eqs. (C.10)–(C.12) in Appendix C. The individual coefficients a_i and b_i are combined using the empirical van-der-Waals mixing rules

$$a = \sum_{i=1}^{N}\sum_{j=1}^{N} X_i X_j a_{i,j}, \quad a_{i,j} = \left(1 - \vartheta_{i,j}\right)\sqrt{a_i a_j}, \quad b = \sum_{i=1}^{N} X_i b_i, \tag{15}$$

where $\vartheta_{i,j}$ are binary-interaction parameters listed in Appendix C.

Volume-translating corrections to the Peng-Robinson equation (14) exist that provide a higher accuracy of the density near the critical point [93–95], but are not considered in the present study since they tend to lead to a mismatch of the specific heat, which is an undesirable characteristic for describing the transfer of heat across the transcritical interface. As a result, all supplementary thermodynamic relations written in Appendix C have been particularized for the standard version of the Peng-Robinson equation (14).

The particular choice of Eq. (14) as equation of state is not fundamental to the theory developed here. The only indispensable characteristic of Eq. (14) is that it is capable of reproducing

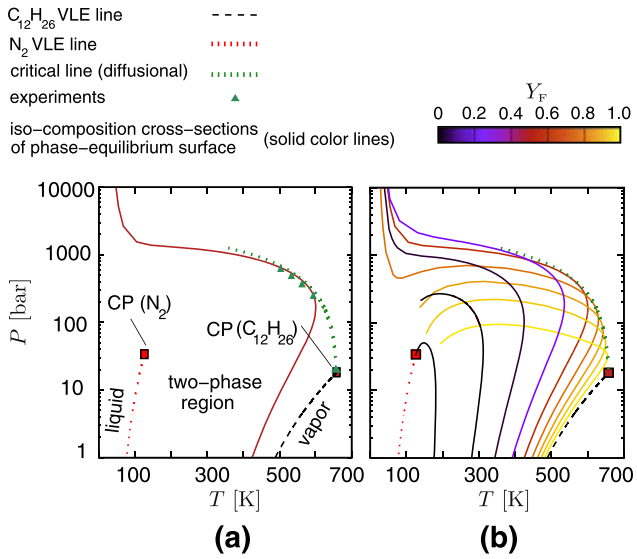

Fig. 7. Iso-composition cross-sections of the phase-equilibrium surface projected on the $P-T$ plane for $C_{12}H_{26}/N_2$ mixtures, including (a) a qualitative description of the diagram for dodecane mass fraction $Y_F = 0.5$, along with (b) a more detailed diagram for multiple values of Y_F. Experimentally measured critical points obtained from Ref. [75] are denoted by triangles in panel (a).

– in conditions of coexistence – the multivalued character of the density (in monocomponent flows) and the fugacity (in multicomponent flows), as discussed in Section 4. Like many other members of the family of cubic equations of state, Eq. (14) provides three values of the density for the same pressure P in the coexistence region in monocomponent flows. Correspondingly, every isotherm passing through the coexistence region contains a single oscillation or Maxwell loop, as shown in Fig. 4. This behavior is consistent with thermodynamic stability theory, which predicts two neutral-stability points, namely the spinodal points. The latter can be unambiguously identified with the maximum and minimum of the looping isotherm. Several other cubic equations of state, including the classic interpolating formula of van der Waals [51], are available in the literature that have similar characteristics and have been ubiquitously employed for treating real-gas effects at high pressures [54,96–99]. Enhanced accuracy in the prediction of thermodynamic states outside the coexistence region can be achieved by using multiparameter equations of state. However, these equations tend to contain multiple Maxwell loops within the coexistence region that lead to artificial intermediate pseudo-stable states [99]. Improved multi-parameter equations of state with depressed or no intermediate loops in the coexistence region have been recently developed that may be amenable to coupling with diffuse-interface formulations [100].

3.2. Critical-point elevation in hydrocarbon-fueled mixtures

This section focuses on numerical calculations of thermodynamic phase diagrams of selected mixtures. Basic concepts of thermodynamic stability and phase equilibrium, including formal definitions of the VLE lines, along with mechanical and diffusional critical lines for mixtures, are required to follow this discussion. Those are provided in Appendix A. In particular, the calculations in this section employ Eq. (A.3) for the mechanical spinodals, Eqs. (A.3) and (A.4) for the mechanical critical line, Eq. (A.9) for the diffusional spinodals, Eqs. (A.9)–(A.11) for the diffusional critical line, along with Eqs. (A.12), (A.13) and (A.15) for the coexistence envelope, with the fugacity being defined in Eq. (B.21) from Appendix B and particularized for the Peng-Robinson equation of state in Eq. (C.47) from Appendix C. These constraints are supplemented with the equation of state (14), where the coefficients a

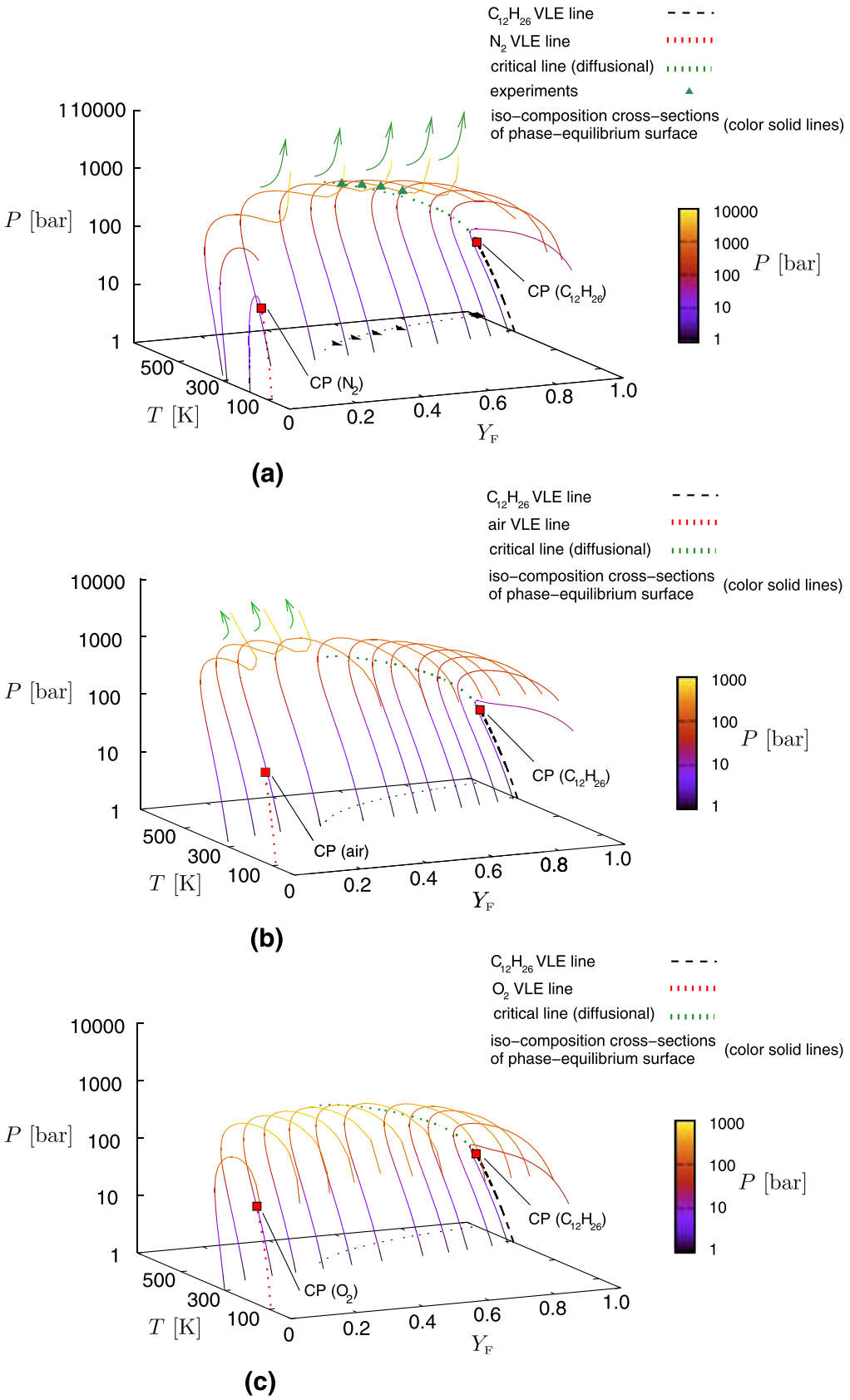

Fig. 8. Iso-composition cross-sections of the phase-equilibrium surface colored by pressure for (a) $C_{12}H_{26}/N_2$ mixtures, (b) $C_{12}H_{26}$/air mixtures, and (c) $C_{12}H_{26}/O_2$ mixtures. Pure-substance boiling lines for $C_{12}H_{26}$ (dark dashed lines) and N_2/O_2/air (red dotted lines) are shown, along with their corresponding critical points (CP; squares) and the critical line of the mixture (green dotted lines). Experimentally measured critical points obtained from Ref. [75] are denoted by green triangles in panel (a). 2D projections of the critical line (dark dotted lines) and experimental data (dark triangles) on the $T - Y_F$ plane are also provided. Arrows indicate diverging behavior of isocomposition lines along the pressure axis. (For interpretation of the references to color in this figure legend, the reader is referred to the web version of this article.)

and b are computed using the mixing rules (15) in conjunction with Eqs. (C.10)–(C.12). Auxiliary quantities required for the calculations include the critical pressures and temperatures listed in Table 1, along with the acentric and binary-interaction parameters listed in Appendix C. Combustion chemical reactions are neglected here when constructing phase diagrams involving mixtures of fuel and oxidizer because of the relatively low temperatures considered within the visualization windows. Practical methods for the calculation of VLE and diffusional critical lines are available in Refs. [101–105].

Depending on the physical properties of the mixture components, binary mixtures can be classified in types that display vastly different forms of the phase diagram. Details on such classification can be found in Ref. [106], which employs the van der Waals equation of state subject to phase-equilibrium and critical-point constraints such as those in Appendix A (see also Ref. [107] for a historical perspective on this subject). Specifically, the analysis and associated simplifications carried out in Ref. [106], including the assumption of equal excluded volumes $b_F \approx b_O$ (or equivalently, $T_{c,O}/T_{c,F} \approx P_{c,O}/P_{c,F}$), pointed at the difference between the critical temperatures of the two components, $|T_{c,F} - T_{c,O}|$, as an important factor in determining the structure of the coexistence region of the mixture at high pressures. Several other factors may however participate when more complex equations of state are used because of the additional parameters involved. In addition, in the mixtures fueled by heavy hydrocarbons examined here, the less volatile component (i.e., the heavy-hydrocarbon fuel) does not always have the largest critical pressure. Despite these shortcomings, some of the qualitative observations made in Ref. [106], including the occurrence of coexistence regions that are unbounded in pressure, hold true in the present analysis.

In $C_{12}H_{26}/N_2$ mixtures described by the Peng-Robinson equation of state (14) and the mixing rules (15), the phase diagram does not contain a continuous critical line joining the critical points of the individual components, and the coexistence region becomes unbounded in pressure. This phenomenon is shown in the thermodynamic phase diagram in Fig. 7, where isocomposition projections of the phase-equilibrium surface on the $P-T$ plane are provided. A three-dimensional visualization of the elevation of the critical point in the thermodynamic space formed by P, T, and Y_F is shown in Fig. 8(a) also for $C_{12}H_{26}/N_2$ mixtures. There, the coexistence region is enclosed under the surface enveloping the isocomposition curves and reaches pressures of order 1500 bar at ambient temperature.

The computation of critical points in complex mixtures involves a number of assumptions and model-parameter values that find no clear justification on physical grounds. For instance, the mixing rules (15) correspond to molar weighting of the individual coefficients a_i and b_i, whose expressions depend on calibrated interaction parameters and measured critical points of the pure substances (see Appendix C). It is however remarkable that the critical line calculated in Figs. 7 and 8(a) agrees well with values experimentally obtained in Ref. [75], including the divergent trend of the critical pressure.

Since N_2 is a major component of air, both $C_{12}H_{26}/N_2$ and $C_{12}H_{26}$/air mixtures lead to similar thermodynamic behavior, as shown in Fig. 8(b). Note that the mechanical critical point of air provided in Table 1 is very similar to its diffusional critical point ($P_c = 37$ bar, $T_c = 131$ K) obtained in Fig. 9(a) using Eqs. (A.9) and (A.11). This is because the coexistence envelope of N_2/O_2 mixtures does not exceed the critical pressures of the separate components.

Mixtures of heavy hydrocarbons with O_2 do not generally lead to coexistence envelopes unbounded in pressure. However, a bounded elevation of the critical point still occurs in those mixtures, as shown in Figs. 8(c) and 9(b), where a promontory in pressure is observed in the coexistence region up to approximately 700 bar at ambient temperature.

Table 3
Pressure, temperature, and composition at diffusional critical points and critical mixing conditions in $C_{12}H_{26}/N_2$ mixtures.

	Diffusional critical point		Critical mixing conditions	
P_∞ [bar]	$T_{c,\mathrm{diff}}$ [K]	$Y_{\mathrm{Fc,diff}}$	$T_{c,\mathrm{mix}}$ [K]	$Y_{\mathrm{Fc,mix}}$
20	658	0.99	658	0.99
50	650	0.93	651	0.94
100	639	0.85	641	0.86
200	615	0.72	620	0.76

Additional phase diagrams of relevant binary mixtures are provided in Fig. 9(c–f). Mixtures of N_2 with C_7H_{16}, or with a major combustion product such as CO_2, along with mixtures of H_2 with O_2 or N_2, all lead to a very similar behavior to the one described above for $C_{12}H_{26}/N_2$ systems. However, the coexistence region in H_2-fueled mixtures exists only for a narrow interval of cryogenic temperatures, whose width decreases rapidly with increasing pressure. In contrast, mixtures of O_2 with C_7H_{16} or CO_2 lead to bounded coexistence regions similar to that observed in Fig. 8(c) for $C_{12}H_{26}/O_2$ mixtures.

Important practical systems that do not feature any significant elevation of the critical point are mixtures of CH_4 with O_2, and CH_4 with air or N_2, which are relevant for new generations of rocket engines (e.g., BE-4 and Raptor) and for land-based gas turbines, respectively. In those mixtures, the pressure of the diffusional critical line is never too far above the critical pressures of the separate components. As a result, those systems are mostly dominated by interfaceless, homogeneously mixed states when the pressure is supercritical with respect to both components ($P \gtrsim 50$ bar).

Constant-pressure cross-sections of the $P-T-Y_F$ phase diagram are provided in Fig. 10 for $C_{12}H_{26}/N_2$ mixtures. As the pressure increases, Fig. 10 indicates that the mixture composition and temperature corresponding to the diffusional critical point becomes fuel-leaner and colder, respectively. For $C_{12}H_{26}/N_2$ mixtures, and within the interval of pressures reported in Fig. 10, the temperature of the diffusional critical point $T_{c,\mathrm{diff}}$ does not differ much from the fuel critical temperature $T_{c,F}$, with $T_{c,F} - T_{c,\mathrm{mix}} \sim 43$ K being the largest difference observed at 200 bar. Similarly, $T_{c,\mathrm{diff}}$ is approximately equal to the critical mixing temperature $T_{c,\mathrm{mix}}$ corresponding to the maximum temperature attained along the VLE line at a given pressure. Table 3 shows that the difference $T_{c,\mathrm{mix}} - T_{c,\mathrm{diff}}$ increases as the pressure increases, although the maximum value is only 5 K at 200 bar. The system may sample the coexistence region within the very small gap of temperatures $T_{c,\mathrm{diff}} \le T \le T_{c,\mathrm{mix}}$, but the thermodynamic states there are metastable, and for all practical purposes, they can be considered as fully supercritical.

Although no equilibrium trajectories connecting the two injection states of the propellants exist in general flows, it is convenient to locate along a trajectory on the phase diagram the local thermodynamic state of points normal to the transcritical interface in the configurations that will be addressed in Sections 6 and 7. In this study, these trajectories are referred to as pseudo-trajectories to emphasize that they are not thermodynamic trajectories followed by the system by quasi-statically changing its state, as traditionally meant in the theory of thermodynamics of closed systems. A notional envelope of transcritical pseudo-trajectories is provided in Fig. 10 that joins the characteristic injection-temperature ranges $T_F \sim 300$–450 K and $T_O \sim 700$–1000 K of the propellant streams. It will be shown in Sections 6 and 7 that transcritical pseudo-trajectories are characterized by crossing the coexistence region of the thermodynamic phase diagram of the mixture. Note, however, that any pseudo-trajectory plotted on constant-pressure cross-sections of the thermodynamic phase diagram, such as those in

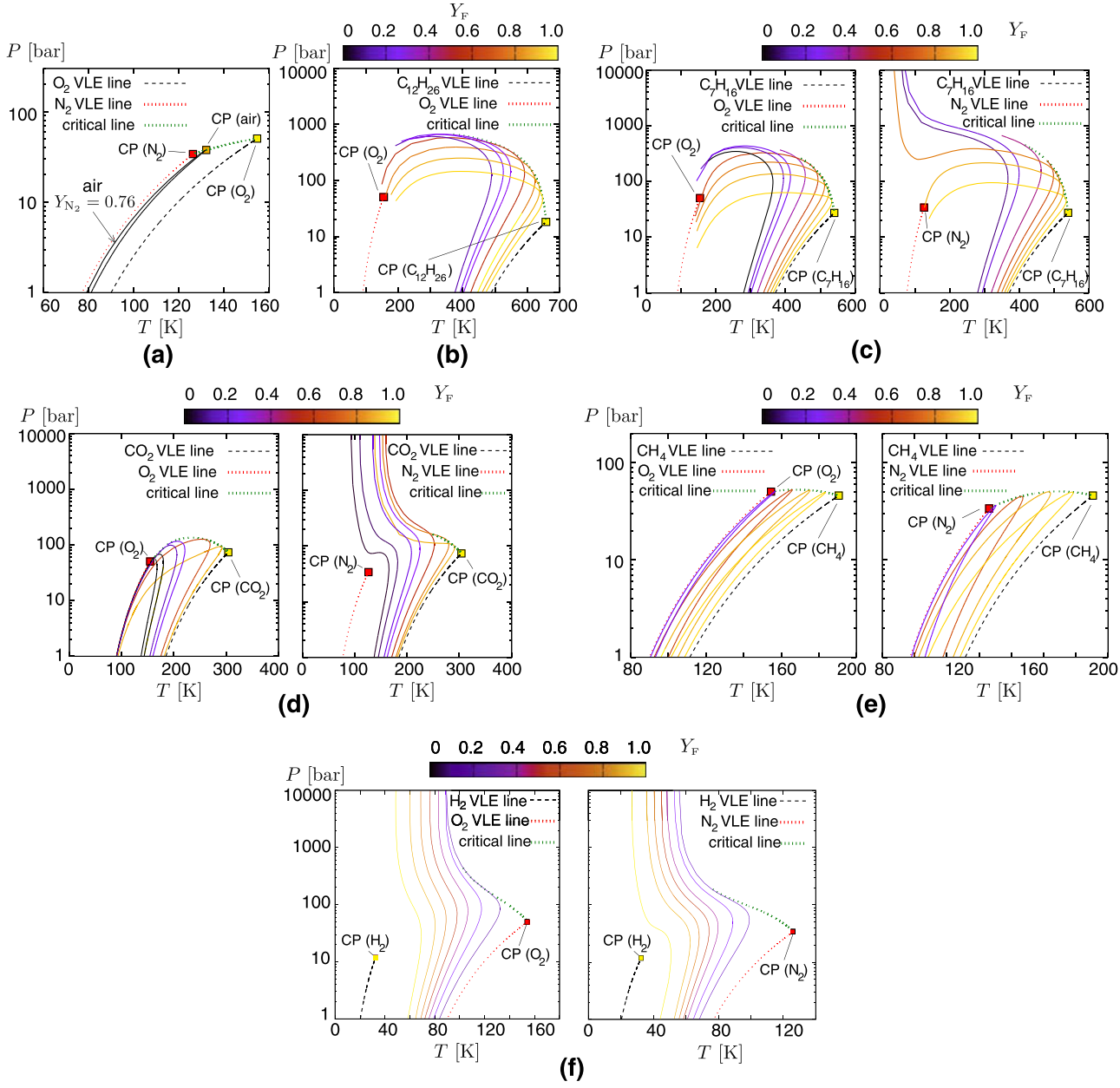

Fig. 9. Iso-composition cross-sections of the phase-equilibrium surface projected on the $P-T$ plane for (a) N_2/O_2 mixtures, (b) $C_{12}H_{26}/O_2$ mixtures, (c) C_7H_{16} mixed with O_2 (left) or N_2 (right), (d) CO_2 mixed with O_2 (left) or N_2 (right), (e) CH_4 mixed with O_2 (left) or N_2 (right), and (f) H_2 mixed with O_2 (left) or N_2 (right). The diagrams include diffusional critical lines (green-dotted lines), and pure-substance VLE lines (dark dashed and red-dotted lines) with their corresponding critical points (CP; squares). (For interpretation of the references to color in this figure legend, the reader is referred to the web version of this article.)

Fig. 10, should be interpreted with caution, since significant variations of the thermodynamic pressure occur across the interface away from the edge, as discussed in Sections 4 and 5.

The considerations above suggest that the selection of particular values of injection temperatures and combustor pressures may lead to operating conditions without transcritical interfaces. For instance, if the injection temperature of $C_{12}H_{26}$ in Fig. 10 is increased to values larger than $T_{c,\mathrm{diff}}$ while maintaining constant the hot temperature of the nitrogen coflow, the pseudo-trajectories will not cross the coexistence region, and the flow will not bear any transcritical interfaces. This circumvention of the coexistence region may be achieved dynamically because of supercriticalization of the fuel stream by heat transfer from the coflow, as shown in Fig. 2 and discussed in Section 7.

The limiting pressure above which interfaces cannot exist at a given injection temperature of the cold propellant stream is provided in Fig. 11 for two different configurations: (a) one in which the fuel is cold and the coflow (N_2 or O_2) is hot (a configuration relevant for propulsion systems fueled by heavy hydrocarbons as in Fig. 1), and (b) one in which the fuel is hot and the oxidizer is cold (a configuration relevant for rocket engines fueled by hydrogen). Specifically, Fig. 11 provides $T_{c,\mathrm{diff}}$ as a function of P_∞ for different mixtures. The point of intersection between the diffusional critical temperature and the horizontal line corresponding to the chosen value of the injection temperature of the cold propellant stream defines the combustor pressure above which interfaces cannot exist because the pseudo-trajectories of the system will circumvent the coexistence region. For instance, considering an injection temperature $T_F = 300$ K for a fuel stream of $C_{12}H_{26}$ or C_7H_{16} into a coflow of N_2 or O_2, the limiting pressures that lead to absence of interfaces are $P_\infty \simeq 1500$ bar (for $C_{12}H_{26}/N_2$), $P_\infty \simeq 690$ bar (for $C_{12}H_{26}/O_2$), $P_\infty \simeq 820$ bar (for C_7H_{16}/N_2), and $P_\infty \simeq 410$ bar (for

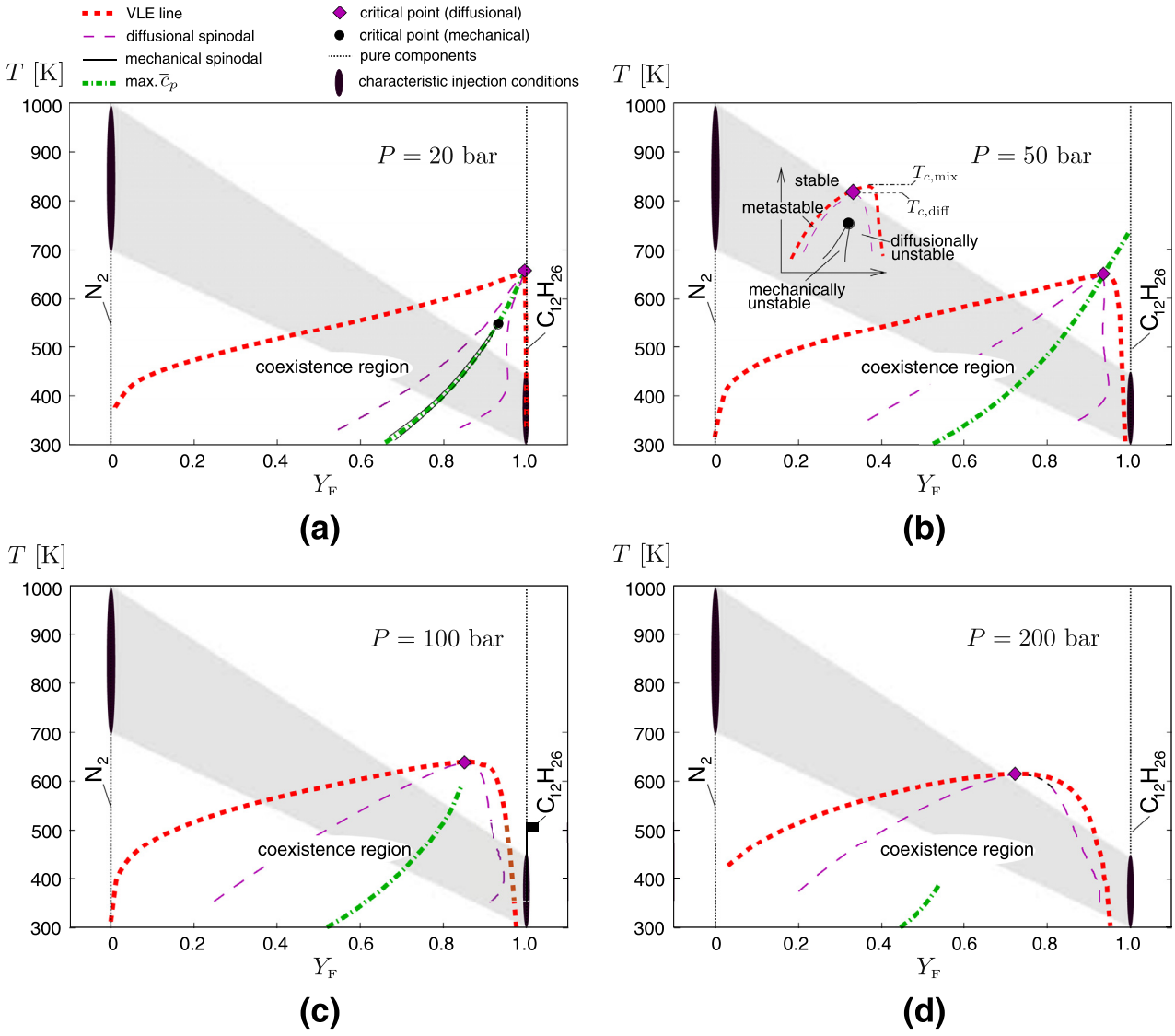

Fig. 10. Constant-pressure $T - Y_F$ cross-sections of the phase diagram, including diffusional critical points (diamond symbols with coordinates) and vapor-equilibrium lines (thick red dashed lines) bounding the coexistence region of $C_{12}H_{26}/N_2$ mixtures at different pressures, along with the corresponding diffusional spinodal lines (thin purple dashed lines) and the loci of the maximum of the molar heat at constant pressure (thick green dot-dashed line) at each pressure. The mechanical critical point (solid circle) and the mechanical spinodal lines (thin solid lines) are provided only for the lowest pressure case. For pressures larger than 30 bar, the mechanically unstable region lies at much lower temperatures than those shown in the figure. Solid ellipses denote characteristic injection conditions of N_2 (left) and $C_{12}H_{26}$ (right), while shaded regions are notional envelopes of pseudo-trajectories joining thermodynamic states along the normal to the interface. (For interpretation of the references to color in this figure legend, the reader is referred to the web version of this article.)

C_7H_{16}/O_2). Similarly, for a cryogenic O_2 stream at $T_O = 110$ K surrounded by a hot coaxial stream of H_2, the corresponding limiting pressure above which the flow cannot bear transcritical interfaces is $P_\infty \simeq 290$ bar.

3.3. Conditions suppressing transcritical behavior

The combustor pressure and injection temperatures can be varied in the following manner in order to suppress transcritical interfaces in the flow:

(a) Increasing the combustor pressure: The higher P_∞, the smaller $T_{c,\mathrm{mix}}$ and $T_{c,\mathrm{diff}}$ are, and the narrower the coexistence region is along the temperature and composition axes of the thermodynamic phase diagram.
(b) Increasing the temperature of the coflow stream: The higher T_O, the more likely pseudo-trajectories will circumvent the coexistence region or will traverse it across its largest pressure values, where the density gradients are small.
(c) Increasing the temperature of the fuel stream: The higher T_F, the less likely the pseudo-trajectories will cross the coexistence region.

These observations have been ratified by recent experiments [18,19].

4. Theoretical foundations of the diffuse-interface theory for transcritical flows

Crossings of the thermodynamically unstable regions in Fig. 10 require modifications of the constitutive laws in the Navier-Stokes equations. This section introduces basic assumptions, parameters, and scalings of the diffuse-interface theory, and outlines a set of conservation equations that serve as groundwork for the derivation of constitutive laws in Section 5.

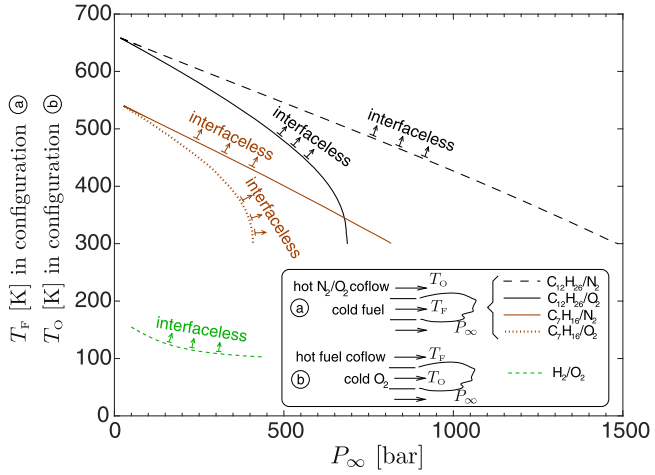

Fig. 11. Combustor pressures and injection temperatures of the cold propellant stream leading to absence of interfaces. The lines denote the diffusional critical temperature $T_{c,\mathrm{diff}}$ of the corresponding mixture. For a given value of T_F (in configuration ⓐ) or T_O (in configuration ⓑ), the intersection with the diffusional critical temperature provides the limiting combustor pressure P_∞ above which interfaces cannot exist.

4.1. Gradient-dependent thermodynamic potentials

The diffuse-interface theory was first formulated by van der Waals in Ref. [108], where the finite-thickness structure of an interface between liquid and vapor phases in isothermal hydrostatic monocomponent systems was described by performing spatial integrations of the intermolecular potential in the presence of a mean density gradient. The reader is referred to seminal treatises based on the molecular theory of liquids for in-depth expositions of the topic [53]. This formalism was later extended to study binary mixtures near the critical point by Cahn and Hilliard [109]. More recently, notable work has been done to couple consistently the diffuse-interface theory of van der Waals with conservation equations of fluid motion [110–115]. Developments of the diffuse-interface theory for treating the mechanics of interfaces in complex mixtures have been applied mostly to 1D phase-transitioning systems in hydrostatic equilibrium at uniform temperature to provide predictions of the surface-tension coefficients [116–118]. The investigation of hydrodynamic and thermal effects in the formulation is a discipline that is currently in its infancy.

The diffuse-interface theory of van der Waals addresses monocomponent thermodynamic systems traversing the coexistence region as they become macroscopically separated into phases. Specifically, the diffuse-interface theory describes the mechanics of the transition layer, which gives rise to familiar surface-tension forces emerging from the resistance of the interface to get deformed. Although the predicted interfaces are hydrodynamically thin, and the theory is formulated at the continuum level, the results agree well with experiments and molecular dynamics simulations [99,116–119].

On average, molecules in ideal gases are separated by long distances that make the intermolecular forces negligible. In contrast, the increased molecular packing at high pressures requires consideration of intermolecular forces, which are manifested by the second term in the equation of state (14) involving the coefficient a. The latter is proportional to the zeroth-moment of the intermolecular potential in the far-field attraction range [53]. In highly density-stratified conditions as those found across interfaces in monocomponent systems, the effect of long-range attraction forces is compounded by the fact that the integration of the spherico-symmetric intermolecular potential across the stratified zone results in a gradient-dependent free energy [108]. This is represented by a correction to the bulk free energy that involves a coefficient multiplied by the square of the density gradient [111].

The equivalent description of thermodynamic potentials in multicomponent systems is based on the gradients of the partial densities [116,117]. For instance, the specific values of the gradient-dependent Helmholtz free energy f, internal energy e, and entropy s are [38,39,110]

$$f_{\mathrm{GD}} = f + \frac{1}{2\rho}\sum_{i=1}^{N}\sum_{j=1}^{N}\kappa_{i,j}\nabla(\rho Y_i)\cdot\nabla(\rho Y_j), \tag{16}$$

$$e_{\mathrm{GD}} = e + \frac{1}{2\rho}\sum_{i=1}^{N}\sum_{j=1}^{N}\kappa^{e}_{i,j}\nabla(\rho Y_i)\cdot\nabla(\rho Y_j), \tag{17}$$

$$s_{\mathrm{GD}} = s + \frac{1}{2\rho}\sum_{i=1}^{N}\sum_{j=1}^{N}\kappa^{s}_{i,j}\nabla(\rho Y_i)\cdot\nabla(\rho Y_j), \tag{18}$$

where f is defined as

$$f = e - Ts. \tag{19}$$

In this notation, N is the number of species, and $\kappa_{i,j}$, $\kappa^{e}_{i,j}$, and $\kappa^{s}_{i,j}$ are gradient-energy coefficients discussed in Section 4.2. In this formulation, f, e and s are evaluated at local conditions $\{P,\ \rho,\ T,$ and $Y_1,\ Y_2 \ldots Y_{N-1}\}$ within the interface.

4.2. Gradient-energy coefficients

Expressions relating $\kappa^{e}_{i,j}$, $\kappa^{s}_{i,j}$ and $\kappa_{i,j}$ can be easily derived by substituting Eqs. (16)–(18) into Eq. (19), which gives

$$\kappa^{e}_{i,j} = \kappa_{i,j} + T\left(\frac{\partial\kappa_{i,j}}{\partial T}\right)_{\rho,Y_{k|k=1,\ldots N}} \quad \text{and} \quad \kappa^{s}_{i,j} = -\left(\frac{\partial\kappa_{i,j}}{\partial T}\right)_{\rho,Y_{k|k=1,\ldots N}}, \tag{20}$$

where the definition $s = -(\partial f/\partial T)_{\rho,Y_i|i=1,\ldots N-1}$ has been used. The determination of the gradient-energy coefficients, which are directly related to the interface thickness and surface tension, constitutes a major source of uncertainty in the formulation, since they either require knowledge of the underlying molecular structure of the fluid, or must be tuned by comparing theoretical results with experimental data.

Models for the gradient-energy coefficients often rely on correlations such as

$$\frac{\kappa_{i,i}W_i^2N_A^{2/3}}{a_i{b_i}^{2/3}} = \mathcal{G}(\theta_i). \tag{21}$$

In this formulation, $T_{c,i}$ is the critical temperature of species i, N_A is the Avogadro's number, and a_i and b_i correspond to coefficients of the equation of state. The function $\mathcal{G}(\theta_i)$ depends on the reduced temperature $\theta_i = 1 - T/T_{c,i}$ and is calibrated from experimental data. One class of experiments used for calibration consists in enclosing a monocomponent fluid in an equilibrium cell [e.g., see Fig. 5(a)] and measuring its surface-tension coefficient σ [15,72,116–118]. As discussed in Section 5.3 (see also Ref. [117]), the diffuse-interface theory for monocomponent flows predicts that σ is given by

$$\sigma = \int_{-\infty}^{\infty}\kappa\left(\frac{\partial\rho}{\partial\hat{n}}\right)^2 d\hat{n}, \tag{22}$$

where $\hat{n}$ is a spatial coordinate locally normal to the interface. Values of κ as a function of temperature can be inferred from Eq.

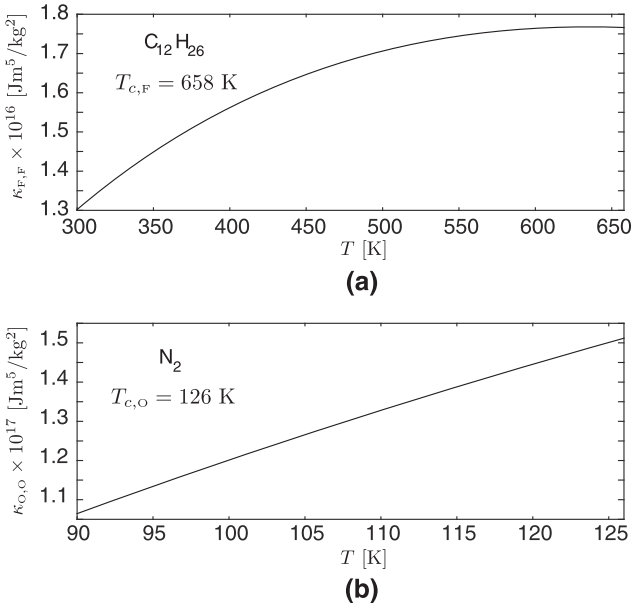

Fig. 12. Gradient-energy coefficients $\kappa_{i,i}$ for monocomponent systems composed of (a) $C_{12}H_{26}$ and (b) N_2, as obtained by using expression (23) in conjunction with the equation of state (14).

(22) by using measurements of σ in the equilibrium cell. The resulting function $\mathcal{G}(\theta_i)$ can be represented as [120]

$$\frac{\kappa_{i,i} W_i^2 N_A^{2/3}}{a_i {b_i}^{2/3}} = \mathcal{A}_i \left(1 - \frac{T}{T_{c,i}}\right) + \mathcal{B}_i. \tag{23}$$

The dimensionless coefficients $\mathcal{A}_i$ and $\mathcal{B}_i$ are provided in Eqs. (C.17) and (C.18) (see also Refs. [116,120]). The resulting dependency of the gradient-energy coefficient on temperature is shown in Fig. 12 for $C_{12}H_{26}$ and N_2. Validations of the model (23) are provided in Section 6 and Appendix D.

Three approximations in the gradient-energy coefficients are made in the theory developed here:

(a) For simplicity, the gradient dependency of s is neglected in comparison with similar long-range effects on f and e, or equivalently

$$\left| T \left(\frac{\partial \kappa_{i,j}}{\partial T} \right)_{\rho, Y_{k|k=1,\dots N}} \right| \ll \kappa_{i,j}, \tag{24}$$

which gives $\kappa^e_{i,j} \approx \kappa_{i,j}$ and $T|\kappa^s_{i,j}| \ll \kappa_{i,j}$.

(b) The long-range interaction between components in mixtures, measured by the cross-influence parameters $\kappa_{i,j}$ $(i \neq j)$ are modeled as

$$\kappa_{i,j} = (1 - \upsilon_{i,j}) \sqrt{\kappa_{i,i} \kappa_{j,j}} = \kappa_{j,i}, \tag{25}$$

with $\upsilon_{i,j} = 0$ chosen for simplicity [117], although no rigorous justification for such geometric averaging appears to exist yet other than experimental observations of indirect quantities that ratify this choice [121].

(c) As shown in Section 5.6, the largest variations of the temperature occur across distances much larger than the interface thickness. Correspondingly, it is assumed herein that $\kappa_{i,j}$ varies slowly in space around the interface, and therefore commutes with spatial derivatives. Temperature-induced variations in $\kappa_{i,j}$ are included explicitly by evaluating $\kappa_{i,j}$ at the local temperature in all expressions.

These approximations were also implicitly used in the original diffuse-interface theory of van der Waals [108].

4.3. Open issues of experimentally calibrated models for gradient-energy coefficients

Gradient-energy coefficients computed from experimentally calibrated relations such as Eq. (23) are contrived by the manner that experiments are carried out. As the equilibrium cell is heated, and starting from a phase-separated state in vapor-liquid equilibrium, both P and T reach their critical values simultaneously because of vapor-liquid equilibrium. As a result, the pressure dependency on Eq. (23), and similar ones encountered in the literature, is artificially concealed in the temperature. Relevant steps toward improved models of gradient-energy coefficients have been recently undertaken by Dahms [100] using parametrizations of $\kappa_{i,j}$ in terms of the local partial-density gradients instead of temperature.

Contrary to theoretical predictions [53,120], which suggest that the gradient-energy coefficient diverges near the critical point of the component, there are experimentally calibrated models such as Eq. (23) that remain finite there, as observed in Fig. 12. However, the singularity predicted by the theory is weak and in practice is overruled by the rapid decrease in the density gradients on approach to the critical point, where both σ and $d\sigma/dT$ vanish.

Additional complications arising from the utilization of Eq. (23) or analogous ones [118] is that the experimentally calibrated gradient-energy coefficients are not defined for $T > T_{c,i}$. Recall that a monocomponent system cannot engender any surface tension for $T > T_c$, since, as indicated in Fig. 4, only a single homogeneous thermodynamic state is possible above the critical point. As a result, the calibration of $\kappa_{i,i}$ must necessarily stop at $T > T_{c,i}$. In the transcritical conditions in Fig. 1, in which $T_O > T_{c,F} > T_F > T_{c,O}$, the gradient-energy coefficients given by Eq. (23) are not defined in regions of the flow where the local temperature is larger than the critical temperature of the corresponding component. This has the following implications:

(a) Since the injection temperatures considered here are $T_F \sim 300$–450 K and $T_O \sim 700$–1000 K, the temperature is everywhere larger than the critical temperatures of typical coflowing species, including N_2, O_2, and air. Consequently, the only gradient-energy coefficient that is defined and explicitly appears in the formulation is that of the fuel, denoted here by $\kappa_{F,F}$.

(b) The fuel gradient-energy coefficient $\kappa_{F,F}$ ceases to be defined on the coflow side of the interface where $T > T_{c,F}$.

However, these limitations do not have significant consequences on the theory developed here. As discussed in Section 1, the interface vanishes at an edge when its temperature nears the temperature of the diffusional critical point $T_{c,\text{diff}}$, which is $10 - 40$ K smaller than $T_{c,F}$ in the pressure range P_∞=50–200 bar. Correspondingly, regions where $\kappa_{F,F}$ is not defined because $T > T_{c,F}$ are located either far away from the interface on the coflow side, or downstream of the interface edge, as schematically indicated in Fig. 13. Since composition gradients in those regions are small compared to those encountered across the interface, the gradient-dependent corrections of the local thermodynamic potentials are dynamically irrelevant there regardless of whether $\kappa_{F,F}$ is made to artificially plunge to zero at $T = T_{c,F}$, or is extrapolated for $T > T_{c,F}$.

From a molecular-scale perspective, $\kappa_{i,j}$ can be shown to be proportional to the second moment of the intermolecular potential (e.g., see Ch. 4 in Ref. [53] for details). It can also be expressed in terms of the direct correlation function in both single- and multicomponent systems [122,123]. It is conceivable that future developments in hydrodynamic applications of the diffuse-interface theory for high-pressure interfaces would benefit from models of $\kappa_{i,j}$ that could be cognizant of the microscale structure of supercritical fluids and their mixtures. Multiscale modeling strategies based on combination of molecular dynamics and continuum-level theories

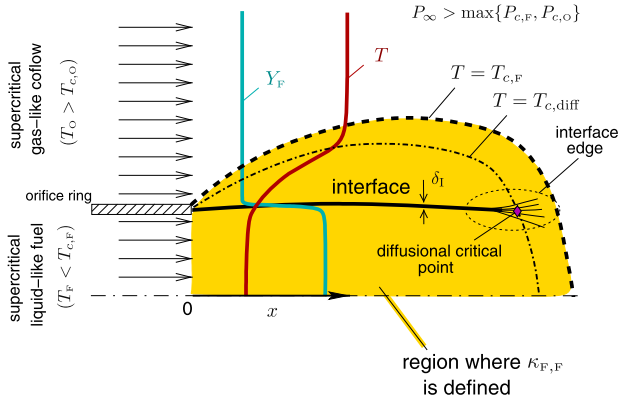

Fig. 13. Schematics of the region enclosed by the fuel critical isotherm $T = T_{c,F}$ (gold colored zone), where the fuel gradient-energy coefficient $\kappa_{F,F}$ is defined according to the model (23).

or simulations may bear some potential for on-the-fly calculations of $\kappa_{i,j}$ based on direct correlation functions [124,125].

4.4. Characteristic scales in the diffuse-interface theory

The disparity between the interface thickness δ_I and the macroscopic flow scales δ_T, R_I, and R_F plays a central role in the dynamics of the interface. The value of δ_I is closely connected with the gradient-energy coefficient and with the surface tension σ. In particular, Eq. (22) indicates that the gradient-energy coefficient scales as

$$\kappa \sim \sigma_0 \delta_I / \rho_F^2, \tag{26}$$

where σ_0 is a characteristic value of the surface tension, and ρ_F is the density of the fuel stream. In performing the estimate (26), the characteristic density difference across the interface has been approximated as $\rho_F(1 - 1/\mathcal{R}) \approx \rho_F$, with $\mathcal{R} \gg 1$ the density ratio defined in Eq. (4).

To understand the role of the gradient-energy coefficient in the present theory, it is important to note that any thermodynamic variable that oscillates across the coexistence region in the phase diagram can be mapped into physical space within an interface-like profile of an indicator function such as $\rho(\hat{n})$ in monocomponent flows, or the partial densities in multicomponent flows. Although the details of the mapping depend on the particular problem and thermodynamic quantity under consideration, it is illustrative to momentarily sideline the problem in Fig. 1 and focus on the most idealized case that can be addressed with the diffuse-interface theory, namely that of a flat interface in a monocomponent isothermal flow. In this case, the mapping is simpler and the free-stream densities correspond to those in phase equilibrium, i.e., $\rho_F = \rho_e^\ell$ and $\rho_O = \rho_e^g$.

As discussed in Appendix A.2, in phase equilibrium, the chemical potentials in both streams are the same and equal to the equilibrium value μ_e [see Eq. (A.16)]. Similarly, since the temperatures of the streams must be equal in phase equilibrium, Eqs. (C.4) and (C.5) simplify, respectively, to

$$d\mu = dP/\rho \tag{27}$$

and

$$df = -Pd(1/\rho). \tag{28}$$

In particular, Eq. (28) provides the definition of the pressure in terms of the free energy

$$P = \rho^2 \left(\frac{\partial f}{\partial \rho} \right)_T, \tag{29}$$

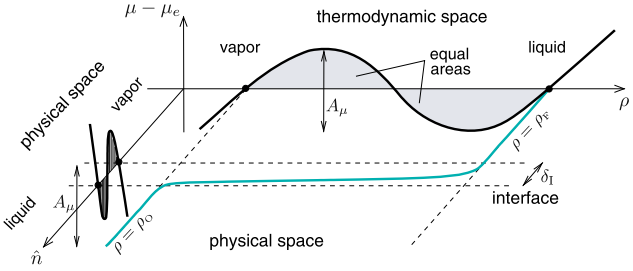

Fig. 14. Schematics of the thermodynamic-to-physical space mapping (31) built in the diffuse-interface theory for transforming the variations of the chemical potential into a sharp monotonic density profile in a monocomponent isothermal system.

which can be combined with Eq. (C.7) giving

$$\mu = \left[\frac{\partial}{\partial \rho}(\rho f) \right]_T. \tag{30}$$

By substituting P from Eq. (14) into Eq. (29) and integrating the resulting equation, an expression for f can be found and be later substituted into Eq. (30) to obtain one for μ. The resulting expressions for f and μ are not essential here and are deferred to Appendix C.

Equations (27) –(30) are standard expressions in thermodynamics that are useful here for the following reason. Since the pressure P is an oscillatory function of ρ across the coexistence region of the thermodynamic phase diagram (e.g., see Fig. 4), f and μ are also oscillatory functions of ρ there. In particular, μ satisfies a Maxwell's construction rule [126], in that the oscillation of $\mu - \mu_e$ in the coexistence region encloses zero net area, $\int_{\rho_O}^{\rho_F} (\mu - \mu_e) d\rho = 0$, as observed by using Eqs. (30) and (C.7).

A fundamental result of the diffuse-interface theory for monocomponent isothermal systems is the equation

$$\mu - \mu_e = \kappa \left(\frac{\partial^2 \rho}{\partial \hat{n}^2} \right), \tag{31}$$

which relates μ, ρ, and the normal coordinate to the interface $\hat{n}$. The derivation of Eq. (31) is deferred to Section 5.3. It will also be shown in Section 5.6 that an equation similar to (31) exists for multicomponent isothermal systems. The boundary conditions of Eq. (31) are $\rho = \rho_F$ at $\hat{n} \to -\infty$ and $\rho = \rho_O$ at $\hat{n} \to +\infty$. The right-hand side of Eq. (31) vanishes far away on both sides of the interface, where the density gradients are negligible and the chemical potential attains the phase-equilibrium value μ_e.

As illustrated in Fig. 14, the expression (31) is responsible for mapping the oscillations of the chemical potential in the two-phase region of the thermodynamic space $\mu = \mu(\rho)$ into an interface-like profile $\rho = \rho(\hat{n})$, in which ρ undergoes a rapid variation of order ρ_F within a very short distance of order δ_I. To obtain an estimate of δ_I, Eq. (31) can be rewritten in terms of a nondimensional density

$$\rho^\star = \rho / \rho_F \tag{32}$$

and a nondimensional chemical potential $\mu^\star = (\mu - \mu_e)/A_\mu$, with A_μ the characteristic amplitude of the oscillation of μ in the coexistence region. In these variables, the first integral of Eq. (31) is

$$\int_{1/\mathcal{R}}^{\rho^\star} \mu^\star d\rho^\star = \frac{\kappa \rho_F}{A_\mu} \left(\frac{\partial \rho^\star}{\partial \hat{n}} \right)^2. \tag{33}$$

Equation (33) evaluated far away from the interface, where $\rho^\star \to 1$ and $\partial \rho^\star / \partial \hat{n} \to 0$, is consistent with Maxwell's construction rule. The parameters κ, ρ_F, and A_μ can be scaled out of Eq. (33) by defining a dimensionless normal coordinate $\hat{n}^\star = \hat{n}/\delta_I$, with

$$\delta_I = (\kappa \rho_F / A_\mu)^{1/2}. \tag{34}$$

The combination of Eqs. (26) and (34) yields

$$A_\mu \sim \sigma_0/(\delta_I \rho_F). \tag{35}$$

In particular, Eq. (35) connects the oscillation amplitude A_μ, which can be obtained independently from the thermodynamic relations (14) and (30), with the intrinsic properties of the interface δ_I and σ_0, the latter being a measurable quantity. A cornerstone of the diffuse-interface theory is that the order of magnitude of κ is set such that δ_I estimated from (34) is small enough to yield values of σ_0 from Eq. (22) comparable to the experimentally observed ones $\sigma_0 \sim 0.001$–0.1 N/m. This gives $\delta_I \sim 1$–100 nm and $\kappa \sim 10^{-15}$–10^{-17} $\mathrm{Jm^5/kg^2}$ (see Fig. 12).

The characteristic amplitude of the pressure oscillation within the interface, denoted by A_P, is obtained from Eqs. (29), (30), and (35) giving

$$A_P \sim \rho_F A_\mu \sim \sigma_0/\delta_I. \tag{36}$$

Equation (36) yields $A_P \sim 10$–100 bar when the estimates for σ_0 and δ_I introduced above are employed. A dimensionless pressure parameter $\mathcal{P}$ can be defined as the ratio of the characteristic pressure variation A_P across the interface to the combustor pressure P_∞,

$$\mathcal{P} = \frac{\sigma_0}{\delta_I P_\infty}, \tag{37}$$

which is related by Eq. (36) to A_μ as

$$\mathcal{P} \sim \frac{A_\mu W_F}{Z_F \mathrm{R}^0 T_F}, \tag{38}$$

where

$$Z_F = \frac{P_\infty W_F}{\rho_F \mathrm{R}^0 T_F} \tag{39}$$

is the compressibility factor. The dimensionless pressure parameter $\mathcal{P}$ increases with decreasing pressures. At near-atmospheric pressures, $\mathcal{P}$ is much larger than unity, and the pressure oscillation predicted by the equation of state (14) can induce large negative pressures oftentimes observed in the form of tensile strength in liquids brought to metastable states by superheating them above the boiling temperature, or by stretching them below the vapor pressure [104,127,128]. As P_∞ increases, σ_0 decreases and δ_I increases, thereby rendering smaller values of A_P and $\mathcal{P}$.

The numerical results presented in Sections 6 and 7 indicate that the dimensionless pressure parameter $\mathcal{P}$ is of order unity in transcritical conditions. As a result, despite the large values of P_∞ involved, the present theory predicts that mechanically subcritical pressures, and even negative pressures, may occur within the interface. These aspects are further discussed in Appendix E as they may appear controversial in the description, although they do not have any significant effect on the results presented here.

4.5. The interface-continuum hypothesis

The approximation of operating with a continuous field across the transcritical interface while keeping only the gradient terms in the series expansion of the thermodynamic potentials, as in Eqs. (16)–(18), is justified when the interface thickness δ_I is large compared to the characteristic mean free path Λ, or equivalently, when the Knudsen number

$$Kn_I = \Lambda/\delta_I \tag{40}$$

is much smaller than unity. In multicomponent mixtures described by the hard-sphere model, Λ is given by [129]

$$\Lambda = \frac{1}{\rho \pi N_A \left[\dfrac{Y_F d_F^2 \sqrt{2}}{W_F} + \dfrac{(1-Y_F) d_{FO}^2 \sqrt{1 + W_F/W_O}}{W_O} \right]}. \tag{41}$$

In this formulation, d_F and d_O are the equivalent hard-sphere diameters of the fuel and coflow species, respectively, with $d_{FO} = (d_F + d_O)/2$ the mean diameter (i.e., $d_F = d_{C_{12}H_{26}} = 0.712$ nm, $d_O = d_{N_2} = 0.362$ nm, and $d_{F,O} = 0.537$ nm for $C_{12}H_{26}/N_2$ mixtures [130]).

The direct application of Eq. (41) to the present problem is problematic because of the strong composition gradients associated with transcritical interfaces. In the calculations of Kn_I shown in Section 6, the partial densities in Eq. (41) are approximated as $\rho Y_F \sim X_{F,\max} P_\infty W_F/(Z_{F,\max} \mathrm{R}^0 T_e)$ and $\rho(1-Y_F) \sim (1 - X_{F,\max}) P_\infty W_O/(Z_{O,\max} \mathrm{R}^0 T_e)$, where T_e is a characteristic interface temperature, and the subindex max denotes quantities evaluated at the location of maximum density gradient across the interface. With these approximations in mind, Eq. (41) becomes

$$\Lambda \approx \frac{k_B T_e}{\pi P_\infty \left[\dfrac{X_{F,\max} d_F^2 \sqrt{2}}{Z_{F,\max}} + \dfrac{(1 - X_{F,\max}) d_{FO}^2 \sqrt{1 + W_F/W_O}}{Z_{O,\max}} \right]}, \tag{42}$$

where k_B is the Boltzmann constant. For the monocomponent systems calculated in Appendix D, Eq. (42) is used with $X_{F,\max} = 1$, $Z_{F,\max} = Z_{\max}$, and $d_F = d$.

Small Knudsen numbers (40) are often found in monocomponent systems as the critical point is neared, when δ_I increases and Λ decreases. For instance, the interface thickness calculated in Appendix D for a monocomponent N_2 system at $P_\infty = 0.9 P_{c,N_2} \approx 31$ bar is $\delta_I \sim 5$ nm. This translates into approximately $32\,N_2$ molecules across, along with a Knudsen number $Kn_I \sim 0.05$ (see Fig. D.3 in Appendix D). However, it is widely accepted that the requirement $Kn_I \ll 1$ is not always satisfied by the diffuse-interface theory of van der Waals as the pressure becomes increasingly smaller than P_c [53,131,132]. This can be seen in the same monocomponent N_2 system mentioned above at $P_\infty = 0.4 P_{c,N_2} \approx 14$ bar, for which $\delta_I \sim 2$ nm and $Kn_I \sim 0.15$, thereby indicating a larger rarefaction and a weaker foundation for the continuum character of the theory. Despite these shortfalls, the diffuse-interface theory of van der Waals tends to reproduce well numerical results obtained from molecular dynamics (e.g., see Fig. 6 in Ref. [99]).

The considerations above indicate that the continuum assumption across the interface is often on the borderline of invalidity. In the hydrocarbon-fueled mixtures analyzed in Figs. 7–9(b–e), the pressures that can be reached before Kn_I becomes much smaller than unity and are much larger than those in monocomponent systems because of the elevation of the critical point caused by mixing. It is however remarkable that no excessively large values of Kn_I that would indicate a flagrant violation of the continuum assumption are encountered at the high pressures studied here. Field formulations of fluid motion are well-known for performing correctly even in flows where the continuum hypothesis may not be strictly satisfied [129]. The continuum treatment of diffuse interfaces is reminiscent of the description of the internal structure of weak shock waves by using the Navier–Stokes equations despite the small shock thicknesses involved [133]. However, one important difference between shocks and interfaces is that the dynamics outside the shock discontinuity are independent of its internal structure, whereas the transport across the interface and its mechanical coupling with the flow fundamentally depend on the internal structure of the interface, as discussed in Section 5.

The appropriateness of Eq. (41) as the relevant length scale to evaluate the continuum character of transcritical interfaces is also under suspicion. Recent molecular dynamics simulations [134] indicate that confined gases undergo higher rates of collisions than those predicted by Eq. (41). It could be plausible that an interface may lead to an effect similar to confinement for the fluids on each side and within the interface itself. Similarly, a recent study by Dahms [135] has found that the effective mean free path near the

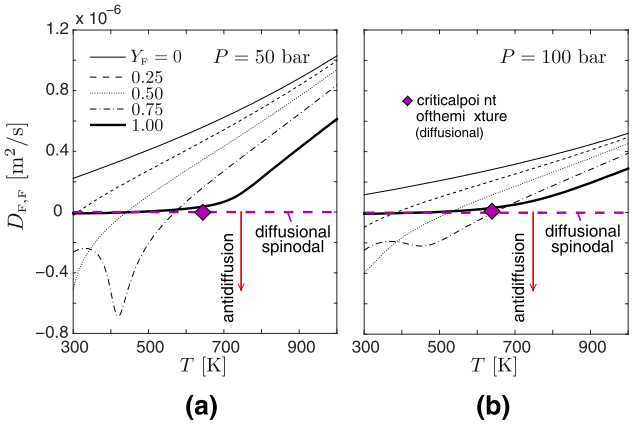

Fig. 15. Constant-pressure distributions of the effective Fickian diffusivity of dodecane in $C_{12}H_{26}/N_2$ mixtures at (a) $P = 50$ bar and (b) 100 bar as a function of temperature and mass fraction of dodecane Y_F (refer to the legend in the left panel). The plots include the diffusional critical point of the mixture at the corresponding pressure (purple diamond symbol) and the diffusional spinodals (thick purple dashed lines). (For interpretation of the references to color in this figure legend, the reader is referred to the web version of this article.)

interface should be 0.55 times smaller than the classic definition in Eq. (41). Whether interfaces at high pressures fully satisfy the continuum requirement $Kn_I \ll 1$ remains a subject open to debate.

4.6. The role of antidiffusion in transcritical flows

An important characteristic of the mass transport across transcritical interfaces at sufficiently high pressures is the prevailing antidiffusion of matter that is predicted by the standard transport theory in conjunction with the equation of state (14). To understand this, notice that the effective Fickian diffusion coefficient participating in the standard species diffusion flux of fuel at high pressures is not the binary diffusion coefficient $\mathcal{D}_{F,O}$ but [136,137]

$$D_{F,F} = \mathcal{D}_{F,O}\left(\frac{\partial \ln \mathrm{f_F}}{\partial \ln X_F}\right)_{P,T}, \tag{43}$$

where $\mathrm{f_F}$ is the fuel fugacity defined in Eq. (B.21) as a function of the fugacity coefficient (B.22), the latter being particularized in Eq. (C.47) for the Peng-Robinson equation of state (14). A formal derivation of Eq. (43) is deferred to Section 5.

In contrast to $\mathcal{D}_{F,O}$, which is always positive (see Fig. B.3 and related discussion in Appendix B.4), the effective Fickian diffusion coefficient $D_{F,F}$ can be negative for intermediate compositions at temperatures smaller than $T_{c,\mathrm{diff}}$, as shown in Fig. 15 for $C_{12}H_{26}/N_2$ mixtures. The change in sign can be explained by the fact that the fuel fugacity oscillates across the coexistence region (and therefore across the interface) similarly to the fuel chemical potential, as discussed in Appendix A.1 and illustrated in Fig. A.1(a,b) for $C_{12}H_{26}/N_2$ mixtures.

At moderate pressures or high temperatures approaching ideal-gas conditions, the non-ideal diffusion prefactor becomes unity, $(\partial \ln \mathrm{f_F}/\partial \ln X_F)_{P,T} \to 1$. Therefore $D_{F,F} \simeq \mathcal{D}_{F,O}$ and traditional forward molecular diffusion (i.e., diffusion in the direction of decreasing fuel concentration) prevails. At high pressures, forward diffusion dominates in the compositional mixing layer downstream of the interface edge. In contrast, near the injection orifice, where the fuel is cold, the non-ideal prefactor $(\partial \ln \mathrm{f_F}/\partial \ln X_F)_{P,T}$ departs from unity and its sign changes depending on the local composition. In particular, $(\partial \ln \mathrm{f_F}/\partial \ln X_F)_{P,T}$ varies from positive values on the coflow and fuel sides of the interface, where forward diffusion prevails, to negative values within the transcritical interface, where mass is transported in an antidiffusive manner in the direction of positive

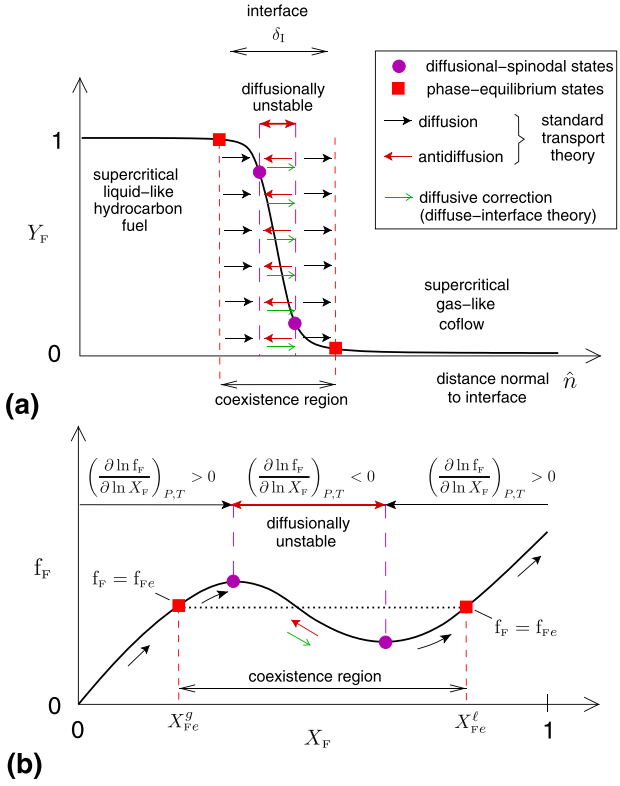

Fig. 16. Schematics of diffusional processes across a notional transcritical interface separating fuel and coflow streams at high pressures. The sketch includes (a) diffusional processes in physical space, and (b) associated evolution of the fugacity of the fuel species $\mathrm{f_F}$ in thermodynamic space. Note that the fugacity profile in panel (b) does not necessarily correspond to one at uniform pressure such as those presented in Fig. A.1(a), since the pressure generally varies within the coexistence region.

composition gradients because of the diffusional instability of the mixture, as sketched in Fig. 16. The antidiffusion of matter predicted by the standard transport theory, which would lead to unphysical results, can be regularized by a an extra diffusion flux derived from the diffuse-interface theory, as described in Section 5.

4.7. Conservation equations for transcritical flows

The consideration of gradient-dependent thermodynamic potentials, as in Eqs. (16)–(17), leads to interface-related transport fluxes and mechanical stresses in the conservation equations. In this study, a phenomenological approach described in Section 5 is followed based on linear augmentations of the deviatoric part of the stress tensor $\boldsymbol{\tau}$, and the heat and species diffusion fluxes $\boldsymbol{q}$ and $\boldsymbol{J_i}$, with the interfacial stress tensor $\mathcal{K}$ and transport fluxes $\mathcal{Q}$ and $\mathcal{J}_i$. Expressions for $\mathcal{K}$, $\mathcal{Q}$, and $\mathcal{J}_i$ are derived in Section 5. In terms of the material-derivative operator $D/Dt = \partial/\partial t + \mathbf{v}\cdot\nabla$, the resulting conservation equations for mass, momentum, species, and total energy are

$$\frac{D\rho}{Dt} = -\rho(\nabla\cdot\mathbf{v}), \tag{44}$$

$$\rho\frac{D\mathbf{v}}{Dt} = -\nabla P_{GD} + \nabla\cdot(\boldsymbol{\tau}+\mathcal{K}), \tag{45}$$

$$\rho\frac{DY_i}{Dt} = -\nabla\cdot(\boldsymbol{J_i}+\mathcal{J}_i), \quad i = 1,\ldots,N, \tag{46}$$

$$\rho\frac{DE}{Dt} = -\nabla\cdot(P_{GD}\mathbf{v}) - \nabla\cdot(\boldsymbol{q}+\mathcal{Q}) + \nabla\cdot[(\boldsymbol{\tau}+\mathcal{K})\cdot\mathbf{v}], \tag{47}$$

which describe the continuum mechanics of a multiphase, multicomponent fluid of N species that moves at a mass-averaged velocity $\mathbf{v}$ and has a density ρ and total energy E. The latter is related to the specific gradient-dependent internal energy (17) by the definition

$$E = e_{\text{GD}} + |\mathbf{v}|^2/2. \tag{48}$$

Additionally, $\boldsymbol{q}$ is a molecular heat flux defined as

$$\boldsymbol{q} = \boldsymbol{q_t} + \sum_{i=1}^{N-1} (h_i - h_N)\boldsymbol{J_i}. \tag{49}$$

The first term $\boldsymbol{q_t}$ on the right-hand side of Eq. (49) comprises Fourier and Dufour mechanisms of heat transfer, while the second term corresponds to heat transport by interdiffusion of species with different partial specific enthalpies h_i, which are discussed in Appendices B.1 and C.8. In addition, the symbol P_{GD} is a gradient-dependent pressure given by

$$P_{\text{GD}} = P - \frac{1}{2}\sum_{i=1}^{N}\sum_{j=1}^{N}\kappa_{i,j}\nabla\rho_i\nabla\rho_j, \tag{50}$$

with P being related to ρ, T and Y_i through the equation of state (14). The convenience of delocalizing the pressure as in Eq. (50) will become clearer upon deriving an expression for the interfacial stress tensor $\mathcal{K}$ in Section 5.

An alternative form of the energy Eq. (47) that will be employed in the analysis is the enthalpy conservation equation

$$\rho\frac{Dh}{Dt} = \frac{DP_{\text{GD}}}{Dt} - \nabla\cdot(\boldsymbol{q} + \mathcal{Q}) - (\boldsymbol{\tau} + \mathcal{K}) : \nabla\mathbf{v}. \tag{51}$$

Equation (51) is obtained by subtracting the momentum conservation Eq. (45) multiplied by $\mathbf{v}$ from the total-energy conservation equation (47), and by making use of the relation

$$h = e_{\text{GD}} + P_{\text{GD}}/\rho \tag{52}$$

obtained from the definition of the local specific enthalpy h (C.3) along with Eqs. (17) and (50). Methods for calculation of h at high pressures are discussed in Appendices B.1 and C.6.

The integration of the conservation equations Eqs. (44)–(47) is complicated by the additional terms $\mathcal{K}$, $\mathcal{J_i}$, and $\mathcal{Q}$, which will be shown to depend on the square of gradients and higher-order derivatives of the partial densities across the interface. For instance, a full numerical integration of the momentum Eq. (45) in the flow sketched in Fig. 1 would incur significant numerical stiffness, because the ratio of the interfacial terms to the convection terms would be a large parameter,

$$\frac{||\nabla\cdot(-P_{\text{GD}}\boldsymbol{I} + \mathcal{K})||}{||\rho\mathbf{v}\cdot\nabla\mathbf{v}||} \sim \frac{\sigma_0/\delta_{\text{I}}^2}{\rho_{\text{O}}U_{\text{O}}^2/R_{\text{F}}} \sim \frac{1}{\epsilon_R^2 We_{\text{O}}} \gg 1, \tag{53}$$

where

$$We_{\text{O}} = \rho_{\text{O}}U_{\text{O}}^2 R_{\text{F}}/\sigma_0 \gg 1 \tag{54}$$

is a Weber number, and ϵ_R is a large-scale Cahn number defined in Eq. (9). Typical orders of magnitude are $We_{\text{O}} = O(10^2 - 10^3)$ and $\epsilon_R = O(10^{-4} - 10^{-5})$ in the present conditions, thereby making the ratio (53) a large number of order $1/(\epsilon_R^2 We_{\text{O}}) = O(10^6 - 10^7)$ due to the much smaller value of δ_{I} compared to R_{F}.

5. The structure of transcritical interfaces

This section focuses on the derivation of the additional terms $\mathcal{K}$, $\mathcal{Q}$, and $\mathcal{J_i}$ in the constitutive laws of the Navier–Stokes Eqs. (44)–(47) by using the diffuse-interface theory of van der Waals extended to multicomponent flows. Using those expressions and exploiting the small thickness of the interface relative to all other macroscopic lengths, a local formulation in the moving frame attached to the interface is developed that provides mechanical and transport equilibrium constraints applicable to interfaces in isothermal systems. Moderate temperature gradients across the interface, such as those encountered in Fig. 1, are shown to require the consideration of small deviations from equilibrium.

5.1. Entropy-production sources

The derivation of $\mathcal{K}$, $\mathcal{Q}$, and $\mathcal{J_i}$ is performed here using the method of irreversible thermodynamics and Onsager's reciprocal relations. The premise of this method is that the constitutive relations must lead to non-negative entropy production in accordance with the second principle of thermodynamics. This method parallels the one utilized to determine the analytical form of the transport fluxes in the standard theory [138–140]. However, this method cannot give expressions for the transport coefficients in terms of molecular properties. Those are provided separately in Appendices B.4 and F.

The analysis begins by substituting Eqs. (17) and (50) into the first principle (C.1), and using the assumption of constant and symmetric κ_{ij} coefficients, which leads to

$$Tds = de_{\text{GD}} + P_{\text{GD}}d(1/\rho) - \sum_{i=1}^{N-1}(\mu_i - \mu_N)dY_i - \sum_{i=1}^{N}\boldsymbol{\psi_i}\cdot[d(\nabla(\rho Y_i)]/\rho, \tag{55}$$

where

$$\boldsymbol{\psi_i} = \sum_{j=1}^{N}\kappa_{i,j}\nabla(\rho Y_j) \tag{56}$$

is an auxiliary vector. A transport equation for the specific entropy s can be derived by substituting Eqs. (44)–(47) and the definition (49) into the expression resulting from taking the material derivative of Eq. (55), which yields

$$\begin{aligned}\rho\frac{Ds}{Dt} + \nabla\cdot\Bigg\{\frac{1}{T}\Bigg[&\boldsymbol{q_t} + \mathcal{Q} - \sum_{i=1}^{N}\boldsymbol{\psi_i}(\rho Y_i\nabla\cdot\mathbf{v}) \\ &- \sum_{i=1}^{N-1}(\boldsymbol{\psi_i} - \boldsymbol{\psi_N})\nabla\cdot(\boldsymbol{J_i} + \mathcal{J_i}) \\ &+ \sum_{i=1}^{N-1}[T(\widetilde{s}_i - \widetilde{s}_N)\boldsymbol{J_i} - (\widetilde{\mu}_i - \widetilde{\mu}_N)\mathcal{J_i}]\Bigg]\Bigg\} = \dot{s}_{\text{prod}},\end{aligned} \tag{57}$$

where

$$\widetilde{s}_i = s_i + (\nabla\cdot\boldsymbol{\psi_i})/T \quad \text{and} \quad \widetilde{\mu}_i = \mu_i - \nabla\cdot\boldsymbol{\psi_i} \tag{58}$$

are generalized versions of the partial specific entropy $s_i = (\partial S/\partial n_i)_{P,T,n_j||j=1,\dots N(j\neq i)}$ and specific chemical potential μ_i, respectively. In addition, $\dot{s}_{\text{prod}}$ is an entropy source given by

$$\begin{aligned}\dot{s}_{\text{prod}} =& \frac{1}{T}\left\{\boldsymbol{\tau} + \mathcal{K} - \sum_{i=1}^{N}\left[\rho Y_i\nabla\cdot\boldsymbol{\psi_i}\boldsymbol{I} - \nabla(\rho Y_i)\otimes\boldsymbol{\psi_i}\right]\right\} : \nabla\mathbf{v} \\ &+ \left\{\boldsymbol{q_t} + \mathcal{Q} - \sum_{i=1}^{N}\boldsymbol{\psi_i}(\rho Y_i\nabla\cdot\mathbf{v}) - \sum_{i=1}^{N-1}(\boldsymbol{\psi_i} - \boldsymbol{\psi_N})\nabla\cdot(\boldsymbol{J_i} + \mathcal{J_i})\right. \\ &\left. + \sum_{i=1}^{N-1}[T(\widetilde{s}_i - \widetilde{s}_N)(\boldsymbol{J_i} + \mathcal{J_i}) - (h_i - h_N)\mathcal{J_i}]\right\}\cdot\nabla\left(\frac{1}{T}\right) \\ &- \sum_{i=1}^{N-1}(\boldsymbol{J_i} + \mathcal{J_i})\cdot\frac{\nabla(\widetilde{\mu}_i - \widetilde{\mu}_N)}{T},\end{aligned} \tag{59}$$

with $\boldsymbol{I}$ being the identity matrix and $\otimes$ denoting the dyadic product. The definition

$$\mu_i = h_i - Ts_i, \tag{60}$$

the mass-conservation constraint

$$\sum_{i=1}^{N} (\boldsymbol{J_i} + \boldsymbol{\mathcal{J}_i}) = \boldsymbol{J_N} + \boldsymbol{\mathcal{J}_N} + \sum_{i=1}^{N-1} (\boldsymbol{J_i} + \boldsymbol{\mathcal{J}_i}) = 0, \tag{61}$$

and the vector identity

$$\boldsymbol{\psi_i} \cdot \frac{D}{Dt}[\nabla(\rho Y_i)] = \boldsymbol{\psi_i} \cdot \nabla\left[\frac{D}{Dt}(\rho Y_i)\right] - [\nabla(\rho Y_i) \otimes \boldsymbol{\psi_i}] : \nabla \mathbf{v} \tag{62}$$

have been used in deriving Eq. (59), with $D(\rho Y_i)/Dt$ being replaced by $-\nabla \cdot (\boldsymbol{J_i} + \boldsymbol{\mathcal{J}_i}) - \rho Y_i \nabla \cdot \mathbf{v}$ in accordance with Eq. (46). To separate transport by temperature gradients, the decomposition

$$\nabla(\widetilde{\mu}_i - \widetilde{\mu}_N) = \nabla_T(\widetilde{\mu}_i - \widetilde{\mu}_N) - \left\{ s_i - s_N + \left[\frac{\partial}{\partial T}\left[\nabla \cdot (\boldsymbol{\psi_i} - \boldsymbol{\psi_N})\right] \right]_{P,Y_j|j=1,\dots N-1} \right\} \nabla T \tag{63}$$

is performed, where use of Eq. (58) and of the reciprocity relation for the partial specific entropy $s_i = -(\partial \mu_i/\partial T)_{P,Y_i|i=1,\dots N-1}$ have been made. In the formulation, the operator ∇_T indicates spatial differentiation at constant temperature. Substitution of Eq. (63) into Eq. (59) yields

$$\dot{s}_{\text{prod}} = \underbrace{\frac{1}{T}\left\{ \boldsymbol{\tau} + \mathcal{K} - \sum_{i=1}^{N}\left[\rho Y_i \nabla \cdot \boldsymbol{\psi_i} \boldsymbol{I} - \nabla(\rho Y_i) \otimes \boldsymbol{\psi_i}\right] \right\} : \underbrace{\nabla \mathbf{v}}_{\text{force}}}_{\text{current}} + \underbrace{\left\{ \boldsymbol{q_t} + \mathcal{Q} - \sum_{i=1}^{N} \boldsymbol{\psi_i}(\rho Y_i \nabla \cdot \mathbf{v}) - \sum_{i=1}^{N-1} (\boldsymbol{\psi_i} - \boldsymbol{\psi_N}) \nabla \cdot (\boldsymbol{J_i} + \boldsymbol{\mathcal{J}_i}) \right.}_{\text{current}}$$
$$\underbrace{\left. + \sum_{i=1}^{N-1} [(\chi_i - \chi_N)(\boldsymbol{J_i} + \boldsymbol{\mathcal{J}_i}) - (h_i - h_N)\mathcal{J}_i] \right\} \cdot \underbrace{\nabla\left(\frac{1}{T}\right)}_{\text{force}}}_{\text{current(cont.)}}$$
$$- \sum_{i=1}^{N-1} \underbrace{(\boldsymbol{J_i} + \boldsymbol{\mathcal{J}_i})}_{\text{currents}} \cdot \underbrace{\frac{\nabla_T(\widetilde{\mu}_i - \widetilde{\mu}_N)}{T}}_{\text{forces}}, \tag{64}$$

where

$$\chi_i = \nabla \cdot \boldsymbol{\psi_i} - T\left[\frac{\partial}{\partial T}\left(\nabla \cdot \boldsymbol{\psi_i}\right)\right]_{P,Y_j|j=1,\dots N-1} \tag{65}$$

is an auxiliary variable. The last term on the right-hand side of Eq. (65) can be expressed as

$$T\left[\frac{\partial}{\partial T}\left(\nabla \cdot \boldsymbol{\psi_i}\right)\right]_{P,Y_j|j=1,\dots N-1} = -\sum_{j=1}^{N} \kappa_{ij} T \nabla^2\left(\rho \beta_v Y_j\right) \tag{66}$$

by making use of the equation of state (14) and the definition of $\boldsymbol{\psi_i}$ in Eq. (56). In this formulation, β_v is the volume expansivity defined in Eq. (B.7) and particularized for the Peng-Robinson equation of state (14) in Eq. (C.22).

Following an approach similar to that provided by Onsager [138] (see also Ch. 11.2 in [140], and Ch. 6 in Ref. [139]), the entropy source (64) is interpreted as consisting of three production terms that have a similar form. Specifically, each term consists of a current multiplied by one of the following thermodynamic forces:

$$\nabla \mathbf{v},\ \nabla\left(\frac{1}{T}\right),\ \frac{\nabla_T(\widetilde{\mu}_1 - \widetilde{\mu}_N)}{T}, \dots \frac{\nabla_T(\widetilde{\mu}_{N-1} - \widetilde{\mu}_N)}{T}. \tag{67}$$

The quantities (67) are drivers of molecular transport, and consequently of entropy production.

Different transport processes induced by different thermodynamic forces interfere with one another. For instance, in addition to causing heat conduction, temperature gradients also induce mass transport through the Soret effect. More generally, the transport fluxes in the conservation equations can be written as a combination of all thermodynamic forces, and such combination is linear in the first approximation [138–140]. The derivation of these expressions is facilitated by assuming that the transport fluxes and thermodynamic forces of different tensorial character do not couple [141]. This simplification implies that there are no crossed effects between the mechanical stresses, which are driven by the velocity-gradient tensor, and the fluxes of heat and species, which are driven by gradients of temperature and chemical potentials. Based on these considerations, a closure is formulated for $\mathcal{K}$ in Section 5.2, followed by a discussion in Section 5.3 on the effective surface-tension coefficient σ arising from this formulation. Onsager's methodology will be used in Section 5.4 to determine the interfacial fluxes of heat $\mathcal{Q}$ and species $\boldsymbol{\mathcal{J}_i}$.

5.2. Closure for the interfacial stress tensor

In the case of Newtonian fluids under zero bulk viscosity, the expression for the viscous stress tensor is

$$\boldsymbol{\tau} = \eta\left(\nabla \mathbf{v} + \nabla \mathbf{v}^T\right) - (2\eta/3)(\nabla \cdot \mathbf{v})\boldsymbol{I}, \tag{68}$$

where η is the dynamic viscosity modeled in Appendix F.1. Variations of η with temperature and composition are studied in Appendix B.4 for $C_{12}H_{26}/N_2$ mixtures at high pressures. Equation (68) implies that the viscous dissipation $\boldsymbol{\tau}$: $\nabla \mathbf{v} \geq 0$ is a positive quadratic and therefore leads to positive entropy production. In contrast, the interfacial stress tensor $\mathcal{K}$ is assumed to be elastically restoring, such that the production of entropy by the diffuse-interface terms multiplying the velocity-gradient tensor in Eq. (64) is zero, namely

$$\left\{ \mathcal{K} - \sum_{i=1}^{N}\left[\rho Y_i \nabla \cdot \boldsymbol{\psi_i} \boldsymbol{I} - \nabla(\rho Y_i) \otimes \boldsymbol{\psi_i}\right] \right\} : \nabla \mathbf{v} = 0, \tag{69}$$

which gives

$$\mathcal{K} = \sum_{i=1}^{N}\left[\rho Y_i \nabla \cdot \boldsymbol{\psi_i} \boldsymbol{I} - \nabla(\rho Y_i) \otimes \boldsymbol{\psi_i}\right]. \tag{70}$$

The interfacial stress tensor $\mathcal{K}$ was originally introduced by Korteweg in a phenomenological manner [142]. The effects of $\mathcal{K}$ are concentrated in the vicinity of the interface, where the partial-density gradients are the largest. In that region, the first of the two terms on the right-hand side of Eq. (70) represents a hydrostatic stress. As shown in Section 5.3, this term gives rise to a curvature-dependent pressure jump across the interface. The second term is an anisotropic stress that acts primarily in the direction normal to the interface.

In this formulation, there is no explicit surface-tension coefficient σ appearing in Eqs. (44)–(47) and (70). However, σ resurfaces when the integral form of the momentum conservation equation (45) is considered, as shown in the next section.

5.3. Mechanical equilibrium conditions

This section focuses on the derivation of mechanical equilibrium conditions across the interface. The analysis is first particularized for the bicomponent flow depicted in Fig. 1. The problem is best illustrated by analyzing a zoomed-up view of a segment of an interface embedded in a much wider thermal mixing layer, as sketched in Fig. 17. The thickness of the mixing layer δ_T grows

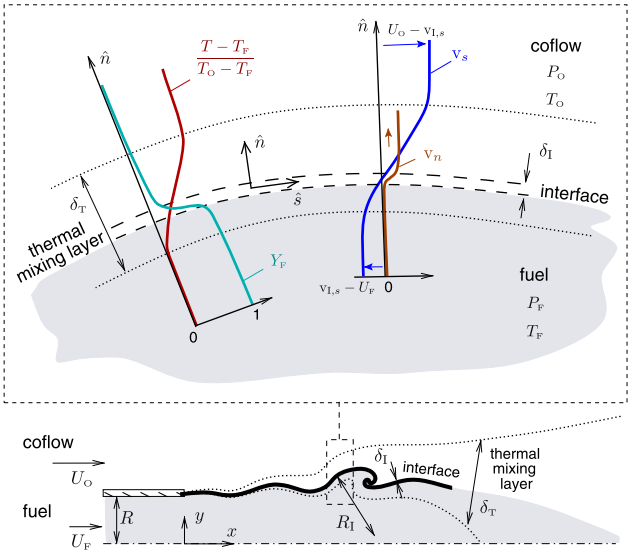

Fig. 17. Zoomed-in schematics of a transcritical interface embedded in a thermal mixing layer.

slowly with distance downstream and mostly coincides with the shear-layer thickness because of the near-unity Prandtl numbers and the order-unity relative differences of velocities and temperatures between the free streams, as discussed in Section 1. The thermal mixing layer is slanted toward the coflow side because $D_{T,O}/D_{T,F} \ll 1$ (e.g., $D_{T,O}/D_{T,F} \simeq 51$ in $C_{12}H_26/N_2$ systems at $P_\infty = 50$ bar, $T_F = 350$ K, and $T_O = 1000$ K).

The asymptotic limit considered in this analysis corresponds to thin interfaces compared to the thermal mixing layer, or equivalently, $\epsilon_T \ll 1$, with ϵ_T being a thermal Cahn number defined in Eq. (10). As the pressure increases, δ_T decreases and δ_I increases, and therefore ϵ_T becomes increasingly larger. However, despite the high pressures, ϵ_T always remains small because of the critical-point elevation phenomenon discussed in Section 3.2.

This analysis is limited to two dimensions, although the formulation can be easily extended to a third dimension by incorporating a second curvature. More general multiscale treatments, albeit based on a significantly simpler incompressible diffuse-interface formulation, can be found in Ref. [143].

Two different reference frames are sketched in Fig. 17 that are relevant for this analysis: the Cartesian laboratory frame $\{x, y\}$ and the curvilinear orthogonal frame $\{\hat{n}, \hat{s}\}$. The latter moves with the interface at its local absolute velocity $\mathbf{v}_I$. The local curvature interface is denoted as $K_I = 1/R_I$, with $K_I > 0$ for interfaces concave toward the coflow (i.e., for interfaces such as the one sketched in the upper panel in Fig. 17). In all cases of practical interest, the radius of curvature is much larger than the interface thickness, $R_I \gg \delta_I$. In contrast, the magnitude of R_I relative to δ_T depends on the particular problem under consideration. This scaling analysis considers the case in which

$$\mathcal{N} = \delta_T/R_I \tag{71}$$

is an order-unity parameter.

Under the conditions $\epsilon_T \ll 1$ and $\mathcal{N} = O(1)$, the interface is slender and the largest variations in all variables are along the normal $\hat{n}$. Consequently, $-P_{GD}\boldsymbol{I} + \mathcal{K}$ is diagonally dominant with diagonal components given by

$$-P_{GD} + \mathcal{K}_{n,n} = -P + \rho\kappa_{F,F}Y_F\frac{\partial^2}{\partial\hat{n}^2}(\rho Y_F) - \frac{1}{2}\kappa_{F,F}\left[\frac{\partial}{\partial\hat{n}}(\rho Y_F)\right]^2 + \rho\kappa_{F,F}K_I Y_F\frac{\partial}{\partial\hat{n}}(\rho Y_F) \tag{72}$$

and

$$-P_{GD} + \mathcal{K}_{s,s} = -P + \rho\kappa_{F,F}Y_F\frac{\partial^2}{\partial\hat{n}^2}(\rho Y_F) + \frac{1}{2}\kappa_{F,F}\left[\frac{\partial}{\partial\hat{n}}(\rho Y_F)\right]^2 + \rho\kappa_{F,F}K_I Y_F\frac{\partial}{\partial\hat{n}}(\rho Y_F), \tag{73}$$

where use of Eqs. (50) and (70) has been made in conjunction with the assumption that only the fuel gradient-energy coefficient participates in the conditions addressed in this study, as discussed in Section 4.2. The curvature-related terms in Eqs. (72) and (73), which arise from the divergence operator in the curvilinear system, are much smaller than the terms involving squared and second-order gradients normal to the interface. Equations (72) and (73) can be combined to give

$$\mathcal{K}_{s,s} = \mathcal{K}_{n,n} + \kappa_{F,F}\left[\frac{\partial}{\partial\hat{n}}(\rho Y_F)\right]^2. \tag{74}$$

In the reference frame $\{\hat{n}, \hat{s}\}$, the continuity Eq. (44) can be written as

$$\frac{\partial\rho}{\partial t} + \frac{\partial}{\partial\hat{n}}(\rho v_n) + \rho v_n K_I = 0, \tag{75}$$

whereas the normal and tangential components of the momentum conservation equation (45) can also be expressed as

$$\rho\frac{\partial v_n}{\partial t} + \rho v_n\frac{\partial v_n}{\partial\hat{n}} = \frac{\partial}{\partial\hat{n}}(-P_{GD} + \mathcal{K}_{n,n} + \tau_{n,n}) + K_I(\mathcal{K}_{n,n} - \mathcal{K}_{s,s} + \tau_{n,n} - \tau_{s,s}) - \rho\frac{\partial v_{I,n}}{\partial t} \tag{76}$$

and

$$\rho v_n\frac{\partial v_s}{\partial\hat{n}} = \frac{\partial}{\partial\hat{s}}(-P_{GD} + \mathcal{K}_{s,s}) + \frac{\partial\tau_{n,s}}{\partial\hat{n}} + 2K_I\tau_{n,s} - \rho\frac{\partial v_{I,s}}{\partial t}, \tag{77}$$

respectively, where

$$\tau_{n,n} = \frac{2\eta}{3}\left(2\frac{\partial v_n}{\partial\hat{n}} - K_I v_n\right), \quad \tau_{s,s} = -\frac{2\eta}{3}\left(\frac{\partial v_n}{\partial\hat{n}} - 2K_I v_n\right), \quad \tau_{n,s} = \eta\left(\frac{\partial v_s}{\partial\hat{n}} - K_I v_s\right) \tag{78}$$

are viscous stresses. In this formulation, $v_{I,n} = \mathbf{v}_I \cdot \mathbf{e_n}$ and $v_{I,s} = \mathbf{v}_I \cdot \mathbf{e_s}$ are, respectively, the normal and tangential components of the interface absolute velocity, and $v_n = (\mathbf{v} - \mathbf{v}_I) \cdot \mathbf{e_n}$ is the normal component of the relative fluid velocity, with $\mathbf{e_n}$ and $\mathbf{e_s}$ being unit vectors in the normal and tangential directions, respectively. The interface does not slip on the fluid in the tangential direction because of the continuity of the tangential velocity. As a result, the tangential component of the relative velocity $v_s = (\mathbf{v} - \mathbf{v}_I) \cdot \mathbf{e_s}$ vanishes in the vicinity of the interface, as depicted in Fig. 17.

In general, the absolute velocity of the interface $v_{I,n}$ is a function of time, and consequently the momentum Eqs. (76) and (77) require a fictitious acceleration given by the last term on their corresponding right-hand sides. Following experimental analyses of interface acceleration in liquid jets at normal pressure [144], it is assumed herein that the characteristic value of the interface acceleration is a fraction of order $1/\mathcal{R} \ll 1$ of the convective acceleration U_O^2/δ_T in the shear layer.

5.3.1. Mechanical equilibrium normal to the interface

The transfer of heat into the fuel stream decreases the fuel density near the interface and produces an outwards flow-displacement velocity whose order of magnitude is given by a balance between convection and heat conduction across the thermal mixing layer,

$$\rho_O U_T c_{p,O}\frac{(T_O - T_e)}{\delta_T} \sim \lambda_O\frac{(T_O - T_e)}{\delta_T^2}. \tag{79}$$

The interface temperature T_e is much closer to T_F than to T_O because $D_{T,O}/D_{T,F} \gg 1$. The symbol T_e, which coincides with the phase-equilibrium temperature in Eq. (A.13), is purposely chosen here because it will be shown in Section 5.6 that the conditions in the vicinity of the interface are near phase equilibrium when the temperature gradients are not too large. The balance (79) yields the thermal-expansion velocity scale

$$U_T \sim D_{T,O}/\delta_T, \tag{80}$$

with $U_T/U_O = 1/Pe_T \ll 1$ being the inverse of a large Péclet number.

In order to normalize Eq. (76), consider the dimensionless normal coordinate

$$\hat{n}^\star = \hat{n}/(\epsilon_T \delta_T), \tag{81}$$

and the dimensionless relative velocity

$$\mathrm{v}_n^\star = \mathrm{v}_n/\mathrm{U}_T. \tag{82}$$

Based on (81) and (82), the nondimensional time coordinate is defined as

$$t^\star = t/t_I, \tag{83}$$

where

$$t_I = \epsilon_T \delta_T / U_T \tag{84}$$

represents a flow transit time across the interface. The pressure is normalized by its variation (36) through the interface

$$P^\star = \frac{\epsilon_T \delta_T P}{\sigma_0}, \tag{85}$$

whereas the gradient-energy coefficient is nondimensionalized using Eq. (26) as

$$\kappa_{F,F}^\star = \frac{\rho_F^2 \kappa_{F,F}}{\epsilon_T \delta_T \sigma_0}. \tag{86}$$

The unit of interfacial stresses is obtained by utilizing Eq. (86) and the estimate $\partial(\rho Y_F)/\partial\hat{n} \sim \rho_F/\delta_I$ in Eq. (70), which gives

$$\mathcal{K}_{n,n}^\star = \frac{\mathcal{K}_{n,n}}{A_P} = \frac{\epsilon_T \delta_T \mathcal{K}_{n,n}}{\sigma_0}, \quad \mathcal{K}_{s,s}^\star = \frac{\mathcal{K}_{s,s}}{A_P} = \frac{\epsilon_T \delta_T \mathcal{K}_{s,s}}{\sigma_0}. \tag{87}$$

The rest of the variables are nondimensionalized as

$$\tau_{n,n}^\star = \frac{\epsilon_T \delta_T \tau_{n,n}}{\eta_O U_T}, \quad \tau_{n,s}^\star = \frac{\delta_T \tau_{n,s}}{\eta_O U_O}, \quad \tau_{s,s}^\star = \frac{\epsilon_T \delta_T \tau_{s,s}}{\eta_O U_T}$$
$$\left(\frac{\partial \mathrm{v}_{I,n}}{\partial t}\right)^\star = \frac{\mathcal{R}\delta_T}{U_O^2}\left(\frac{\partial \mathrm{v}_{I,n}}{\partial t}\right). \tag{88}$$

In the dimensionless variables (81)–(88), the normal component of the momentum conservation equation (76) becomes

$$\rho^\star \frac{\partial \mathrm{v}_n^\star}{\partial t^\star} + \rho^\star \mathrm{v}_n^\star \frac{\partial \mathrm{v}_n^\star}{\partial \hat{n}^\star} = -\frac{1}{\mathcal{E}_m}\left(\frac{\partial P_{GD}^\star}{\partial \hat{n}^\star} - \frac{\partial \mathcal{K}_{n,n}^\star}{\partial \hat{n}^\star}\right)$$
$$+ \frac{\mathcal{N} Pr_O^2}{Oh_T^2 \mathcal{R}}\left(\mathcal{K}_{n,n}^\star - \mathcal{K}_{s,s}^\star\right) + \frac{Pr_O}{\epsilon_T \mathcal{R}} \frac{\partial \tau_{n,n}^\star}{\partial \hat{n}^\star}$$
$$+ \frac{\mathcal{N} Pr_O}{\mathcal{R}}\left(\tau_{n,n}^\star - \tau_{s,s}^\star\right) - \frac{\epsilon_T Pe_T^2}{\mathcal{R}^2}\rho^\star \left(\frac{\partial \mathrm{v}_{I,n}}{\partial t}\right)^\star, \tag{89}$$

with

$$P_{GD}^\star = P^\star - \frac{\kappa_{F,F}^\star}{2}\left[\frac{\partial}{\partial \hat{n}}(\rho^\star Y_F)\right]^2 \tag{90}$$

as the nondimensional gradient-dependent pressure,

$$\mathcal{K}_{n,n}^\star = \rho^\star \kappa_{F,F}^\star Y_F \frac{\partial^2}{\partial \hat{n}^{\star 2}}(\rho Y_F)$$
$$- \kappa_{F,F}^\star \left[\frac{\partial}{\partial \hat{n}^\star}(\rho^\star Y_F)\right]^2 + \epsilon_T \mathcal{N} \rho^\star \kappa_{F,F}^\star Y_F \frac{\partial}{\partial \hat{n}^\star}(\rho^\star Y_F), \tag{91}$$

$$\mathcal{K}_{s,s}^\star = \rho^\star \kappa_{F,F}^\star Y_F \frac{\partial^2}{\partial \hat{n}^{\star 2}}(\rho Y_F) + \epsilon_T \mathcal{N} \rho^\star \kappa_{F,F}^\star Y_F \frac{\partial}{\partial \hat{n}^\star}(\rho^\star Y_F) \tag{92}$$

as the nondimensional interfacial stresses, and

$$\tau_{n,n} = \frac{2\eta^\star}{3}\left(2\frac{\partial \mathrm{v}_n^\star}{\partial \hat{n}^\star} - \epsilon_T \mathcal{N} \mathrm{v}_n^\star\right), \quad \tau_{s,s} = -\frac{2\eta^\star}{3}\left(\frac{\partial \mathrm{v}_n^\star}{\partial \hat{n}^\star} - 2\epsilon_T \mathcal{N} \mathrm{v}_n^\star\right), \tag{93}$$

as the nondimensional viscous stresses, where

$$\eta^\star = \eta/\eta_O \tag{94}$$

is the nondimensional dynamic viscosity. Additionally, $Pr_O = \nu_O/D_{T,O}$ is the Prandtl number based on the kinematic viscosity $\nu_O = \eta_O/\rho_O$ in the coflow, and $Oh_T = \eta_O/\sqrt{\rho_O \sigma_0 \delta_T}$ is an Ohnesorge number.

Characteristic parameters are provided in Table 4 for typical transcritical conditions. Following those, the orders of magnitude of the dimensionless groups multiplying the last four terms on the right-hand side of Eq. (89) are $\epsilon_T Pe_T^2/\mathcal{R}^2 = O(10^{-2})$, $\mathcal{N} Pr_O/\mathcal{R} = O(10^{-1})$, $\mathcal{N} Pr_O^2/(Oh_T^2 \mathcal{R}) = O(10^2)$, and $Pr_O/(\epsilon_T \mathcal{R}) = O(10^2)$. Of particular interest is the much larger value of the inverse of the mechanical-equilibrium parameter $\mathcal{E}_m$ multiplying the first term on the right hand side of Eq. (89),

$$\mathcal{E}_m = \frac{\epsilon_T Oh_T^2 \mathcal{R}}{Pr_O^2} = \frac{\rho_F D_{T,O}^2}{\sigma_0 \delta_T}\left(\frac{\delta_I}{\delta_T}\right) = O(10^{-6}) \ll 1. \tag{95}$$

These estimates indicate that the derivative of $P_{GD}^\star - \mathcal{K}_{n,n}^\star$ along the normal direction in Eq. (89) is zero in the first approximation. Retaining the higher-order effects of the normal derivative of the normal viscous stress and the curvature terms arising from the divergence of the interfacial stress tensor, Eq. (89) simplifies to

$$\frac{\partial}{\partial \hat{n}^\star}\left(-P_{GD}^\star + \mathcal{K}_{n,n}^\star + \frac{Oh_T^2}{Pr_O}\tau_{n,n}^\star\right) + \epsilon_T \mathcal{N}(\mathcal{K}_{n,n}^\star - \mathcal{K}_{s,s}^\star) = 0. \tag{96}$$

The integral of Eq. (96) yields the mechanical equilibrium condition in the normal direction to the interface

$$-P + \tau_{n,n} + \rho \kappa_{F,F} Y_F \frac{\partial^2}{\partial \hat{n}^2}(\rho Y_F) - \frac{1}{2}\kappa_{F,F}\left[\frac{\partial}{\partial \hat{n}}(\rho Y_F)\right]^2$$
$$+ \rho \kappa_{F,F} \mathrm{K}_I Y_F \frac{\partial}{\partial \hat{n}}(\rho Y_F) = -P_O + \tau_{n,nO}$$
$$- \mathrm{K}_I \int_{\hat{n}}^{+\infty} \kappa_{F,F}\left[\frac{\partial}{\partial \hat{n}}(\rho Y_F)\right]^2 d\hat{n}, \tag{97}$$

where use of Eqs. (72), (74), and (90) has been made, and where dimensional variables have been recovered in the notation. In this formulation, P_O and $\tau_{n,nO}$ are the local thermodynamic pressure and normal viscous stress away from the interface at intermediate distances $\delta_I \ll \hat{n} \ll \delta_T$ on the coflow side.

Equation (97) is a fundamental mechanical equilibrium condition that relates – locally through the interface – the partial-density gradients, the thermodynamic pressure, the interface curvature, and the normal viscous stress. It corresponds to the first integral of the normal component of the momentum Eq. (76) in the moving frame. Evaluation of Eq. (97) at large negative $\hat{n}$ into the fuel stream yields the familiar Young-Laplace jump condition

$$P_F - P_O + \tau_{n,nO} - \tau_{n,nF} = \sigma \mathrm{K}_I, \tag{98}$$

where P_F and $\tau_{n,nF}$ are the local thermodynamic pressure and normal viscous stress away from the interface at intermediate distances $-\delta_T \ll \hat{n} \ll -\delta_I$ on the fuel side. Additionally, σ is the surface tension coefficient

$$\sigma = \int_{-\infty}^{+\infty} \kappa_{F,F}\left[\frac{\partial}{\partial \hat{n}}(\rho Y_F)\right]^2 d\hat{n}, \tag{99}$$

Table 4
Characteristic dimensional and nondimensional parameters for a typical high-pressure two-stream flow similar to that depicted in Fig. 1, where the coflow and fuel streams consist of N_2 and $C_{12}H_{26}$, respectively.

Dimensional parameters

R_F [m]	R_I [m]	δ_T [m]	δ_I [m]	$U_O\left[\frac{m}{s}\right]$	$U_F\left[\frac{m}{s}\right]$	P_∞ [bar]	T_O [K]	T_F [K]	T_e [K]	$\rho_O\left[\frac{kg}{m^3}\right]$	$\rho_F\left[\frac{kg}{m^3}\right]$	$W_O\left[\frac{kg}{mol}\right]$	$W_F\left[\frac{kg}{mol}\right]$
$5\cdot10^{-4}$	$5\cdot10^{-5}$	$5\cdot10^{-5}$	$5\cdot10^{-9}$	50	10	50	1000	350	500	16.67	640.62	$28\cdot10^{-3}$	$170\cdot10^{-3}$

η_O [Pa·s]	η_F [Pa·s]	$\lambda_O\left[\frac{W}{mK}\right]$	$\lambda_F\left[\frac{W}{mK}\right]$	$c_{p,O}\left[\frac{kJ}{kgK}\right]$	$c_{p,F}\left[\frac{kJ}{kgK}\right]$	$D_{T,O}\left[\frac{m^2}{s}\right]$	$D_{T,F}\left[\frac{m^2}{s}\right]$	$\mathcal{D}_{F,OO}\left[\frac{m^2}{s}\right]$	$\mathcal{D}_{FF,O}\left[\frac{m^2}{s}\right]$
$4.11\cdot10^{-5}$	$4.76\cdot10^{-4}$	0.07	0.10	1.17	2.25	$3.53\cdot10^{-6}$	$6.93\cdot10^{-8}$	$6.20\cdot10^{-7}$	$1.03\cdot10^{-8}$

$U_T\left[\frac{m}{s}\right]$	$c_O\left[\frac{m}{s}\right]$	$c_O^{IG}\left[\frac{m}{s}\right]$	$c_F\left[\frac{m}{s}\right]$	$\beta_{vO}\left[\frac{1}{K}\right]$	$\beta_{vF}\left[\frac{1}{K}\right]$	$\sigma_0\left[\frac{N}{m}\right]$	$\kappa_{F,F}\left[\frac{Jm^5}{kg^2}\right]$	t_I [s]	ℓ_{ca} [m]
0.07	642	630	1,100	$0.99\cdot10^{-3}$	$0.64\cdot10^{-3}$	0.01	$1.22\cdot10^{-16}$	$7.15\cdot10^{-8}$	$2.40\cdot10^{-7}$

Nondimensional parameters

γ_O^{IG}	Pr_F	Pr_O	Re_F	Re_O	We_F	We_O	ϵ_R	ϵ_T	$\mathcal{N}$	Pe_T	Oh_T	Ma_F	Ma_O
1.34	10.38	0.70	33,646	10,140	3300	2084	10^{-5}	10^{-4}	1.0	714	0.01	0.01	0.08

$\mathcal{R}$	Le_F	α	Z_O	Z_F	$\mathfrak{b}_O$	$\mathfrak{b}_F$	$\hat{c}_O$	$\mathcal{P}$	$\mathcal{W}$	τ
38.42	5.69	1.85	1.01	0.44	0.99	0.22	1.01	0.40	6.07	1.42

which represents the extension of Eq. (22) to bicomponent systems. Physical interpretations of σ based on the excess of the Landau's potential energy of the interface are discussed in Section 5.6.3.

5.3.2. Mechanical equilibrium tangential to the interface

Additional considerations are required in order to normalize Eq. (89). Close to the interface, the tangential relative velocity v_s vanishes and its normal gradient $\partial v_s/\partial\hat{n}$ is locally a constant of order U_O/δ_T. This motivates the introduction of the dimensionless variable

$$v_s^\star = v_s/(\epsilon_T U_O). \tag{100}$$

The tangential coordinate is normalized with the thermal mixing-layer thickness as

$$\hat{s}^\star = \hat{s}/\delta_T, \tag{101}$$

whereas the units of interface acceleration in the tangential and normal directions are assumed to be the same and equal to that used in Eq. (88). In the dimensionless variables (81)–(88) and (100) and (101), the tangential component of the momentum conservation Eq. (77) becomes

$$\rho^\star v_n^\star \frac{\partial v_s^\star}{\partial\hat{n}^\star} = \frac{Pr_O^2}{\epsilon_T Oh_T^2 Pe_T \mathcal{R}}\frac{\partial}{\partial\hat{s}^\star}\left(-P_{GD}^\star + \mathcal{K}_{s,s}^\star\right) + \frac{Pr_O}{\epsilon_T\mathcal{R}}\frac{\partial\tau_{n,s}^\star}{\partial\hat{n}^\star} + \frac{2\mathcal{N}Pr_O}{\mathcal{R}}\tau_{n,s}^\star - \frac{Pe_T}{\mathcal{R}^2}\rho^\star\left(\frac{\partial v_{I,s}}{\partial t}\right)^\star, \tag{102}$$

with

$$\tau_{n,s}^\star = \eta^\star\left(\frac{\partial v_s^\star}{\partial\hat{n}^\star} - \epsilon_T\mathcal{N}v_s^\star\right) \tag{103}$$

the nondimensional shear stress. Upon substituting (92) into Eq. (102), making use of Eqs. (74) and (97), neglecting the tangential gradients of thermodynamic pressure, and retaining the two most dominant terms multiplied by the largest dimensionless groups in accordance with Table 4, the simplified tangential momentum balance

$$\frac{\partial}{\partial\hat{s}^\star}\left(\mathcal{K}_{s,s}^\star - \mathcal{K}_{n,n}^\star\right) + \frac{Oh_T^2 Pe_T}{Pr_O}\frac{\partial\tau_{n,s}^\star}{\partial\hat{n}^\star} = 0 \tag{104}$$

is obtained, with $Oh_T^2 Pe_T/Pr_O = O(10^{-1})$ in the conditions addressed in Table 4. The integration of Eq. (104) and the substitution of Eqs. (74) and (99) provides the mechanical equilibrium condition in the tangential direction to the interface

$$\tau_{n,sO} - \tau_{n,sF} = -\frac{\partial\sigma}{\partial\hat{s}}, \tag{105}$$

where dimensional variables have been recovered in the notation. Equation (105) is commonly known as the Marangoni effect, and describes the onset of fluid motion along the interface due to tangential variations of the surface tension.

5.3.3. The thermodynamic pressure near the interface

The analyses in Sections 5.3.1 and 5.3.2 highlight the multiscale nature of the problem and the corresponding challenges associated with the integration of the momentum Eq. (45) because of the mostly balanced, spatially localized behavior of the gradient-dependent pressure and the interfacial stress tensor in the vicinity of the interface. The role of the thermodynamic pressure, which participates in this balance by linking the mechanical equilibrium conditions with the equation of state, is studied in this section.

Consider the schematics in Fig. 18(a) depicting the spatial distribution of the thermodynamic pressure P around the interface at scales much larger than δ_I. The Young-Laplace condition (98) states that the local thermodynamic pressures P_F and P_O on each side of the curved interface in Fig. 18(a) differ from one another by amounts of order σ_0/R_I. However, this pressure difference is much smaller than the combustor pressure P_∞ because R_I is typically much larger than σ_0/P_∞ even at high pressures (e.g., $\sigma_0/P_\infty =$ 1 nm at $P_\infty = 100$ bar in the conditions addressed in Table 4.).

The interfacial stresses and the gradient component of the pressure are negligible at distances $|n| \gg \delta_I$ on both sides away from the interface, where the momentum Eq. (45) becomes

$$\rho\frac{\partial\mathbf{v}}{\partial t} + \rho\mathbf{v}\cdot\nabla\mathbf{v} = -\nabla p + \nabla\cdot\boldsymbol{\tau}. \tag{106}$$

In Eq. (106), the thermodynamic pressure P has been replaced by a hydrodynamic pressure p by assuming $P \simeq P_\infty + p$. This decomposition requires the free-stream Mach numbers $Ma_O = U_O/c_O$ and $Ma_F = U_F/c_F$ to be small compared to unity. In the notation, c_O and c_F are the speed of the sound waves in the coflow and fuel free streams, respectively. An expression for the speed of sound c at high pressures, which generally differs from that of an ideal gas, is provided in Eq. (C.48). At small Mach numbers, the local departures of P from its corresponding mean values on each side of

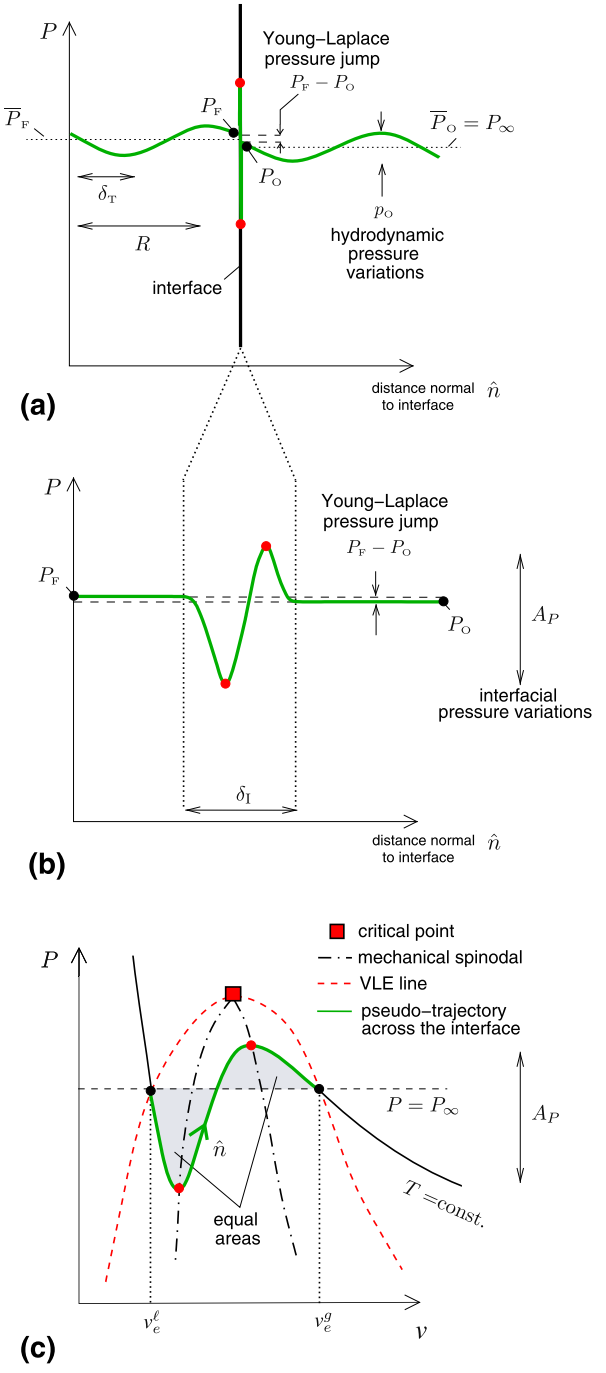

Fig. 18. Schematics of the pressure variations (a) near the interface, (b) within the interface, and (c) in thermodynamic space, the latter being particularized for a flat interface in a monocomponent isothermal flow.

the interface $\overline{P}_F$ and $\overline{P}_O = P_\infty$ are small. The condition that must be satisfied for these departures to be larger than the Young-Laplace pressure jump σ_0/R_I is that R_I must be larger than the capillary length $\ell_{ca} = \sigma_0/(\rho_O U_O^2)$. This condition tends to be always satisfied at high pressures, since ℓ_{ca} becomes very small because of the large values of density encountered in conjunction with the small values of surface tension, as suggested by the estimates provided in Table 4.

The above considerations suggest that the curvature-related terms in the mechanical equilibrium condition (97) can be neglected with relative errors of order $\sigma_0/(P_\infty R_I) \ll 1$, and the local coflow pressure P_O can be replaced by the combustor pressure P_∞ with relative errors of order $Ma_O^2 \ll 1$. With these simplifications in mind, and neglecting also the viscous stresses, Eq. (97) becomes

$$P_\infty - P + \rho\kappa_{F,F} Y_F \frac{\partial^2}{\partial\hat{n}^2}(\rho Y_F) - \frac{1}{2}\kappa_{F,F}\left[\frac{\partial}{\partial\hat{n}}(\rho Y_F)\right]^2 = 0. \tag{107}$$

Equation (107) can be integrated once yielding

$$\sigma = \frac{2}{3}\int_{-\infty}^{+\infty}(P_\infty - P)d\hat{n}, \tag{108}$$

which indicates that the surface tension is originated by a net underpressure within the interface. Specifically, Eq. (108) predicts strongly localized variations of the thermodynamic pressure of order $A_P \sim \sigma_0/\delta_I$ within the interface, as anticipated in Section 4.4 and shown schematically in Fig. 18(b). These variations are always much larger than those engendered by curvature by a factor of order $1/(\mathcal{N}\epsilon_T) \gg 1$, and they are also much larger than the hydrodynamic pressure variations by a factor of order $1/(\epsilon_R We_O) \gg 1$.

The boundary conditions employed in integrating Eq. (107) correspond to the fuel partial densities away from the interface. In the limit $\epsilon_T \ll 1$, it will be shown in Section 5.6 that the temperature gradient across the interface is small compared to the composition gradient. To leading order in ϵ_T, the interface is in phase equilibrium and consequently the fuel partial densities tend to their phase-equilibrium values on both sides of the interface,

$$\rho Y_F \to \rho_e^\ell Y_{Fe}^\ell \quad \text{at} \quad \hat{n} \to -\infty, \tag{109}$$

$$\rho Y_F \to \rho_e^g Y_{Fe}^g \quad \text{at} \quad \hat{n} \to +\infty, \tag{110}$$

where the limit $\hat{n} \to \pm\infty$ denotes distances much larger than δ_I but much smaller than δ_T. In this limit, the relative temperature variations across the interface are of order ϵ_T, and as a result the temperature becomes approximately uniform in the vicinity of the interface. The interface temperature T_e evolves with distance downstream, with $T_e \sim T_F$ near the injector orifice, and $T_e \sim T_{c,\mathrm{diff}}$ near the interface edge. Both phase-equilibrium values Y_{Fe}^ℓ and Y_{Fe}^g are therefore evaluated at P_∞ and T_e. Because of the locally uniform temperature, the normal directional derivative of the Gibbs-Duhem relation (C.9) simplifies to

$$\frac{\partial P}{\partial\hat{n}} = \rho Y_F \frac{\partial\mu_F}{\partial\hat{n}} + \rho(1 - Y_F)\frac{\partial\mu_O}{\partial\hat{n}}. \tag{111}$$

Upon substituting Eq. (111) into Eq. (107) differentiated with respect to $\hat{n}$, the alternative form of the mechanical equilibrium condition (107)

$$\rho Y_F \kappa_{F,F}\frac{\partial^3}{\partial\hat{n}^3}(\rho Y_F) = \rho Y_F \frac{\partial\mu_F}{\partial\hat{n}} + \rho(1 - Y_F)\frac{\partial\mu_O}{\partial\hat{n}} \tag{112}$$

is obtained. At long distances from the interface, Eq. (112) is subject to conditions (109) and (110), to the phase-equilibrium values for chemical potentials,

$$\mu_F \to \mu_{Fe} \quad \text{and} \quad \mu_O \to \mu_{Oe} \quad \text{at} \quad \hat{n} \to +\infty, \tag{113}$$

and to vanishing composition gradients,

$$\frac{\partial}{\partial\hat{n}}(\rho Y_F) \to 0 \quad \text{at} \quad \hat{n} \to +\infty. \tag{114}$$

5.3.4. Generalizations to multicomponent systems

The formulation above can be straightforwardly generalized to multicomponent flows. Specifically, the definition (90) for P_{GD}, along with general forms of Eqs. (72)–(74), namely

$$-P_{GD} + \mathcal{K}_{n,n} = -P + \sum_{i=1}^{N}\sum_{j=1}^{N}\left[\rho Y_i \kappa_{i,j}\frac{\partial^2}{\partial\hat{n}^2}(\rho Y_j)\right.$$

$$-\frac{1}{2}\kappa_{i,j}\frac{\partial}{\partial\hat{n}}(\rho Y_i)\frac{\partial}{\partial\hat{n}}(\rho Y_j)+\mathrm{K_I}\rho Y_i\kappa_{i,j}\frac{\partial}{\partial\hat{n}}(\rho Y_j)\Bigg], \quad (115)$$

$$-P_{\mathrm{GD}}+\mathcal{K}_{s,s}=-P+\sum_{i=1}^{N}\sum_{j=1}^{N}\Bigg[\rho Y_i\kappa_{i,j}\frac{\partial^2}{\partial\hat{n}^2}(\rho Y_j) +\frac{1}{2}\kappa_{i,j}\frac{\partial}{\partial\hat{n}}(\rho Y_i)\frac{\partial}{\partial\hat{n}}(\rho Y_j)+\mathrm{K_I}\rho Y_i\kappa_{i,j}\frac{\partial}{\partial\hat{n}}(\rho Y_j)\Bigg], \quad (116)$$

and

$$\mathcal{K}_{s,s}=\mathcal{K}_{n,n}+\sum_{i=1}^{N}\sum_{j=1}^{N}\kappa_{i,j}\frac{\partial}{\partial\hat{n}}(\rho Y_i)\frac{\partial}{\partial\hat{n}}(\rho Y_j), \quad (117)$$

can be substituted into Eq. (96) yielding

$$-P+\tau_{n,n}+\sum_{i=1}^{N}\sum_{j=1}^{N}\Bigg[\rho Y_i\kappa_{i,j}\frac{\partial^2}{\partial\hat{n}^2}(\rho Y_j) -\frac{1}{2}\kappa_{i,j}\frac{\partial}{\partial\hat{n}}(\rho Y_i)\frac{\partial}{\partial\hat{n}}(\rho Y_j)+\mathrm{K_I}\rho Y_i\kappa_{i,j}\frac{\partial}{\partial\hat{n}}(\rho Y_j)\Bigg] =-P_{\mathrm{O}}+\tau_{n,n\mathrm{O}}-\mathrm{K_I}\int_{\hat{n}}^{+\infty}\sum_{i=1}^{N}\sum_{j=1}^{N}\Bigg[\kappa_{i,j}\frac{\partial}{\partial\hat{n}}(\rho Y_i)\frac{\partial}{\partial\hat{n}}(\rho Y_j)\Bigg]d\hat{n}, \quad (118)$$

which represents the mechanical equilibrium condition normal to the interface for multicomponent flows. Evaluation of Eq. (118) away from the interface yields the Young-Laplace jump condition (98), with σ given by the general expression

$$\sigma=\int_{-\infty}^{+\infty}(\mathcal{K}_{s,s}-\mathcal{K}_{n,n})d\hat{n} =\int_{-\infty}^{+\infty}\sum_{i=1}^{N}\sum_{j=1}^{N}\Bigg[\kappa_{i,j}\frac{\partial}{\partial\hat{n}}(\rho Y_i)\frac{\partial}{\partial\hat{n}}(\rho Y_j)\Bigg]d\hat{n}. \quad (119)$$

It can be shown by using Eqs. (116)–(118) that variations of the surface tension coefficient along the interface in multicomponent flows give rise to the same tangential mechanical equilibrium condition (105) as in bicomponent flows.

Under the same assumptions used in Section 5.3.3 with regard to small curvatures and Mach numbers, Eq. (118) simplifies to

$$P_\infty-P+\sum_{i=1}^{N}\sum_{j=1}^{N}\Bigg[\rho Y_i\kappa_{i,j}\frac{\partial^2}{\partial\hat{n}^2}(\rho Y_j)-\frac{1}{2}\kappa_{i,j}\frac{\partial}{\partial\hat{n}}(\rho Y_i)\frac{\partial}{\partial\hat{n}}(\rho Y_j)\Bigg]=0, \quad (120)$$

which represents the multicomponent version of Eq. (107). For $\epsilon_{\mathrm{T}}\ll 1$, the boundary conditions employed to integrate Eq. (120) are analogous to (109) and (110) for every component. In that limit, the generalization of Eq. (112) to multicomponent mixtures is

$$\sum_{k=1}^{N}\sum_{j=1}^{N}\rho_k\kappa_{k,j}\frac{\partial^3}{\partial\hat{n}^3}(\rho Y_j)=\sum_{k=1}^{N}\rho_k\frac{\partial\mu_k}{\partial\hat{n}}. \quad (121)$$

For $k=1,\dots N$, Eq. (121) is subject to equilibrium values of the chemical potentials,

$$\mu_k\to\mu_{ke}\quad\text{at}\quad\hat{n}\to+\infty, \quad (122)$$

and to vanishing composition gradients,

$$\frac{\partial}{\partial\hat{n}}(\rho Y_k)\to 0\quad\text{at}\quad\hat{n}\to+\infty. \quad (123)$$

5.4. Closures for the interfacial transport fluxes of heat and species

Upon substituting Eq. (70) into Eq. (64), the entropy production source can be expressed as

$$\dot{s}_{\mathrm{prod}}=\frac{(\boldsymbol{\tau}:\nabla\mathbf{v})}{T}+\boldsymbol{\phi}\cdot\boldsymbol{F} \quad (124)$$

in terms of the scalar product of a vector of N thermodynamic forces

$$\boldsymbol{F}=\left[\nabla\left(\frac{1}{T}\right),-\frac{\nabla_T(\widetilde{\mu}_1-\widetilde{\mu}_N)}{T},\cdots-\frac{\nabla_T(\widetilde{\mu}_{N-1}-\widetilde{\mu}_N)}{T}\right] \quad (125)$$

and a vector of N currents

$$\boldsymbol{\phi}=\Bigg[\boldsymbol{q_t}+\boldsymbol{\mathcal{Q}}-\sum_{i=1}^{N}\boldsymbol{\psi_i}(\rho Y_i\nabla\cdot\mathbf{v})-\sum_{i=1}^{N-1}(\boldsymbol{\psi_i}-\boldsymbol{\psi_N})\nabla\cdot(\boldsymbol{J_i}+\boldsymbol{\mathcal{J}_i}) +\sum_{i=1}^{N-1}[(\chi_i-\chi_N)(\boldsymbol{J_i}+\boldsymbol{\mathcal{J}_i})-(h_i-h_N)\boldsymbol{\mathcal{J}_i}], \quad (\boldsymbol{J_1}+\boldsymbol{\mathcal{J}_1}),\dots(\boldsymbol{J_{N-1}}+\boldsymbol{\mathcal{J}_{N-1}})\Bigg]. \quad (126)$$

In dissipative systems, the second principle of thermodynamics requires $\dot{s}_{\mathrm{prod}}\geq 0$, which translates into

$$\dot{s}_{\mathrm{prod}}-\frac{(\boldsymbol{\tau}:\nabla\mathbf{v})}{T}=\boldsymbol{\phi}\cdot\boldsymbol{F}\geq 0, \quad (127)$$

because the viscous dissipation $\boldsymbol{\tau}$: $\nabla\mathbf{v}$ in Eq. (124) is a positive quadratic. The transport fluxes in $\boldsymbol{\phi}$ must be such that Eq. (127) is satisfied. The linear relation

$$\boldsymbol{\phi}=\boldsymbol{\mathcal{L}}\boldsymbol{F} \quad (128)$$

is the simplest approach that satisfies Eq. (127). In Eq. (128), $\boldsymbol{\mathcal{L}}=[\mathcal{L}_{i,k}]$ is a matrix of Onsager phenomenological coefficients, with $i,k=1,\dots N$. Specifically, in order to satisfy Eq. (127), $\boldsymbol{\mathcal{L}}$ must be symmetric and positive semidefinite, in that its elements $\mathcal{L}_{ik}$ must satisfy the conditions [138–140]

$$\mathcal{L}_{i,k}=\mathcal{L}_{k,i},\quad \mathcal{L}_{i,i}\geq 0,\quad \mathcal{L}_{i,k}^2\leq\mathcal{L}_{i,i}\mathcal{L}_{k,k},\quad \det\left(\mathcal{L}_{i,k}\right)\geq 0. \quad (129)$$

Using Eq. (128) in Eq. (124), the expression

$$\dot{s}_{\mathrm{prod}}-\frac{(\boldsymbol{\tau}:\nabla\mathbf{v})}{T}=\sum_{i=1}^{N}\sum_{k=1}^{N}\mathcal{L}_{ik}\boldsymbol{F_i}\boldsymbol{F_k} =\left(L_{q,q}\boldsymbol{F_1}+\sum_{k=1}^{N-1}L_{q,k}\boldsymbol{F}_{k+1}\right)\boldsymbol{F}_1+\sum_{i=1}^{N-1}\left(L_{i,q}\boldsymbol{F}_1+\sum_{k=1}^{N-1}L_{i,k}\boldsymbol{F}_{k+1}\right)\boldsymbol{F_{i+1}} \quad (130)$$

is obtained. In Eq. (130), the symbols $\boldsymbol{F_i}$, $\boldsymbol{F_k}$, and $\boldsymbol{F_{k+1}}$ denote components of $\boldsymbol{F}$, with $\boldsymbol{F_1}=\nabla(1/T)$ and

$$\boldsymbol{F_{i+1}}=-\frac{\nabla_T(\widetilde{\mu}_i-\widetilde{\mu}_N)}{T}=-\frac{\nabla_T(\mu_i-\mu_N)}{T}+\frac{\nabla_T\left[\nabla\cdot(\boldsymbol{\psi_i}-\boldsymbol{\psi_N})\right]}{T} \quad (131)$$

for $i=1,\dots,N-1$. In writing Eq. (131), use has been made of the definition (58) for the generalized chemical potential $\widetilde{\mu}_i$. Additionally, in Eq. (130), the Onsager coefficients have been renamed as

$$L_{q,q}=\mathcal{L}_{1,1},\quad L_{q,k}=\mathcal{L}_{1,k+1},\quad L_{i,q}=\mathcal{L}_{i+1,1},\quad L_{i,k}=\mathcal{L}_{i+1,k+1}, \quad (132)$$

with $i,k=1,\dots N-1$. A physical interpretation of these coefficients will be provided in Section 5.5.

The first bracketed term in the second line in Eq. (130) corresponds to the first element of the vector of currents (126). Equating these quantities gives

$$\boldsymbol{q_t}+\boldsymbol{\mathcal{Q}}-\sum_{i=1}^{N}\boldsymbol{\psi_i}(\rho Y_i\nabla\cdot\mathbf{v})-\sum_{i=1}^{N-1}(\boldsymbol{\psi_i}-\boldsymbol{\psi_N})\nabla\cdot(\boldsymbol{J_i}+\boldsymbol{\mathcal{J}_i})$$

$$+\sum_{i=1}^{N-1}\left[(\chi_i-\chi_N)(\boldsymbol{J_i}+\boldsymbol{\mathcal{J}_i})-(h_i-h_N)\boldsymbol{\mathcal{J}_i}\right]$$
$$=L_{q,q}\boldsymbol{F_1}+\sum_{k=1}^{N-1}L_{q,k}\boldsymbol{F}_{k+1}. \tag{133}$$

Similarly, the second bracketed term in the second line in Eq. (130) corresponds to the $i+1$ element of the vector of currents (126),

$$\boldsymbol{J_i}+\boldsymbol{\mathcal{J}_i}=\left(L_{i,q}\boldsymbol{F}_1+\sum_{k=1}^{N-1}L_{i,k}\boldsymbol{F}_{k+1}\right), \tag{134}$$

with $i=1,\dots N-1$.

In Eqs. (133) and (134), terms on the left-hand side can be associated with those on the right-hand side depending on whether they are functions of the gradient-energy coefficients. For instance, on the left-hand side of Eq. (133), $\boldsymbol{q_t}$ can be matched with those terms on the right-hand side that are independent of the gradient-energy coefficients,

$$\boldsymbol{q_t}=-\frac{L_{q,q}}{T^2}\nabla T-\sum_{k=1}^{N-1}\frac{L_{q,k}}{T}\nabla_T(\mu_k-\mu_N). \tag{135}$$

Substituting Eq. (135) into Eq. (49) gives the standard heat flux

$$\boldsymbol{q}=\underbrace{-\frac{L_{q,q}}{T^2}\nabla T}_{\text{Fourier conduction}}\underbrace{+\sum_{i=1}^{N-1}(h_i-h_N)\boldsymbol{J_i}}_{\text{interdiffusion}}\underbrace{-\sum_{k=1}^{N-1}\frac{L_{q,k}}{T}\nabla_T(\mu_k-\mu_N)}_{\text{Dufour effect}}. \tag{136}$$

Similarly, on the left-hand side of Eq. (134), $\boldsymbol{J_i}$ can be matched with those terms on the right-hand side that are independent of the gradient-energy coefficients, giving the standard species diffusion flux

$$\boldsymbol{J_i}=\underbrace{-\sum_{k=1}^{N-1}\frac{L_{i,k}}{T}\nabla_T(\mu_k-\mu_N)}_{\text{Fickian diffusion and barodiffusion}}\underbrace{-\frac{L_{q,i}}{T^2}\nabla T}_{\text{Soret effect (thermal diffusion)}}. \tag{137}$$

In Eqs. (136) and (137), the constant-temperature gradient of the chemical potential can be expanded in terms of gradients of composition and pressure, as shown in Appendix F.3, leading to the more familiar representation of these fluxes in Stefan–Maxwell form.

The interfacial corrections to $\boldsymbol{q}$ and $\boldsymbol{J_i}$ are derived by matching the remainders on both sides of Eqs. (133) and (134), respectively. This procedure gives the interfacial heat flux

$$\mathcal{Q}=\sum_{k=1}^{N-1}\frac{L_{q,k}}{T}\nabla_T\left[\nabla\cdot\left(\boldsymbol{\psi}_k-\boldsymbol{\psi}_N\right)\right]$$
$$+\sum_{i=1}^{N}\boldsymbol{\psi_i}(\rho Y_i\nabla\cdot\mathbf{v})+\sum_{i=1}^{N-1}(\boldsymbol{\psi_i}-\boldsymbol{\psi_N})\nabla\cdot(\boldsymbol{J_i}+\boldsymbol{\mathcal{J}_i})$$
$$-\sum_{i=1}^{N-1}\left[(\chi_i-\chi_N)(\boldsymbol{J_i}+\boldsymbol{\mathcal{J}_i})-(h_i-h_N)\boldsymbol{\mathcal{J}_i}\right] \tag{138}$$

and the interfacial species flux

$$\boldsymbol{\mathcal{J}_i}=\sum_{k=1}^{N-1}\frac{L_{i,k}}{T}\nabla_T\left[\nabla\cdot\left(\boldsymbol{\psi}_k-\boldsymbol{\psi}_N\right)\right], \tag{139}$$

with $\boldsymbol{\psi_i}$ and χ_i being defined in Eqs. (56) and (65), respectively. Similarly to the interfacial stress tensor $\mathcal{K}$, the species and heat fluxes $\boldsymbol{\mathcal{J}_i}$ and $\mathcal{Q}$ are also highly localized at the interface, where the partial-density gradients multiplied by the gradient-energy coefficients are dynamically relevant quantities.

In practical implementations of the transport fluxes (136)–(139), the constant-temperature gradients of μ_i and $\boldsymbol{\psi_i}$ are eliminated in favor of the full gradients ∇ by making use of Eqs. (63) and (65). The resulting expressions

$$\nabla(\mu_i-\mu_N)=\nabla_T(\mu_i-\mu_N)-(s_i-s_N)\nabla T, \tag{140}$$

$$\nabla\left[\nabla\cdot(\boldsymbol{\psi_i}-\boldsymbol{\psi_N})\right]=\nabla_T\left[\nabla\cdot(\boldsymbol{\psi_i}-\boldsymbol{\psi_N})\right]$$
$$+\left[\nabla\cdot(\boldsymbol{\psi_i}-\boldsymbol{\psi_N})-(\chi_i-\chi_N)\right]\frac{\nabla T}{T} \tag{141}$$

can be readily used to exchange $\nabla_T(\mu_i-\mu_N)$ for $\nabla(\mu_i-\mu_N)$, and $\nabla_T\left[\nabla\cdot(\boldsymbol{\psi_i}-\boldsymbol{\psi_N})\right]$ for $\nabla\left[\nabla\cdot(\boldsymbol{\psi_i}-\boldsymbol{\psi_N})\right]$, respectively.

5.5. The Onsager coefficients in transcritical conditions

The fluxes (136)–(139), along with the viscous and interfacial stresses (68) and (70), can be substituted into the entropy production rate (64), yielding

$$\dot{s}_{\text{prod}}=\frac{(\boldsymbol{\tau}:\nabla\mathbf{v})}{T}+L_{q,q}\left(\frac{|\nabla T|}{T^2}\right)^2$$
$$+\sum_{i=1}^{N-1}\sum_{k=1}^{N-1}\frac{L_{i,k}}{T^2}\nabla_T(\tilde{\mu}_k-\tilde{\mu}_N)\cdot\nabla_T(\tilde{\mu}_i-\tilde{\mu}_N)$$
$$+2\sum_{i=1}^{N-1}\frac{L_{q,i}}{T^3}\nabla_T(\tilde{\mu}_i-\tilde{\mu}_N)\cdot\nabla T. \tag{142}$$

It is shown in this section that the right-hand side of Eq. (142) is a positive quadratic in the transcritical conditions studied here.

In Eqs. (136)–(139) and (142), the N^2 coefficients $L_{q,q}$, $L_{q,i}$ ($i=1,\dots N-1$), and $L_{i,k}$ ($i,k=1,\dots N-1$) are arranged in the Onsager matrix as

$$\mathcal{L}=\begin{pmatrix}\boxed{L_{q,q}} & \boxed{L_{q,1} & \cdots & L_{q,N-1}}\\ \boxed{\begin{matrix}L_{q,1}\\ \vdots\\ L_{q,N-1}\end{matrix}} & \boxed{\begin{matrix}L_{1,1} & \cdots & L_{1,N-1}\\ \vdots & \ddots & \vdots\\ L_{1,N-1} & \cdots & L_{N-1,N-1}\end{matrix}}\end{pmatrix}. \tag{143}$$

The first subset of $\mathcal{L}$ consists of the single coefficient $L_{q,q}$, which participates in the Fourier conduction component of the standard heat flux $\boldsymbol{q}$. By simple inspection of Eqs. (136) or (F.24), the coefficient $L_{q,q}$ can be written as

$$L_{q,q}=\lambda T^2, \tag{144}$$

with λ being a thermal conductivity modeled in Appendix F.2.

The second subset of $\mathcal{L}$ corresponds to the coefficients $L_{i,k}$ [i.e., dot-dashed line rectangle in Eq. (143)], which are related to the interfacial species flux $\boldsymbol{\mathcal{J}_i}$ in Eq. (139) and to the Fickian component of $\boldsymbol{J_i}$ in Eq. (F.25). The calculation of $L_{i,k}$ is summarized in Appendix F.4 and involves the utilization of Eq. (F.34) relating the coefficients $L_{i,k}$ with the binary diffusion coefficients $\mathcal{D}_{i,j}$ modeled in Appendix F.5. For binary mixtures, Eq. (F.34) becomes a scalar equation that yields

$$L_{\text{F,F}}=\frac{\rho\mathcal{D}_{\text{F,O}}W_{\text{F}}W_{\text{O}}X_{\text{F}}(1-X_{\text{F}})}{\text{R}^0\overline{W}}. \tag{145}$$

The third subset of $\mathcal{L}$ are the coefficients $L_{q,i}$ [i.e., solid line rectangles in Eq. (143)], which are involved in the computation of the Soret and Dufour effects appearing, respectively, in the standard diffusion fluxes of heat $\boldsymbol{q}$ in Eq. (136) and species $\boldsymbol{J_i}$ in Eq. (137) [see also Eqs. (F.24) and (F.25) for the corresponding Stefan–Maxwell forms of these fluxes]. In particular, the coefficients $L_{q,i}$

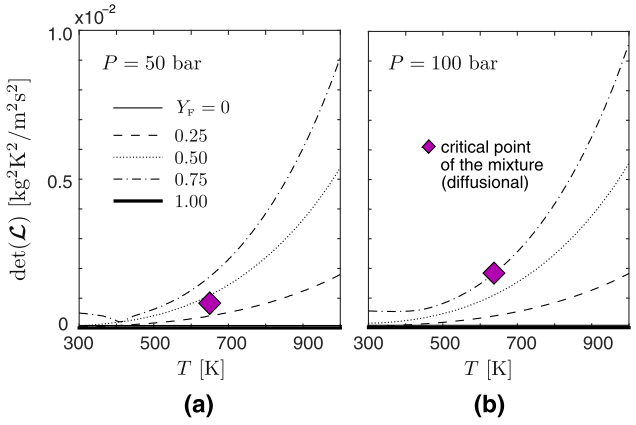

Fig. 19. Constant-pressure distributions of the determinant of the Onsager matrix for $C_{12}H_{26}/N_2$ mixtures at (a) $P = 50$ bar and (b) 100 bar as a function of temperature and mass fraction of dodecane Y_F (refer to the legend in the left panel). The plots include the diffusional critical point of the mixture at the corresponding pressure (purple diamond symbol). (For interpretation of the references to color in this figure legend, the reader is referred to the web version of this article.)

can be related through Eq. (F.43) to the diagonal coefficients $L_{i,i}$ and to the thermal-diffusion ratio $k_{i,T}$, the latter being modeled in Appendix F.6. For binary mixtures, Eq. (F.43) simplifies to

$$L_{q,F} = \rho T \mathcal{D}_{F,O} k_{F,T}. \tag{146}$$

The distributions of λ, $\mathcal{D}_{F,O}$, and $k_{F,T}$ with temperature and composition are studied in Appendix B.4 for $C_{12}H_{26}/N_2$ mixtures at high pressures.

The size of the Onsager matrix $\mathcal{L}$ in binary mixtures is 2×2 and its determinant is given by $\det(\mathcal{L}) = L_{q,q}L_{F,F} - L_{q,F}^2$. The requirement that $\mathcal{L}$ be positive semidefinite, and therefore that the entropy production source (142) be zero or positive, implies the condition $\det(\mathcal{L}) \geq 0$. Numerical evaluations for $15\,\text{bar} \leq P \leq 100\,\text{bar}$ indicate that the condition $\det(\mathcal{L}) \geq 0$ is satisfied for $C_{12}H_{26}/N_2$ mixtures at temperatures $300\,\text{K} \leq T \leq 1000\,\text{K}$ as long as the parameter constant ι participating in the calculation of $k_{F,T}$ is recalibrated within 10% of its standard value (see Appendix F.6 for details). These considerations are illustrated in Fig. 19 for two representative pressures.

Upon substituting the Onsager coefficients (144)–(146) into Eqs. (136)–(139) particularized for $N = 2$, the expressions

$$\begin{aligned}\mathcal{Q} = {}& \rho\kappa_{F,F}\mathcal{D}_{F,O}k_{F,T}\left\{\nabla\left[\nabla^2(\rho Y_F)\right] + \nabla^2(\rho\beta_\nu Y_F)\nabla T\right\}\\ &+ \kappa_{F,F}\nabla(\rho Y_F)[\rho Y_F \nabla\cdot\mathbf{v} + \nabla\cdot(\boldsymbol{J_F} + \mathcal{J_F})]\\ &- \kappa_{F,F}(\boldsymbol{J_F} + \mathcal{J_F})\left[\nabla^2(\rho Y_F) + T\nabla^2(\rho\beta_\nu Y_F)\right] + (h_F - h_O)\mathcal{J_F}\end{aligned} \tag{147}$$

and

$$\begin{aligned}\mathcal{J_F} = {}& \frac{\rho\kappa_{F,F}\mathcal{D}_{F,O}W_F W_O X_F(1-X_F)}{R^0 T\overline{W}}\\ &\times\left\{\nabla\left[\nabla^2(\rho Y_F)\right] + \nabla^2(\rho\beta_\nu Y_F)\nabla T\right\}\end{aligned} \tag{148}$$

are obtained for the interfacial fluxes of heat and species, respectively, along with

$$\boldsymbol{q} = -\lambda\nabla T + (h_F - h_O)\boldsymbol{J_F} - \rho\mathcal{D}_{F,O}k_{F,T}[\nabla(\mu_F - \mu_O) + (s_F - s_O)\nabla T] \tag{149}$$

and

$$\begin{aligned}\boldsymbol{J_F} = {}& -\frac{\rho\mathcal{D}_{F,O}W_F W_O X_F(1-X_F)}{R^0 T\overline{W}}[\nabla(\mu_F - \mu_O) + (s_F - s_O)\nabla T]\\ &- \rho\mathcal{D}_{F,O}k_{F,T}(\nabla T/T),\end{aligned} \tag{150}$$

for the standard diffusion fluxes of heat and species, respectively, where additional use of Eqs. (140) and (141) has been made. In Eqs. (149) and (150), the difference of partial specific entropies can be calculated as

$$s_F - s_O = (h_F - h_O + \mu_O - \mu_F)/T \tag{151}$$

by making use of the definition (60). Alternatively, based on the analysis outlined in Section F.3, $\boldsymbol{q}$ and $\boldsymbol{J_F}$ can be recast in traditional Stefan–Maxwell form as

$$\begin{aligned}\boldsymbol{q} = {}& -\lambda\nabla T - \frac{\rho\mathcal{D}_{F,O}R^0 T\overline{W}k_{F,T}}{W_F W_O X_F(1-X_F)}\left[\left(\frac{\partial\ln f_F}{\partial\ln X_F}\right)_{P,T}\nabla X_F\right.\\ &\left.+\frac{X_F}{R^0 T}\left(\tilde{\mathcal{V}}_F - \frac{\nu W_F}{\overline{W}}\right)\nabla P\right] + (h_F - h_O)\boldsymbol{J_F}\end{aligned} \tag{152}$$

and

$$\begin{aligned}\boldsymbol{J_F} = {}& -\rho\mathcal{D}_{F,O}\left[\left(\frac{\partial\ln f_F}{\partial\ln X_F}\right)_{P,T}\nabla X_F + \frac{X_F}{R^0 T}\left(\tilde{\mathcal{V}}_F - \frac{\nu W_F}{\overline{W}}\right)\nabla P\right]\\ &- \rho\mathcal{D}_{F,O}k_{F,T}(\nabla T/T),\end{aligned} \tag{153}$$

as shown by evaluating Eqs. (F.24) and (F.25) for $N = 2$ and utilizing Eqs. (145) and (146). Despite the fact that the Stefan-Maxwell forms (152) and (153) are more insightful than their unexpanded counterparts (149) and (150), their utilization in transcritical flows is not advantageous when the combustor pressure is not sufficiently high and the system crosses the mechanical spinodals. In those conditions, singularities arise in the non-ideal diffusion prefactor $(\partial\ln f_F/\partial\ln X_F)_{P,T}$ and in the fuel partial molar volume $\tilde{\mathcal{V}}_F$ [defined in Eq. (B.18) and particularized for the Peng-Robinson equation of state in Eq. (C.43)] that prevent from splitting the constant-temperature gradient of chemical potential into barodiffusion and Fickian diffusion, as discussed in Appendix E.1.

5.6. Transport equilibrium condition

In a similar way as the gradient-dependent pressure and interfacial stresses are balanced when the interface is in mechanical equilibrium, a balance between interfacial fluxes and standard diffusion fluxes exists when the interface is in transport equilibrium, as discussed in this section.

5.6.1. The transport equilibrium condition in terms of a balance of species fluxes

Consider again the slender interface separating two propellant streams in Fig. 17. The analysis begins by recalling that the characteristic length of the variation of the temperature downstream of the injection orifice is the thickness of the thermal mixing layer δ_T. In contrast, the composition across the interface undergoes rapid changes along much smaller distances of the same order as the interface thickness $\delta_I = \epsilon_T\delta_T \ll \delta_T$. This large composition gradient is due to the suppression of molecular diffusion in thermodynamically unstable conditions at high pressures, where the standard transport theory predicts antidiffusion of fuel and an ever-increasing composition gradient, as discussed in Section 4.6. It will be shown here that a mutual cancellation of the standard and interfacial species fluxes occurs at the interface in the limit $\epsilon_T \ll 1$ corresponding to small temperature gradients compared to the composition gradients across the interface. The resulting transport equilibrium condition provides a quasi-steady thermochemical description of the interface structure that is shown schematically in Fig. 20 and is elaborated in the remainder of this section.

The normal components of the species fluxes (148) and (153) ca be decomposed as

$$J_{F,n} = J'_{F,n} + J^{\Delta T}_{F,n} \quad \text{and} \quad \mathcal{J}_{F,n} = \mathcal{J}'_{F,n} + \mathcal{J}^{\Delta T}_{F,n}. \tag{154}$$

In this notation, the prime symbols refer to portions of the standard and interfacial species fluxes (153) and (148) that are inde-

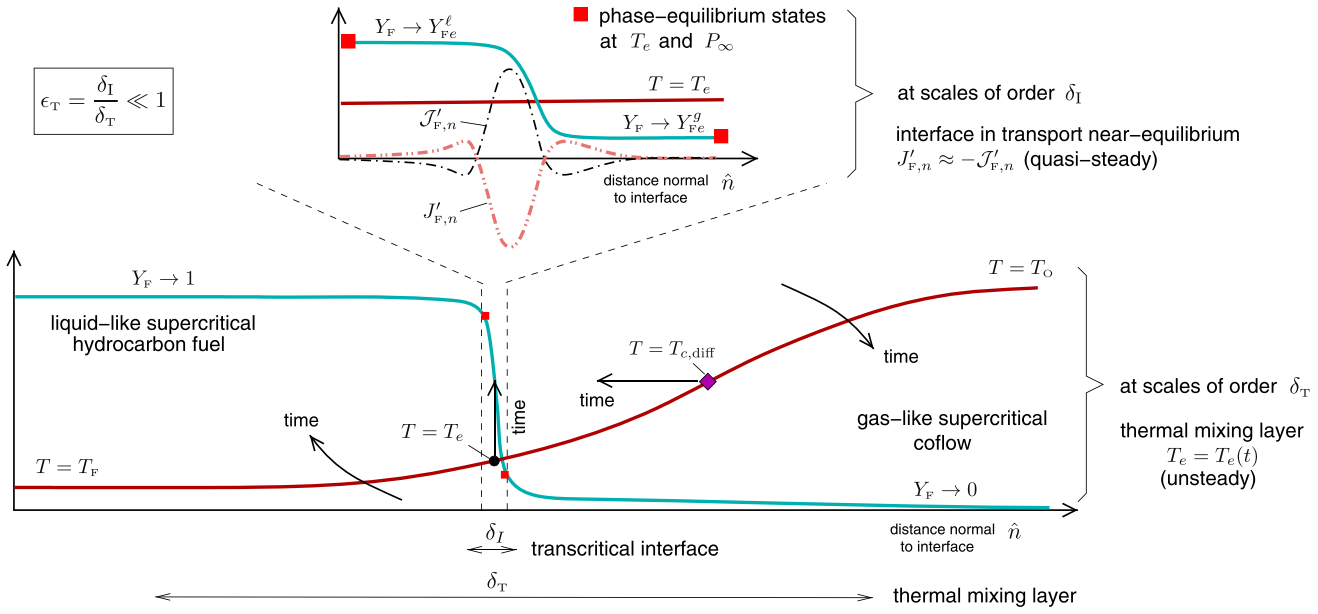

Fig. 20. Schematics of the quasi-steady thermochemical structure of a transcritical interface near transport equilibrium in a non-isothermal system at small thermal Cahn numbers, $\epsilon_T \ll 1$.

pendent of the temperature gradients:

$$J'_{F,n} = -\rho \mathcal{D}_{F,O}\left[\left(\frac{\partial \ln f_F}{\partial \ln X_F}\right)_{P,T}\frac{\partial X_F}{\partial \hat{n}} + \frac{X_F}{R^0 T}\left(\bar{\mathcal{V}}_F - \frac{\nu W_F}{\overline{W}}\right)\frac{\partial P}{\partial \hat{n}}\right], \tag{155}$$

$$\mathcal{J}'_{F,n} = \frac{\rho \kappa_{F,F}\mathcal{D}_{F,O}W_F W_O X_F(1-X_F)}{R^0 T \overline{W}}\left[\frac{\partial^3}{\partial \hat{n}^3}(\rho Y_F) + K_I \frac{\partial^2}{\partial \hat{n}^2}(\rho Y_F)\right]. \tag{156}$$

The superindex ΔT refers to the portions of fluxes directly proportional to the temperature gradients:

$$J^{\Delta T}_{F,n} = -\frac{\rho \mathcal{D}_{F,O} k_{F,T}}{T}\frac{\partial T}{\partial \hat{n}}, \tag{157}$$

$$\mathcal{J}^{\Delta T}_{F,n} = \frac{\rho \kappa_{F,F}\mathcal{D}_{F,O}W_F W_O X_F(1-X_F)}{R^0 T \overline{W}} \times \frac{\partial T}{\partial \hat{n}}\left[\frac{\partial^2}{\partial n^2}(\rho \beta_v Y_F) + K_I \frac{\partial}{\partial \hat{n}}(\rho \beta_v Y_F)\right]. \tag{158}$$

Using this notation, and in the moving curvilinear frame described in Section 5.3, the species conservation equation (46) for the fuel near the interface becomes

$$\rho \frac{\partial Y_F}{\partial t} + \rho v_n \frac{\partial Y_F}{\partial \hat{n}} = -\frac{\partial}{\partial \hat{n}}\left(J'_{F,n} + J^{\Delta T}_{F,n} + \mathcal{J}'_{F,n} + \mathcal{J}^{\Delta T}_{F,n}\right) - K_I\left(J'_{F,n} + J^{\Delta T}_{F,n} + \mathcal{J}'_{F,n} + \mathcal{J}^{\Delta T}_{F,n}\right). \tag{159}$$

In order to isolate the most important terms in Eq. (159), consider nondimensionalizing Eq. (159) with the same units as those employed to write the momentum Eq. (89), namely Eqs. (32) and (81)–(86). Additional characteristic scales for the temperature and species fluxes are obtained as follows.

For $\epsilon_T \ll 1$, the temperature gradient near the interface is locally a constant that can be approximated as $\partial T/\partial \hat{n} \sim (T_O - T_F)/\delta_T$. As a result, the variations of the temperature across the interface with respect to the interface temperature T_e are of order ϵ_T relative to the temperature difference between the free streams $T_O - T_F$. The dimensionless temperature is therefore defined as

$$T^\star = \frac{T - T_e}{\epsilon_T (T_O - T_F)}. \tag{160}$$

The chemical-potential variations through the interface A_μ, defined in Eq. (35), also correspond to the variations of μ_F through the coexistence region in thermodynamic space. These variations are related by Eq. (F.23) to the variations of the logarithm of the fugacity with respect to composition as

$$\left(\frac{\partial \ln f_F}{\partial \ln X_F}\right)_{P,T} \sim \left(\frac{\partial \ln f_F}{\partial X_F}\right)_{P,T} \sim \frac{A_\mu W_F}{R^0 T_F} \sim \mathcal{P} Z_F \tag{161}$$

across the interface, where the fuel molar fraction X_F is of order unity. In writing Eq. (161), use of Eq. (38) has been made in conjunction with the definitions (37) and (39) for the pressure ratio $\mathcal{P}$ and the fuel compressibility factor Z_F, respectively. Utilization of Eqs. (32) and (161) in Eq. (155), along with $\mathcal{D}^\star_{F,O} = \mathcal{D}_{F,O}/\mathcal{D}_{F,OO}$ as the binary diffusion coefficient normalized with its value $\mathcal{D}_{F,OO}$ in the coflow stream, provides the definition of the nondimensional portion of the standard species flux involving barodiffusion transport,

$$J'^\star_{F,n} = \frac{\epsilon_T \delta_T J'_{F,n}}{\rho_F \mathcal{D}_{F,OO}\mathcal{P} Z_F}. \tag{162}$$

Using Eqs. (81) and (160) in Eq. (157), the remainder $J^{\Delta T}_{F,n}$, corresponding to the Soret effect, is nondimensionalized as

$$J^{\Delta T\star}_{F,n} = \frac{\delta_T J^{\Delta T}_{F,n}}{\alpha \rho_F \mathcal{D}_{F,OO}}, \tag{163}$$

where α is a thermal-expansion ratio defined in Eq. (5).

The portion of the interfacial flux independent of the temperature gradient $\mathcal{J}'_{F,n}$ is normalized by substituting Eqs. (32), (81), (86), (32), (160), the nondimensional molecular weight $\overline{W}^\star = \overline{W}/W_O$ and the nondimensional partial molar volume $v^\star = \rho_F v/W_F$ into Eq. (156), thereby yielding

$$\mathcal{J}'^\star_{F,n} = \frac{\epsilon_T \delta_T \mathcal{J}'_{n,F}}{\rho_F \mathcal{D}_{F,OO}\mathcal{P} Z_F}. \tag{164}$$

The remainder $\mathcal{J}^{\Delta T}_{F,n}$ is normalized as

$$\mathcal{J}^{\Delta T\star}_{F,n} = \frac{\delta_T \mathcal{W} \mathcal{J}^{\Delta T}_{n,F}}{\alpha \bar{b}_F \rho_F \mathcal{D}_{F,OO}\mathcal{P} Z_F} \tag{165}$$

by using Eqs. (81), (86), (32), and (160) in Eq. (158), along with $\beta_\nu^\star = \beta_\nu/\beta_{\nu\mathrm{F}}$ for the nondimensional volume expansivity, with $\beta_{\nu\mathrm{F}}$ being the corresponding value in the fuel stream [see Eqs. (C.22) for an expression of β_ν particularized for the equation of state (14)]. In this formulation, $\mathfrak{b}_\mathrm{F} = T_\mathrm{F}\beta_{\nu\mathrm{F}}$ is the ratio of $\beta_{\nu\mathrm{F}}$ to the ideal-gas volume expansivity in the fuel stream $1/T_\mathrm{F}$, whereas $\mathcal{W} = W_\mathrm{F}/W_\mathrm{O}$ is the ratio of molecular weights.

The scalings in Eqs. (162)–(165) anticipate that the effect of the temperature gradients on the species transport fluxes near the interface is small,

$$\frac{J_{\mathrm{F},n}^{\Delta\mathrm{T}}}{J'_{\mathrm{F},n}} \sim \frac{\epsilon_\mathrm{T}\alpha}{\mathcal{P}Z_\mathrm{F}} \ll 1 \quad \text{and} \quad \frac{\mathcal{J}_{\mathrm{F},n}^{\Delta\mathrm{T}}}{\mathcal{J}'_{\mathrm{F},n}} \sim \frac{\epsilon_\mathrm{T}\alpha\mathfrak{b}_\mathrm{F}}{\mathcal{W}} \ll 1, \tag{166}$$

(see Table 4 for typical values of α, ϵ_T, $\mathcal{P}$, Z_F, $\mathfrak{b}_\mathrm{F}$ and $\mathcal{W}$), whereas the dominant components of the standard and interfacial species fluxes are of the same order of magnitude

$$J'_{\mathrm{F,n}}/\mathcal{J}'_{\mathrm{F,n}} = O(1). \tag{167}$$

Eq. (167) suggests a balance between the two portions of the species fluxes that are independent of the temperature gradients. This aspect is further investigated below by examining the species conservation equation and is ratified by the numerical examples that will be provided in Sections 6 and 7.

Upon substituting the variables (32), (81)–(86), and (162)–(165) into Eq. (159), the nondimensional species conservation equation

$$\rho^\star\frac{\partial Y_\mathrm{F}^\star}{\partial t^\star} + \rho^\star \mathrm{v}_\mathrm{n}^\star\frac{\partial Y_\mathrm{F}^\star}{\partial \hat{n}^\star} = -\frac{1}{\mathcal{E}_s}\left[\frac{\partial}{\partial \hat{n}^\star}\left(\mathrm{J}_{\mathrm{F,n}}^{\prime\star} + \mathcal{J}_{\mathrm{F,n}}^{\prime\star}\right) + \epsilon_\mathrm{T}\mathcal{N}\left(\mathrm{J}_{\mathrm{F,n}}^{\prime\star} + \mathcal{J}_{\mathrm{F,n}}^{\prime\star}\right)\right] - \frac{\alpha}{Le_\mathrm{F}}\left(\frac{\partial J_{\mathrm{F},n}^{\Delta\mathrm{T}\star}}{\partial \hat{n}^\star} + \epsilon_\mathrm{T}\mathcal{N}J_{\mathrm{F},n}^{\Delta\mathrm{T}\star}\right) - \frac{\alpha\mathfrak{b}_\mathrm{F}\mathcal{P}Z_\mathrm{F}}{Le_\mathrm{F}\mathcal{W}}\left(\frac{\partial \mathcal{J}_{\mathrm{F},n}^{\Delta\mathrm{T}\star}}{\partial \hat{n}^\star} + \epsilon_\mathrm{T}\mathcal{N}\mathcal{J}_{\mathrm{F},n}^{\Delta\mathrm{T}\star}\right) \tag{168}$$

is obtained, with

$$J_{\mathrm{F,n}}^{\prime\star} = -\rho^\star\mathcal{D}_{\mathrm{F,O}}^\star\left[\left(\frac{\partial \ln \mathrm{f}_\mathrm{F}}{\partial \ln X_\mathrm{F}}\right)_{P,T}^\star\frac{\partial X_\mathrm{F}}{\partial \hat{n}^\star} + \frac{X_\mathrm{F}}{(\tau+\alpha\epsilon_\mathrm{T}T^\star)}\left(\bar{\mathcal{V}}_\mathrm{F}^\star - \frac{\nu^\star\mathcal{W}}{\overline{W}^\star}\right)\frac{\partial P^\star}{\partial \hat{n}^\star}\right], \tag{169}$$

$$\mathcal{J}_{\mathrm{F,n}}^{\prime\star} = \frac{\rho^\star\kappa_{\mathrm{F,F}}^\star\mathcal{D}_{\mathrm{F,O}}^\star X_\mathrm{F}(1-X_\mathrm{F})}{(\tau+\alpha\epsilon_\mathrm{T}T^\star)\overline{W}^\star}\left[\frac{\partial^3}{\partial n^{\star 3}}(\rho^\star Y_\mathrm{F}) + \epsilon_\mathrm{T}\mathcal{N}\frac{\partial^2}{\partial n^{\star 2}}(\rho^\star Y_\mathrm{F})\right], \tag{170}$$

$$J_{\mathrm{F,n}}^{\Delta\mathrm{T}\star} = -\frac{\rho^\star\mathcal{D}_{\mathrm{F,O}}^\star k_{\mathrm{F,T}}}{(\tau+\alpha\epsilon_\mathrm{T}T^\star)}\frac{\partial T^\star}{\partial \hat{n}^\star}, \tag{171}$$

$$\mathcal{J}_{\mathrm{F,n}}^{\Delta\mathrm{T}\star} = \frac{\rho^\star\kappa_{\mathrm{F,F}}^\star\mathcal{D}_{\mathrm{F,O}}^\star X_\mathrm{F}(1-X_\mathrm{F})}{\overline{W}^\star(\tau+\alpha\epsilon_\mathrm{T}T^\star)} \times \frac{\partial T^\star}{\partial \hat{n}^\star}\left[\frac{\partial^2}{\partial n^{\star 2}}(\rho^\star\beta_\nu^\star Y_\mathrm{F}) + \epsilon_\mathrm{T}\mathcal{N}\frac{\partial}{\partial \hat{n}^\star}(\rho^\star\beta_\nu^\star Y_\mathrm{F})\right]. \tag{172}$$

In this formulation, $\bar{\mathcal{V}}_\mathrm{F}^\star = \rho_\mathrm{F}\bar{\mathcal{V}}_\mathrm{F}/W_\mathrm{F}$ is the nondimensional fuel partial volume, $\tau = T_e/T_\mathrm{F}$ is a temperature ratio, and $Le_\mathrm{F} = D_{\mathrm{T,O}}/\mathcal{D}_{\mathrm{F,OO}}$ is the fuel Lewis number evaluated in the coflow stream (see Table 4 for typical values of τ and Le_F). Additionally, $(\partial \ln \mathrm{f}_\mathrm{F}/\partial \ln \mathrm{X}_\mathrm{F})_{\mathrm{P,T}}^\star$ denotes the partial derivative of the logarithm of the fugacity with respect to the logarithm of the fuel molar fraction divided by $\mathcal{P}Z_\mathrm{F}$, as suggested by Eq. (161).

Following Table 4, the largest factor premultiplying the different terms in Eq. (168) is the one associated with the first term on the right-hand side, which is inversely proportional to ϵ_T and corresponds to the inverse of the transport-equilibrium parameter

$$\mathcal{E}_s = \frac{\epsilon_\mathrm{T}Le_\mathrm{F}}{\mathcal{P}Z_\mathrm{F}} = \frac{\rho_\mathrm{F}D_{\mathrm{T,O}}\mathrm{R}^0T_\mathrm{F}\delta_\mathrm{I}^2}{\sigma_0\mathcal{D}_{\mathrm{F,OO}}W_\mathrm{F}\delta_\mathrm{T}} = O(10^{-3}) \ll 1, \tag{173}$$

whereas $\alpha/Le_\mathrm{F} = O(1)$, $\mathcal{P}Z_\mathrm{F}/Le_\mathrm{F} = O(10^{-1})$, $\mathcal{N}\mathcal{P}Z_\mathrm{F}/Le_\mathrm{F} = O(10^{-1})$, and $(\alpha\mathfrak{b}_\mathrm{F}\mathcal{P}Z_\mathrm{F})/(Le_\mathrm{F}\mathcal{W}) = O(10^{-3})$ are much smaller. Correspondingly, the first approximation to Eq. (168) is

$$\frac{\partial}{\partial n^\star}\left(J_{\mathrm{F,n}}^{\prime\star} + \mathcal{J}_{\mathrm{F,n}}^{\prime\star}\right) = 0. \tag{174}$$

The integration of Eq. (174) up to large distances compared with the interface thickness involves a constant that corresponds to the sum of fluxes $J_{\mathrm{F,n}}^{\prime\star}|_{\hat{n}^\star\to+\infty} + \mathcal{J}_{\mathrm{F,n}}^{\prime\star}|_{\hat{n}^\star\to+\infty}$. While the interfacial component of that constant is zero for all practical purposes, the standard one $J_{\mathrm{F,n}}^{\prime\star}|_{\hat{n}\to+\infty}$ may not be zero away from the interface, since the coflow may mix with hot gas-like fuel transferred from the fuel side. This large-scale mixing of propellants away from the interface is described by the species conservation equation (46) minus the interfacial transport term,

$$\rho\frac{\partial Y_\mathrm{F}}{\partial t} + \rho\mathbf{v}\cdot\nabla Y_\mathrm{F} = -\nabla\cdot\boldsymbol{J}_\mathbf{F}, \tag{175}$$

whose solution near the interface provides the aforementioned integration constant $J_{\mathrm{F,n}}^{\prime\star}|_{\hat{n}\to+\infty}$. However, since Eq. (175) is driven by gradients of composition over distances comparable to the thermal mixing-layer thickness, the standard flux away from the interface $J_{\mathrm{F,n}}^{\prime\star}|_{\hat{n}\to+\infty}$ is anticipated to be of order ϵ_T compared to that near the interface $J_{\mathrm{F,n}}^{\prime\star}$, and can therefore be neglected. As a result, the integration of Eq. (174) leads to the transport equilibrium condition

$$J'_{\mathrm{F,n}} + \mathcal{J}'_{\mathrm{F,n}} = 0, \tag{176}$$

or equivalently

$$\left(\frac{\partial \ln \mathrm{f}_\mathrm{F}}{\partial \ln X_\mathrm{F}}\right)_{P,T}\frac{\partial X_\mathrm{F}}{\partial \hat{n}} + \frac{X_\mathrm{F}}{\mathrm{R}^0T_e}\left(\bar{\mathcal{V}}_\mathrm{F} - \frac{\nu W_\mathrm{F}}{\overline{W}}\right)\frac{\partial P}{\partial \hat{n}} = \frac{\kappa_{\mathrm{F,F}}W_\mathrm{F}W_\mathrm{O}X_\mathrm{F}(1-X_\mathrm{F})}{\mathrm{R}^0T_e\overline{W}}\frac{\partial^3}{\partial \hat{n}^3}(\rho Y_\mathrm{F}), \tag{177}$$

where use of Eqs. (155) and (156) has been made, and where dimensional variables have been recovered in the notation. The transport equilibrium condition (176) states that the Fickian and barodiffusion components of the standard species flux (153) balance the portion of the interfacial species flux (148) independent of the temperature gradient, as sketched in Fig. 20.

The interface temperature T_e, which is generally a function of time and the tangential coordinate $\hat{s}$, participates in Eq. (177) as demanded by the leading-order asymptotic expansion of the fluxes (169) and (170) for $\epsilon_\mathrm{T} \ll 1$. The temperature field around the interface evolves in time scales of order $\delta_\mathrm{T}^2/D_{\mathrm{T,O}}$, which are much larger than the flow transit time across the interface $\delta_\mathrm{I}/U_\mathrm{T}$. As a result, T_e is a quantity that varies mostly quasi-steadily at interfacial scales.

The boundary conditions required in the integration of Eq. (177) can be summarized as follows. First, the local thermodynamic pressure on the coflow side of the interface (see Fig. 17), which can be approximated as the combustor pressure P_∞ at sufficiently small Mach numbers, is recovered by the solution away from the interface,

$$P \to P_\mathrm{O} \sim P_\infty \quad \text{at} \quad \hat{n} \to +\infty. \tag{178}$$

Second, the fuel partial densities tend to their phase-equilibrium values away from the interface,

$$\rho Y_\mathrm{F} \to \rho_e^\ell Y_\mathrm{Fe}^\ell \quad \text{at} \quad \hat{n} \to -\infty, \tag{179}$$

$$\rho Y_\mathrm{F} \to \rho_e^g Y_\mathrm{Fe}^g \quad \text{at} \quad \hat{n} \to +\infty. \tag{180}$$

Concurrent with (180) and the equation of state (14) is the recovery of the phase-equilibrium molar fraction on the coflow side of the interface,

$$X_\mathrm{F} \to X_\mathrm{Fe} = Y_\mathrm{Fe}^g\overline{W}_e^g/W_\mathrm{F} \quad \text{at} \quad \hat{n} \to +\infty. \tag{181}$$

In Eqs. (178)–(181), the limit $\hat{n} \to \pm\infty$ denotes distances much larger than $\delta_{\rm I}$ but much smaller than $\delta_{\rm T}$. Both phase-equilibrium values $Y_{\rm Fe}^{\ell}$ and $Y_{\rm Fe}^{g}$ are evaluated at P_∞ and T_e.

5.6.2. The transport equilibrium condition in terms of a balance of heat fluxes

Utilizing Eqs. (147) and (152), it can be shown that the transport equilibrium condition (177) is equivalent to a balance of heat fluxes across the interface,

$$q_n' + \mathcal{Q}_n' = 0, \tag{182}$$

where q_n' is the sum of the Dufour effect and the interdiffusion of heat by $J_{n,\rm F}'$,

$$q_n' = -\frac{\rho \mathcal{D}_{\rm F,O} \mathrm{R}^0 T_{\rm F} \overline{W} k_{\rm F,T}}{W_{\rm F} W_{\rm O} X_{\rm F}(1-X_{\rm F})}\left[\left(\frac{\partial \ln \mathrm{f_F}}{\partial \ln X_{\rm F}}\right)_{P,T}\frac{\partial X_{\rm F}}{\partial \hat{n}} + \frac{X_{\rm F}}{\mathrm{R}^0 T_{\rm F}}\left(\bar{\mathcal{V}}_{\rm F} - \frac{\nu W_{\rm F}}{\overline{W}}\right)\frac{\partial P}{\partial \hat{n}}\right] + (h_{\rm F} - h_{\rm O}) J_{n,\rm F}' \tag{183}$$

and $\mathcal{Q}_n'$ is the portion of the interfacial heat flux independent of temperature gradients

$$\mathcal{Q}_n' = \rho \kappa_{\rm F,F} \mathcal{D}_{\rm F,O} k_{\rm F,T}\left[\frac{\partial^3}{\partial \hat{n}^3}(\rho Y_{\rm F}) + \mathrm{K_I}\frac{\partial^2}{\partial \hat{n}^2}(\rho Y_{\rm F})\right] + (h_{\rm F} - h_{\rm O})\mathcal{J}_{n,\rm F}'. \tag{184}$$

Both q_n' and $\mathcal{Q}_n'$ participate in the enthalpy conservation equation (51) when referred to the same curvilinear, moving coordinate system described above,

$$\rho\frac{\partial h}{\partial t} + \rho \mathrm{v_n}\frac{\partial \mathrm{h}}{\partial \hat{n}} = \frac{\partial \mathrm{P_{GD}}}{\partial \mathrm{t}} + \mathrm{v_n}\frac{\partial \mathrm{P_{GD}}}{\partial \hat{n}} - \frac{\partial}{\partial \hat{n}}\left(\mathrm{q_n'} + \mathrm{q_n^{\Delta T}} + \mathcal{Q}_{\rm n}' + \mathcal{Q}_{\rm n}^{\Delta \rm T}\right) - \mathrm{K_I}\left(q_n' + q_n^{\Delta \rm T} + \mathcal{Q}_n' + \mathcal{Q}_n^{\Delta \rm T}\right) + \mathcal{K}_{n,n}\frac{\partial \mathrm{v_n}}{\partial \hat{n}}, \tag{185}$$

where the viscous dissipation has been neglected by assuming small Mach numbers. In Eq. (185), the flux $q_n^{\Delta \rm T}$ is the sum of Fourier conduction and interdiffusion of heat by the Soret effect,

$$q_n^{\Delta \rm T} = -\lambda \nabla T + (h_{\rm F} - h_{\rm O}) J_{\rm F,n}^{\Delta T}, \tag{186}$$

while $\mathcal{Q}_n^{\Delta \rm T}$ is the portion of the interfacial heat flux that depends on temperature gradients,

$$\begin{aligned}\mathcal{Q}_n^{\Delta \rm T} = {} & \rho \kappa_{\rm F,F} \mathcal{D}_{\rm F,O} k_{\rm F,T}\frac{\partial T}{\partial \hat{n}}\left[\frac{\partial^2}{\partial \hat{n}^2}(\rho \beta_v Y_{\rm F}) + \mathrm{K_I}\frac{\partial}{\partial \hat{n}}(\rho \beta_v Y_{\rm F})\right] \\ & + \kappa_{\rm F,F}\frac{\partial}{\partial \hat{n}}(\rho Y_{\rm F})\left[\rho Y_{\rm F}\left(\frac{\partial \mathrm{v_n}}{\partial \hat{n}} + \mathrm{K_I v_n}\right)\right. \\ & \left. + \frac{\partial}{\partial \hat{n}}\left(J_{\rm F,n}^{\Delta T} + \mathcal{J}_{\rm F,n}^{\Delta T}\right) + \mathrm{K_I}\left(J_{\rm F,n}^{\Delta T} + \mathcal{J}_{\rm F,n}^{\Delta T}\right)\right] \\ & - \kappa_{\rm F,F}\left(J_{\rm F,n}^{\Delta T} + \mathcal{J}_{\rm F,n}^{\Delta T}\right)\left[\frac{\partial^2}{\partial \hat{n}^2}(\rho Y_{\rm F}) + \mathrm{K_I}\frac{\partial}{\partial \hat{n}}(\rho Y_{\rm F})\right. \\ & \left. + T\frac{\partial^2}{\partial \hat{n}^2}(\rho \beta_v Y_{\rm F}) + T\mathrm{K_I}\frac{\partial}{\partial \hat{n}}(\rho \beta_v Y_{\rm F})\right] + (h_{\rm F} - h_{\rm O})\mathcal{J}_{\rm F,n}^{\Delta T}.\end{aligned} \tag{187}$$

Similarly to the scaling analysis made for the species conservation Eq. (159), it can be shown that the heat balance (182) is the result of integrating the first approximation to the enthalpy conservation Eq. (185),

$$\frac{\partial}{\partial \hat{n}}(q_n' + \mathrm{Q}_n') = 0. \tag{188}$$

Expressions (183), (184), (186) and (187), along with the relation (161) and the dimensionless variables (32), (81), (82), (85), (86), and (160)–(165), motivate the characteristic scales

$$q_n' \sim \mathrm{Q}_n' \sim \frac{\rho_{\rm F} \mathcal{D}_{\rm F,OO} \mathrm{R}^0 T_{\rm F} \mathcal{P} Z_{\rm F}}{\epsilon_{\rm T} \delta_{\rm T} W_{\rm F}},$$

$$q_n^{\Delta \rm T} \sim \frac{\alpha \lambda_{\rm O} T_{\rm F}}{\delta_{\rm T}}, \quad \mathrm{Q}_n^{\Delta \rm T} \sim \frac{\alpha \mathfrak{b}_{\rm F} \rho_{\rm F} \mathcal{D}_{\rm F,OO} \mathrm{R}^0 T_{\rm F} \mathcal{P} Z_{\rm F}}{\delta_{\rm T} W_{\rm F} \mathcal{W}}, \tag{189}$$

for the heat fluxes. These expressions indicate that q_n' and Q_n' are of the same order of magnitude, whereas $q_n^{\Delta \rm T}$ and $\mathrm{Q}_n^{\Delta \rm T}$ are negligible since

$$\frac{q_n^{\Delta T}}{q_n'} \sim \frac{\epsilon_{\rm T} \alpha Le_{\rm F} \hat{\mathrm{c}}_{\rm O} \mathcal{W}}{\mathcal{R}\mathcal{P} Z_{\rm F}}\left(\frac{\gamma_{\rm O}^{\rm IG}}{\gamma_{\rm O}^{\rm IG} - 1}\right) \ll 1 \quad \text{and} \quad \frac{\mathcal{Q}_n^{\Delta T}}{\mathcal{Q}_n'} \sim \frac{\epsilon_{\rm T} \alpha \mathfrak{b}_{\rm F}}{\mathcal{W}} \ll 1. \tag{190}$$

In Eq. (190), $\gamma_{\rm O}^{\rm IG}$ is the ideal-gas adiabatic coefficient defined in Eq. (C.27), and $\hat{\mathrm{c}}_{\rm O} = \mathrm{c_{p,O}}/\mathrm{c_{p,O}^{IG}}$ is a ratio of real-to-ideal specific heats at constant pressure, both parameters being evaluated in the coflow stream (see Table 4 for typical values of $\gamma_{\rm O}^{\rm IG}$ and $\hat{\mathrm{c}}_{\rm O}$). In the vicinity of the interface, it can be also shown that convection of enthalpy, viscous dissipation, pressure advection, curvature-related terms, and enthalpy production by interfacial forces in Eq. (185) are negligible compared to the normal derivative of the sum $q_n' + \mathcal{Q}_n'$.

5.6.3. Combination of mechanical and transport equilibrium conditions in terms of chemical potentials

As discussed in Appendix E.1, the pressures within the interface may become small enough to cross the mechanical spinodals when the combustor pressure decreases but it is still high relative to the atmospheric value. In that case, singularities in $\bar{\mathcal{V}}_{\rm F}$ and $(\partial \ln \mathrm{f_F}/\partial \ln X_{\rm F})_{P,T}$ arise that can be regularized by combining the Fickian and barodiffusion components into a single finite term given by the relation

$$\frac{\partial}{\partial \hat{n}}(\mu_{\rm F} - \mu_{\rm O}) = \frac{\overline{W}}{W_{\rm F} W_{\rm O}(1 - X_{\rm F})}\left[\left(\bar{\mathcal{V}}_{\rm F} - \frac{\nu W_{\rm F}}{\overline{W}}\right)\frac{\partial P}{\partial \hat{n}} + \frac{\mathrm{R}^0 T}{X_{\rm F}}\left(\frac{\partial \ln \mathrm{f_F}}{\partial \ln X_{\rm F}}\right)_{P,T}\frac{\partial X_{\rm F}}{\partial \hat{n}}\right] \tag{191}$$

obtained by evaluating Eq. (F.22) for $N = 2$ and approximating the constant-temperature gradients by ordinary ones because of the locally uniform temperature prevailing in the vicinity of the interface in the limit $\epsilon_{\rm T} \ll 1$. When expression (191) is used in Eqs. (155) and (183), the scaling analysis performed above does not change in any fundamental manner and gives a transport equilibrium condition valid over the entire high-pressure range that can be written as

$$\frac{\partial}{\partial \hat{n}}(\mu_{\rm F} - \mu_{\rm O}) = \kappa_{\rm F,F}\frac{\partial^3}{\partial \hat{n}^3}(\rho Y_{\rm F}). \tag{192}$$

Eq. (192) is subject to the boundary conditions (113)-(114) away from the interface.

The transport equilibrium condition (192) can be combined with the mechanical equilibrium condition (112) and integrated once giving the system of equations

$$\mu_{\rm F} - \mu_{\rm Fe} = \kappa_{\rm F,F}\frac{\partial^2}{\partial \hat{n}^2}(\rho Y_{\rm F}), \tag{193}$$

$$\mu_{\rm O} - \mu_{\rm Oe} = 0. \tag{194}$$

Eq. (193) is subject to the boundary conditions (109)–(110), whereas Eq. (194) predicts that the chemical potential of the coflow species remains constant across the interface, and equal to its phase-equilibrium value, when only the fuel gradient-energy coefficient is considered in the analysis.

5.6.4. Generalizations to multicomponent systems

The formulation can be easily generalized to multicomponent systems. First, consider the generalized version of the species flux balance (176), namely

$$J'_{i,n} + \mathcal{J}'_{i,n} = 0, \qquad i = 1, \dots N-1. \tag{195}$$

In multicomponent systems, the species fluxes of the i-th component, Eqs. (139) and (F.25), depend on the Onsager coefficients of $N-1$ components, thereby making Eq. (195) of little interest for large N. A more useful version of Eq. (195) independent of the Onsager coefficients is derived in this section.

Upon substituting the species fluxes (139) and (F.25) into Eq. (195), the system of $N-1$ equations

$$\sum_{k=1}^{N-1} L_{i,k}\mathcal{F}_k = 0 \tag{196}$$

is obtained, with $i = 1, \dots N-1$. In this formulation, $\mathcal{F}_k$ are components of an auxiliary vector defined as

$$\begin{aligned}\mathcal{F}_k = &\sum_{j=1}^{N}(\kappa_{k,j} - \kappa_{N,j})\frac{\partial^3}{\partial \hat{n}^3}(\rho Y_j) \\ &- \sum_{m=1}^{N-1}\left(\frac{X_m}{W_N X_N} + \frac{\delta_{m,k}}{W_k}\right)\sum_{j=1}^{N-1}\mathrm{R}^0 T_e \frac{\partial X_j}{\partial \hat{n}}\left(\frac{\partial \ln f_m}{\partial X_j}\right)_{P,T,X_{r|r=1,\dots N-1\ (r\neq j)}} \\ &- \left(\frac{\bar{\mathcal{V}}_k}{W_k} - \frac{v}{W_N X_N} + \sum_{m=1}^{N-1}\frac{X_m \bar{\mathcal{V}}_m}{W_N X_N}\right)\frac{\partial P}{\partial \hat{n}},\end{aligned} \tag{197}$$

where use of Eqs. (56) and (140) has been made in order to replace the symbols ∇_{T}, $\boldsymbol{\psi_k}$, and $\boldsymbol{\psi_N}$ in Eq. (139) by their corresponding expressions under the approximation of locally uniform temperature. A similar substitution of the definition of heat fluxes (138) and (F.24) into Eq. (182) yields

$$\sum_{k=1}^{N-1} L_{q,k}\mathcal{F}_k = 0. \tag{198}$$

The concatenation of Eqs. (196) and (198) represents an over-determined system $\boldsymbol{\mathcal{M}}\boldsymbol{\mathcal{F}} = 0$, with N equations for $N-1$ unknowns. The resulting matrix of coefficients $\boldsymbol{\mathcal{M}}$ is the Onsager matrix $\boldsymbol{\mathcal{L}}$ given in Eq. (143) excluding the first column, with $\mathrm{rank}(\boldsymbol{\mathcal{M}}) \leq \mathrm{N}-1$ because $\boldsymbol{\mathcal{L}}$ is positive semidefinite. In particular, $\mathrm{rank}(\boldsymbol{\mathcal{M}}) = \mathrm{N}-1$ is achieved when $\boldsymbol{\mathcal{L}}$ is positive definite, or equivalently, when the entropy production (142) is strictly positive. In that case, the only possible solution to the over-determined system (196) and (198) is the trivial one,

$$\mathcal{F}_k = 0 \tag{199}$$

for $k = 1, \dots N-1$.

Equation (199) represents the multicomponent version of the transport equilibrium condition (177) and is also equivalent to the simultaneous verification of the heat and species flux balances (182) and (195). Using Eq. (F.22), the multicomponent transport equilibrium condition (199) can be rewritten in terms of gradients of chemical potentials as

$$\frac{\partial}{\partial \hat{n}}(\mu_k - \mu_N) = \sum_{j=1}^{N}(\kappa_{k,j} - \kappa_{N,j})\frac{\partial^3}{\partial \hat{n}^3}(\rho Y_j) \tag{200}$$

for $k = 1, \dots N-1$. The combination of the multicomponent mechanical equilibrium condition (121) and the multicomponent transport equilibrium condition (200) gives

$$\frac{\partial \mu_k}{\partial \hat{n}} = \sum_{j=1}^{N}\kappa_{k,j}\frac{\partial^3}{\partial \hat{n}^3}(\rho Y_j) \tag{201}$$

for $k = 1, \dots N$, which can be integrated once subject to the boundary conditions (122) and (123) yielding

$$\mu_k - \mu_{ke} = \sum_{j=1}^{N}\kappa_{k,j}\frac{\partial^2}{\partial \hat{n}^2}(\rho Y_j) \tag{202}$$

for $k = 1, \dots N$. The system of Eq. (202) is subject to the boundary conditions

$$\rho Y_i \to \rho_e^{\ell} Y_{ie}^{\ell} \quad \text{at} \quad \hat{n} \to -\infty \quad \text{for} \quad i = 1, \dots N, \tag{203}$$

$$\rho Y_i \to \rho_e^{g} Y_{ie}^{g} \quad \text{at} \quad \hat{n} \to +\infty \quad \text{for} \quad i = 1, \dots N, \tag{204}$$

corresponding to the phase-equilibrium compositions away from the interface evaluated at P_∞ and T_e. Additional approximations made to arrive at Eq. (202) involve negligible curvatures, small Mach numbers, and negligible effects of viscous stresses at interface scales, as explained in Section 5.3.3; the consideration of these effects would require modification of Eq. (202) by using instead the general form of the mechanical equilibrium condition (118) in the derivations above.

A relation exists between σ and the energy excess, or Landau potential, $\Omega = \rho(f - \sum_{k=1}^{N} Y_k \mu_{ke})$ at the interface in conditions of mechanical and transport equilibrium. Upon multiplying Eq. (202) by ρY_k, summing the resulting expression from $k = 1$ to N, and using Eqs. (120), (16), and (C.7) and (C.8), the equation

$$\Omega_{\mathrm{GD}} - \Omega_e = \sum_{k=1}^{N}\sum_{j=1}^{N}\kappa_{k,j}\frac{\partial}{\partial \hat{n}}(\rho Y_k)\frac{\partial}{\partial \hat{n}}(\rho Y_j) \tag{205}$$

is obtained. In Eq. (205), $\Omega_e = -P_\infty$ is the phase-equilibrium value of Ω, as prescribed by Eq. (C.7), and Ω_{GD} is the gradient-dependent Landau potential

$$\Omega_{\mathrm{GD}} = \rho\left(f_{\mathrm{GD}} - \sum_{k=1}^{N} Y_k \mu_{ke}\right). \tag{206}$$

The integration of Eq. (205) across the interface yields

$$\sigma = \int_{-\infty}^{\infty}(\Omega_{\mathrm{GD}} - \Omega_e)\, d\hat{n}, \tag{207}$$

which provides a quantitative link between the interfacial excess energy and the surface-tension coefficient.

5.7. Remarks on transcritical interfaces in equilibrium and near-equilibrium conditions

The dimensionless parameters $\mathcal{E}_m$ in Eq. (95) and $\mathcal{E}_s$ in Eq. (173) measure, respectively, the tendency of the interface to attain mechanical and transport equilibrium. The smaller $\mathcal{E}_m$ and $\mathcal{E}_s$, the more equilibrated the interface is. Both $\mathcal{E}_m$ and $\mathcal{E}_s$ are proportional to the thermal Cahn number ϵ_{T}, or dimensionally, to the temperature gradient across to the interface.

In isothermal systems, the thermal Cahn number is exactly zero, $\epsilon_{\mathrm{T}} = 0$, and therefore $\mathcal{E}_m = \mathcal{E}_s = 0$. The interface is in mechanical and transport equilibrium, in that the variations of the gradient-dependent pressure are exactly balanced with the variations of the interfacial stress normal to the interface, and the sum of the standard and interfacial species fluxes is exactly zero. The structure of the interface can be described by the combination of the mechanical equilibrium condition (120) and the transport equilibrium condition (199), or equivalently, by the system of Eq. (202) subject to the phase-equilibrium partial densities (203) and (204) in the far field. The system of Eqs. (202) has been utilized in early work addressing interfaces in multicomponent equilibrium isothermal systems [17,37,100,109,118,121,131,132], and can be alternatively derived by minimizing the volume integral of the

gradient-dependent Helmholtz free energy [116,117,120]. In addition, the system (202) equivalently states that the generalized chemical potential $\widetilde{\mu}_k$ given by Eq. (58) remains constant through the interface and equal to the phase-equilibrium chemical potential μ_{ke}. Correspondingly, the sources of entropy related to gradients of temperature and generalized chemical potential in Eq. (142) are exactly zero in mechanical and transport equilibrium.

For the binary mixtures studied here, the system of Eqs. (202) simplifies to Eqs. (193) and (194) subject to the boundary conditions (109) and (110). The solution to that problem is a steady planar transcritical interface bearing surface tension and separating a liquid-like supercritical mixture rich in fuel from a gas-like supercritical mixture rich in coflow species, with both mixtures being in phase equilibrium as discussed in Section 6.

None of the different forms of the transport equilibrium condition [i.e., Eqs. (176), (177), (182), (192), (199), (200), and (202)] depend on transport coefficients. Similarly, although high-order viscous effects can be retained in the derivation of the mechanical equilibrium condition in Eq. (97), the leading-order balance is independent of viscosity, as suggested by Eqs. (107), (112), and (120). As a result, the internal structure of a transcritical interface in mechanical and transport equilibrium is independent of viscosity, thermal conductivity, binary diffusion coefficient, and thermal-diffusion ratio.

In non-isothermal systems, the thermal Cahn number is larger than zero, although in practical situations it remains small compared to unity, $\epsilon_{\mathrm{T}} \ll 1$, because the temperature gradients created by the flow are never as large as the composition gradients across the interface. Even in the wake of the orifice ring separating both propellant streams in Fig. 1, where the temperature gradient is the largest, the characteristic length for the temperature variations is the thickness of the orifice ring, which is always much larger than the interface thickness.

For $0 < \epsilon_{\mathrm{T}} \ll 1$, the mechanical (95) and transport (173) equilibrium parameters attain small but non-zero values, $0 < \{\mathcal{E}_m, \mathcal{E}_s\} \ll 1$. As a result, the interface is neither in mechanical equilibrium nor in transport equilibrium. However, the departures from equilibrium are small, and the equilibrium conditions still describe the overall structure of the interface to a good approximation, as discussed in Section 7. The interface temperature T_e and the far-field boundary conditions away from the interface may become functions of space and time because of the large-scale evolution of the flow, but the characteristic length and time scales of these variations, $\delta_{\mathrm{T}} = \delta_{\mathrm{I}}/\epsilon_{\mathrm{T}}$ and $\delta_{\mathrm{T}}^2/D_{\mathrm{T}} = t_{\mathrm{I}}/\epsilon_{\mathrm{T}}$, are much larger, respectively, than the interface thickness δ_{I} and the flow transit time across the interface t_{I} (see Table 4 for typical values of δ_{I} and t_{I}). As a result, the structure of the interface evolves quasi-steadily in response to those flow variations, as sketched in Fig. 20. The complete description of the evolution of the interface and the flow surrounding it requires the Navier-Stokes equations outlined in Section 4.7 supplemented with the closures for interfacial terms derived above.

An intermediate case may exist in non-isothermal systems in which the interface is much closer to mechanical equilibrium than to transport equilibrium, $0 < \mathcal{E}_m \ll \mathcal{E}_s \ll 1$ [e.g., $\mathcal{E}_m/\mathcal{E}_s = O(10^{-3})$ in the conditions addressed in Table 4]. In this case, the species conservation equation (46) can be integrated simultaneously with the mechanical equilibrium condition (120). The latter is subject to boundary conditions corresponding to partial densities generally away from phase equilibrium, and may involve pure components in the propellant streams. This intermediate case is addressed in Section 7. The solution provides the spatiotemporal evolution of the transcritical interface and the associated surface-tension coefficient downstream of the injection orifice, as previewed in Figs. 2 and 3.

6. Transcritical interfaces in isothermal bicomponent systems

This section provides numerical results describing steady transcritical interfaces in $C_{12}H_{26}/N_2$ isothermal systems. The configuration analyzed here corresponds to the limit of infinitely thick thermal mixing layers, or equivalently, to the case of zero thermal Cahn numbers, $\epsilon_{\mathrm{T}} = 0$, in which the interface is in mechanical and transport equilibrium.

6.1. Formulation

The equations integrated here are (193) and (194), which are supplemented with the equation of state (14) and mixing rules (15) particularized for binary mixtures [see Eq. (212) introduced below], along with the expressions for the gradient-energy coefficient (23), chemical potential (B.23), ideal-gas Gibbs free energy (C.46), fugacity coefficient (C.47), and the constants provided in Table C.1 and Appendix C. The boundary conditions away from the interface are the phase-equilibrium partial densities (109) and (110). The problem has a steady solution consisting of a thin interface that bears surface tension and separates a liquid-like $C_{12}H_{26}$-rich supercritical mixture from a gas-like nitrogen-rich supercritical mixture. A summary of the formulation is provided in Table 5. Details associated with the numerical integration of these equations are discussed in Appendix G.

The calculations focus on the four cases summarized in Table 6. In all cases, the thermodynamic pressure away from the interface $P_\infty = 50 - 100$ bar is larger than the critical pressures of the individual components, while the temperature $T_e = 350 - 500$ K is smaller than both the fuel critical temperature $T_{\mathrm{c,F}} = 658$ K and the temperature of the diffusional critical point $T_{\mathrm{c,diff}}$ at the corresponding pressure (i.e., see Table 3). As a result, the pseudo-trajectories along the interface in thermodynamic space traverse the coexistence region, as shown in Fig. 21. Furthermore, while case D only involves crossings of the diffusional spinodal, cases A, B, and C involve crossings of both diffusional and mechanical spinodals. It is therefore convenient to use the combined mechanical and transport equilibrium conditions written in terms of gradients of chemical potentials (193) and (194), since, as explained in Appendix E.1, these forms are unaffected by singularities arising in the fuel partial molar volume and non-ideal diffusion prefactor near the mechanical spinodals. It is also in cases A, B, and C where the thermodynamic pressure reaches negative values within the interface. This effect is inconsequential because the formulation in Table 5 is independent of the transport coefficients.

6.2. Results: the steady transcritical interface

The profiles of density, fuel mass fraction, and thermodynamic pressure across the interface are shown in Fig. 22(a–c). Density ratios of order $\mathcal{R} \sim 13$ (for cases A and C at $P_\infty = 50$ bar) and $\mathcal{R} \sim 7$ (for cases B and D at $P_\infty = 100$ bar) are observed in the solution that are spatially localized and accompanied by order-unity variations of the fuel mass fraction in accordance with the phase-equilibrium composition on each side of the interface. In particular, on the fuel side of the interface, the mixtures are rich in $C_{12}H_{26}$ and have compressibility factors within the range $Z \sim 0.30$–0.75, which clearly depart from the ideal behavior corresponding to unity. The oscillation of the pressure across the coexistence region is localized near the fuel side of the interface, where an underpressure of order unity relative to P_∞ occurs. It will be shown that this large underpressure leads to significant values of surface tension in accord with Eq. (108). In contrast, on the other side of the interface, the mixture is rich in N_2 and much less dense. The corresponding compressibility factors are within the range $Z \sim 1.01$–1.03, thereby indicating that the fluid approaches there the behavior of

Table 5
Dimensional formulation for equilibrium transcritical flat interfaces in isothermal bicomponent systems.

Conservation equations	
Mechanical and transport equilibrium	$\mu_F - \mu_{Fe} = \kappa_{F,F}\dfrac{d^2}{d\hat{n}^2}(\rho Y_F)$, $\mu_O - \mu_{Oe} = 0$.
Boundary conditions	
Phase-equilibrium composition	$\rho Y_F \to \rho_e^\ell Y_{Fe}^\ell$ at $\hat{n} \to -\infty$, $\rho Y_F \to \rho_e^g Y_{Fe}^g$ at $\hat{n} \to +\infty$.
Supplementary expressions (see Appendix B, Appendix C, and Appendix F for details)	
Equation of state	Eq. (14),
Coefficients of the equation of state	Eqs. (212), and (C.10)-(C.12),
Gradient-energy coefficient	Eqs. (23), (C.17), and (C.18),
Thermodynamic relations	Eqs. (213), (214), (B.19), (B.20), (C.43), and (C.47).

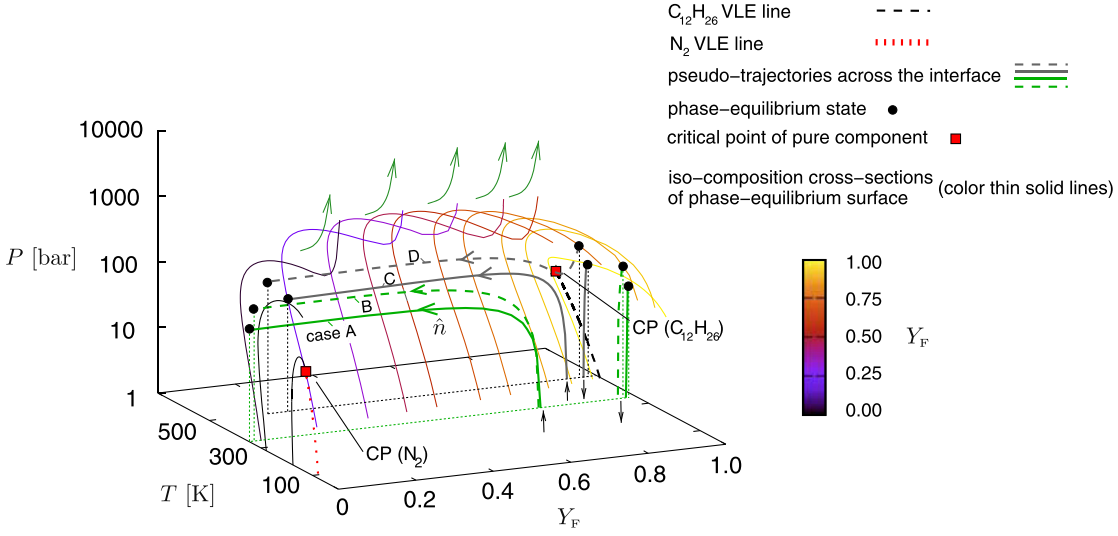

Fig. 21. Thermodynamic-space pseudo-trajectories across transcritical interfaces in $C_{12}H_{26}/N_2$ isothermal systems for cases A-D described in Table 6. The figure includes isocomposition cross-sections of the phase-equilibrium surface colored by fuel mass fraction.

Table 6
Thermodynamic conditions and phase-equilibrium composition corresponding to the pseudo-trajectories A-D in Fig. 21 for transcritical interfaces in $C_{12}H_{26}/N_2$ isothermal systems.

			Phase-equilibrium composition			
			$\hat{n} \to -\infty$ (liquid-like supercritical)		$\hat{n} \to +\infty$ (gas-like supercritical)	
case	T_e [K]	P_∞ [bar]	$\rho_e^\ell \left[\frac{kg}{m^3}\right]$	Y_{Fe}^ℓ	$\rho_e^g \left[\frac{kg}{m^3}\right]$	Y_{Fe}^g
A	350	50	642.1	0.983	48.1	0.002
B	350	100	642.5	0.966	95.3	0.003
C	500	50	541.9	0.979	40.2	0.202
D	500	100	539.8	0.957	74.9	0.151

an ideal gas despite the high pressures, the reason being that N_2 is highly supercritical in temperature.

A point-wise cancellation between the standard and interfacial fluxes of species is observed within the interface in Fig. 22(d). Positive values of the standard diffusion flux J_F (i.e., in the direction of decreasing fuel concentration) are observed on both flanks of the interface, whereas negative values (i.e., in the direction of increasing fuel concentration) occur inside.

A detailed breakdown of the species fluxes is provided in Fig. 23(a) for case D. In the diffusionally unstable region of the interface, the Fickian component of the species flux antidiffuses fuel in the direction of increasing concentration, as anticipated in Section 4.6. In contrast, the barodiffusion component acts in the opposite direction by transporting fuel along the positive pressure gradient, albeit with less intensity than the Fickian component. As a result, the standard species flux J_F is dominated by Fickian antidiffusion within the interface, with zero-flux points $J_F = 0$ being coincident with the diffusional-spinodal states given by the maximum and minimum locations of the fuel chemical potential, as shown in Fig. 23(b).

No steady solution of the problem exists for $\kappa_{F,F} = 0$ (i.e., $\mathcal{J}_F = 0$). Specifically, $\kappa_{F,F} = 0$ would impede the balance shown in Fig. 23(a) between the interfacial species flux $\mathcal{J}_F$ and the standard one J_F. The interfacial species flux $\mathcal{J}_F$ provides the necessary amount of positive transport of fuel, in the direction of decreasing fuel concentration, to yield a finite-thickness interface that persists indefinitely in time.

The interface thickness can be computed as

$$\delta_I = \frac{\rho_e^\ell Y_{Fe}^\ell - \rho_e^g Y_{Fe}^g}{\max\left|\dfrac{d(\rho Y_F)}{d\hat{n}}\right|}. \tag{208}$$

Despite the high pressures considered here, Fig. 24(a) indicates that δ_I calculated using Eq. (208) remains small compared to hydrodynamic scales of interest in practical systems (i.e., δ_I=1.59–2.98 nm). Specifically, the values of δ_I observed here are comparable to those arising in subcritical monocomponent systems of sep-

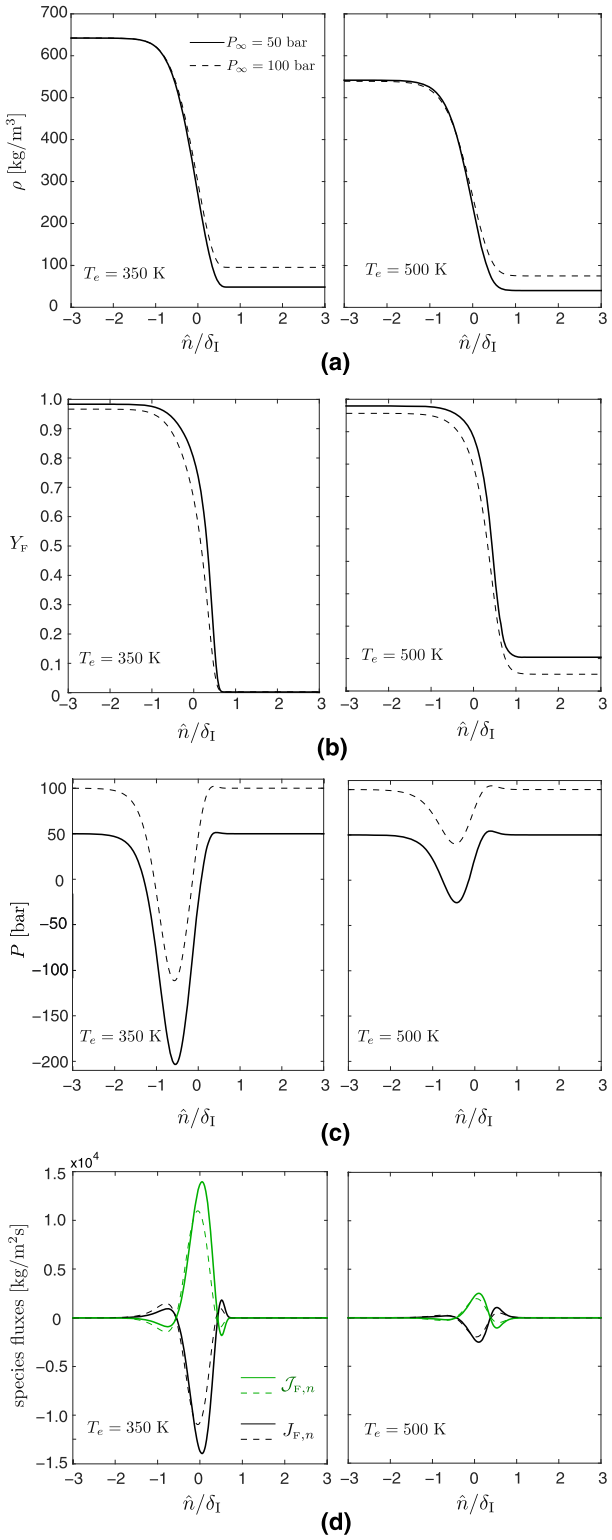

Fig. 22. (a) Density, (b) fuel mass fraction, (c) thermodynamic pressure, and (d) fuel species flux across transcritical interfaces in $C_{12}H_{26}/N_2$ isothermal systems at $T_e = 350$ K (left column) and $T_e = 500$ K (right column) at the pressures indicated in panel (a). Panel (d) includes the interfacial species flux $\mathcal{J}_F$ (green lines), and the standard species flux J_F (dark lines). The spatial coordinate is normalized with $\delta_I = 1.59$ nm, 1.71 nm, 2.75 nm, and 2.98 nm for cases A, B, C, and D, respectively (see Table 6). (For interpretation of the references to color in this figure legend, the reader is referred to the web version of this article.)

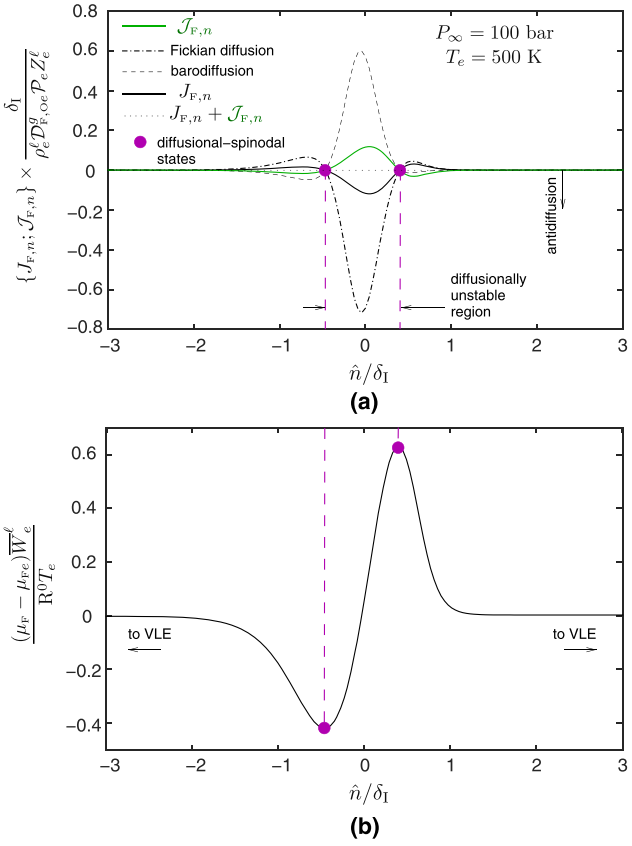

Fig. 23. (a) Standard species flux J_F (dark line), including the Fickian (dot-dashed line) and barodiffusion (dashed line) components, along with the interfacial species flux $\mathcal{J}_F$ (green line) arising from the present diffuse-interface theory. (b) Specific fuel chemical potential highlighting the diffusional-spinodal states. The results shown in this figure correspond to case D in Table 6 for transcritical interfaces in $C_{12}H_{26}/N_2$ isothermal systems. The normalizations in this figure have been carried out with the phase-equilibrium composition provided in Table 6 along with the phase-equilibrium values for the binary diffusion coefficient $\mathcal{D}^g_{F,Oe} = 2.1 \cdot 10^{-7}$ m²/s, compressibility factor $Z^\ell_e = 0.62$, molecular weight $\overline{W}^\ell_e = 139$ g/mol, fuel specific chemical potential $\mu_{Fe} = -3.63$ MJ/kg, and pressure parameter $\mathcal{P}_e = 0.64$. (For interpretation of the references to color in this figure legend, the reader is referred to the web version of this article.)

arate N_2 or $C_{12}H_{26}$ close to their critical points (see Appendix D). However, because of the high pressures attainable in the coexistence region of hydrocarbon-fueled mixtures, the associated Knudsen numbers $Kn_I \sim 0.02 - 0.15$ are relatively smaller here [see Fig. 24(b)], and can be made arbitrarily smaller by further increasing the pressure, or by increasing the temperature, with $Kn_I \to 0$ as the pressure or temperature conditions approach those of the diffusional critical point. As a result, the continuum hypothesis underlying the present diffuse-interface theory may be much more appropriate in transcritical bicomponent systems than in subcritical monocomponent ones.

The surface tension coefficient σ computed from Eq. (99) is shown in Fig. 25(a). Despite the high pressures, the predicted values of σ are dynamically significant over a wide temperature range. They amount to 30–40% of σ of water in air at atmospheric pressure. Discrepancies of 10–20% are observed between these calculations and experimental measurements of σ in diesel/nitrogen interfaces reported in Ref. [15] [e.g., σ(50 bar, 308 K) ≈ 23.0 mN/m and σ(50 bar, 323 K) ≈ 21.0 mN/m in experiments [15], versus σ(50 bar, 308 K) = 28.1 mN/m and σ(50 bar, 323 K) = 27.2 mN/m in the present work]. Similar discrepancies are observed in Fig. 26 between the present work and the experiments

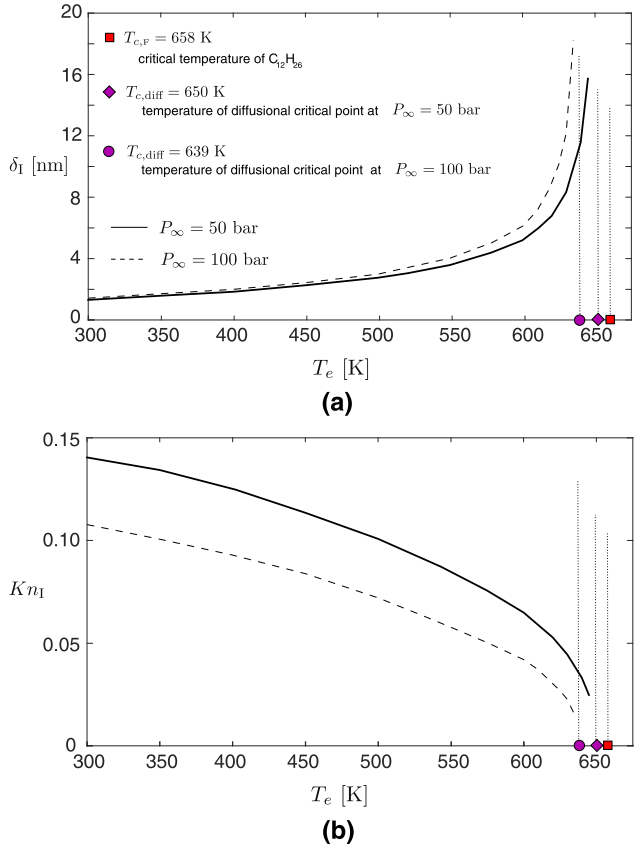

Fig. 24. (a) Interface thickness and (b) Knudsen number as a function of temperature in $C_{12}H_{26}/N_2$ isothermal systems at two pressures [refer to legend in panel (a)].

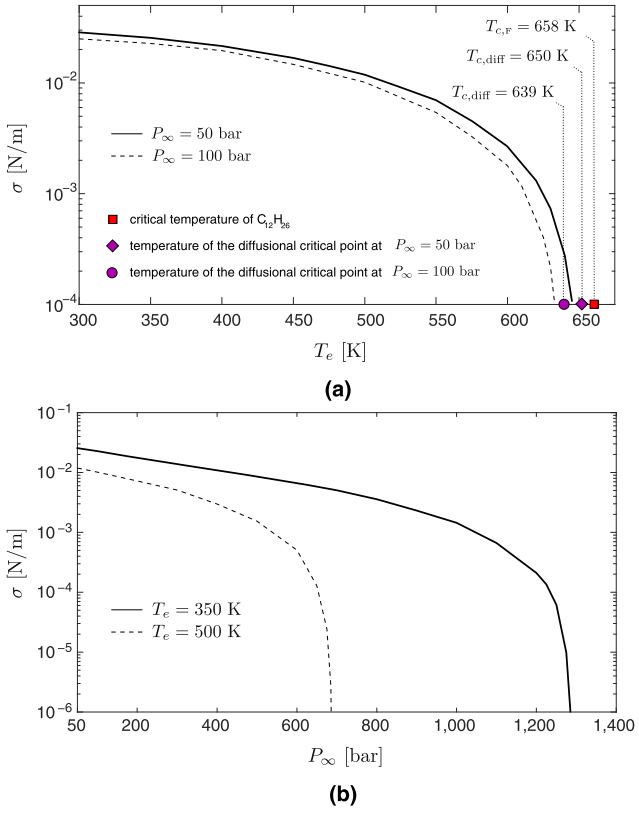

Fig. 25. Surface-tension coefficient (a) as a function of temperature at different pressures, and (b) as a function of pressure for different temperatures. All cases correspond to $C_{12}H_{26}/N_2$ isothermal systems.

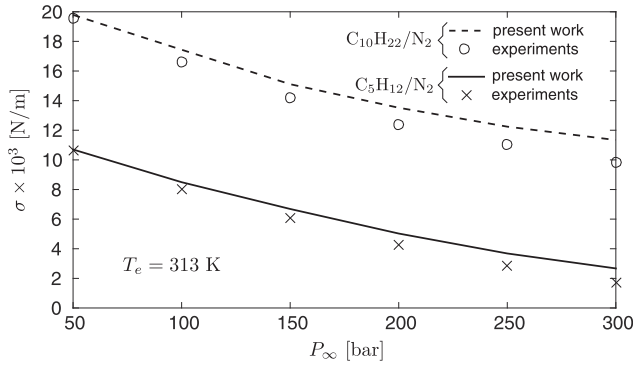

Fig. 26. Surface-tension coefficient as a function of pressure in isothermal systems at $T_e = 313$ K composed of N_2 and decane ($C_{10}H_{22}$) or pentane (C_5H_{12}), including experiments (symbols from Ref. [16]) and numerical results from the present work (solid and dashed lines).

in Ref. [16] when decane and pentane are used instead of dodecane.

As P_∞ and T_e increase, the amplitudes of the species fluxes decrease, the interface becomes thicker, the Knudsen number decreases, and the variations of density, pressure, and composition across the interface decrease, thereby causing a decrease in σ, as shown in Fig. 25(a). In particular, the surface tension vanishes and δ_I diverges to infinity when T_e equals the temperature of the diffusional critical point $T_{c,diff}$ at $P = P_\infty$. Steady transcritical interfaces cannot exist for $T_e > T_{c,diff}$ in $C_{12}H_{26}/N_2$ mixtures. In those conditions, the mixture is fully supercritical, there is no mechanism that opposes the diffusion of fuel in the direction of decreasing concentrations, and therefore the composition gradient decreases with time.

The limiting value for the temperature above which transcritical interfaces disappear may not necessarily be $T_{c,diff}$ in mixtures whose thermodynamic phase diagram is substantially different from the ones engendered by the hydrocarbon-fueled mixtures studied here. For instance, while $C_{12}H_{26}/N_2$ mixtures are characterized by $T_{c,diff} \simeq T_{c,mix}$ (see Table 3), other mixtures may have $T_{c,mix} \gg T_{c,diff}$, in such a way that the maximum temperature of the diffusional spinodal surface could be intermediate to $T_{c,diff}$ and $T_{c,mix}$. In that case, transcritical interfaces could still exist for $T_e > T_{c,diff}$, but would disappear if T_e becomes larger than the maximum temperature of the diffusional spinodal surface.

Transcritical interfaces persist even after large increments in pressure. As shown in Fig. 25(b), at fixed temperatures of practical interest, T_e=350–500 K, transcritical interfaces survive until pressures $P_\infty \sim$600–1200 bar, above which the coexistence region disappears and the mixture becomes fully supercritical.

6.3. The generalized Cahn-Hilliard equation

In isothermal systems, the constant-temperature gradient of chemical potentials becomes an ordinary gradient, and therefore the species conservation equation (46) can be written as

$$\rho \frac{\partial Y_i}{\partial t} + \rho \mathbf{v} \cdot \nabla Y_i = \nabla \cdot \left\{ \sum_{k=1}^{N-1} \frac{L_{i,k}}{T_e} \nabla \Big[\underbrace{\mu_k - \mu_N}_{\substack{\text{Standard transport} \\ \text{(Fickian+barodiffusion)}}} - \underbrace{\nabla \cdot (\boldsymbol{\psi}_k - \boldsymbol{\psi}_N)}_{\text{Diffuse-interface correction}} \Big] \right\} \tag{209}$$

for $i = 1, \ldots, N$, where use of Eqs. (137) and (139) has been made. In Eq. (209), the auxiliary vectors $\boldsymbol{\psi}_k$ are defined in Eq. (56), whereas the Onsager coefficient $L_{i,k}$ are calculated using Eq. (F.30) and the method described in Appendix F.4.

Equation (209) is a generalized multicomponent version of the original Cahn-Hilliard equation derived in Ref. [109] for binary systems near the critical point. In contrast to Ref. [109], no assumption of a simplified predetermined form of the difference of chemical potentials $\mu_k - \mu_N$ has been made here. Instead, the chemical potentials are described exactly by Eqs. (B.22), (B.23), and by Eq. (C.47) for the Peng-Robinson equation of state (14). Setting the right-hand side of the generalized Cahn-Hilliard Eq. (209) to zero gives the transport equilibrium condition (200). That is an undetermined system of $N-1$ equations that needs to be combined with the mechanical equilibrium condition (121) and integrated once to yield the determined system of N Eq. (202), as described in Section 5.6.4.

Numerical simulations employing diffuse-interface frameworks in CFD codes have been aimed at predicting complex two-phase flows at near-atmospheric pressures [145–148]. Those simulations employ ad-hoc versions of Eq. (209) to avoid numerical smearing of the interface [e.g., see Eq. (57) in Ref. [147]]. Key assumptions made in those formulations are:

(a) P and ρ are uniform through the interface.
(b) $L_{i,k}$ and $\kappa_{i,j}$ are constants.
(c) The standard component of the species flux is approximated by a polynomial expansion.
(d) The order of the Cahn-Hilliard equation is dropped twice to make it second order, and therefore numerically more manageable.

It is shown in this section that approximations (a), (b), and (c) incur large errors in the predictions of this theory unless the conditions are very close to the diffusional critical point. Approximation (d) does not bear any physical justification.

To examine approximations (a-c), consider Eq. (209) particularized for a bicomponent hydrocarbon-fueled system,

$$\rho\frac{\partial Y_\mathrm{F}}{\partial t} + \rho\mathbf{v}\cdot\nabla Y_\mathrm{F} = \nabla\cdot\left\{\frac{L_{\mathrm{F,F}}}{T_e}\nabla\left[\mu_\mathrm{F} - \mu_\mathrm{O} - \kappa_{\mathrm{F,F}}\nabla^2(\rho Y_\mathrm{F})\right]\right\}, \quad (210)$$

with $\kappa_{\mathrm{F,F}}$ and $L_{\mathrm{F,F}}$ being defined, respectively, in Eqs. (23) and (145). Upon combining Eqs. (B.19), (B.20), and (C.47), the difference between chemical potentials can be expressed in dimensionless form as

$$\begin{aligned}\frac{\mu_\mathrm{F}-\mu_\mathrm{O}}{\mathrm{R}^0T_e/W_\mathrm{F}} &= \frac{\bar{g}^0_\mathrm{F}(P^0,T_e)}{\mathrm{R}^0T_e} - \mathcal{W}\frac{\bar{g}^0_\mathrm{O}(P^0,T_e)}{\mathrm{R}^0T_e}\\ &+\left(\frac{b_\mathrm{F}}{b}-\mathcal{W}\frac{b_\mathrm{O}}{b}\right)\left(\frac{P\overline{W}}{\rho\mathrm{R}^0T_e}-1\right)\\ &+\ln\left[\frac{\rho X_\mathrm{F}\mathrm{R}^0T_e}{P^0\overline{W}(1-\rho b/\overline{W})}\right]-\mathcal{W}\ln\left[\frac{\rho(1-X_\mathrm{F})\mathrm{R}^0T_e}{P^0\overline{W}(1-\rho b/\overline{W})}\right]\\ &+\frac{a}{2\sqrt{2}b\mathrm{R}^0T_e}\ln\left[\frac{1+\left(1-\sqrt{2}\right)\rho b/\overline{W}}{1+\left(1+\sqrt{2}\right)\rho b/\overline{W}}\right]\\ &\times\left\{\left[\frac{2(X_\mathrm{F}a_\mathrm{F}+(1-X_\mathrm{F})a_{\mathrm{F,O}})}{a}-\frac{b_\mathrm{F}}{b}\right]\right.\\ &\left.-\mathcal{W}\left[\frac{2(X_\mathrm{F}a_{\mathrm{F,O}}+(1-X_\mathrm{F})a_\mathrm{O})}{a}-\frac{b_\mathrm{O}}{b}\right]\right\}. \quad (211)\end{aligned}$$

In this formulation, $\bar{g}^0_\mathrm{F}$ and $\bar{g}^0_\mathrm{O}$ are ideal-gas Gibbs free energies defined in Eq. (C.46). In addition, a and b are the Peng-Robinson coefficients obtained from the mixing rules (15) particularized for binary mixtures, namely

$$\begin{aligned}a &= X_\mathrm{F}^2a_\mathrm{F}(T_e)+(1-X_\mathrm{F})^2a_\mathrm{O}(T_e)+2X_\mathrm{F}(1-X_\mathrm{F})a_{\mathrm{F,O}}(T_e),\\ b &= X_\mathrm{F}b_\mathrm{F}+(1-X_\mathrm{F})b_\mathrm{O},\\ a_{\mathrm{F,O}}(T_e) &= (1-\vartheta_{\mathrm{F,O}})\sqrt{a_\mathrm{F}(T_e)a_\mathrm{O}(T_e)}, \quad (212)\end{aligned}$$

with a_F, a_O, b_F, and b_O being functions of temperature defined in Eqs. (C.10) and (C.11), whereas $\vartheta_{\mathrm{F,O}}$ is a binary-interaction parameter provided in Appendix C. In Eqs. (211) and (212), the molar and mass fractions of fuel species are related as

$$X_\mathrm{F} = Y_\mathrm{F}\overline{W}/W_\mathrm{F}, \quad (213)$$

where $\overline{W}$ is the mean molecular weight defined as

$$\overline{W} = W_\mathrm{F}/[Y_\mathrm{F}+\mathcal{W}(1-Y_\mathrm{F})]. \quad (214)$$

The substitution of Eqs. (C.46) and (212)–(214) into Eq. (211), with P being computed from the equation of state (14), makes $\mu_\mathrm{F}-\mu_\mathrm{O}$ a sole function of ρ and Y_F in isothermal systems.

A constant-pressure approximation $P \approx P_\infty$ in Eq. (211) becomes appropriate only at sufficiently high pressures near the diffusional critical point. For $C_{12}H_{26}/N_2$ mixtures at uniform temperature of 500 K, the pressure at the diffusional critical point is 688 bar, as shown in Fig. A.1. On approach to the diffusional critical point at that temperature, the pressure parameter $\mathcal{P}$ defined in Eq. (38), corresponding to the ratio of the characteristic amplitude of the pressure oscillation through the interface to the combustor pressure, is $\mathcal{P} = 4\cdot10^{-3}$, $8\cdot10^{-4}$, $1\cdot10^{-4}$, and $6\cdot10^{-7}$ at $P_\infty = 500$, 600, 650, and 685 bar, respectively. As a result, the thermodynamic pressure becomes increasingly more uniform near the diffusional critical point.

The equation of state (14) with fixed $P = P_\infty$ and $T = T_e$ makes the density an implicit function of the fuel mass fraction, $\rho = \rho(Y_\mathrm{F})$. However, the density variations across the interface decrease as the diffusional critical point is approached. For $C_{12}H_{26}/N_2$ mixtures at uniform temperature of 500 K, the relative density variations across the interface are $(\rho_e^\ell - \rho_e^g)/\rho_e^\ell = 37\%$, 24%, 15%, and 4% at $P_\infty = 500$, 600, 650, and 685 bar, respectively. These variations decrease with pressure at a much slower rate than the pressure variations.

The gradient-energy coefficient $\kappa_{\mathrm{F,F}}$ is a sole function of temperature, and therefore remains constant in the isothermal conditions that lead to Eq. (210). In contrast, the Onsager coefficient $L_{\mathrm{F,F}}$ is a function of P, T, and X_F, as indicated by Eq. (145). For $C_{12}H_{26}/N_2$ at uniform temperature of 500 K, the variations of $L_{\mathrm{F,F}}$ induced by variations of composition across the interface are $(L^\ell_{\mathrm{F,Fe}} - L^g_{\mathrm{F,Fe}})/L^\ell_{\mathrm{F,Fe}} = 73\%$, 60%, 45%, and 15% at $P_\infty = 500$, 600, 650, and 685 bar, respectively. Similarly to the approximation of constant density, the approximation of constant $L_{\mathrm{F,F}}$ involves significant errors of order 15% even at 99.5% of the diffusional critical pressure.

As shown in Fig. 23, the standard species flux engenders antidiffusive transport of fuel species within the diffusionally unstable zone of the interface, and forward diffusion everywhere else. The slope of the chemical-potential difference must therefore change sign twice along the Y_F axis. An approximate model for $\mu_\mathrm{F}-\mu_\mathrm{O}$ that fulfills this requirement is [149]

$$\mu_\mathrm{F}-\mu_\mathrm{O} \approx \mu_\mathrm{Fe}-\mu_\mathrm{Oe}+\hat{A}_\mu(Y_\mathrm{F}-Y^g_\mathrm{Fe})(Y_\mathrm{F}-Y^\ell_\mathrm{Fe})\left(Y_\mathrm{F}-\frac{Y^g_\mathrm{Fe}+Y^\ell_\mathrm{Fe}}{2}\right), \quad (215)$$

where $\hat{A}_\mu = \hat{A}_\mu(P_\infty, T_e)$ is a calibrated model coefficient. The model (215) intersects the ordinate $\mu_\mathrm{F}-\mu_\mathrm{O} = \mu_\mathrm{Fe}-\mu_\mathrm{Oe}$ at the phase-equilibrium fuel mass fractions Y^g_Fe and Y^ℓ_Fe, and at their average value $(Y^g_\mathrm{Fe}+Y^\ell_\mathrm{Fe})/2$. Its oscillatory trend is such that the integral of $\mu_\mathrm{F}-\mu_\mathrm{O}$ with respect to Y_F equals $(\mu_\mathrm{Fe}-\mu_\mathrm{Oe})(Y^\ell_\mathrm{F}-Y^g_\mathrm{F})$ in accordance with Maxwell's construction rule.

Comparisons between the model (215) and the exact difference of chemical potentials (211) are provided in Fig. 27(a). The coefficient $\hat{A}_\mu$ has been tuned such that the model (215) reproduces the

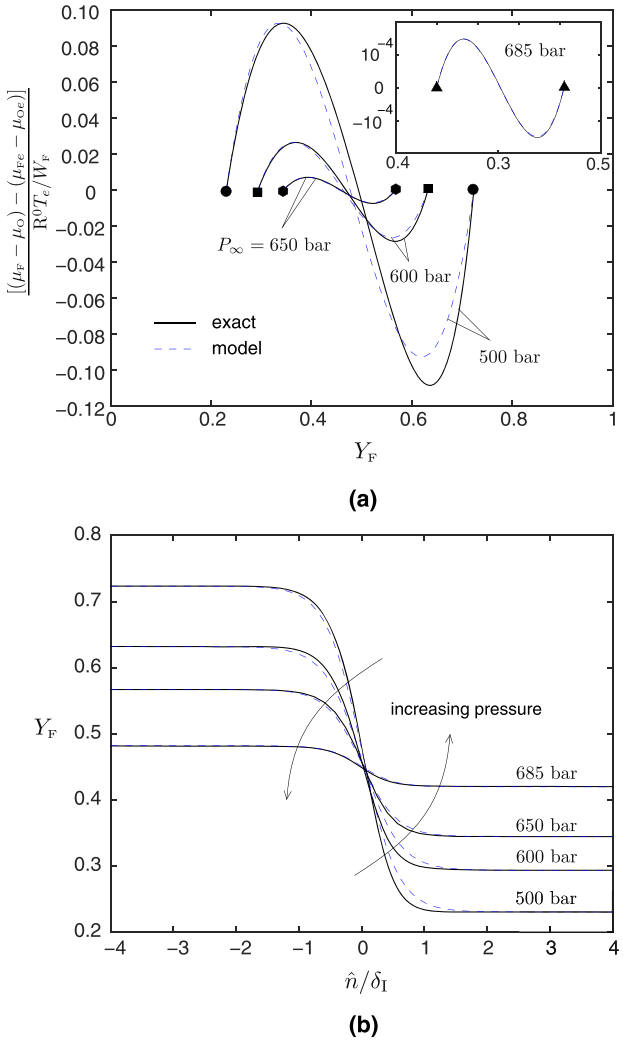

Fig. 27. Comparison between modeled (blue dashed lines) and exact (dark solid lines) profiles of (a) dimensionless chemical-potential difference in $C_{12}H_{26}/N_2$ isothermal systems at $T_e = 500$ K and different pressures, and (b) corresponding mass fractions as a function of distance normalized with the interface thickness computed using Eq. (208) based on the exact solution ($\delta_I = 6.8$ nm, 9.9 nm, 16.4 nm, and 62.3 nm for $P_\infty = 500$, 600, 650, and 685 bar, respectively). To obtain these profiles, the coefficient $\hat{A}_\mu$ in Eq. (215) has been calibrated as $\hat{A}_\mu =$ 391.8 kJ/kg, 344.4 kJ/kg, 323.5 kJ/kg, and 313.2 kJ/kg for $P_\infty = 500$, 600, 650, and 685 bar, respectively. Similarly, the equilibrium densities on the liquid-like side are $\rho_e^\ell = 520.6$ kg/m^3, 509.7 kg/m^3, 499.0 kg/m^3, and 478.8 kg/m^3 for $P_\infty = 500$, 600, 650, and 685 bar, respectively. (For interpretation of the references to color in this figure legend, the reader is referred to the web version of this article.)

maximum value of (211) evaluated at $P = P_\infty$. However, the amplitude match occurs at increasingly dissimilar fuel mass fractions as the pressure decreases, since the exact profile of $\mu_F - \mu_O$ becomes increasingly asymmetric.

The good agreement between the model and the exact expression (211) at high pressures in Fig. 27(a) translates into correspondingly good predictions of the spatial distribution of fuel, with discrepancies with the numerical results subsiding with increasing pressures, as observed in Fig. 27(b). An expression for $Y_F(\hat{n})$ can be derived from the model (215) by integrating twice the right-hand side of Eq. (210), subject to zero gradients and phase-equilibrium conditions away from the interface, giving

$$\kappa_{F,F}\frac{d^2}{d\hat{n}^2}(\rho Y_F) = \mu_F - \mu_O - (\mu_{Fe} - \mu_{Oe}). \tag{216}$$

Equation (216) can be integrated once more by using the identity $d^2Y_F/d\hat{n}^2 = (d/dY_F)(dY_F/d\hat{n})^2$, and by assuming uniform pressure and density, the latter being approximately equal to the phase-equilibrium density on the liquid-like side, $\rho \approx \rho_e^\ell$. With these approximations, Eq. (216) becomes

$$\kappa_{F,F}\rho_e^\ell\left(\frac{dY_F}{d\hat{n}}\right)^2 \approx \frac{\hat{A}_\mu}{4}(Y_F - Y_{Fe}^g)^2(Y_F - Y_{Fe}^\ell)^2, \tag{217}$$

subject to $Y_F \to Y_{Fe}^\ell$ at $\hat{n} \to -\infty$. The solution of Eq. (217) is

$$Y_F(\hat{n}) = \frac{Y_{Fe}^\ell + Y_{Fe}^g}{2} - \frac{Y_{Fe}^\ell - Y_{Fe}^g}{2}\tanh\left(\frac{2\hat{n}}{\hat{\delta}_I}\right), \tag{218}$$

with

$$\hat{\delta}_I = \frac{Y_F^\ell - Y_F^g}{\max\left|\frac{dY_F}{d\hat{n}}\right|} = \frac{8}{Y_F^\ell - Y_F^g}\sqrt{\frac{\rho_e^\ell\kappa_{F,F}}{A'_\mu}} \tag{219}$$

being a modeled interface thickness. The mass fraction profile (218) can be substituted into Eq. (99) under the assumption of constant density $\rho \approx \rho_e^\ell$, which gives the modeled surface-tension coefficient

$$\hat{\sigma} = \frac{(Y_{Fe}^\ell - Y_{Fe}^g)^3}{12}\sqrt{(\rho_e^\ell)^3\kappa_{F,F}\hat{A}_\mu}. \tag{220}$$

The model $\hat{\sigma}$ leads to large errors with respect to the exact surface-tension σ coefficient because (a) the density is not constant across the interface, and (b) the discrepancies in the mass-fraction profiles in Fig. 27(b) get amplified when they are differentiated, squared, and integrated to obtain $\hat{\sigma}$. For instance, at $P_\infty = 500$ bar and $T_e = 500$ K, the model predicts $\hat{\sigma} = 1.0$ mN/m, while the exact calculation gives $\sigma = 1.5$ mN/m. Similar errors are observed for all tested pressures up to 685 bar. Additional shortfalls of the model expressions (218)–(220) are that their derivation does not involve the equation of state (14) nor the mechanical equilibrium condition (107). Near the diffusional critical point, it is however plausible that Eq. (107) simplifies to $P \approx P_\infty$ with relative errors of order $\mathcal{P} \ll 1$. In contrast, the equation of state (14) is strictly incompatible with variations in Y_F once P, T, and ρ are set to their constant values P_∞, T_e, and ρ_e^ℓ.

7. Transcritical interfaces in non-isothermal bicomponent systems

This section provides numerical results describing unsteady transcritical interfaces in $C_{12}H_{26}/N_2$ non-isothermal systems. This configuration corresponds to small but non-zero thermal Cahn numbers, $0 < \epsilon_T \ll 1$. In this limit, which is perhaps the one that has the most practical interest, temperature gradients exist across the interface that are however small compared to the composition gradients.

7.1. Formulation

The temperature gradient across the interface changes fundamentally the solution with respect to that described in Section 6. Here, T_e varies along the interface, and therefore the structure of the interface evolves with distance downstream of the injection orifice. The spatial functionality of T_e is determined by the rate of heat transfer across the interface. The solution provides the size of the transcritical region, within which the interface survives, and where σ attains values of practical relevance before vanishing at the interface edge. The transcritical interface is away from equilibrium, although the departures are small, as discussed in Section 5.7. The problem must be solved using the Navier-Stokes equations in Section 4.7, along with the closures for the interfacial stress $\mathcal{K}$ and interfacial fluxes $\mathcal{J}_F$ and $\mathcal{Q}$ provided in Section 5. The numerical simulation of the problem sketched in Fig. 1 is not

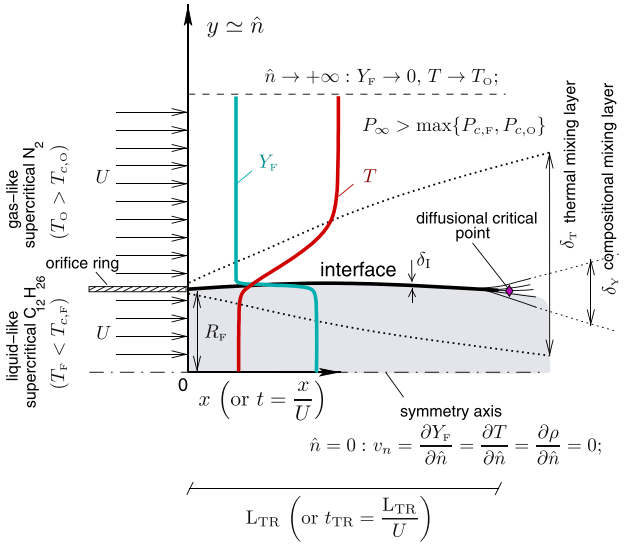

Fig. 28. Schematics of the non-isothermal bicomponent model problem.

straightforward, in that the large disparity between the interface thickness δ_I and the orifice radius R_F involves significant numerical stiffness, as discussed in Section 4.7. A number of simplifications outlined below are employed in order to facilitate the analysis.

The configuration studied in this section is summarized in Fig. 28 and corresponds to a simpler version of that depicted in Fig. 1. This configuration does however serve to illustrate the development and disappearance of the transcritical interface in a manner qualitatively analogous to that sketched in Fig. 1. The two propellant streams are injected at the same velocity U creating a slender, planar, laminar thermal mixing layer at a moderately high Péclet number $Pe_R = UR_F/D_{T,O} \gg 1$. The transcritical interface separating both propellant streams remains hydrodynamically thin and slender until it vanishes downstream at an edge, where the transverse velocity, which is of the same order as the thermal-expansion velocity scale U_T defined in Eq. (80), is much smaller than U by a factor of order $1/(Pe_R\mathcal{R}) \ll 1$. Because of this slenderness, the transversal coordinate y and the coordinate normal to the interface $\hat{n}$ are approximately equal, $y \simeq \hat{n}$. The Marangoni effect is neglected for simplicity.

Table 7 summarizes the operating conditions of the configuration. The fuel ($C_{12}H_{26}$) and coflow (N_2) injection conditions correspond, respectively, to liquid-like and gas-like supercritical fluids, with injection temperatures $T_F = 450$ K and $T_O = 1000$ K. Additionally, the combustor pressure $P_\infty = 100$ bar is larger than the critical pressures of the separate components.

Under these simplifying assumptions, the boundary-layer approximation, in which streamwise diffusion is neglected, may be used for describing the dynamics of the interface along with the mixing process. A solution of the streamwise momentum equation exists in which the streamwise velocity remains equal to U everywhere. In this way, time and space can be used interchangeably in the equations of motion by means of the relation

$$t = x/U. \tag{221}$$

The origins $t = 0$ and $x = 0$ are chosen such that the initial material surface coincides with the fluid state of the propellants at the injection plane. Using Eq. (221), the characteristic supercriticalization length (13) can be alternatively expressed as the time scale

$$t_{TR} = L_{TR}/U, \tag{222}$$

which is used for normalization of the results.

The formulation integrated in this section is summarized in Table 8, where t plays the role of the streamwise marching coordinate x in accordance with Eq. (221). Listed in Table 8 are the conservation equations (44), (46) and (47), along with the species and heat fluxes (148), (147), (150), and (152). The mechanical equilibrium condition (107) is employed in place of the full momentum Eq. (45). These equations are supplemented with the equation of state (14) and the mixing rules (212), along with the expressions for the specific gradient-dependent internal energy (17), gradient-energy coefficient (23), total energy (48), specific entropy (151), fuel molar fraction (213), mean molecular weight (214), enthalpy (B.9), partial enthalpy (B.12), chemical potential (B.19) and (B.20), volume expansivity (C.22), enthalpy departure function (C.23), ideal-gas partial enthalpies (C.33), partial-enthalpy departure function (C.34), partial molar volume (C.43), ideal-gas Gibbs free energies (C.46), fugacity coefficient (C.47), and the associated constants and supplementary expressions provided in Appendix C. Effects of shear and interface roll-up require the consideration of streamwise transport and interface curvature. Although these effects are not included in this section, they are accounted for in the general formulation provided in Sections 4.7 and 5.

The thermal conductivity, binary diffusion coefficient, and thermal-diffusion ratio are calculated using Eqs. (F.13), (F.36), and (F.43), respectively, along with the supplementary relations in Appendix F. Those expressions are evaluated at $P = P_\infty$, as discussed in Appendix E.2. In addition, the regularization (E.8) introduced in Appendix E.1 is employed here to maintain finite values of the difference of partial specific enthalpies $h_F - h_O$ and of the volume expansivity β_v, since both would otherwise diverge across the mechanical spinodal surface. Specifically, Eq. (E.8) is used with $m = 0.01$ from $x = 0$ (or $t = 0$) until a distance x (or time t) where T_e becomes larger than the corresponding temperature threshold provided in Fig. E.1 at the operating pressure (i.e., $T_e > 480$ K at $P_\infty = 100$ bar). A sweep in the regularization constant m is performed in Appendix E.1 that suggests negligible influences on the streamwise evolution of σ, as shown in Fig. E.4.

The boundary condition far away from the axis ($\hat{n} \to +\infty$) corresponds to the coflow temperature $T = T_O$ and composition $Y_F = 0$. A symmetry boundary condition is used at the axis $\hat{n} = 0$, where

Table 7
Operating conditions employed for the investigation of transcritical interfaces in $C_{12}H_{26}/N_2$ non-isothermal systems. The regularization constant is $m = 0.01$ in Eq. (E.8), and the dimensional radius of the orifice is assumed to be $R_F = 50$ μm.

	propellant streams							
	fuel liquid-like supercritical $C_{12}H_{26}$ ($Y_F = 1$)			coflow gas-like supercritical N_2 ($Y_F = 0$)		parameters for initial conditions			
P_∞ [bar]	T_F [K]	$\rho_F \left[\frac{kg}{m^3}\right]$		T_O [K]	$\rho_O \left[\frac{kg}{m^3}\right]$	$\epsilon_R^0 = \delta_I^0/R_F$	$\epsilon_T^0 = \delta_I^0/\delta_T^0$	δ_I^0 [nm]	T_e^0 [K]
100	450	606		1000	33	$5 \cdot 10^{-5}$	$5 \cdot 10^{-4}$	2.5	460

Table 8
Dimensional formulation for transcritical interfaces in non-isothermal bicomponent systems. (⋆) Using Eq. (221), $\partial/\partial x$ has been replaced by $(1/U)\partial/\partial t$.

Conservation equations⋆	
Continuity	$\frac{\partial \rho}{\partial t} + \frac{\partial}{\partial \hat{n}}(\rho v_n) = 0,$
Mechanical equilibrium	$P_\infty - P + \rho Y_F \kappa_{F,F} \frac{\partial^2}{\partial \hat{n}^2}(\rho Y_F) - \frac{1}{2}\kappa_{F,F}\left[\frac{\partial}{\partial \hat{n}}(\rho Y_F)\right]^2 = 0,$
Fuel species	$\frac{\partial}{\partial t}(\rho Y_F) + \frac{\partial}{\partial \hat{n}}(\rho v_n Y_F) = -\frac{\partial}{\partial \hat{n}}(J_F + \mathcal{J}_F),$
Total energy	$\frac{\partial}{\partial t}(\rho E) + \frac{\partial}{\partial \hat{n}}(\rho v_n E) = -\frac{\partial}{\partial \hat{n}}(q + \mathcal{Q}) - P_\infty \frac{\partial v_n}{\partial \hat{n}}.$
Transport fluxes	
Standard (fuel species)	$J_F = -\frac{\rho \mathcal{D}_{F,O} W_F W_O X_F (1 - X_F)}{R^0 T \overline{W}}\left[\frac{\partial}{\partial \hat{n}}(\mu_F - \mu_O) + (s_F - s_O)\frac{\partial T}{\partial \hat{n}}\right] - \frac{\rho \mathcal{D}_{F,O} k_{F,T}}{T}\frac{\partial T}{\partial \hat{n}},$
Interfacial (fuel species)	$\mathcal{J}_F = \frac{\rho \kappa_{F,F} \mathcal{D}_{F,O} W_F W_O X_F (1 - X_F)}{R^0 T \overline{W}}\left\{\frac{\partial}{\partial \hat{n}}\left[\frac{\partial^2}{\partial \hat{n}^2}(\rho Y_F)\right] + \frac{\partial T}{\partial \hat{n}}\frac{\partial^2}{\partial \hat{n}^2}(\rho \beta_v Y_F)\right\},$
Standard (heat)	$q = -\lambda \frac{\partial T}{\partial \hat{n}} + (h_F - h_O) J_F - \rho \mathcal{D}_{F,O} k_{F,T}\left[\frac{\partial}{\partial \hat{n}}(\mu_F - \mu_O) + (s_F - s_O)\frac{\partial T}{\partial \hat{n}}\right],$
Interfacial (heat)	$\mathcal{Q} = \rho \kappa_{F,F} \mathcal{D}_{F,O} k_{F,T}\left\{\frac{\partial}{\partial \hat{n}}\left[\frac{\partial^2}{\partial \hat{n}^2}(\rho Y_F)\right] + \frac{\partial T}{\partial \hat{n}}\frac{\partial^2}{\partial \hat{n}^2}(\rho \beta_v Y_F)\right\} + \kappa_{F,F}\frac{\partial}{\partial \hat{n}}(\rho Y_F)\left[\rho Y_F \frac{\partial v_n}{\partial \hat{n}} + \frac{\partial (J_F + \mathcal{J}_F)}{\partial \hat{n}}\right]$ $- \kappa_{F,F}(J_F + \mathcal{J}_F)\left[\frac{\partial^2}{\partial \hat{n}^2}(\rho Y_F) + T\frac{\partial^2}{\partial \hat{n}^2}(\rho \beta_v Y_F)\right] + (h_F - h_O)\mathcal{J}_F.$
Boundary conditions	
Symmetry at the axis	$\frac{\partial \rho}{\partial \hat{n}} = \frac{\partial Y_F}{\partial \hat{n}} = \frac{\partial T}{\partial \hat{n}} = 0 \quad \text{and} \quad v_n = 0 \quad \text{at} \quad \hat{n} = 0,$
Coflow free stream	$Y_F \to 0 \quad \text{and} \quad T \to T_O \quad \text{at} \quad \hat{n} \to +\infty.$
Initial conditions ($t = 0$)	
Density	$\rho(\hat{n}) = \frac{\rho_F + \rho_O}{2} - \frac{\rho_F - \rho_O}{2}\tanh\left[\frac{2(\hat{n} - R_F)}{\delta_\rho^0}\right] \quad \text{for} \quad 0 \le \hat{n} < +\infty,$
Fuel mass fraction	$Y_F(\hat{n}) = \frac{1}{2}\left\{1 - \tanh\left[\frac{2(\hat{n} - R_F)}{\delta_Y^0}\right]\right\} \quad \text{for} \quad 0 \le \hat{n} < +\infty,$
Temperature	$T(\hat{n}) = \frac{T_F + T_O}{2} - \frac{T_F - T_O}{2}\tanh\left[\frac{2(\hat{n} - R_e)}{\delta_T^0}\right] \quad \text{for} \quad 0 \le \hat{n} < +\infty,$
Velocity	$v_n = 0 \quad \text{for} \quad 0 \le \hat{n} < +\infty.$
Supplementary expressions (see Appendix B, Appendix E, Appendix C, and Appendix F for details)	
Equation of state	Eq. (14).
Coefficients of the equation of state	Eqs. (212), and (C.10)-(C.12).
Gradient-energy coefficient	Eqs. (23), (C.17), and (C.18).
Transport coefficients	Eqs. (F.13), (F.36), and (F.43).
Regularizations†	Eqs. (E.8) and (E.9).
Thermodynamic relations	Eqs. (17), (48), (B.9), (B.12), (B.19), (B.20), (C.22), (C.23), (C.33), (C.34), (C.43), (C.46), and (C.47).

the transversal velocity along with the gradients of temperature, fuel mass fraction, and density are zero.

The presence of the interface complicates the characterization of the initial conditions, which may otherwise be calculated from the self-similar solution of the conservation equations near the orifice at $x/R_F \ll 1$ and $\hat{n}/R_F \sim 1$, when the thickness of the separating plate is also neglected. This procedure is not attempted here because of the relatively unknown character of the formulation in Table 8 at present time, and is deferred to future work. Instead, at $t = 0$ (or $x = 0$), the initial conditions for the density and fuel mass fraction are assumed to be hyperbolic tangents centered at $\hat{n} = R_F$, whereas that of the temperature has a wider support and is centered at $\hat{n} = R_e > R_F$, as formulated in Table 8. The origin of the temperature profile R_e is chosen such that the initial value of the interface temperature, denoted by T_e^0, is initially imposed at $\hat{n} = R_F$. Specifically, the value of T_e^0 is selected such that $T_e^0 < T_{c,\mathrm{diff}}$, and is assumed to be closer to the fuel temperature than to the coflow one because of the much smaller thermal diffusivity of the fuel stream. The parameters δ_ρ^0 and δ_Y^0 for the initial profiles of density and fuel mass fraction are such that the resulting initial value of the interface thickness δ_I^0 is equal to that calculated in the isothermal case at $T = T_e^0$ using the formulation outlined in Section 6. In particular, δ_I^0 can be obtained by substituting the initial value of the fuel partial density at the symmetry axis $\hat{n} = 0$ (i.e., $\rho Y_F = \rho_F = 606\ \mathrm{kg/m^3}$) into the definition

$$\delta_I = \frac{\rho(\hat{n} = 0) Y_F(\hat{n} = 0)}{\max\left|\frac{\partial(\rho Y_F)}{\partial \hat{n}}\right|}. \tag{223}$$

The resulting value of the initial large-scale Cahn number is $\epsilon_R^0 = \delta_I^0/R_F = 5 \cdot 10^{-5}$. Similarly, the initial value δ_T^0 of the thermal mixing-layer thickness can be obtained by substituting the initial value of the temperature at the symmetry axis $\hat{n} = 0$ (i.e., $T = T_F = 450\ \mathrm{K}$) into the definition

$$\delta_T = \frac{T_O - T(\hat{n} = 0)}{\max\left|\frac{\partial T}{\partial \hat{n}}\right|}, \tag{224}$$

which yields an initial thermal Cahn number of $\epsilon_T^0 = \delta_I^0/\delta_T^0 = 5 \cdot 10^{-4}$, with $\delta_T^0/R_F = \epsilon_R^0/\epsilon_T^0 = 0.1$. Further details of the configuration, including the numerical methods employed to integrate the formulation in Table 8, are provided in Appendix G.

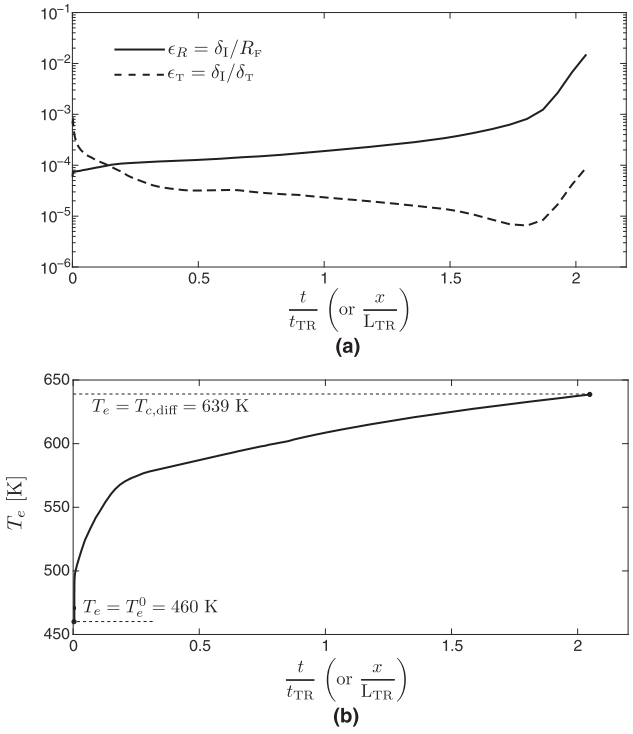

Fig. 29. Evolution with downstream distance (or time) of (a) large-scale (ϵ_R) and thermal (ϵ_T) Cahn numbers, and (b) interface temperature T_e. In this figure, the interface thickness δ_I and the thermal mixing-layer thickness δ_T are computed, respectively, using Eqs. (223) and (224). The interface temperature T_e is computed as the temperature where the absolute value of the fuel partial-density gradient $\partial(\rho Y_F)/\partial\hat{n}$ attains its maximum value.

7.2. Results: The evolution of a transcritical interface downstream of the injection orifice

The slowly growing values of ϵ_R in Fig. 29(a) indicate that the large composition gradients persist until the interface edge is neared. In contrast, the temperature gradient across the interface becomes increasingly smaller as the thermal mixing layer grows, thereby leading to decreasingly small values of ϵ_T for most of the length or lifetime of the interface. The interface temperature T_e, shown in Fig. 29(b), increases monotonically because the fuel is increasingly heated by the hot coflow as it flows downstream of the injection orifice. Near the interface edge, where the interface approaches the supercriticalization temperature $T_{TR} \simeq T_{c,\text{diff}}$, the interface thickness increases sharply, becoming more than 100 times thicker than its initial value δ_I^0, and causing a noticeable increase in both ϵ_R and ϵ_T.

The bathtub-like shape of the evolution of the thermal Cahn number ϵ_T in Fig. 29(a) indicates that the interface is closest to transport equilibrium in the intermediate region away from the orifice (where the temperature gradients are the largest) and away from the interface edge (where the composition gradients are the smallest). The near-equilibrium behavior in that intermediate region is manifested in Figs. 30(a,b) as almost-complete cancellations between the components of the standard (q_n') and interfacial ($\mathcal{Q}_n'$) heat fluxes independent of the temperature gradient [see Eqs. (183) and (184)], and between the corresponding components of the standard ($J_{F,n}'$) and interfacial ($\mathcal{J}_{F,n}'$) species fluxes [Eqs. (155) and (156)]. In contrast, Fig. 30(c) shows that the standard ($q_n^{\Delta T}$) and interfacial ($Q_n^{\Delta T}$) components of the heat fluxes that depend on the temperature gradient [Eqs. (186) and (187)] do not cancel each other, but are much smaller than their counterparts q_n' and $\mathcal{Q}_n'$, as anticipated in Eq. (190). A similar result is observed in Fig. 30(d) for the species fluxes $J_{F,n}^{\Delta T}$ and $\mathcal{J}_{F,n}^{\Delta T}$ [Eqs. (157) and (158)], which do not cancel each other and are much smaller than $J_{F,n}'$ and $\mathcal{J}_{F,n}'$, as anticipated in Eq. (166).

These results ratify the analysis in Section 5.6, in that most of the interfacial species flux is invested in counteracting the antidiffusion of fuel induced by the sum of Fickian and barodiffusion mechanisms, whereas most of the interfacial heat flux is invested in counteracting the Dufour effect. The small remainders of those cancellations, along with the components of the standard fluxes that are dependent on temperature gradients (Soret, Fourier, and interdiffusion), describe the transport of mass and energy across the interface in non-equilibrium conditions.

The near-equilibrium behavior persists until the interface vanishes downstream at an edge. Because of the much smaller thermal diffusivity of the fuel, $D_{T,F}/D_{T,O} = 0.03$, the cold fuel stream cools down the hot coflow more than what the hot coflow is capable of heating the fuel stream, as observed in the large-scale view of the temperature field in Fig. 31. As a result, all isotherms, including the supercriticalization one $T_{TR} \simeq T_{c,\text{diff}}$, are initially displaced outwards away from the axis into the coflow. This phenomenon is exacerbated by a mixing-induced augmentation of the constant-pressure specific heat c_p, whose global maximum is attained within the interface for a significant portion of its length or lifetime, as shown in Fig. 33. The line joining the global maxima of c_p is the physical-space representation of the pseudo-boiling line discussed in Section 2.2 and Appendix B.2. Similarly to the abrupt termination of the pseudo-boiling line observed before intercepting the diffusional critical point in the $C_{12}H_{26}/N_2$ phase diagram in Fig. 10(c), the global maximum of c_p in physical space in Fig. 33(a) ceases to be within the interface upstream of the interface edge, and switches abruptly thereafter to the jet axis.

As the fuel is heated by the hot coflow, the supercriticalization isotherm eventually turns back toward the jet axis and crosses the transcritical interface. It is at that crossing point where the interface vanishes at an edge. The latter is located at a distance of order unity from the orifice when normalized with the characteristic supercriticalization length (13) [or after a time of order unity has passed when normalized with the characteristic supercriticalization time (222)], as shown in Figs. 32 and 33.

A zoomed view of the structure of the interface edge is provided in Fig. 2. For $C_{12}H_{26}/N_2$ systems, the diffusional critical point at the combustor pressure $P_\infty = 100$ bar plays a central role at the interface edge because of the following reasons:

(a) Whereas the thermodynamic pressure undergoes order-unity oscillations across the interface in the near-equilibrium region, the flow in the vicinity of the interface edge is characterized by being mostly isobaric at $P \simeq P_\infty$.
(b) The isocontour $Y_{Fc,\text{diff}} = 0.85$, corresponding to the fuel mass fraction of the diffusional critical point at 100 bar (see Table 3), must necessarily emanate from within the transcritical interface since it is engendered in the coexistence region of the thermodynamic phase diagram, as shown in Fig. 10(c).
(c) The temperature of the diffusional critical point $T_{c,\text{diff}}$ is the maximum temperature of the diffusionally unstable region.

As discussed in Sections 3.2 and 6.2, different mixtures may exist that may lead to a maximum value of the diffusional spinodal surface that may be larger than the diffusional critical temperature. In those mixtures, the supercriticalization isotherm would correspond to the maximum temperature of the diffusional spinodal surface, and the diffusional critical point would not be located at the interface edge, but at some distance upstream within the transcritical interface.

Downstream of the interface edge, the temperature is everywhere larger than $T_{c,\text{diff}}$, and consequently the system becomes dif-

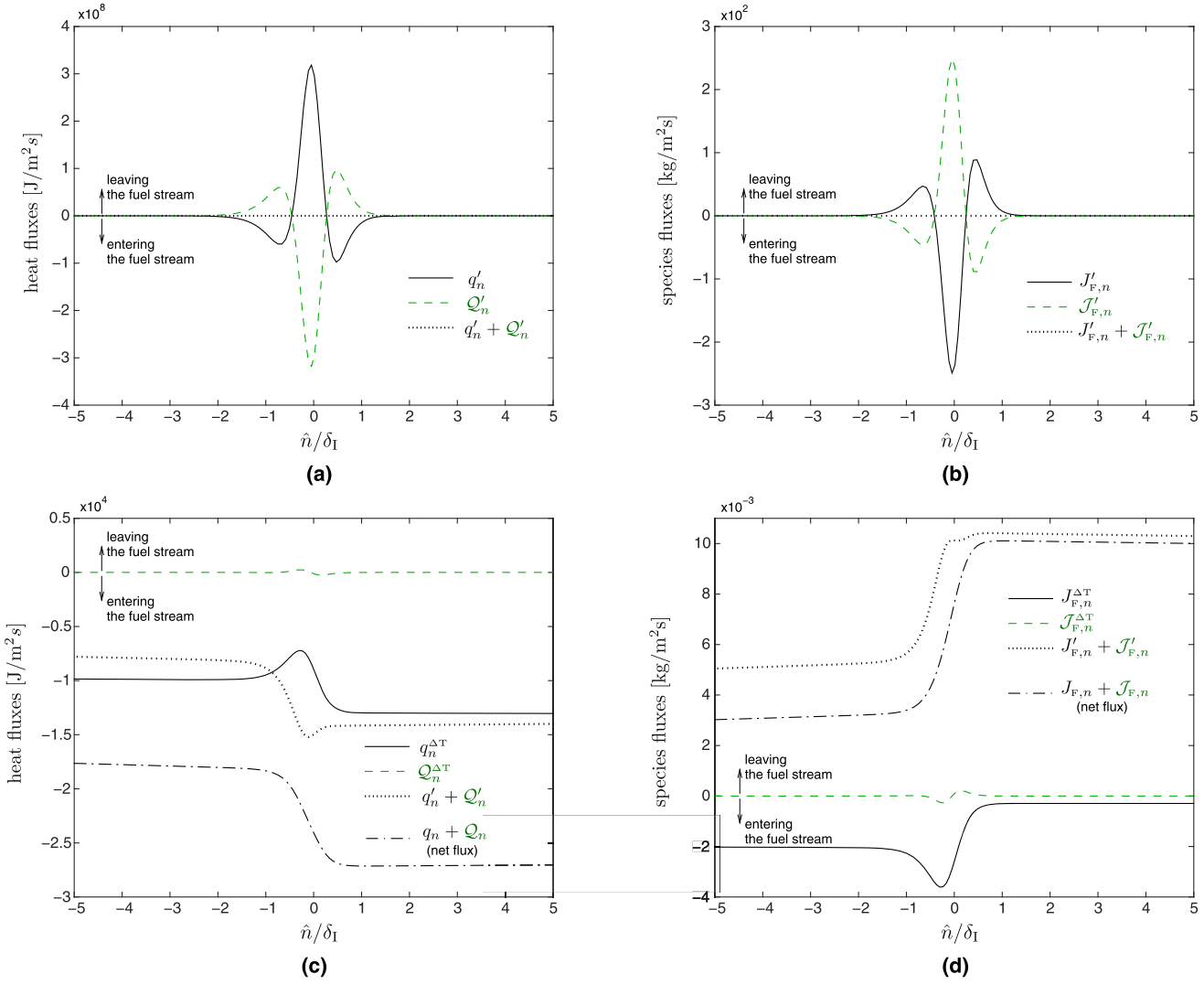

Fig. 30. Spatial distributions of heat and species fluxes across the interface at $t/t_{TR} = x/L_{TR} = 0.4$, where its thickness computed using Eq. (223) is $\delta_I = 5.96$ nm. (a) Temperature-gradient-independent components of the standard heat flux q'_n [dark solid line, Eq. (183)] and interfacial heat flux $\mathcal{Q}'_n$ [green dashed line, Eq. (184)]. (b) Temperature-gradient-independent components of the standard species flux $J'_{F,n}$ [dark solid line, Eq. (155)] and interfacial species flux $\mathcal{J}'_{F,n}$ [green dashed line, Eq. (156)]. (c) Temperature-gradient-dependent components of the standard heat flux $q_n^{\Delta T}$ [dark solid line, Eq. (186)] and interfacial heat flux $\mathcal{Q}_n^{\Delta T}$ [green dashed line, Eq. (187)], along with the net heat flux. (d) Temperature-gradient-dependent components of the standard heat flux $J_{F,n}^{\Delta T}$ [dark solid line, Eq. (157)] and interfacial species flux $\mathcal{J}_{F,n}^{\Delta T}$ [green dashed line, Eq. (158)], along with the net species flux. (For interpretation of the references to color in this figure legend, the reader is referred to the web version of this article.)

fusionally stable. The interfacial fluxes of heat and species become negligible, and the standard diffusion flux of fuel reverses to the usual forward direction along decreasing fuel concentrations, as shown in Fig. 34. The transcritical interface morphs into a fully supercritical mixing layer that grows with distance downstream and is characterized by unimpeded mixing of the propellants by molecular diffusion, as observed in Fig. 2. In this zone, both propellants resemble supercritical gas-like fluids.

The evolution of the pseudo-trajectories of the system with distance (or time) are overlaid in Fig. 35 on a $T - Y_F$ thermodynamic phase diagram evaluated at $P = P_\infty$. As the edge conditions are approached, Fig. 35 shows that the thermodynamic states of the mixture across the interface tend to intersect the coexistence region at increasingly higher temperatures until the diffusional critical temperature is reached, above which intersections cannot occur.

As indicated by the solid line in Fig. 36, the surface-tension coefficient σ, obtained from Eq. (99), decays monotonically with downstream distance (or time) and vanishes simultaneously with the interface at the edge. The first stage of the decay is from $t/t_{TR} = x/L_{TR} = 0$ to 0.3, and is characterized by a rapid increase of the interface temperature near the orifice, as shown in Fig. 29(b). The decay of σ slows down from $t/t_{TR} = x/L_{TR} = 0.3$ to 1.5, where near-equilibrium transport conditions are attained. Beyond $t/t_{TR} = x/L_{TR} = 1.5$, the decay rate increases on approach to the diffusional critical point, with σ plunging at the interface edge to dynamically irrelevant values.

An accurate prediction of σ, given by the square symbols in Fig. 36, can be obtained by solving an isothermal interface at every time step using the formulation in Table 6 and the set-up described Section 6, where the local interface temperature T_e is obtained from Fig. 29(b). This observation is consistent with the attainment of near-equilibrium conditions for most of the transcritical region. Most importantly, it also suggests a potential route for subgrid-scale modeling of transcritical flows based on pretabulation of equilibrium isothermal cases, with T_e acting as a table input obtained from a coarse-grained calculation of the temperature field.

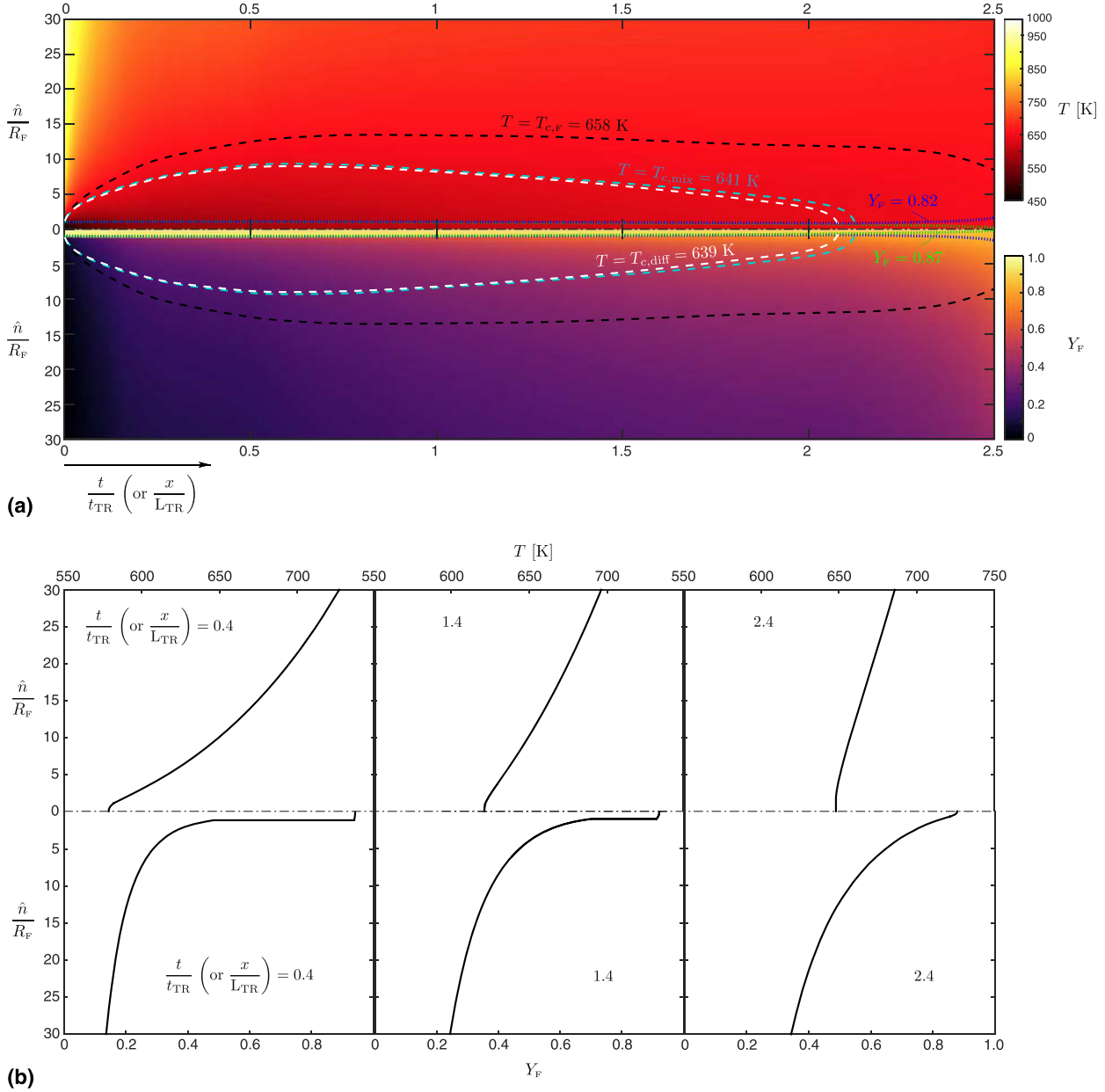

Fig. 31. Large field of view of (a) solid contours of temperature (upper half) and fuel mass fraction (lower half), along with (b) corresponding profiles extracted at $t/t_{\mathrm{TR}} = x/\mathrm{L_{TR}} = 0.4$, 1.4, and 2.4. The figure includes isotherms corresponding to the fuel critical temperature (dark dashed line), critical mixing temperature (blue dashed line), and diffusional critical temperature (white dashed line).. (For interpretation of the references to color in this figure legend, the reader is referred to the web version of this article.)

8. Concluding remarks

Despite the remarkable progress made on augmenting the thrust, range, and reliability of chemical propulsion technologies over the last several decades, which has often relied on large investments in experimentation and testing, the fundamental fluid mechanical processes participating in the injection, atomization, vaporization, mixing, and combustion of propellants at high pressures remain largely unknown. Specifically, the extreme pressure conditions involved in the transcritical flow of propellants into combustors make this problem quite formidable compared to many other open questions in the technical discipline of general multiphase flows.

The present study has focused on a selected number of basic aspects of the problem of transcriticality. Particular emphasis has been made on describing thermodynamically complex systems involving two components at high pressures. When the pressure is supercritical with respect to both components, and when at least one of the propellants is injected at subcritical temperature, transcritical conditions develop that appear to lead to atomization and spray phenomena according to existing experimental visualizations.

The process of interface formation at high pressures cannot be explained using the thermodynamics of monocomponent systems, since only one thermodynamic state is possible in those when the temperature is fixed at supercritical pressures. In contrast, in bicomponent systems, at least two states may be possible at a given temperature for pressures above the critical pressures of the separate components. Using previously well-established high-pressure equations of state and mixing rules, it is shown

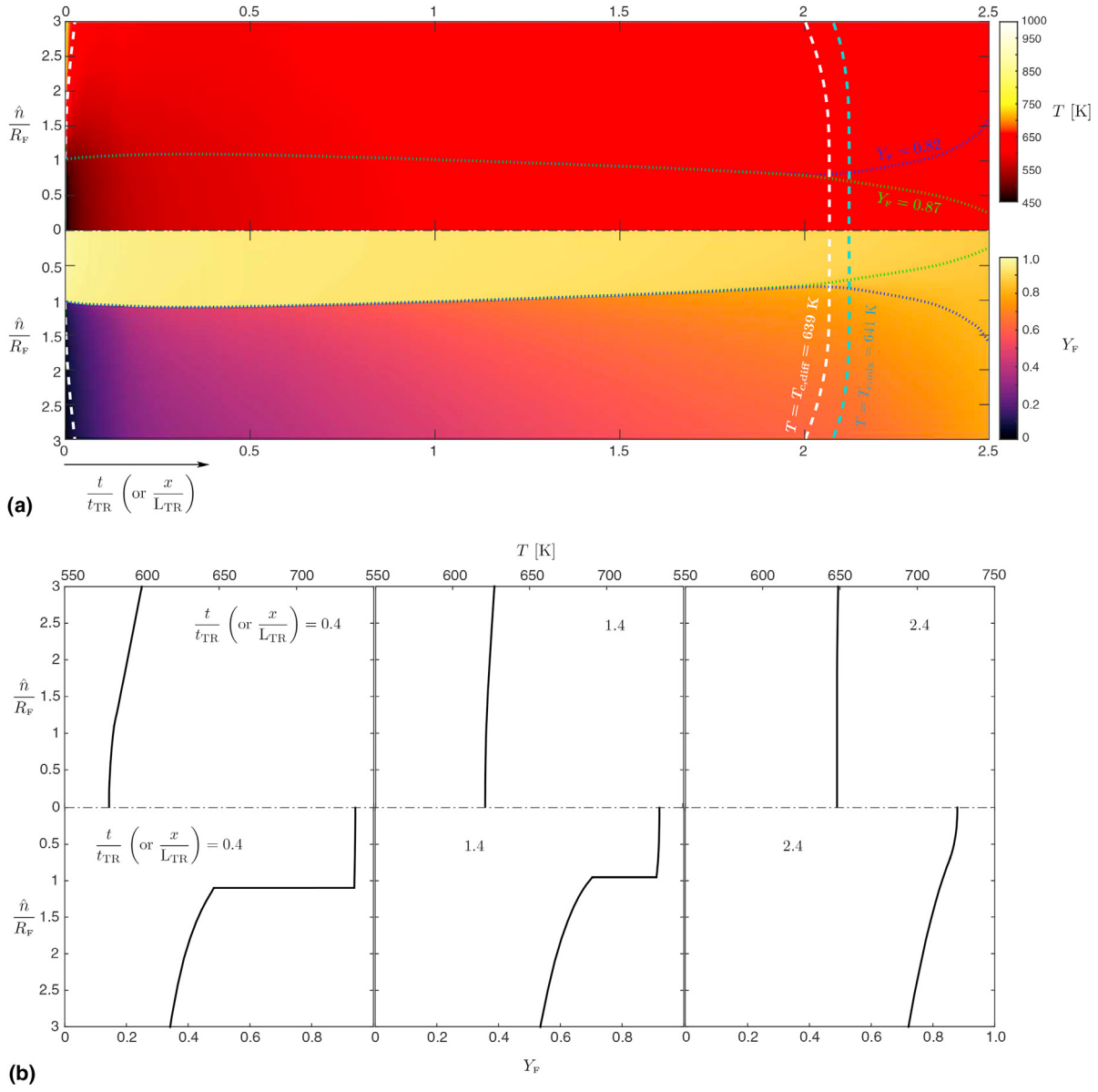

Fig. 32. Zoomed version of Fig. 31 showing (a) solid contours of temperature (upper half) and fuel mass fraction (lower half), along with (b) corresponding profiles extracted at $t/t_{TR} = x/L_{TR} = 0.4$. 1.4, and 2.4. Panel (a) includes isotherms corresponding to the critical mixing temperature (blue dashed line), diffusional critical temperature (white dashed line), along with isocomposition lines corresponding to $Y_F = 0.82$ (blue dotted line) and $Y_F = 0.87$ (green dotted line).. (For interpretation of the references to color in this figure legend, the reader is referred to the web version of this article.)

that the coexistence region extends up to more than 100-fold higher pressures than the critical pressures of the separate components in systems of heavy-hydrocarbon fuels mixed with N_2, O_2, or air.

At high pressures, the thermodynamic structure of the coexistence region is dominated by diffusional instabilities. Specifically, the components tend to separate in the coexistence region because of an antidiffusion process that proves energetically favorable. In ordinary practice, systems like water brought into the coexistence region of their thermodynamic phase diagram at standard pressure tend to separate into different phases, namely liquid and vapor, across an interface. However, at high pressures, the phases are no longer vapor and liquid, but two supercritical fluids of distinct character which, in the transcritical conditions addressed in this study, behave at injection as a liquid-like supercritical fluid (for the heavy hydrocarbon fuel) and a gas-like supercritical fluid (for N_2, O_2, or air).

The problem of translating by theoretical means the aforementioned diffusional instability into an observable process in physical space is nothing short of laborious. Such translation requires a tight connection between the thermodynamic space and the transport of the propellants in physical space, and must therefore involve finite-rate processes of molecular diffusion that cannot be described with the standard transport theory. This work has investigated one possible way of addressing this question by coupling an extension of the diffuse-interface theory of van der Waals flows with the Navier-Stokes conservation equations. The core of this theory is the folding of the coexistence region in thermodynamic space into a thin interface in physical space. This can only be made possible by redefining the thermodynamic potentials in the presence of strong composition gradients, and by revisiting the constitutive laws participating in the Navier-Stokes conservation equations. When these modifications are coupled with a high-pressure equation of state that reproduces a single

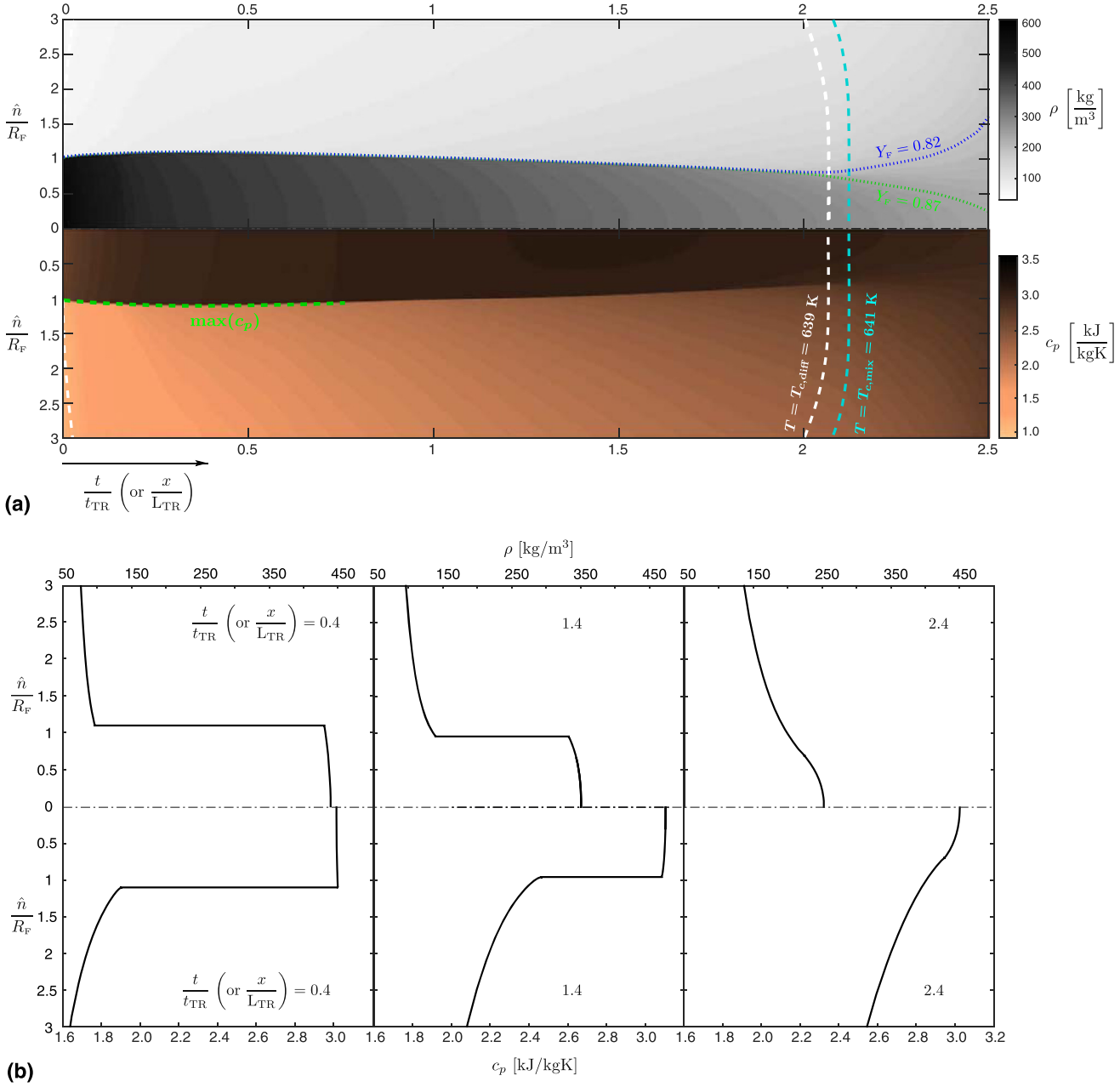

Fig. 33. (a) Solid contours of density (upper half) and constant-pressure specific heat (lower half), along with (b) corresponding profiles extracted at $t/t_{TR} = x/L_{TR} = 0.4$, 1.4, and 2.4. In panel (a), the thick green dashed line indicates the loci of points where the constant-pressure specific heat attains a global maximum; this line is not plotted for $t/t_{TR} = x/L_{TR} > 0.75$, when the global maximum switches from the interface to the jet axis. Additionally, panel (a) includes isotherms corresponding to the critical mixing temperature (blue dashed line), diffusional critical temperature (white dashed line), along with isocomposition lines corresponding to $Y_F = 0.82$ (blue dotted line) and $Y_F = 0.87$ (green dotted line).. (For interpretation of the references to color in this figure legend, the reader is referred to the web version of this article.)

Maxwell loop within the coexistence region, the formulation can describe separation or mixing of phases or fluids in accordance with their thermodynamic phase diagram. The ensuing interface has a non-zero thickness set by the nearly mutual cancellation between an antidiffusion flux of matter provided by the standard transport theory, and an opposing interfacial flux arising as a regularization introduced by the diffuse-interface theory. The formulation is not exempt of approximations, among which the most notable one is related to the continuum hypothesis across the interface. This is a comfortable approximation only at high pressures because the interface broadens relative to intercollision distances.

The theory of transcritical flows outlined in this work incorporates high-pressure models for thermophysical and transport properties. Those are subject to large uncertainties, and their determination through analysis or experiments is a broad and active area of research. Furthermore, the formulation has introduced additional parameters in the form of gradient-energy coefficients that are directly related to the thickness and surface tension of the interface. Most of the existing models for these coefficients rely on experimental calibration. Recent improvements in experimental techniques for diagnostics of high-pressure flow fields, along with new developments in molecular-dynamics simulations for the computation of thermo-

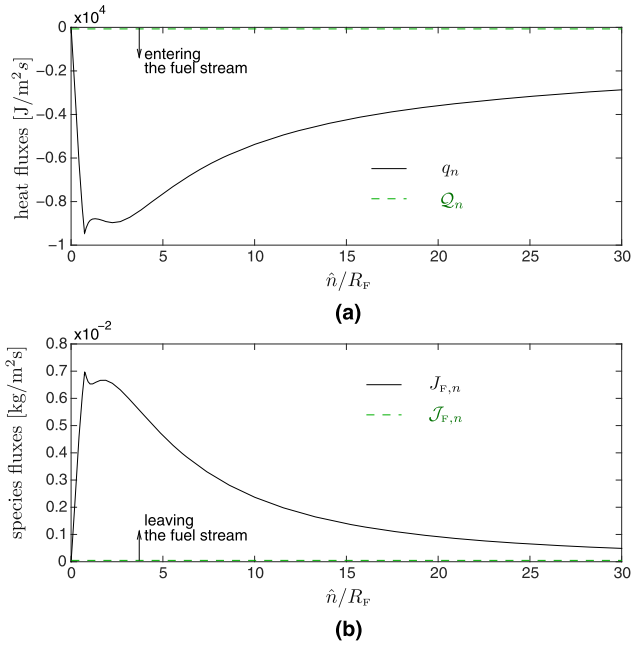

Fig. 34. Spatial distributions of (a) heat and (b) species fluxes at $t/t_{TR} = x/L_{TR} = 2.4$ shortly downstream of the interface edge.

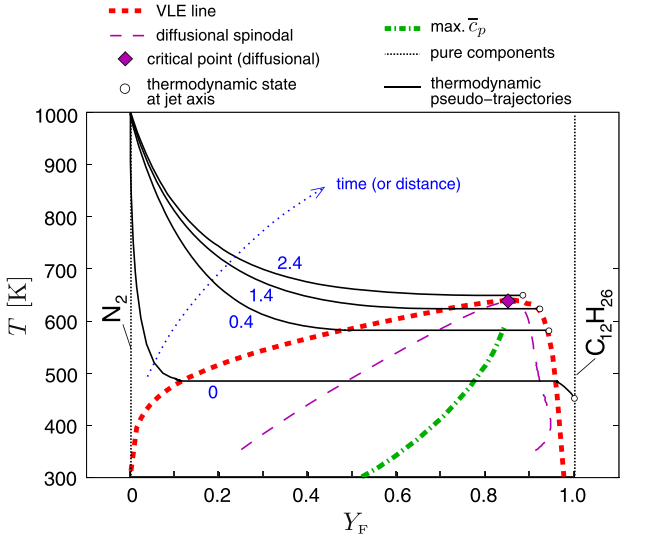

Fig. 35. Thermodynamic-space pseudo-trajectories at $t/t_{TR} = x/L_{TR} = 0$, 0.4, 1.4, and 2.4, projected on a constant-pressure ($P = P_\infty = 100$ bar) cross-section of the thermodynamic-phase diagram. The figure includes the diffusional critical point (purple diamond symbol), the VLE line (thick red dashed line), the diffusional spinodals (thin purple dashed lines), and the loci of the maximum of the molar heat at constant pressure (thick green dot-dashed line). (For interpretation of the references to color in this figure legend, the reader is referred to the web version of this article.)

physical properties, transport coefficients, and possibly gradient-energy coefficients, may assist in future work to reduce the uncertainties.

The utilization of this theory has discovered quantitative information about the dynamics of transcritical interfaces in coflowing configurations consisting of two propellant streams injected at different temperatures. The interface separating both propellant streams, along with the surface tension it engenders, survive from the injection orifice until a supercriticalization zone downstream, where the interface vanishes at an edge upon reaching the temperature of the diffusional critical point. The latter plays a prominent role at the interface edge in the $C_{12}H_{26}/N_2$ systems tested here. Specifically, the interface edge is characterized by a fundamental transition in the transport characteristics of the mixture that prevents separation of the components thereafter. A fully supercritical mixing layer ensues from the interface edge, across which the propellants mix by molecular diffusion as if they were two gas-like fluids.

A central motivation of this study has been to highlight that a number of extensions of this theory could be made in order to relax the simplifying assumptions used in the examples above. These extensions could include the effects of turbulence, which is expected to play an important role in the transport of heat in practical systems at high pressures, and consequently in the determination of the supercriticalization length. However, even in the simple cases that have been addressed in this work, the description of the coupling between the interface structure and the hydrodynamic field is computationally expensive because of the resulting

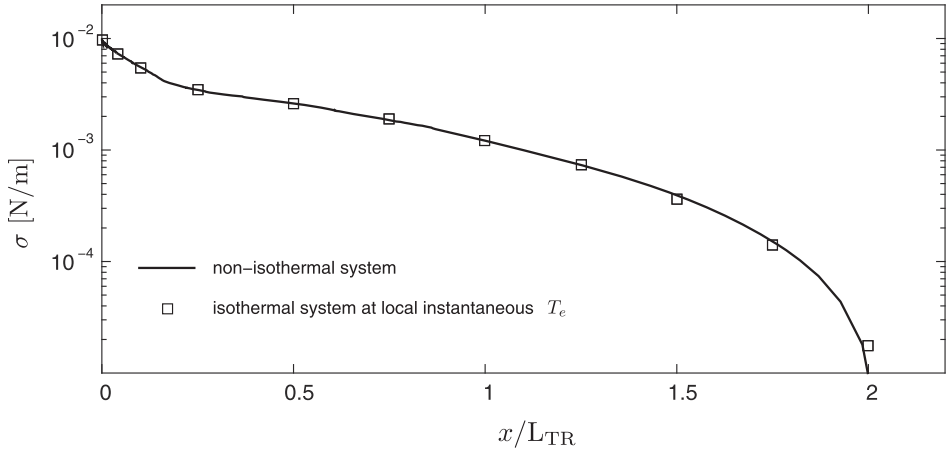

Fig. 36. Surface-tension coefficient in a $C_{12}H_{26}/N_2$ non-isothermal system as a function of downstream distance (or time). The figure includes the solution obtained by a numerical integration of the formulation in Table 8 for non-isothermal bicomponent systems (solid line), along with solutions in mechanical and transport equilibrium (square symbols) obtained by a numerical integration of the formulation in Table 6 for isothermal systems assuming constant temperature equal to the local (or instantaneous) interface temperature T_e read from Fig. 29(b).

large disparity of scales. The reader should therefore be forewarned that the formulation that has been presented here involves interfacial terms in the conservation equations whose spatiotemporal resolution requirements are most likely untenable in CFD simulations of full engineering systems with current standard hardware and numerical methods.

Worthy extensions of this work that may decrease the computational cost could involve investigations of filtered versions of the Navier-Stokes conservation equations augmented with the interfacial terms derived here, where the filter width would be much larger than the interface thickness but much smaller than the hydrodynamic scales. This would necessarily lead to closure problems in subgrid-scale interfacial terms, including the surface-tension force. The results presented here suggest that the interface is in mechanical and transport near-equilibrium for a significant portion of its length, except near the orifice and near the interface edge, where non-equilibrium considerations may become important. It could therefore be of some interest to investigate the closure of subgrid-scale interfacial terms by reading them on-the-fly from pre-tabulated solutions of isothermal transcritical interfaces at a local interface temperature provided by the resolved flow field.

Declaration of Competing Interest

The authors declare that they have no known competing financial interests or personal relationships that could have appeared to influence the work reported in this paper.

Acknowledgments

This work was funded by the US Department of Energy through the National Nuclear Security Administration (NNSA) Grant #DE-NA0002373 as part of the PSAAP-II Center at Stanford University. The authors are grateful to Dr. Mario Di Renzo for useful suggestions on the numerical integrations.

Appendix A. Basic aspects of thermodynamic stability and phase equilibrium for transcritical systems

The coupling between the diffuse-interface theory and the Navier-Stokes conservation equations depends fundamentally on the diffusional stability of the mixture. In unstable conditions, a transcritical interface is generated that separates mixtures near phase equilibrium. This appendix reviews basic concepts related to thermodynamic stability and phase equilibrium that are ubiquitously employed throughout the main text.

A1. Thermodynamic-stability considerations

The Peng-Robinson equation of state (14), and all others available, constrain all possible thermodynamic states of the system on a hypersurface $P = P(\rho, T, Y_1, Y_2 \dots Y_{N-1})$. However, not all thermodynamic states on that hypersurface are observable. Specifically, there exist regions on that hypersurface where the system is thermodynamically unstable. There, a homogeneous mixture of the components is energetically less favorable than a configuration where different phases or different fluids are separated by interfaces. The criteria that determine whether the system is thermodynamically stable are independent of the equation of state. However, the single Maxwell loop predicted by cubic equations of state such as (14) naturally accommodates the stability landscape.

In closed multicomponent systems subject to differential disturbances from equilibrium, thermodynamic stability occurs when three different conditions corresponding to thermal, mechanical, and diffusional stability are simultaneously satisfied. Motivated by Fig. 1, the discussion here will be precluded to bicomponent systems ($N = 2$), with brief references being made to monocomponent systems ($N = 1$) for conceptual comparisons. The explanations are supplemented by the thermodynamic phase diagrams in Figs. 4 and A.1. The reader is referred to Refs. [103–105] for generalizations and full derivations of these conditions.

Thermal stability is observed when the constant-volume molar heat of the mixture is positive,

$$\bar{c}_v = \left(\frac{\partial \bar{e}}{\partial T}\right)_{v,X_F} > 0, \tag{A.1}$$

where X_F is the molar fraction of fuel. In particular, Eq. (A.1) ensures that the molar internal energy $\bar{e}$ increases with increasing temperatures at constant volume and composition. The condition (A.1) is satisfied by specific heats $\bar{c}_v$ calculated using the Peng-Robinson equation of state (14) in the conditions of interest for the present study. Formulas for the calculation of $\bar{c}_v$ are outlined in Appendix C.7, and a closer analysis of the resulting variations of specific heat with temperature and composition is provided in Appendix B.2 for $C_{12}H_{26}/N_2$ mixtures.

Mechanical stability is attained when the isothermal compressibility of the mixture β_T is positive,

$$\beta_T = -\frac{1}{v}\left(\frac{\partial v}{\partial P}\right)_{T,X_F} > 0, \tag{A.2}$$

which guarantees that the molar volume decreases as the pressure increases at constant temperature and composition. An expression for β_T particularized for the Peng-Robinson equation of state (14) is provided in Eq. (C.44). It can be shown that a system that is mechanically stable is also thermally stable, but a system thermally stable is not necessarily mechanically stable [104]. Most importantly, the limit of mechanical stability is delineated by the mechanical spinodal surface, whose equation is given by

$$\left(\frac{\partial P}{\partial v}\right)_{T,X_F} = 0, \tag{A.3}$$

or equivalently $\beta_T \to \infty$. In monocomponent systems, the mechanical spinodals are easily visualized as lines intersecting all minima and maxima of the Maxwell loop in a $P - v$ diagram, as shown in Fig. 4. Within the region of the $P - v$ diagram enclosed by the mechanical spinodals, the isothermal compressibility is negative and the system becomes mechanically unstable. In this unstable region, the system tends to separate into two phases by means of a thin interface.

A mechanical critical line exists on the mechanical spinodal surface where the pressure reaches an inflection point along the v axis at constant temperature and composition. The mechanical critical line is therefore defined as the locus of points in the thermodynamic space $\{P, T, X_F\}$ where the condition (A.3) is satisfied simultaneously with

$$\left(\frac{\partial^2 P}{\partial v^2}\right)_{T,X_F} = 0. \tag{A.4}$$

A mechanical critical point is therefore defined as the intersection of the mechanical critical line with constant-pressure, constant-temperature, or constant-composition planes.

In monocomponent systems, the mechanical critical line (A.3) and (A.4) collapses on a single critical point in the thermodynamic phase diagram, as observed in Fig. 4. This critical point determines the critical pressure above which the two-phase region ceases to exist, or equivalently, the pressure above which the monocomponent system is unconditionally stable. In contrast, mechanical stability is not a sufficient condition for thermodynamic stability in multicomponent systems, since diffusional processes

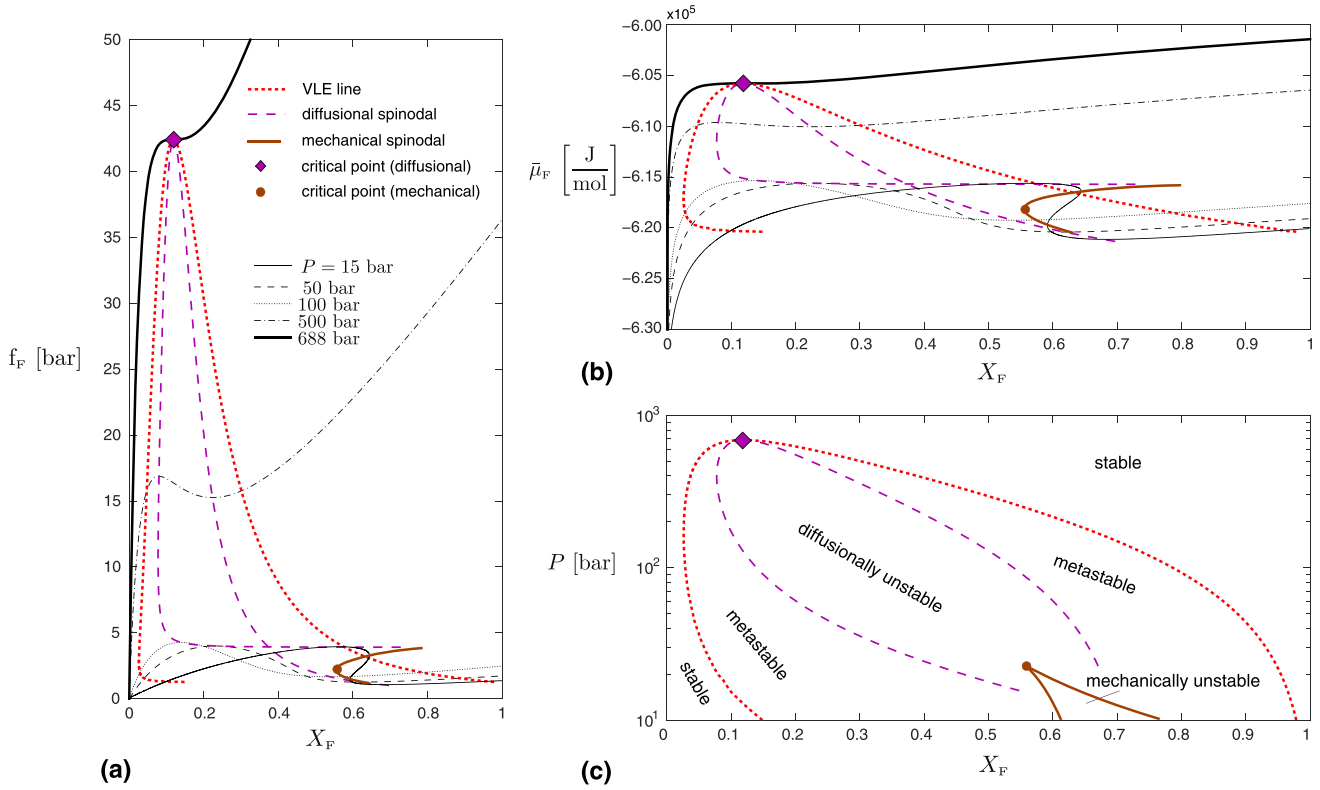

Fig. A.1. Thermodynamic phase diagrams for $C_{12}H_{26}/N_2$ mixtures at uniform temperature $T = 500$ K in terms of (a) fuel fugacity f_F as a function of the fuel molar fraction at different constant pressures, (b) fuel molar chemical potential $\bar{\mu}_F$ as a function of the fuel molar fraction at different pressures [refer to legend in panel (a)], and (c) pressure as a function of the fuel molar fraction indicating different stability regions of the diagram.

can additionally drive separation of components at pressures above the mechanical critical point. Diffusional stability requires that the molar chemical potential of one of the constituents, for instance that of the fuel $\bar{\mu}_F$, increases upon increasing the concentration of the same species, namely

$$\left(\frac{\partial \bar{\mu}_F}{\partial X_F}\right)_{P,T} > 0. \tag{A.5}$$

The partial derivative of the fuel chemical potential $\bar{\mu}_F$ with respect to X_F can be rewritten in terms of the fuel fugacity $f_F = X_F \varphi_F P$ as

$$\left(\frac{\partial \bar{\mu}_F}{\partial X_F}\right)_{P,T} = \frac{R^0 T}{X_F}\left(\frac{\partial \ln f_F}{\partial \ln X_F}\right)_{P,T}, \tag{A.6}$$

where φ_F is the corresponding fugacity coefficient defined in Eq. (C.47). The formal justification for Eq. (A.6) can be found in Appendix B.3. In particular, Eq. (A.6) indicates that the diffusional stability criterion (A.5) can be alternatively stated as

$$\left(\frac{\partial \ln f_F}{\partial \ln X_F}\right)_{P,T} > 0. \tag{A.7}$$

It can be shown that a diffusionally stable system is also both thermally and mechanically stable, but a system both thermally and mechanically stable is not necessarily diffusionally stable [104]. The limit of diffusional stability is attained at the diffusional spinodal surfaces, where

$$\left(\frac{\partial \bar{\mu}_F}{\partial X_F}\right)_{P,T} = 0 \tag{A.8}$$

is satisfied, or alternatively

$$\left(\frac{\partial \ln f_F}{\partial \ln X_F}\right)_{P,T} = 0, \tag{A.9}$$

as prescribed by Eq. (A.6).

The transcritical $C_{12}H_{26}/N_2$ systems analyzed in this study are diffusionally unstable but thermally and mechanically stable at pressures larger than approximately 200 bar, whereas they become both mechanically and diffusionally unstable at pressures lower than those (see Appendix E). It is the breach of the diffusional stability constraint (A.5) what induces transcritical interfaces in the flow field, as discussed in Sections 4.6 and 5.4–5.6. Briefly, the diffusional spinodals represent thermodynamic states where the Fickian diffusion coefficient becomes zero. In particular, the quantity $(\partial \ln f_F/\partial \ln X_F)_{P,T}$ fundamentally participates as a non-ideal prefactor in the Fickian diffusion coefficient at high pressures defined in Eq. (43), in such a way that changes in the sign of $(\partial \ln f_F/\partial \ln X_F)_{P,T}$ change the direction of the diffusion flux. Outside the region delimited by the diffusional spinodals [i.e., $(\partial \ln f_F/\partial \ln X_F)_{P,T} > 0$], the mixture is stable and the components tend to diffuse into flow regions in directions aligned with decreasing gradients of their concentration. In contrast, within the region delimited by the diffusional spinodals [i.e., $(\partial \ln f_F/\partial \ln X_F)_{P,T} < 0$], the chemical potential decreases with increasing molar fraction. As a result, the mixture is unstable there and tends to separate by means of antidiffusion of matter. This phenomenon is well characterized in physical chemistry [136], and cannot be described by the standard transport theory.

A relevant curve on the diffusional spinodal surfaces is the diffusional critical line of the mixture, which is defined as the locus

of points where (A.8) is satisfied along with

$$\left(\frac{\partial^2 \bar{\mu}_{\mathrm{F}}}{\partial X_{\mathrm{F}}^2}\right)_{P,T} = 0, \tag{A.10}$$

or equivalently, where the chemical potential reaches an inflection point along the X_{F} axis at constant pressure and temperature. Alternatively, based on Eq. (A.6), the diffusional critical line can be defined as the locus of points in the thermodynamic space $\{P, T, X_{\mathrm{F}}\}$ where Eq. (A.9) is satisfied along with

$$\left(\frac{\partial^2 \ln \mathrm{f}_{\mathrm{F}}}{\partial X_{\mathrm{F}}^2}\right)_{P,T} = 0. \tag{A.11}$$

The diffusional and mechanical critical lines of the mixture are generally different. The intersection of the diffusional critical line with constant-pressure, constant-temperature, or constant-composition planes gives rise to a diffusional critical point. These considerations are summarized in the thermodynamic phase diagrams shown in Fig. A.1.

The verification of the stability criteria (A.1), (A.2), and (A.5) [or (A.7)], does not prevent the system from becoming unstable to finite-amplitude disturbances. Whereas unconditional stability is achieved along the phase-equilibrium surface, or coexistence envelope, and everywhere outside the volume enclosed by it, interstitial regions exist in the thermodynamic phase diagrams in Fig. 4 and A.1(c) that are enclosed between the phase-equilibrium and spinodal surfaces. The system is metastable there, in that finite-amplitude disturbances can render it unstable [103,104].

A2. Phase equilibrium

Consider two thermodynamic states $\{P^\ell, T^\ell, X_{\mathrm{F}}^\ell\}$ and $\{P^g, T^g, X_{\mathrm{F}}^g\}$ in the same bicomponent system addressed above. These states are in phase equilibrium across flat interfaces when the following three conditions corresponding to equal pressures

$$P^\ell = P^g = P_e, \tag{A.12}$$

equal temperatures

$$T^\ell = T^g = T_e, \tag{A.13}$$

and equal chemical potentials

$$\bar{\mu}_{\mathrm{F}}^\ell = \bar{\mu}_{\mathrm{F}}^g = \bar{\mu}_{\mathrm{Fe}}, \quad \bar{\mu}_{\mathrm{O}}^\ell = \bar{\mu}_{\mathrm{O}}^g = \bar{\mu}_{\mathrm{Oe}}, \tag{A.14}$$

are simultaneously satisfied [103,104], with the subindex e being employed here to indicate phase-equilibrium values. At low pressures, ℓ and g denote liquid and vapor phases, respectively. In the high-pressure systems studied here, and more particularly above the critical pressures of the separate components, ℓ and g denote liquid-like and gas-like supercritical fluids, respectively.

Based on Eq. (A.6), the condition (A.14) is equivalent to the condition of equal fugacities,

$$\mathrm{f}_{\mathrm{F}}^\ell = \mathrm{f}_{\mathrm{F}}^g = \mathrm{f}_{\mathrm{Fe}}, \quad \mathrm{f}_{\mathrm{O}}^\ell = \mathrm{f}_{\mathrm{O}}^g = \mathrm{f}_{\mathrm{Oe}}. \tag{A.15}$$

In monocomponent systems, the two conditions in (A.14) are replaced by the single constraint

$$\bar{\mu}^\ell = \bar{\mu}^g = \bar{\mu}_e, \tag{A.16}$$

where $\bar{\mu}$ is the molar Gibbs free energy.

At the equilibrium values of pressure P_e and temperature T_e, the combination of Eqs. (A.12), (A.13) and (A.15), along with the equation of state (14) and the fugacity (B.21), provides the equilibrium molar volumes v_e^ℓ and v_e^g, as well as the equilibrium molar fractions X_{Fe}^ℓ and X_{Fe}^g. The subspace of states satisfying the above phase-equilibrium constraints forms a surface or coexistence envelope in the thermodynamic space $\{P, T, X_{\mathrm{F}}\}$. A constant-temperature cross-section of the coexistence envelope, indicated by the VLE lines, is provided in the phase diagrams presented in Fig. A.1.

As discussed in Appendix A.1, the system is thermodynamically stable along the coexistence envelope and everywhere outside the volume enclosed by the coexistence envelope. The system is metastable in the concentric volume enclosed between the coexistence envelope and the diffusional spinodal surface, as indicated in Fig. A.1(c). Thermodynamic instability occurs within the volume enclosed by the diffusional spinodal surface, where no homogeneously mixed state consisting of phases ℓ and g can exist. Under these unstable conditions, the system tends to become separated into the two equilibrium states ℓ and g by means of a thin interface.

As explained in Section 4.4, the diffuse-interface theory maps the volume enclosed by the phase-equilibrium surface in thermodynamic space into a thin interface in physical space. In its simplest representation corresponding to isothermal systems, the theory predicts that phase-equilibrium conditions are exactly satisfied on both sides of the interface. In most practical cases, however, the propellant streams are injected in the combustor at different temperatures, as depicted in Fig. 1. In the presence of temperature gradients across the interface, the phase-equilibrium conditions (A.12)–(A.14) are only satisfied in an asymptotic sense up to an appropriate order of approximation provided in Sections 5.3 and 5.6.

Appendix B. Transcritical behavior of thermophysical properties and molecular transport coefficients

A complete description of the fluid motion requires specification of the thermophysical properties and transport coefficients of the mixture. At high pressures, increasing departures from the ideal-gas theory are observed, and consequently derivation of more complex expressions are necessary.

B1. Molar enthalpy

The specific gradient-dependent internal energy e_{GD} can be obtained from the total energy using Eq. (47). The molar enthalpy $\overline{h}$ can be easily related to e_{GD} by rewriting Eq. (52) on a molar basis as

$$\overline{h} = e_{\mathrm{GD}}\overline{W} + P_{\mathrm{GD}}v, \tag{B.1}$$

where P_{GD} is given by Eq. (50). An expression for $\overline{h}$ as a function of the state variables at high pressures is provided in this section.

The utilization of molar rather than specific values is expedient since the resulting departure of the enthalpy from its ideal-gas counterpart involves integration of the equation of state (14), which is written in terms of the molar volume v and of the coefficients a and b on a molar basis. Specific and molar values of the enthalpy are simply related through the mean molecular weight as $h = \overline{h}/\overline{W}$. Similarly, partial specific and partial molar values of the enthalpy are related through the molecular weight of the particular component, $h_i = \overline{h}_i/W_i$. Analogous relations apply to the entropy and all other thermodynamic potentials, including their partial values.

The variation of enthalpy at high pressures can be calculated in the following way. Consider the exact differential of the enthalpy of the system H,

$$dH = \left(\frac{\partial H}{\partial T}\right)_{P,n_i|i=1,\dots N} dT + \left(\frac{\partial H}{\partial P}\right)_{T,n_i|i=1,\dots N} dP + \sum_{i=1}^{N} \overline{h}_i dn_i, \tag{B.2}$$

with n_i being the number of moles of species i and $\overline{h}_i = (\partial H/\partial n_i)_{P,T,n_j|j=1,\dots N;(j\neq i)}$ as the partial molar enthalpy. The enthalpy of the system can be expressed in additive form as $H =$

$\sum_{i=1}^{N} n_i \bar{h}_i$, which can be differentiated and combined with Eq. (B.2) yielding

$$\sum_{i=1}^{N} X_i d\bar{h}_i = \left(\frac{\partial \bar{h}}{\partial T}\right)_{P,X_{i|i=1,\dots N-1}} dT + \left(\frac{\partial \bar{h}}{\partial P}\right)_{T,X_{i|i=1,\dots N-1}} dP. \tag{B.3}$$

Further simplifications of Eq. (B.3) can be made by rewriting the first principle of thermodynamics (C.1) on a molar basis, namely

$$T d\bar{s} = d\bar{h} - \nu dP - \sum_{i=1}^{N-1} (\bar{\mu}_i - \bar{\mu}_N) dX_i, \tag{B.4}$$

where the last term represents a chemical work done at constant volume due to a variation in the composition, with $\bar{\mu}_i$ being the molar chemical potential of species i [defined formally further below in Eq. (B.23)]. In particular, the partial differentiation of Eq. (B.4) with respect to pressure yields

$$\left(\frac{\partial \bar{h}}{\partial P}\right)_{T,X_{i|i=1,\dots N-1}} = T\left(\frac{\partial \bar{s}}{\partial P}\right)_{T,X_{i|i=1,\dots N-1}} + \nu. \tag{B.5}$$

Substituting (B.5) into (B.3) and using the definition of the constant-pressure molar heat $\bar{c}_p = (\partial \bar{h}/\partial T)_{P,X_i|i=1,\dots N-1}$ and the Maxwell relation $(\partial \bar{s}/\partial P)_{T,X_i|i=1,\dots N-1} = -(\partial \nu/\partial T)_{P,X_i|i=1,\dots N-1}$, the expression

$$\sum_{i=1}^{N} X_i d\bar{h}_i = \bar{c}_p dT + (1 - T\beta_\nu)\nu dP \tag{B.6}$$

is obtained, where

$$\beta_\nu = \frac{1}{\nu}\left(\frac{\partial \nu}{\partial T}\right)_{P,X_{i|i=1,\dots N-1}} \tag{B.7}$$

is the volume expansivity. An expression for β_ν particularized for the Peng-Robinson equation of state (14) is given in Eq. (C.22).

Because of its form amenable to isolation of non-ideal effects arising when $T\beta_\nu \neq 1$, the second term on the right-hand side of Eq. (B.6) is the basis for the computation of the pressure-induced departure of the enthalpy with respect to that of an ideal gas [54]. Since that term cannot be straightforwardly expressed as a linear sum of contributions from the different components when the equation of state (14) and the mixing rules (15) are employed, in multicomponent systems the standard approach neglects enthalpy variations due to mixing, in such a way that the total variation of the enthalpy is assumed to be given by the linearized weighted sum of the variations of the partial enthalpies, namely $d\bar{h} = \sum_{i=1}^{N} d(X_i \bar{h}_i) \simeq \sum_{i=1}^{N} X_i d\bar{h}_i$ [150]. This procedure is equivalent to neglecting the last term on the right-hand side of Eq. (B.2) by freezing the chemical composition. In this way, Eq. (B.6) becomes

$$d\bar{h} \simeq \bar{c}_p dT + (1 - T\beta_\nu)\nu dP. \tag{B.8}$$

For ideal gases, $\beta_\nu = 1/T$ and therefore the second term on the right-hand side of Eq. (B.8) vanishes, with $\bar{h}$ being only a function of T and composition. In contrast, the second term on the right-hand side of Eq. (B.8) is not zero at high pressures when real-gas effects are considered, which makes $\bar{h}$ to additionally depend on pressure, $\bar{h} = \bar{h}(P, T, X_1, \dots, X_{N-1})$.

In coupling Eq. (B.8) with the Navier-Stokes equations, it is important to note that the integration of Eq. (B.8) is independent of the thermodynamic trajectory. Consider an arbitrary reference state $\{P^0, T^0\}$ in which the gas is approximately ideal, with the enthalpy there being denoted as $\bar{h}^{\mathrm{IG},0}$. The change in molar enthalpy $\Delta\bar{h} = \bar{h} - \bar{h}^{\mathrm{IG},0}$ between $\{P^0, T^0\}$ and the final state $\{P, T\}$ can be expressed as the sum of an isobaric change from $\{P^0, T^0\}$ to $\{P^0, T\}$, and an isothermal change from $\{P^0, T\}$ to $\{P, T\}$. The value of the reference pressure P^0 is chosen to be small compared to P (i.e., $P^0/P \ll 1$), which makes the change in enthalpy along the isobar of this particular integration path to occur under ideal-gas conditions. The integration of Eq. (B.8) using this combined trajectory yields the expression

$$\bar{h} = \bar{h}^{\mathrm{IG}}(T, X_1, \dots X_{N-1}) + \Delta_d \bar{h}(P, T, X_1, \dots X_{N-1}) \tag{B.9}$$

for the molar enthalpy at the high-pressure state $\{P, T\}$.

The right-hand side of Eq. (B.9) is composed of two different terms corresponding to the two legs of the particular trajectory mentioned above. In particular, $\bar{h}^{\mathrm{IG}}$ is the molar enthalpy of an ideal gas evaluated at the end of the isobaric portion of the trajectory, namely

$$\bar{h}^{\mathrm{IG}} = \bar{h}^{\mathrm{IG},0} + \int_{T^0}^{T} \bar{c}_p^{\mathrm{IG}} dT, \tag{B.10}$$

where $\bar{h}^{\mathrm{IG},0}$ is the enthalpy of an ideal gas at the reference temperature T^0, and $\bar{c}_p^{\mathrm{IG}} = \sum_{i=1}^{N} X_i \bar{c}_{p,i}^{\mathrm{IG}}$ is the ideal-gas value of the constant-pressure molar heat of the mixture, which depends on composition and temperature. A more practical way of computing $\bar{h}^{\mathrm{IG}}$ consists in fixing the arbitrary reference temperature at $T^0 = 298$ K and rewriting (B.10) as

$$\bar{h}^{\mathrm{IG}} = \sum_{i=1}^{N} X_i \left(\bar{h}_{f,i}^{298\,\mathrm{K}} + \int_{298\,\mathrm{K}}^{T} \bar{c}_{p,i}^{\mathrm{IG}} dT\right), \tag{B.11}$$

where $\bar{h}_{f,i}^{298\,\mathrm{K}}$ is the standard enthalpy of formation of element i. The bracketed quantity in (B.11) is the ideal-gas partial molar enthalpy $\bar{h}_i^{\mathrm{IG}}$, whose origin is chosen to be the formation value. By using the conservation equations of mass (44) and species (46), it can be shown that the conservation equations for total energy (47) and enthalpy (51) are independent of this origin as long as there are no chemical reactions in the problem. In chemically reacting systems, the first term on the right hand side of Eq. (B.11), which involves the sum of the formation partial enthalpies multiplied by their corresponding molar fractions, is responsible for the changes in enthalpy due to chemical heat release without the need of adding any chemical sources on the right-hand sides of neither the total-energy Eq. (47) nor the enthalpy equation (51). A chemical source would however have to be added on the right-hand side of the species conservation equation (46). Despite the absence of chemical reactions in the present study, the choice is made here to use the formation enthalpy $\bar{h}_{f,i}^{298\,\mathrm{K}}$ as reference value to facilitate the computation of $\bar{h}_i^{\mathrm{IG}}$ for different species as a function of temperature from existing tables, since the latter are most prominently found within the combustion-related literature [e.g., see Ref. [151] and Eq. (C.33) in Appendix C].

The second term on the right-hand side of Eq. (B.9) corresponds to the enthalpy departure function

$$\Delta_d \bar{h} = \bar{h} - \bar{h}^{\mathrm{IG}} = \int_0^P (1 - T\beta_\nu)\nu dP, \tag{B.12}$$

which quantifies the enthalpy variations of a real gas along the isotherm at temperature T as the pressure changes from $P^0 \to 0$ to P. A closed expression for (B.12) can be obtained upon substituting the equation of state (14) into the integrand [e.g., see Refs. [92,152] and Eq. (C.23) in Appendix C].

A similar methodology can be employed for calculating partial molar enthalpies at high pressures using the expression

$$\bar{h}_i(P, T, X_1, \dots X_{N-1}) = \bar{h}_i^{\mathrm{IG}}(T) + \Delta_d \bar{h}_i(P, T, X_1, \dots X_{N-1}). \tag{B.13}$$

Here, $\Delta_d \bar{h}_i$ is a partial-enthalpy departure function that can be expressed in closed form by making use of the Peng-Robinson equation [e.g., see Ref. [153] and Eq. (C.34) in Appendix C].

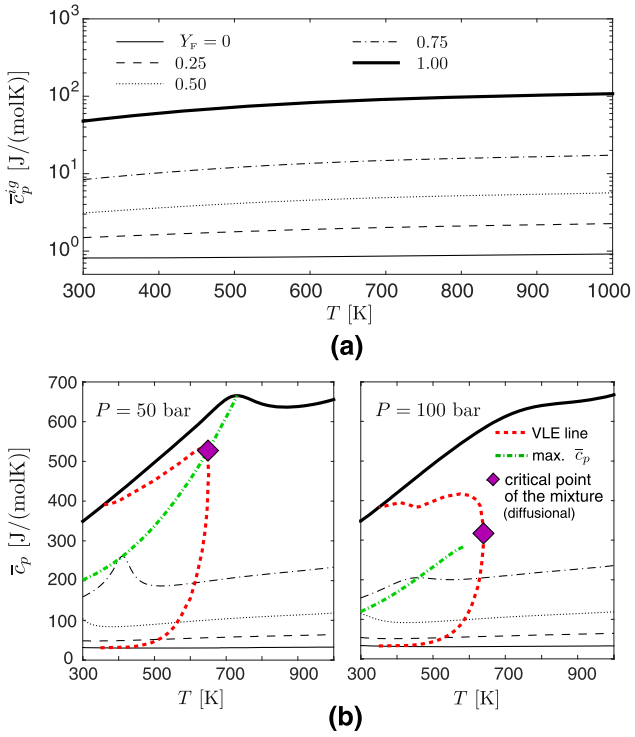

Fig. B.1. Constant-pressure molar heats for $C_{12}H_{26}/N_2$ mixtures as a function of temperature and mass fraction of dodecane Y_F for (a) ideal gases, and (b) real gases at two pressures and different compositions (refer to the legend in the top panel). The plots in (b) include the diffusional critical point of the mixture at the corresponding pressure (purple diamond symbol), the loci of the maximum of the molar heat at constant pressure (thick green dot-dashed line), along with the VLE line (thick red dashed line). (For interpretation of the references to color in this figure legend, the reader is referred to the web version of this article.)

B2. Constant-pressure molar heat

Similar departures to those observed above in the enthalpy occur in the molar heat as a result of the high pressures. To account for these, the constant-pressure molar heat of the mixture can be derived by differentiating Eq. (B.9) with respect to temperature at constant pressure and composition, which gives

$$\bar{c}_p(P,T,X_1,\ldots X_{N-1}) = \bar{c}_p^{\,\mathrm{IG}}(T,X_1,\ldots X_{N-1}) + \left[\frac{\partial(\Delta_d\bar{h})}{\partial T}\right]_{P,X_i|i=1,\ldots N-1}(P,T,X_1,\ldots X_{N-1}). \tag{B.14}$$

The right-hand side of Eq. (B.14) is the sum of two terms corresponding to ideal and non-ideal components. The ideal component is the ideal-gas constant-pressure molar heat that can be obtained from weighted sums of the ideal-gas molar heats of the individual components as $\bar{c}_p^{\,\mathrm{IG}} = \sum_{i=1}^{N} X_i \bar{c}_{p,i}^{\,\mathrm{IG}}$, with $\bar{c}_{p,i}^{\,\mathrm{IG}}$ being a temperature-dependent function typically obtained from tabulated data from different species [e.g., see Ref. [151] and Eq. (C.25) in Appendix C]. The overall dependence of $\bar{c}_p^{\,\mathrm{IG}}$ on temperature and composition for $C_{12}H_{26}/N_2$ mixtures of ideal gases is illustrated in Fig. B.1(a), which indicates that the variations are smooth and monotonic within the range of operating conditions studied here.

The non-ideal component in Eq. (B.14) corresponds to the partial derivative of the enthalpy departure function with respect to temperature. The resulting combined expression (B.14) for the constant-pressure molar heat of the mixture $\bar{c}_p$, which can be readily calculated by making use of the Peng-Robinson equation of state [see Ref. [92] and Eq. (C.28) in Appendix C], accounts for real-gas effects and is plotted in Fig. B.1(b) for $C_{12}H_{26}/N_2$ mixtures at two pressures. Much larger values of $\bar{c}_p$ are observed for dodecane than for nitrogen, with $\bar{c}_{p,F}/\bar{c}_{p,O} = 10 - 15$ under typical injection temperatures. However, as indicated in Eqs. (12) and (13), the relevant ratio of free-stream heat capacities that influences the supercriticalization length is written in specific form and is therefore much smaller, with $c_{p,F}/c_{p,O} = 2$ at $P_\infty = 100$ bar, $T_F = 350$ K and $T_O = 900$ K.

Figure B.1 (b) also provides the loci where local maximum values of $\bar{c}_p$ are attained inside and outside the coexistence region. The resulting line is reminiscent of the pseudo-boiling, or Widom line, observed in monocomponent systems (i.e., see thick green dot-dashed line in Fig. 4), although important differences are worth highlighting. In monocomponent systems undergoing phase change, the temperature remains constant and therefore $\bar{c}_p$ develops a singularity at boiling, where a finite change of enthalpy occurs under zero variations of the temperature. As the pressure is increased above the critical point, a finite-amplitude peak occurs in $\bar{c}_p$ across the pseudo-boiling condition that is characteristic of a second-order phase transition of the monocomponent system and, as described in Section 2.1, is often associated with transcriticality in the existing literature. In monocomponent systems, the pseudo-boiling line therefore emanates from the critical point and penetrates in the supercritical region of the phase diagram to progressively fade away as the peak amplitude of $\bar{c}_p$ vanishes with increasing pressures, as shown in Fig. 4. In contrast, in multicomponent systems, the phase change necessarily requires a finite temperature change at all pressures because of the unfolding of the vapor-equilibrium line into dew and boiling branches, thereby yielding finite-amplitude peaks in $\bar{c}_p$ even inside the coexistence region, as shown in Figs. 10 and B.1(b). The resulting line that joins all local maxima of $\bar{c}_p$ does not necessarily emanate from the critical point, and, depending on the pressure and mixture components, may not even enter the fully supercritical region of the thermodynamic phase diagram.

While the peak in $\bar{c}_p$ for pure dodecane is visible in Fig. B.1(b) at 50 bar and 730 K, the corresponding peak in $\bar{c}_p$ for nitrogen occurs at much lower temperatures of order 130 K that are of no interest for the problem analyzed in Fig. 1. When both components are mixed at not too high pressures such that the peak in $\bar{c}_p$ for each individual component is still discernible, a line can be traced that joins all peaks of the mixture $\bar{c}_p$, traverses the coexistence region, crosses the vapor-liquid equilibrium line at the diffusional critical point, and terminates within the single-phase supercritical region at the peak of $\bar{c}_p$ for dodecane, as shown in the left panel of Fig. B.1(b). However, at higher pressures, as in the right panel in Fig. B.1(b), where the peak of $\bar{c}_p$ for dodecane is no longer discernible, the line of maximum $\bar{c}_p$ ends short within the coexistence region and never crosses the diffusional critical point. Additional lines of maximum $\bar{c}_p$ are observed in molecular-dynamics simulations that tend to occur at much lower temperatures and may be of interest for cryogenic propellants, but those may not be computable using the Peng-Robinson equation of state [154].

B3. Chemical potentials

As shown in Section 5, the diffuse-interface theory for multicomponent flows makes ubiquitous use of chemical potentials. Specifically, the energy excess inherent to the interface structure, along with the different chemical composition of the propellant streams, results in gradients of chemical potentials that are responsible for molecular diffusion.

The molar chemical potential of species i, $\bar{\mu}_i = \bar{\mu}_i(P,T,X_1,\ldots X_N - 1)$, is defined as the partial molar Gibbs

free energy,

$$\bar{\mu}_i = \left(\frac{\partial G}{\partial n_i}\right)_{\substack{P,T,n_{j|j=1,\dots N}\\(j\neq i)}}, \tag{B.15}$$

where $G = n\bar{\mu}$ is the Gibbs free energy of the system, $\bar{\mu}$ is the molar chemical potential of the mixture, and n the total number of moles. A more useful definition of $\bar{\mu}_i$ can be derived by applying the fundamental reciprocity relation to G,

$$\frac{\partial}{\partial P}\left[\left(\frac{\partial G}{\partial n_i}\right)_{\substack{P,T,n_{j|j=1,\dots N}\\(j\neq i)}}\right]_{T,n_{j|j=1,\dots N}} = \frac{\partial}{\partial n_i}\left[\left(\frac{\partial G}{\partial P}\right)_{T,n_{i|i=1,\dots N}}\right]_{\substack{P,T,n_{j|j=1,\dots N}\\(j\neq i)}}, \tag{B.16}$$

or equivalently,

$$\left(\frac{\partial \bar{\mu}_i}{\partial P}\right)_{T,X_{j|j=1,\dots N-1}} = \bar{\mathcal{V}}_i, \tag{B.17}$$

where use of Eq. (B.15) has been made along with the definitions of the system volume $V = (\partial G/\partial P)_{T,n_i|i=1,\dots N}$ and the partial molar volume

$$\bar{\mathcal{V}}_i = \left(\frac{\partial V}{\partial n_i}\right)_{\substack{P,T,n_{j|j=1,\dots N}\\(j\neq i)}}. \tag{B.18}$$

A closed expression for the partial molar volume $\bar{\mathcal{V}}_i$ is provided in Eq. (C.43) for the case of the Peng-Robinson equation of state (14).

Direct integration of Eq. (B.17) yields the expression for the chemical potential

$$\bar{\mu}_i(P,T,X_1,\dots X_{N-1}) = \bar{\mu}_i^{\mathrm{IG}}(P,T,X_i) + \mathrm{R}^0 T \ln\varphi_i(P,T,X_1,\dots X_{N-1}), \tag{B.19}$$

where $\bar{\mu}_i^{\mathrm{IG}}$ is the chemical potential of an ideal gas given by

$$\bar{\mu}_i^{\mathrm{IG}} = \bar{g}_i^0 + \mathrm{R}^0 T \ln(X_i P/P^0). \tag{B.20}$$

In the notation, P^0 is an arbitrary reference value for the pressure that is chosen to be sufficiently low for ideal-gas conditions to prevail, and $\bar{g}_i^0 = \bar{g}_i^0(P^0,T)$ is the partial molar Gibbs free energy of the pure component at that pressure. In practice, $P^0 = 1$ bar and tables are accessed to evaluate the temperature dependence of $\bar{g}_i^0$ [e.g., see Ref. [151] and Eq. (C.46)]. Additionally, φ_i is a fugacity coefficient whose logarithm is defined as

$$\mathrm{R}^0 T \ln\varphi_i = \int_0^P \left(\bar{\mathcal{V}}_i - \frac{\mathrm{R}^0 T}{P}\right) dP. \tag{B.21}$$

The fugacity coefficient φ_i is related to the fugacity $\mathrm{f_i}$ by the expression

$$\mathrm{f_i} = \mathrm{X_i}\varphi_i \mathrm{P}. \tag{B.22}$$

A closed expression for φ_i is provided in Eq. (C.47) by substituting the Peng-Robinson equation of state (14) into Eq. (B.21). The combination of Eqs. (B.19), (B.20) and (B.22) yields the alternative definition of the chemical potential

$$\bar{\mu}_i = \bar{g}_i^0 + \mathrm{R}^0 T \ln(\mathrm{f_i}/\mathrm{P}^0) \tag{B.23}$$

directly in terms of the fugacity $\mathrm{f_i}$. The differentiation of Eq. (B.23) with respect to X_i readily leads to Eq. (A.6) anticipated in Appendix A.1.

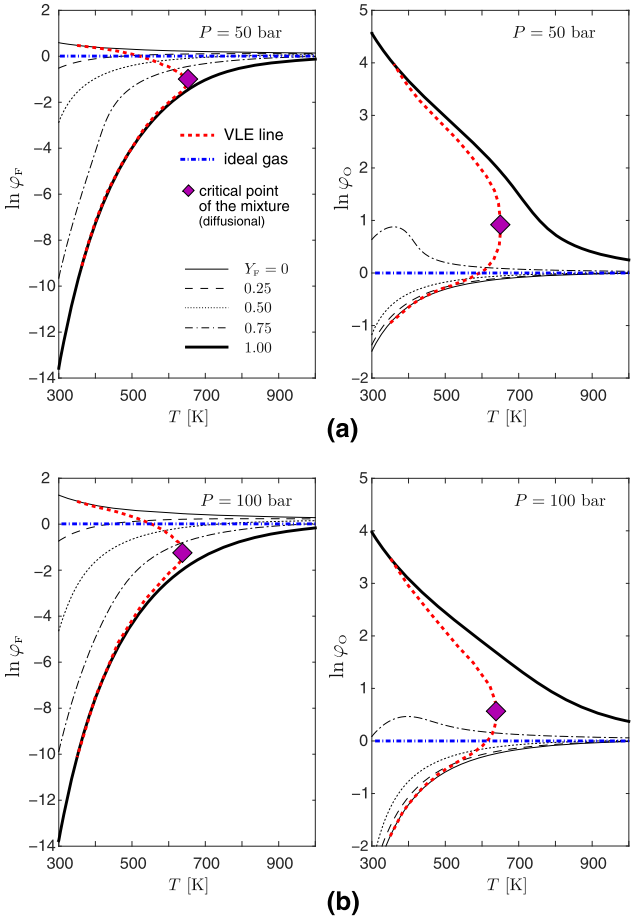

Fig. B.2. Constant-pressure distributions of the logarithm of fugacity coefficients for the individual components (φ_F for $C_{12}H_{26}$ and φ_O for N_2) of a $C_{12}H_{26}/N_2$ mixture as a function of temperature and mass fraction of dodecane Y_F at (a) $P = 50$ bar and (b) $P = 100$ bar. The plots include the zero-fugacity line corresponding to an ideal gas (thick blue dot-dashed line), the diffusional critical point of the mixture at the corresponding pressure (purple diamond symbol), along with the VLE line (thick red dashed line). (For interpretation of the references to color in this figure legend, the reader is referred to the web version of this article.)

The partial molar volume and the molar volume are the same for an ideal gas, $\bar{\mathcal{V}}_i^{\mathrm{IG}} = \mathcal{V}^{\mathrm{IG}} = \mathrm{R}^0 T/P$, as shown by substituting $V = n\mathrm{R}^0 T/P$ along with $n = \sum_{i=1}^N n_i$ into Eq. (B.18). Correspondingly, the fugacity coefficient φ_i tends to unity and the fugacity $\mathrm{f_i}$ tends to the partial pressure in thermodynamic conditions where the ideal-gas approximation is appropriate. Such conditions typically consist of high temperatures in the pressure range studied here, as shown in Fig. B.2 for $C_{12}H_{26}/N_2$ mixtures. Departures from ideality in chemical potentials, which are caused by the second term on the right-hand side of Eq. (B.19), are observed to be the largest at low temperatures, and become increasingly important as the pressure increases. Away from ideality, $\bar{\mathcal{V}}_i$ departs from $\mathcal{V}$, φ_i attains values which are far from unity, and $\mathrm{f_i}$ ceases to be the partial pressure.

B4. Molecular transport coefficients

The high pressures involved in the multicomponent systems studied in this work prevent the use of simple relations for the calculation of the dynamic viscosity η, the thermal conductivity λ, the binary diffusion coefficients $\mathcal{D}_{i,j}$, and the thermal-diffusion ratio $k_{i,T}$. Standard methods for computing η and λ are

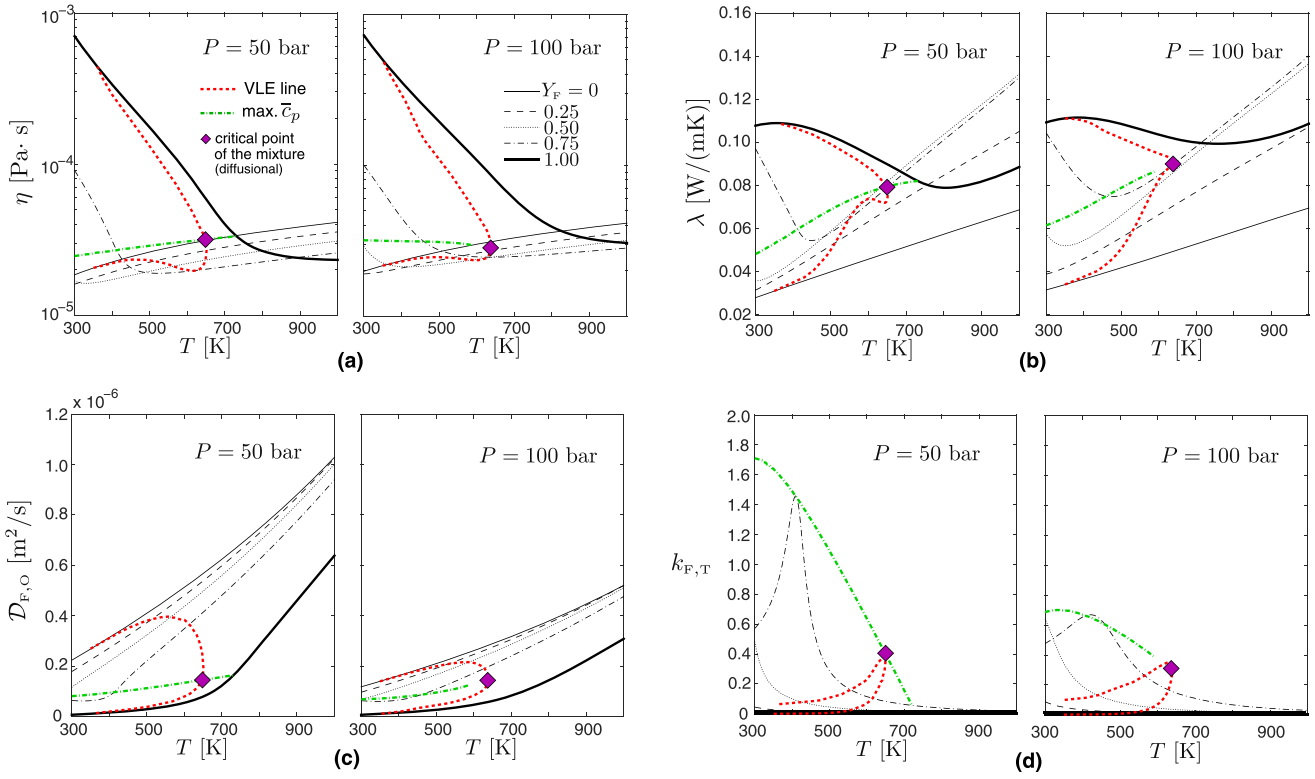

Fig. B.3. Constant-pressure distributions of (a) dynamic viscosity, (b) thermal conductivity, (c) binary diffusion coefficient, and (d) thermal-diffusion ratio for $C_{12}H_{26}/N_2$ mixtures at high pressures as a function of temperature and mass fraction of dodecane Y_F [refer to the legend in the right panel in (a)]. The plots include the diffusional critical point of the mixture at the corresponding pressure (diamond symbol), as well as projections of the loci of the maximum of the molar heat at constant pressure (thick dot-dashed line), and the VLE line (thick dashed line) on the planes $T-\eta$, $T-\lambda$, $T-\mathcal{D}_{F,O}$ and $T-k_{F,T}$. In interpreting these plots, it is important to note that the entire coexistence region is not exactly enclosed within the space bounded by the VLE line in panels (a), (b) and (d) since the partial variation of the transport coefficient with respect to Y_F attains negative values there.

detailed in Appendix F, and follow the modeling approaches in Refs. [155,156]. Those models have been used in previous studies on direct numerical simulations (DNS) of mixing layers [157], large-eddy simulations (LES) of diesel jets [158] and thermoacoustic instabilities [159], and have been successfully utilized to numerically predict experiments of N_2 jets into N_2 environments at high pressures [28,160,161]. The formulation developed in Refs. [162,163] is employed here to compute $\mathcal{D}_{i,j}$ and $k_{i,T}$, and is also explained in Appendix F. That methodology accounts for real-gas effects and has been satisfactorily compared against experimental data involving liquid and gas mixtures of alkanes, CO_2, and N_2 [164–166].

The temperature and composition dependence of η, λ, $\mathcal{D}_{F,O}$, and $k_{F,T}$ for $C_{12}H_{26}/N_2$ mixtures at high pressures is shown in Fig. B.3. In N_2-rich mixtures, η, λ, and $\mathcal{D}_{F,O}$ increase monotonically with temperature in a manner that is reminiscent of that encountered in gases, since the range of temperatures studied here is well above the critical temperature of nitrogen. A similar behavior is also observed in $C_{12}H_{26}$-rich mixtures at sufficiently high temperatures, and more particularly, at temperatures much larger than the critical temperature of $C_{12}H_{26}$.

By definition, the thermal-diffusion ratio of $C_{12}H_{26}$, $k_{F,T}$, becomes zero in the limits $Y_F = 0$ and $Y_F = 1$ corresponding to pure components. At intermediate concentrations and high temperatures, $k_{F,T}$ decays to small values as a result of the particular model employed here, in which $k_{F,T}$ is proportional to the energy-departure function (see Ref. [167] and Appendix F). Linear superposition of the high-pressure model of $k_{F,T}$ in Ref. [167] with the ideal-gas counterpart from kinetic theory [140] would likely yield more realistic values at high temperatures, as suggested by the comparisons between different models in Ref. [168].

The positive values $k_{F,T} \geq 0$ observed in all cases indicate that $C_{12}H_{26}$ tends to migrate toward cold flow zones, thereby sharpening the transcritical interface. Despite the fact that $k_{F,T}$ is an order-unity parameter at high pressures, the contribution of the Soret effect to the species diffusion flux is only fractional compared to the contribution of the composition gradients because of the comparatively smaller temperature gradients across the interface, as discussed in Section 5.6.

A significant change in the temperature dependence of η, λ, and $\mathcal{D}_{F,O}$ is observed in $C_{12}H_{26}$-rich mixtures near ambient temperatures. In particular, it is found that μ and λ increase as T decreases, while $\mathcal{D}_{F,O}$ attains values that are mostly independent of temperature. The aforementioned trends are typical of liquids, and suggest that $C_{12}H_{26}$-rich mixtures behave in a liquid-like manner at high pressures and ambient temperatures. Those correspond to typical conditions in the fuel injection port. This shift in the trend of the transport coefficients is accompanied by a maximum in $k_{F,T}$ at intermediate concentrations, and occurs at a pressure-dependent temperature that is well correlated with the pseudo-boiling one corresponding to the maximum molar heat capacity.

Appendix C. Supplementary thermodynamic expressions applicable to multicomponent systems at high pressures

Despite the gradient corrections used in the thermodynamic potentials (16)–(18), the classic theory of thermodynamics must still be locally satisfied. A number of standard thermodynamic relations are listed in this appendix for use in the analysis. In addition, the formulation of thermodynamic systems at high pressures requires complex equations of state. Quantities including thermodynamic potentials, specific heats, volume expansivity and others are involved in the diffuse-interface formulation described above and depend on the particular form of the equation of state. This appendix provides a summary of expressions for those quantities. A number of relations are particularized for the Peng-Robinson equation of state (14), whose coefficients are also listed here, but general definitions are given as well that allow for utilization of other equations of state by direct substitution. Closure parameters for the gradient-energy coefficient (23) are also supplied here.

C1. Local thermodynamic relations

The first principle of thermodynamics

$$Tds = de + Pd(1/\rho) - \sum_{i=1}^{N-1}(\mu_i - \mu_N)dY_i, \tag{C.1}$$

or its alternative form

$$Tds = dh - \frac{dP}{\rho} - \sum_{i=1}^{N-1}(\mu_i - \mu_N)dY_i, \tag{C.2}$$

are both satisfied locally, with h denoting the specific enthalpy

$$h = e + P/\rho, \tag{C.3}$$

which will be shown to be an exclusively local quantity in this formulation under the approximation (24). In writing Eqs. (C.1) and (C.2), the mass conservation constraint $dY_N = -\sum_{i=1}^{N-1} dY_i$ has been used. Equations (C.1) and (C.2) can be recast in terms of the local specific Helmholtz free energy f as

$$df = -sdT - Pd(1/\rho) + \sum_{i=1}^{N-1}(\mu_i - \mu_N)dY_i, \tag{C.4}$$

or in terms of the local specific Gibbs free energy, or local specific chemical potential of the mixture μ, as

$$d\mu = -sdT + \frac{dP}{\rho} + \sum_{i=1}^{N-1}(\mu_i - \mu_N)dY_i, \tag{C.5}$$

with

$$\mu = h - Ts. \tag{C.6}$$

The combination of Eqs. (19), (C.3) and (C.6) leads to

$$\mu - f = P/\rho. \tag{C.7}$$

In addition, an alternative definition of μ can be given in terms of the weighted sum of partial specific chemical potentials μ_i as

$$\mu = \sum_{i=1}^{N} Y_i\mu_i, \tag{C.8}$$

with μ_i being related to its corresponding partial molar value $\bar{\mu}_i$ as $\mu_i = \bar{\mu}_i/W_i$. Equation (C.8) can be substituted into Eq. (C.5) yielding the Gibbs-Duhem relation

$$\sum_{i=1}^{N} Y_i d\mu_i = -sdT + \frac{dP}{\rho}. \tag{C.9}$$

Interfacial effects are incorporated in the above relations in Section 5 leading to important modifications of the constitutive laws in the Navier-Stokes equations.

C2. Coefficients of the Peng-Robinson equation of state

The individual coefficients a_i and b_i in the mixing rules (15) for the Peng-Robinson equation of state are given by [92]

$$a_i = 0.457\frac{\left(\mathrm{R}^0 T_{c,i}\right)^2}{P_{c,i}}\left[1 + c_i\left(1 - \sqrt{T/T_{c,i}}\right)\right]^2, \tag{C.10}$$

$$b_i = 0.078\frac{\mathrm{R}^0 T_{c,i}}{P_{c,i}}, \tag{C.11}$$

where $P_{c,i}$ and $T_{c,i}$ are, respectively, critical pressures and temperatures obtained from Table 1. Additionally, the coefficients c_i are defined as

$$c_i = \begin{cases} 0.380 + 1.485\omega_i - 0.164\omega_i^2 + 0.017\omega_i^3 & \text{if } \omega_i > 0.49, \\ 0.375 + 1.542\omega_i - 0.270\omega_i^2 & \text{otherwise,} \end{cases} \tag{C.12}$$

with ω_i as the acentric factor. The values of ω_i used in this study are [40]

$$\omega_{\mathrm{N_2}} = 0.037, \quad \omega_{\mathrm{O_2}} = 0.022, \quad \omega_{\mathrm{CO_2}} = 0.224,$$
$$\omega_{\mathrm{CH_4}} = 0.011, \quad \omega_{\mathrm{C_7H_{16}}} = 0.349, \quad \omega_{\mathrm{C_{12}H_{26}}} = 0.574. \tag{C.13}$$

The binary-interaction parameters $\vartheta_{i,j}$ utilized in Eq. (15) are [75,157]

$$\vartheta_{\mathrm{F,O}} = 0.156 \tag{C.14}$$

for mixtures of alkanes with $\mathrm{N_2}$ or $\mathrm{O_2}$, and

$$\vartheta_{\mathrm{F,O}} = -0.017 \tag{C.15}$$

for mixtures of $\mathrm{CO_2}$ with $\mathrm{N_2}$ or $\mathrm{O_2}$. Additionally, the binary-interaction parameter of an element with itself is assumed to be zero,

$$\vartheta_{\mathrm{F,F}} = \vartheta_{\mathrm{O,O}} = 0. \tag{C.16}$$

C3. Parameters of the model for the gradient-energy coefficient

The dimensionless coefficients $\mathcal{A}_i$ and $\mathcal{B}_i$ in the model expression for the gradient-energy coefficient (23) are given by [120]

$$\mathcal{A}_i = -10^{-16}N_A^{2/3}/(1.233 + 1.376\omega_i), \tag{C.17}$$

$$\mathcal{B}_i = 10^{-16}N_A^{2/3}/(0.905 + 1.541\omega_i), \tag{C.18}$$

where the acentric factors ω_i for dodecane and nitrogen are given by Eq. (C.13).

C4. Molar Helmholtz free energy and chemical potential

The molar Helmholtz free energy and chemical potential corresponding to the Peng-Robinson equation of state (14) are

$$\bar{f} = \bar{f}^{\mathrm{IG}} - \mathrm{R}^0 T\ln\left[\frac{P(v-b)}{R^0T}\right] + \frac{a}{2\sqrt{2}b}\ln\left[\frac{v + \left(1-\sqrt{2}\right)b}{v + \left(1+\sqrt{2}\right)b}\right] \tag{C.19}$$

and

$$\bar{\mu} = \bar{f} + Pv = \bar{\mu}^{\mathrm{IG}} - \mathrm{R}^0 T\left\{1 + \ln\left[\frac{P(v-b)}{R^0T}\right] - \frac{v}{v-b}\right\}$$
$$+ \frac{a}{2\sqrt{2}b}\left\{\ln\left[\frac{v + \left(1-\sqrt{2}\right)b}{v + \left(1+\sqrt{2}\right)b}\right] - \frac{2\sqrt{2}bv}{v^2 + 2vb - b^2}\right\}, \tag{C.20}$$

Table C.1
Coefficients for the evaluation of the ideal-gas specific heats, entropies, enthalpies and Gibbs free energies for selected species [151].

Species	$r_{1,i}$ [-]	$r_{2,i}$ [K^{-1}]	$r_{3,i}$ [K^{-2}]	$r_{4,i}$ [K^{-3}]	$r_{5,i}$ [K^{-4}]	$r_{6,i}$ [K]	$r_{7,i}$ [-]
$C_{12}H_{26}$	2.133×10^{1}	-3.864×10^{-2}	3.995×10^{-4}	-5.067×10^{-7}	2.007×10^{-10}	-4.225×10^{4}	-4.858×10^{1}
N_2	3.531	-1.237×10^{-4}	-5.030×10^{-7}	2.435×10^{-9}	-1.409×10^{-12}	-1.047×10^{3}	2.967

respectively. In the notation, $\bar{f}^{\mathrm{IG}} = \bar{\mu}^{\mathrm{IG}} - \mathrm{R}^0 T$ is the molar Helmholtz free energy of an ideal-gas mixture, where

$$\bar{\mu}^{\mathrm{IG}} = \sum_{i=1}^{N} X_i \left[\bar{g}_i^0(P^0, T) + \mathrm{R}^0 T \ln(X_i P / P^0) \right] \tag{C.21}$$

is the corresponding chemical potential and $\bar{g}_i^0$ is the ideal-gas molar Gibbs free energy of species i defined in Appendix Appendix C at a reference pressure P^0.

C5. Volume expansivity

The volume expansivity (B.7) can be expressed as

$$\beta_v = \frac{1}{v}\left(\frac{\partial v}{\partial T}\right)_{P,X_{i|i=1,\dots N-1}} = \frac{1}{v}\left(\frac{\partial T}{\partial v}\right)^{-1}_{P,X_{i|i=1,\dots N-1}} = \frac{\mathrm{R}^0}{v}\left[P - \frac{a(v^2 - 2bv + b^2)}{(v^2 + 2bv - b^2)^2}\right]^{-1} \tag{C.22}$$

for the Peng-Robinson equation of state (14).

C6. Enthalpy departure function

The enthalpy departure function (B.12) particularized for the Peng-Robinson equation of state is [92]

$$\Delta_d \bar{h} = \bar{h} - \bar{h}^{\mathrm{IG}} = Pv - \mathrm{R}^0 T + \frac{1}{2\sqrt{2}b}\left[a - T\left(\frac{\partial a}{\partial T}\right)_{X_{i|i=1,\dots N-1}}\right] \ln\left[\frac{v + (1-\sqrt{2})b}{v + (1+\sqrt{2})b}\right], \tag{C.23}$$

where

$$\left(\frac{\partial a}{\partial T}\right)_{X_{i|i=1,\dots N-1}} = \frac{1}{2}\sum_{i=1}^{N}\sum_{j=1}^{N} \frac{X_i X_j a_{i,j}}{a_i a_j}\left[a_i\left(\frac{da_j}{dT}\right) + a_j\left(\frac{da_i}{dT}\right)\right], \tag{C.24}$$

while the coefficients a and b are obtained by combining Eqs. (15) and (C.10)–(C.12). For a given specific volume and composition field, P and T are related in Eq. (C.23) through the equation of state (14).

C7. Molar heats, adiabatic coefficient, and isentropic compressibility

The ideal-gas constant-pressure molar heat of species i is given by [151]

$$\bar{c}_{p,i}^{\mathrm{IG}} = \left(\frac{\partial \bar{h}_i^{\mathrm{IG}}}{\partial T}\right)_{P,X_{j|j=1,\dots N-1 \atop (j\neq i)}} = \mathrm{R}^0\left(r_{1,i} + r_{2,i}T + r_{3,i}T^2 + r_{4,i}T^3 + r_{5,i}T^4\right), \tag{C.25}$$

where the coefficients $r_{1,i}$, $r_{2,i} \dots r_{5,i}$ are listed in Table C.1 209for $C_{12}H_{26}$ and N_2. The corresponding value of the constant-volume molar heat for an ideal gas can be easily derived by substituting Eq. (C.25) into the Mayer's relation

$$\bar{c}_{v,i}^{\mathrm{IG}} = \bar{c}_{p,i}^{\mathrm{IG}} - \mathrm{R}^0. \tag{C.26}$$

The ideal-gas adiabatic coefficient of the mixture is defined as

$$\gamma^{\mathrm{IG}} = \bar{c}_p^{\mathrm{IG}} / \bar{c}_v^{\mathrm{IG}}, \tag{C.27}$$

with $\bar{c}_p^{\mathrm{IG}} = \sum_{i=1}^{N} X_i \bar{c}_{p,i}^{\mathrm{IG}}$ and $\bar{c}_v^{\mathrm{IG}} = \sum_{i=1}^{N} X_i \bar{c}_{v,i}^{\mathrm{IG}}$ being the ideal-gas specific heats of the mixture.

The real-gas constant-pressure molar heat of the mixture for the Peng-Robinson equation of state (14) is obtained by substituting Eq. (C.23) into Eq. (B.9), which gives [103]

$$\bar{c}_p = \left(\frac{\partial \bar{h}}{\partial T}\right)_{P,X_{i|i=1,\dots N-1}} = \bar{c}_p^{\mathrm{IG}} + \mathrm{R}^0(Z-1) + \mathrm{R}^0 T\left(\frac{\partial Z}{\partial T}\right)_{P,X_{i|i=1,\dots N-1}} + \frac{\partial}{\partial T}\left\{\left[\frac{a - T\left(\frac{\partial a}{\partial T}\right)_{X_{i|i=1,\dots N-1}}}{2\sqrt{2}b}\right] \ln\left[\frac{v + (1-\sqrt{2})b}{v + (1+\sqrt{2})b}\right]\right\}_{P,X_{i|i=1,\dots N-1}}. \tag{C.28}$$

In this formulation, $Z = Pv/\mathrm{R}^0 T$ is the compressibility factor. Its derivative with respect to temperature is given by

$$\left(\frac{\partial Z}{\partial T}\right)_{P,X_{i|i=1,\dots N-1}} = \left[3Z^2 + 2(B-1)Z + (A - 2B - 3B^2)\right]^{-1} \times \left\{\frac{P}{(\mathrm{R}^0 T)^2}\left[\left(\frac{\partial a}{\partial T}\right)_{X_{i|i=1,\dots N-1}} - \frac{2a}{T}\right](B - Z) - \frac{bP}{\mathrm{R}^0 T^2}\left(6BZ + 2Z - 3B^2 - 2B + A - Z^2\right)\right\}, \tag{C.29}$$

where $A = aP/(\mathrm{R}^0 T)^2$ and $B = bP/(\mathrm{R}^0 T)$. The partial derivative $(\partial a/\partial T)_{X_{i|i=1,\dots N-1}}$ in Eq. (C.29) can be calculated by combining Eqs. (C.10) and (C.24).

An expression for the real-gas constant-volume molar heat of the mixture for the Peng-Robinson equation of state (14) can be derived by substituting Eqs. (C.28) and (C.22), along with the isothermal compressibility β_{T} introduced below in Eq. (C.44), into the fundamental equation for the heat capacities

$$\bar{c}_v = \bar{c}_p - \frac{T v \beta_v^2}{\beta_{\mathrm{T}}}, \tag{C.30}$$

which is obtained by substituting the identity $(\partial P/\partial T)_{v,X_{i|i=1,\dots N-1}} = (\bar{c}_p - \bar{c}_v)/(Tv\beta_v)$ into Eq. (E.5). Correspondingly, the adiabatic coefficient for a real gas, defined here as the ratio of molar heats, can be calculated as

$$\gamma = \frac{\bar{c}_p}{\bar{c}_v} = \frac{\beta_{\mathrm{T}}}{\beta_s}, \tag{C.31}$$

with

$$\beta_s = -\frac{1}{v}\left(\frac{\partial v}{\partial P}\right)_{s,X_{i|i=1,\dots N-1}} = \beta_{\mathrm{T}} - \frac{T v \beta_v^2}{\bar{c}_p} \tag{C.32}$$

being the isentropic compressibility.

C8. Partial molar enthalpies and partial-enthalpy departure functions

The partial molar enthalpy $\overline{h}_i^{\mathrm{IG}}$ of an ideal gas referred to the standard reference state can be expressed as the polynomial expansion

$$\overline{h}_i^{\mathrm{IG}} = \mathrm{R}^0 T\left(r_{1,i} + r_{2,i}\frac{T}{2} + r_{3,i}\frac{T^2}{3} + r_{4,i}\frac{T^3}{4} + r_{5,i}\frac{T^4}{5} + \frac{r_{6,i}}{T}\right), \tag{C.33}$$

where the coefficients $r_{1,i}$, $r_{2,i}\dots r_{6,i}$ are listed in Table C.1 for $C_{12}H_{26}$ and N_2 [151]. Note that Eq. (C.33) is equivalent to substituting the polynomial expansion of the specific heat (C.25) into the definition $\overline{h}_i^{\mathrm{IG}} = \overline{h}_{f,i}^{298\,\mathrm{K}} + \int_{298\,\mathrm{K}}^{T} \overline{c}_{p,i}^{\mathrm{IG}} dT$. The coefficient $\mathrm{R}^0 r_{6,i} = \overline{h}_{f,i}^{298\,\mathrm{K}} - \int_0^{298\,\mathrm{K}} \overline{c}_{p,i}^{\mathrm{IG}} dT$ is a constant employed to refer the enthalpy to the formation value $\overline{h}_i^{\mathrm{IG}} = \overline{h}_{f,i}^{298\,\mathrm{K}}$.

The departure function of the partial molar enthalpy of a real gas described by the Peng-Robinson equation of state (14) is given by [153]

$$\begin{aligned}\Delta_d \overline{h}_i = &\left[\frac{\partial(n\Delta_d \overline{h})}{\partial n_i}\right]_{\substack{P,n_{j|j=1,\dots N}\\(j\neq i)}} = P\bar{\mathcal{V}}_i - \mathrm{R}^0 T \\ &+ \left[a - T\left(\frac{\partial a}{\partial T}\right)_{X_{i|i=1,\dots N-1}}\right]\frac{\bar{\mathcal{V}}_i - \nu b_i/b}{\nu^2 + 2b\nu - b^2} \\ &+ \frac{1}{2\sqrt{2}b}\ln\left[\frac{\nu + (1-\sqrt{2})b}{\nu + (1+\sqrt{2})b}\right]\left\{\left(\frac{\partial a}{\partial X_i}\right)_{\substack{T,X_{j|j=1,\dots N-1}\\(j\neq i)}} \right. \\ &\left. - T\left(\frac{\partial^2 a}{\partial X_i \partial T}\right)_{\substack{X_{j|j=1,\dots N-1}\\(j\neq i)}} - \left[a - T\left(\frac{\partial a}{\partial T}\right)_{X_{i|i=1,\dots N-1}}\right]\frac{b_i}{b}\right\}.\end{aligned} \tag{C.34}$$

In Eq. (C.34), the quantity $(\partial a/\partial T)_{X_{i|i=1,\dots N-1}}$ can be obtained using Eq. (C.24), whereas the remaining partial derivatives are calculated as

$$\left(\frac{\partial a}{\partial X_i}\right)_{\substack{T,X_{j|j=1,\dots N-1}\\(j\neq i)}} = 2\sum_{j=1}^{N} X_j a_{i,j}, \tag{C.35}$$

$$\left(\frac{\partial^2 a}{\partial X_i \partial T}\right)_{\substack{X_{j|j=1,\dots N-1}\\(j\neq i)}} = \sum_{j=1}^{N} X_j \frac{a_{i,j}}{a_i a_j}\left[a_i\left(\frac{da_j}{dT}\right) + a_j\left(\frac{da_i}{dT}\right)\right]. \tag{C.36}$$

The partial-enthalpy departure function (C.34) is a sole function of P when the values of the specific volume and molar fractions are fixed, since pressure and temperature are related through the equation of state (14).

C9. Internal-energy departure function

Using the definition

$$\overline{e} = \overline{h} - P\nu, \tag{C.37}$$

the internal molar energy $\overline{e}$ can be computed at high pressures after obtaining $\overline{h}$ from Eq. (B.9). Similarly, its ideal-gas counterpart $\overline{e}^{\mathrm{IG}}$ can be expressed as

$$\overline{e}^{\mathrm{IG}} = \overline{h}^{\mathrm{IG}} - \mathrm{R}^0 T, \tag{C.38}$$

where $\overline{h}^{\mathrm{IG}}$ is the ideal-gas enthalpy defined in Eq. (B.10). Correspondingly, the departure function for the molar internal energy is

$$\Delta_d \overline{e} = \overline{e} - \overline{e}^{\mathrm{IG}} = \Delta_d \overline{h} + \mathrm{R}^0 T(1 - Z), \tag{C.39}$$

with $\Delta_d \overline{h}$ being provided in Eq. (C.23) for the Peng-Robinson equation of state (14).

C10. Partial molar internal energies

The partial molar internal energy of an ideal gas $\overline{e}_i^{\mathrm{IG}}$ referred to the standard reference state can be expressed as

$$\overline{e}_i^{\mathrm{IG}} = \overline{h}_i^{\mathrm{IG}} - \mathrm{R}^0 T, \tag{C.40}$$

where $\overline{h}_i^{\mathrm{IG}}$ is the partial molar enthalpy obtained from the polynomial expansion (C.33). By definition, the partial molar internal energy of a real gas is related to the partial molar enthalpy as

$$\overline{e}_i = \overline{h}_i - P_i \nu_i, \tag{C.41}$$

with $P_i = X_i P$ and $\nu_i = \nu/X_i$. The combination of Eqs. (C.40) and (C.41) yields the departure function of the partial molar internal energy

$$\Delta_d \overline{e}_i = \overline{e}_i - \overline{e}_i^{\mathrm{IG}} = \Delta_d \overline{h}_i + \mathrm{R}^0 T(1 - Z), \tag{C.42}$$

where $\Delta_d \overline{h}_i$ is the departure function of the partial molar enthalpy provided in Eq. (C.34) for the Peng-Robinson equation of state (14).

C11. Partial molar volume and isothermal compressibility

The partial molar volume is given by [92]

$$\begin{aligned}\bar{\mathcal{V}}_i = \left(\frac{\partial V}{\partial n_i}\right)_{\substack{P,T,n_{j|j=1,\dots N}\\(j\neq i)}} = \nu\beta_{\mathrm{T}}&\left[\frac{\mathrm{R}^0 T}{\nu - b} + \frac{\mathrm{R}^0 T b_i}{(\nu - b)^2}\right. \\ &\left. + \frac{2a(\nu - b)b_i}{\left(\nu^2 + 2b\nu - b^2\right)^2} - \frac{2\sum_{j=1}^{N} X_j a_{i,j}}{\nu^2 + 2b\nu - b^2}\right]\end{aligned} \tag{C.43}$$

for the Peng-Robinson equation of state (14). In Eq. (C.43), β_{T} is an isothermal compressibility that can be calculated as

$$\begin{aligned}\beta_{\mathrm{T}} = -\frac{1}{\nu}\left(\frac{\partial \nu}{\partial P}\right)_{T,X_{i|i=1,\dots N-1}} &= -\frac{1}{\nu}\left(\frac{\partial P}{\partial \nu}\right)^{-1}_{T,X_{i|i=1,\dots N-1}} \\ &= \frac{1}{\nu}\left[\frac{\mathrm{R}^0 T B_{\mathrm{T}}}{(\nu - b)^2}\right]^{-1},\end{aligned} \tag{C.44}$$

with B_{T} being a dimensionless variable defined as

$$B_{\mathrm{T}} = 1 - \frac{2a}{(\nu + b)\mathrm{R}^0 T\left[\nu/(\nu - b) + b/(\nu + b)\right]^2}. \tag{C.45}$$

C12. Ideal-gas Gibbs free energies

The molar Gibbs free energy of an ideal gas at the reference pressure $P^0 = 1$ atm is [151]

$$\frac{\bar{g}_i^0}{\mathrm{R}^0 T} = r_{1,i}(1 - \ln T) - r_{2,i}\frac{T}{2} - r_{3,i}\frac{T^2}{6} - r_{4,i}\frac{T^3}{12} - r_{5,i}\frac{T^4}{20} + \frac{r_{6,i}}{T} - r_{7,i}, \tag{C.46}$$

where the coefficients $r_{1,i}$, $r_{2,i}\dots r_{7,i}$ are listed in Table C.1 for $C_{12}H_{26}$ and N_2.

C13. Fugacity coefficients

The logarithm of the fugacity coefficient φ_i is [103]

$$\ln\varphi_i = \frac{b_i}{b}\left(\frac{Pv}{\mathrm{R}^0T}-1\right) - \ln\left[\frac{P}{\mathrm{R}^0T}(v-b)\right] + \frac{a}{2\sqrt{2}b\mathrm{R}^0T}\left[\frac{2\left(\sum_{j=1}^{N}X_j a_{i,j}\right)}{a}-\frac{b_i}{b}\right]\ln\left[\frac{v+\left(1-\sqrt{2}\right)b}{v+\left(1+\sqrt{2}\right)b}\right] \tag{C.47}$$

for the Peng-Robinson equation of state (14).

C14. Speed of sound

The speed of sound c of a real gas is given by

$$c = \sqrt{\left(\frac{\partial P}{\partial\rho}\right)_{s,X_{i|i=1,\dots N-1}}} = (\rho\beta_s)^{-1/2}, \tag{C.48}$$

where β_s is the isothermal compressibility defined in Eq. (C.32).

Appendix D. High-pressure interfaces in subcritical monocomponent systems

This appendix focuses on interfaces arising in monocomponent systems. In this case, interfaces can only emerge at pressures and temperatures below the critical point, where two thermodynamic states are possible at the same pressure. The resulting system is therefore subcritical everywhere. Nonetheless, only relatively high pressures not too far from the critical point can be considered because of the continuum assumption, as emphasized in Section 4.5. Further details on the utilization of diffuse-interface concepts in monocomponent systems can be found in a number of previous investigations [53,111,149,168,169] and in van der Waals' original contribution [108].

D1. Formulation

Similar arguments to the ones made in Section 4.4 for conceptualizing the diffuse-interface formalism as a thermodynamic-to-physical space mapping of the oscillations of the chemical potential also apply to the pressure variations within the interface. To illustrate this, consider the simplified form of the mechanical equilibrium condition (120) for $N=1$,

$$P_\infty - P + \rho\kappa\frac{d^2\rho}{d\hat{n}^2} - \frac{1}{2}\kappa\left(\frac{d\rho}{d\hat{n}}\right)^2 = 0, \tag{D.1}$$

subject to the phase-equilibrium densities

$$\rho\to\rho_e^\ell \quad \text{at} \quad \hat{n}\to-\infty, \tag{D.2}$$

$$\rho\to\rho_e^g \quad \text{at} \quad \hat{n}\to+\infty. \tag{D.3}$$

Similarly to Eq. (31) for the chemical potential in systems in phase equilibrium, Eq. (D.1) maps the pressure oscillations from thermodynamic space into a thin interface in physical space. The oscillation of the pressure in thermodynamic space is induced by the equation of state (14) evaluated in conditions where two phases exist, as sketched in Fig. 18(c) for the simplest case corresponding to a flat interface in phase equilibrium. In that case, a Maxwell's construction rule for P can be obtained by integrating Eq. (28) and using Eq. (C.7) subject to the phase-equilibrium condition (A.16), which gives

$$\frac{1}{W}\int_{v_e^\ell}^{v_e^g}(P-P_\infty)dv = \int_{\rho_e^g}^{\rho_e^\ell}(P-P_\infty)\frac{d\rho}{\rho^2}$$

Table D.1
Dimensional formulation for high-pressure subcritical interfaces in isothermal monocomponent systems.

Conservation equation	
Mechanical equilibrium	$P_\infty - P + \rho\kappa\frac{d^2\rho}{d\hat{n}^2} - \frac{1}{2}\kappa\left(\frac{d\rho}{d\hat{n}}\right)^2 = 0.$
Boundary conditions	
Phase-equilibrium densities	$\rho\to\rho_e^\ell$ at $\hat{n}\to-\infty$, $\rho\to\rho_e^g$ at $\hat{n}\to+\infty$.
Supplementary expressions	
Equation of state	Eq. (14),
Coefficients of the equation of state	Eqs. (C.10)–(C.12),
Gradient-energy coefficient	Eqs. (23), (C.17), and (C.18).

$$= f_e^\ell - f_e^g + P_\infty\left(\frac{1}{\rho_e^\ell}-\frac{1}{\rho_e^g}\right) = 0, \tag{D.4}$$

with f_e^g and f_e^l being the phase-equilibrium Helmholtz free energies. Equation (D.4) indicates that the oscillation of the pressure encloses zero net area along the v axis. In contrast, Eq. (108) states that the net area under the oscillation of the pressure in physical space is non-zero and is proportional to the surface tension. It can be shown that the mechanical equilibrium condition (D.1) is consistent with Maxwell's construction rule (D.4) by substituting the former into the latter and using the identity

$$\int_{-\infty}^{+\infty}\left[\rho\frac{d^2\rho}{d\hat{n}^2}-\frac{1}{2}\left(\frac{d\rho}{d\hat{n}}\right)^2\right]\frac{1}{\rho^2}\left(\frac{d\rho}{d\hat{n}}\right)d\hat{n} = \left[\frac{1}{2\rho}\left(\frac{d\rho}{d\hat{n}}\right)^2\right]_{\hat{n}\to-\infty}^{\hat{n}\to+\infty} = 0, \tag{D.5}$$

as prescribed by the vanishing gradients of the density away from the interface. Analogous oscillatory profiles of P are observed in bicomponent systems, as shown in Section 6.

The origin of Eq. (31) anticipated in Section 4.4, which relates the chemical potential with the density gradients through the interface, is the mechanical equilibrium condition for monocomponent flows (D.1) evaluated at uniform temperature. In this particular case, Eqs. (31) and (D.1) are equivalent, as easily shown by evaluating Eq. (121) for $N=1$, which gives

$$\frac{d\mu}{d\hat{n}} = \kappa\frac{\partial^3\rho}{\partial\hat{n}^3}. \tag{D.6}$$

Eq. (D.6) can be integrated once subject to the phase-equilibrium boundary condition $\mu=\mu_e$ at $\hat{n}\to+\infty$, thus leading to Eq. (31).

The equations integrated in this appendix are summarized in Table D.1 and consist of the mechanical equilibrium condition for monocomponent systems (D.1) supplemented with the equation of state (14) and the model (23) for the gradient-energy coefficient. The numerical results are obtained by solving the system of equations on uniform 1D meshes with approximately 50–75 grid points across the interface. The boundary conditions away from the interface correspond to phase-equilibrium densities (D.2) and (D.3). The problem has a solution consisting of a steady high-pressure subcritical interface that separates a liquid from its vapor in phase equilibrium.

The isothermal cases summarized in Table D.2 for $C_{12}H_{26}$ and N_2 are considered here. In all cases, the temperature T_e and the thermodynamic pressure away from the interface P_∞ are smaller than their corresponding critical values T_c and P_c. As a result, the pseudo-trajectories along the interface in thermodynamic space are subcritical and traverse the coexistence region, as shown in Fig. D.1.

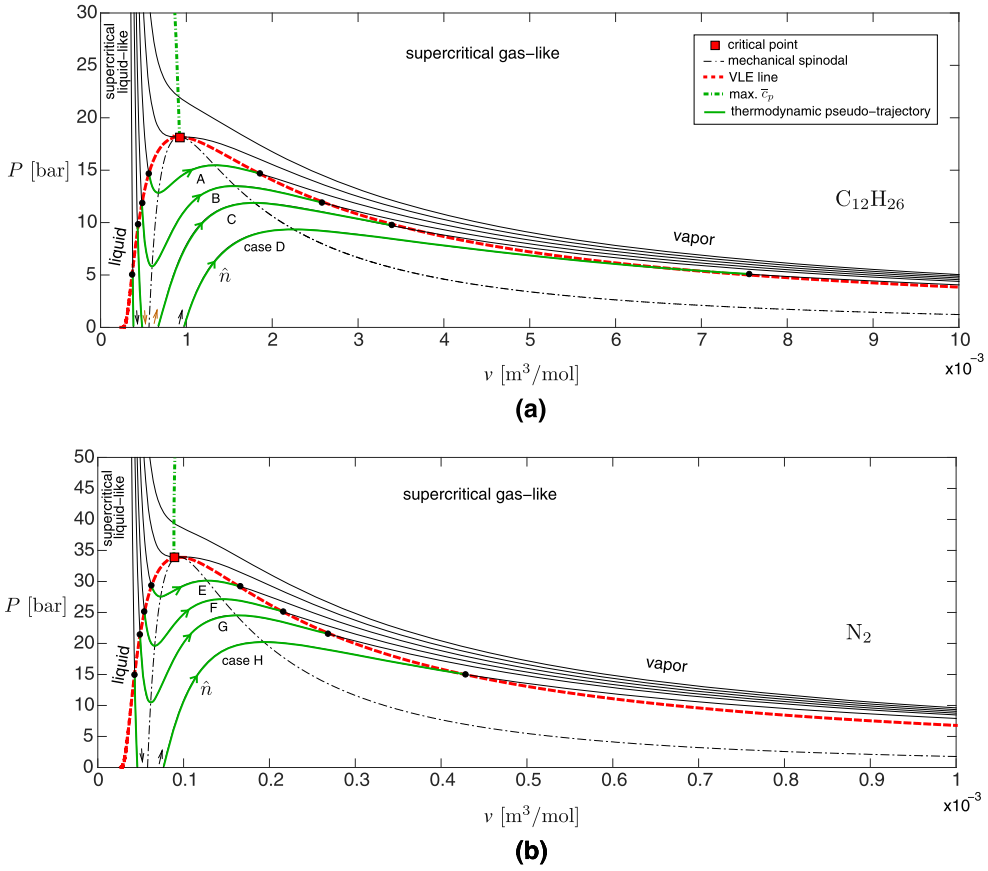

Fig. D.1. Thermodynamic pseudo-trajectories of cases A-H listed in Table D.2 for (a) dodecane and (b) nitrogen subcritical isothermal systems. The portion of the pseudo-trajectories involving negative pressures is not plotted in these diagrams.

Table D.2
Thermodynamic conditions corresponding to cases A-H in Fig. D.1 for subcritical interfaces in monocomponent systems.

			$C_{12}H_{26}$ system			
case	P_∞ [bar]	T_e [K]	$\rho_e^\ell \left[\frac{\text{kg}}{\text{m}^3}\right]$	$\rho_e^g \left[\frac{\text{kg}}{\text{m}^3}\right]$	$\frac{P_\infty}{P_c}$	$\frac{T_e}{T_c}$
A	14.6	641.6	302.0	92.0	0.816	0.975
B	11.7	625.2	353.8	63.2	0.652	0.950
C	9.3	608.7	393.1	46.4	0.516	0.925
D	5.5	575.8	453.0	25.4	0.310	0.875
			N_2 system			
case	P_∞ [bar]	T_e [K]	$\rho_e^\ell \left[\frac{\text{kg}}{\text{m}^3}\right]$	$\rho_e^g \left[\frac{\text{kg}}{\text{m}^3}\right]$	$\frac{P_\infty}{P_c}$	$\frac{T_e}{T_c}$
E	29.2	123.0	446.9	170.9	0.861	0.975
F	25.1	119.9	514.8	129.6	0.738	0.950
G	21.3	116.7	567.7	102.1	0.628	0.925
H	15.1	110.4	651.6	65.9	0.444	0.875

D2. Results

The profiles of density and pressure obtained from integrating the formulation in Table D.1 are provided in Fig. D.2. Density ratios of order 10 are observed in cases D and H, which correspond to the farthest conditions from the critical point. As the critical point is approached, the density and pressure profiles become increasingly flat. This limiting behavior is accompanied by (a) an increase of the interface thickness δ_I [defined in Eq. (208)] and a decrease in the Knudsen number [Eq. (40)], as shown in Fig. D.3, along with (b) a decrease in the surface-tension coefficient [Eq. (22)], as shown in Fig. D.4. The Knudsen number attains acceptable values for the continuum range only when conditions are close to the critical point. The interface disappears and the surface tension vanishes when the critical point is reached.

Figure D.4 shows comparisons between the surface-tension coefficient calculated by utilizing the numerical solution in Eq. (22) and the standard correlation [170]

$$\sigma = P_c^{2/3} T_c^{1/3} \frac{1.86 + 1.18\omega}{19.05} \times \left[\frac{3.75 - 0.91\omega}{0.291 - 0.08\omega}\right]^{2/3} \left(1 - \frac{T}{T_c}\right)^{11/9} \quad [\text{mN/m}] \tag{D.7}$$

[see also Eq. (12-3.7) in Ref. [54]], with ω being the acentric factor provided in Appendix Appendix C. Whereas good agreement is observed in the case of nitrogen over the entire range of tested conditions, the comparison reveals disagreements of order 20%-30% for dodecane. These discrepancies are caused by the relatively large accentric factor of dodecane, for which the standard correlation is not designed to operate accurately [54]. In contrast, the nu-

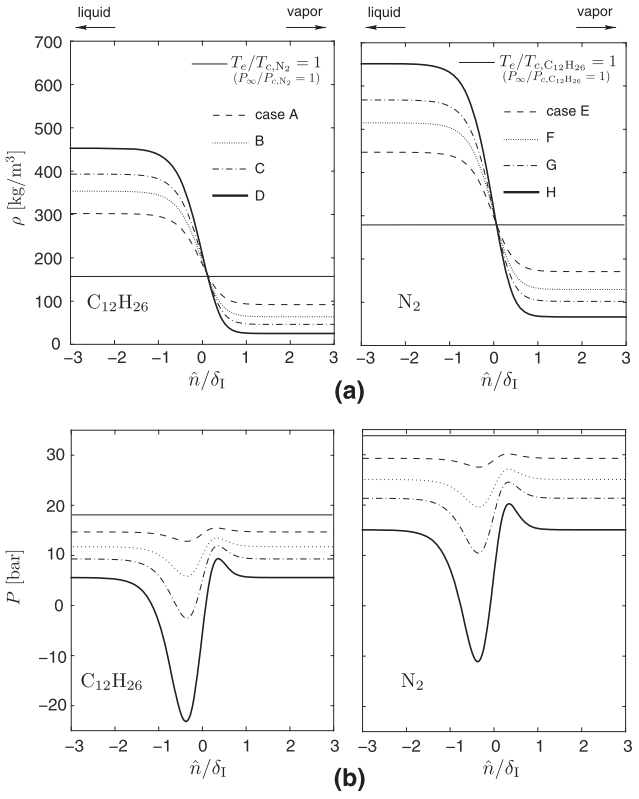

Fig. D.2. Profiles of (a) density and (b) pressure across the interface in isothermal systems composed of dodecane (left panels) and nitrogen (right panels). In dodecane systems, the interface thicknesses used for normalizing the spatial coordinate are $\delta_I = 4.98$ nm, 3.59 nm, 2.91 nm, and 2.18 nm for cases A, B, C, and D, respectively. In nitrogen systems, the corresponding values are $\delta_I = 4.55$ nm, 3.07 nm, 2.42 nm, and 1.77 nm for cases E, F, G, and H, respectively.

merical solution agrees well with experimental data in Refs. [72–74]. Remarkably, the agreements between experiments and numerical results occur even at conditions far away from the critical point, where the continuum hypothesis across the interface becomes hardly justifiable.

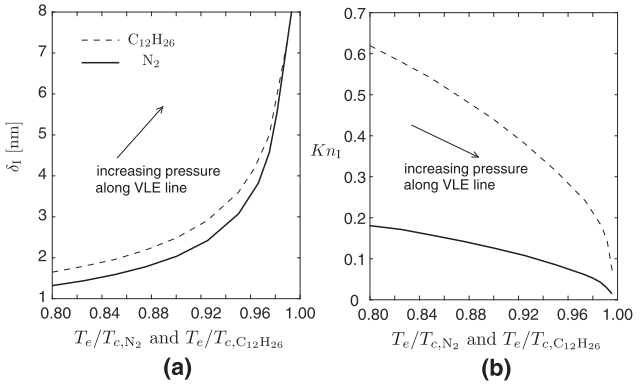

Fig. D.3. Variations of (a) the interface thickness and (b) Knudsen number as a function of the temperature nondimensionalized with the critical temperature of the corresponding component.

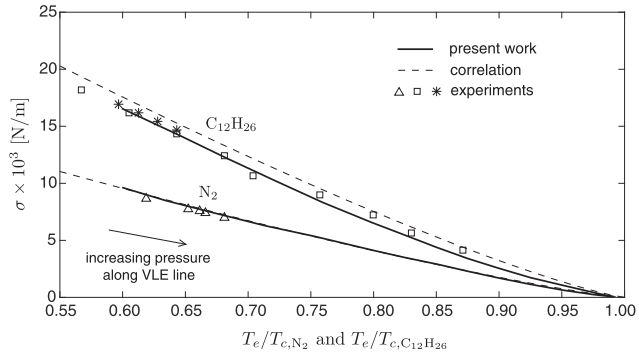

Fig. D.4. Surface-tension coefficient as a function of normalized temperature in monocomponent isothermal systems consisting of nitrogen or dodecane, including numerical results from the present work (solid lines), the standard correlation (D.7) (dashed lines), and experimental measurements for nitrogen (triangles, Ref. [72]) and dodecane (asterisks, Ref. [73]; squares, Ref. [74]).

Appendix E. Transcritical bicomponent systems approaching mechanically unstable conditions

Relevant aspects of the formulation outlined above lead to intrinsic singularities at conditions approaching the limit of mechanical stability (A.2). The analysis in this section builds on considerations made by Gaillard et al. [38,39], and provides thresholds in thermodynamic conditions leading to this behavior along with a palliating regularization.

E1. Singularities of the theory at the limit of mechanical stability

As discussed in Secs. 1, 2.2, and 3.2, transcritical conditions in systems fueled by heavy hydrocarbons involve combustor pressures $P_\infty \gtrsim 34$ bar (for pure nitrogen coflows), $P_\infty \gtrsim 36$ bar (for air coflows), and $P_\infty \gtrsim 50$ bar (for pure oxygen coflows). These combustor pressures lead to fully supercritical pressures with respect to both fuel and coflow propellants (see Table 1). Within the practical range of propellant injection temperatures (300 – 1000 K), those combustor pressures are also larger than the maximum mechanical critical pressures of mixtures of heavy hydrocarbons with N_2, O_2, or air (15–25 bar), and smaller than the maximum diffusional critical pressures (500–1000 bar). However, it is shown in Sections 4.4 and 5.3.3 that the thermodynamic pressure undergoes order-unity oscillations within the interface. These oscillations are the physical-space counterparts of the Maxwell loops in the coexistence region of the thermodynamic phase diagram, and are predicted by the equation of state (14), or any other cubic equation of state available in the literature. Consequently, when P_∞ is not sufficiently high, the Maxwell loops may generate underpressures within the interface smaller than the mechanical critical pressure, including negative thermodynamic pressures.

The Stefan-Maxwell forms of the standard diffusion fluxes of heat and species, given by Eqs. (152) and (153), are of limited practical use in conditions where the mechanical stability criterion (A.2) is not satisfied. This is because both the fuel partial molar volume $\tilde{\mathcal{V}}_F$ and the non-ideal diffusion prefactor $(\partial \ln f_F/\partial \ln X_F)_{P,T}$ participating in the Fickian, barodiffusion, and Dufour components of those fluxes diverge at the mechanical spinodal surface defined in Eq. (A.3). To understand this, note that the partial molar volume defined in Eq. (B.18) can be equivalently expressed for the fuel

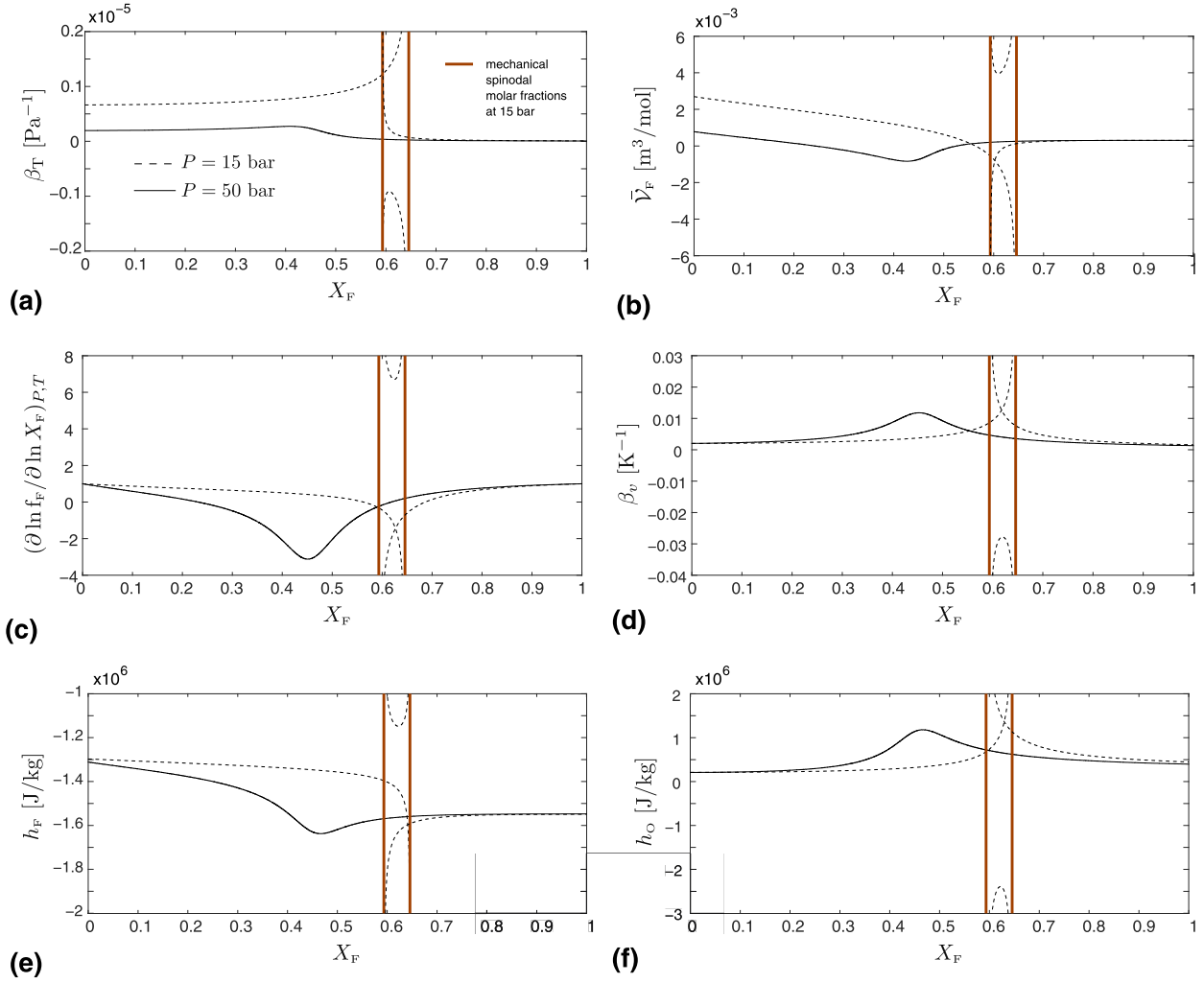

Fig. E.1. Constant-pressure distributions of (a) isothermal compressibility, (b) volume expansivity, (c) fuel partial molar volume, (d) non-ideal diffusion prefactor, and partial specific enthalpies of (e) $C_{12}H_{26}$ and (f) N_2 as a function of the $C_{12}H_{26}$ molar fraction at mechanically supercritical pressure ($P = 50$ bar, solid lines) and mechanically subcritical pressure ($P = 15$ bar, dashed lines). All panels correspond to $C_{12}H_{26}/N_2$ mixtures at uniform temperature $T = 500$ K.

species as

$$\bar{\mathcal{V}}_\mathrm{F} = \nu\beta_\mathrm{T}\left(\frac{\partial P}{\partial n_\mathrm{F}}\right)_{T,V,\,n_\mathrm{O}}, \tag{E.1}$$

where β_T is the isothermal compressibility defined in Eq. (A.2) and particularized for the Peng-Robinson equation of state in Eq. (C.44) in Appendix C. The coflow partial volume satisfies the similar expression

$$\bar{\mathcal{V}}_\mathrm{O} = \nu\beta_\mathrm{T}\left(\frac{\partial P}{\partial n_\mathrm{O}}\right)_{T,V,\,n_\mathrm{F}}. \tag{E.2}$$

Whereas the partial derivatives of the pressure with respect to the number of moles of fuel or coflow species in Eqs. (E.1) and (E.2) are generally finite and different from zero on approach to the mechanical spinodals, the isothermal compressibility diverges there as demanded by Eq. (A.3) and illustrated in Fig. E.1(a). As a consequence, the partial molar volumes diverge, as shown in Fig. E.1(b), although the molar volume $\nu = X_\mathrm{F}\bar{\mathcal{V}}_\mathrm{F} + (1 - X_\mathrm{F})\bar{\mathcal{V}}_\mathrm{O}$ remains finite.

It is also at the mechanical spinodals where the fuel molar chemical potential develops two turning points along the composition axis, as shown in Fig. A.1(b). As a result, its derivative $(\partial\bar{\mu}_\mathrm{F}/\partial X_\mathrm{F})_{P,T}$ becomes infinite there, and correspondingly the non-ideal diffusion prefactor $(\partial \ln \mathrm{f}_\mathrm{F}/\partial \ln X_\mathrm{F})_{P,T}$ also diverges there, as observed in Fig. E.1(c) and prescribed by Eq. (A.6). The singularity in the non-ideal diffusion prefactor can be traced back to the partial molar volume as a consequence of a non-integrable singularity of the latter in pressure,

$$\left(\frac{\partial\bar{\mathcal{V}}_\mathrm{F}}{\partial X_\mathrm{F}}\right)_{P,T} = \frac{\partial}{\partial P}\left[\left(\frac{\partial\bar{\mu}_\mathrm{F}}{\partial X_\mathrm{F}}\right)_{P,T}\right]_{T,X_\mathrm{F}}, \tag{E.3}$$

as indicated by differentiating Eq. (B.17) and utilizing the fundamental reciprocity relation of thermodynamics.

The singularities in $\bar{\mathcal{V}}_\mathrm{F}$ and $(\partial \ln \mathrm{f}_\mathrm{F}/\partial \ln X_\mathrm{F})_{P,T}$ arising at the mechanical spinodals cancel out each other upon summation in Eq. (F.22), in such a way that the constant-temperature gradient of the chemical-potential difference

$$\begin{aligned}\nabla_T(\mu_\mathrm{F} - \mu_\mathrm{O}) &= [\nabla(\mu_\mathrm{F} - \mu_\mathrm{O}) + (s_\mathrm{F} - s_\mathrm{O})\nabla T] \\ &= \frac{\overline{W}}{W_\mathrm{F}W_\mathrm{O}(1 - X_\mathrm{F})}\left[\left(\bar{\mathcal{V}}_\mathrm{F} - \frac{\nu W_\mathrm{F}}{\overline{W}}\right)\nabla P + \frac{\mathrm{R}^0 T}{X_\mathrm{F}}\left(\frac{\partial \ln \mathrm{f}_\mathrm{F}}{\partial \ln X_\mathrm{F}}\right)_{P,T}\nabla X_\mathrm{F}\right]\end{aligned} \tag{E.4}$$

remains finite. Note that other singularities emerging when $\nabla(\mu_\mathrm{F} - \mu_\mathrm{O})$ in Eq. (E.4) is evaluated in the pure components (i.e., $X_\mathrm{F} = 0$ and $X_\mathrm{F} = 1$) disappear upon multiplying Eq. (E.4) by the Onsager coefficients (145) and (146) to construct the standard diffusion fluxes of heat and species (149) and (150).

The considerations above indicate that, in configurations where the temperature gradients are exactly zero, such as those addressed in Section 6, the standard species diffusion flux can be computed across the mechanical spinodals by direct spatial differentiation of the chemical potentials as in Eq. (150), instead of using the Stefan-Maxwell form (153). Similarly, the Dufour effect in the standard heat diffusion flux can also be safely computed across the mechanical spinodals using Eq. (149) instead of the corresponding Stefan-Maxwell form (152).

Additional singularities need to be tackled in configurations such as that addressed in Section 7, in which there is a temperature gradient across the interface. In particular, singularities arising in the volume expansivity β_v and in the partial specific enthalpies h_F and h_O at the mechanical spinodals play a role in transport mechanisms associated with temperature gradients. Note that β_v participates in the portion of the interfacial species flux (148) that depends on the temperature gradient. It is also required for the calculation of the terms in the interfacial heat flux (147) that depend on the temperature gradient and on the heat transport by the net species flux $\boldsymbol{J}_F + \boldsymbol{\mathcal{J}}_F$, the latter being small but non-zero in practice because of the small but non-zero thermal Cahn numbers resulting from moderate temperature gradients. The difference of partial specific enthalpies $h_F - h_O$ participates in the interdiffusion heat flux in Eq. (149), in the last term of the interfacial heat flux (147), and implicitly in the calculation of the constant-temperature gradient of chemical potentials in Eq. (E.4) through the difference of partial entropies in Eq. (151).

Since β_T diverges at the mechanical spinodals by definition, and β_T is related to β_v by the identity

$$\beta_v = \beta_T \left(\frac{\partial P}{\partial T} \right)_{v, X_F}, \tag{E.5}$$

then β_v also diverges there, as shown in Fig. E.1(d). In Eq. (E.5), the partial derivative of P with respect to temperature generally remains finite and different from zero.

The singularities of the partial enthalpies at the mechanical spinodals, shown in Fig. E.1(e and f), can be understood by considering the identities

$$\overline{h}_F = \left(\frac{\partial H}{\partial n_F} \right)_{P,T,n_O} = \left(\frac{\partial H}{\partial n_F} \right)_{V,T,n_O} + \bar{\mathcal{V}}_F \left(\frac{\partial H}{\partial V} \right)_{T,n_F,n_O}, \tag{E.6}$$

$$\overline{h}_O = \left(\frac{\partial H}{\partial n_O} \right)_{P,T,n_F} = \left(\frac{\partial H}{\partial n_O} \right)_{V,T,n_F} + \bar{\mathcal{V}}_O \left(\frac{\partial H}{\partial V} \right)_{T,n_F,n_O}, \tag{E.7}$$

which can be combined with Eqs. (E.1) and (E.2) for the partial molar volumes, thereby suggesting that the singular behavior of $\overline{h}_F$ and $\overline{h}_O$ is closely related to that of β_T, since the remaining partial derivatives generally remain finite and different from zero. Despite the singularities arising in the partial molar enthalpies, the molar enthalpy of the mixture $\overline{h} = X_F \overline{h}_F + (1 - X_F)\overline{h}_O$ remains finite across the mechanical spinodals.

The need to regularize β_v, h_F, and h_O occurs at conditions where temperature gradients exist across the interface and the combustor pressure P_∞ is not sufficiently high. The threshold for P_∞ depends on the interface temperature T_e, since both T_e and the local pressure P determine the values of the fuel molar fraction on the mechanical spinodal surface. A quantification of the range of operating conditions $\{P_\infty, T_e\}$ within which the mechanical spinodal surface is crossed in $C_{12}H_{26}/N_2$ mixtures is provided in Fig. E.2 as the region hatched with red solid lines. Specifically, the results shown in Fig. E.2 pertain to 1D interfaces arising in a phase-equilibrium mixture at pressure P_∞ and uniform temperature equal to T_e. In this case, whose details are provided in Section 6, the singularities in β_v, $\overline{h}_F$, and $\overline{h}_O$ have no effect since

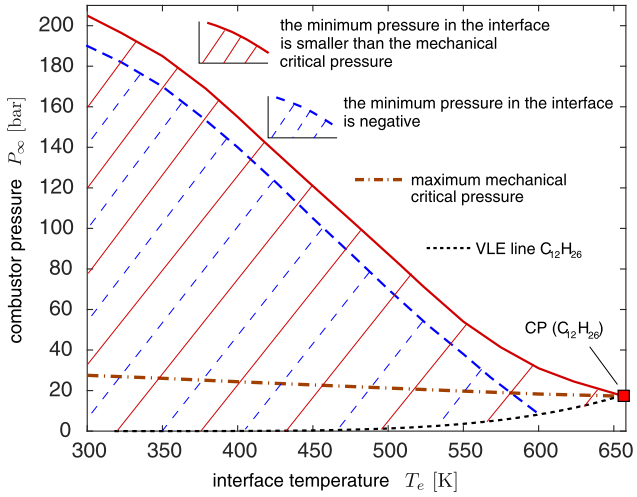

Fig. E.2. Regime map for $C_{12}H_{26}/N_2$ mixtures showing the range of operating combustor pressures leading to crossings of the mechanical spinodals (region hatched with red solid lines) and to negative underpressures (region hatched with blue dashed lines) as a function of the interface temperature. The plot includes the critical point of dodecane (square symbol), the VLE line of dodecane (dotted line), and the maximum mechanical critical pressure (brown dot-dashed line). (For interpretation of the references to color in this figure legend, the reader is referred to the web version of this article.)

$\nabla T = 0$ and $\boldsymbol{J}_F + \boldsymbol{\mathcal{J}}_F = 0$. In this way, the local pressure and composition can be monitored in the calculations to ascertain whether the mixture has entered the mechanically unstable region of the thermodynamic phase diagram, and to evaluate the two problematic quantities β_v and $h_F - h_O$ participating in the formulation of non-isothermal systems.

As indicated in Fig. E.2, the minimum combustor pressure P_∞ required to initiate crossings of the mechanical spinodals in $C_{12}H_{26}/N_2$ mixtures increases with decreasing values of the interface temperature T_e. No regularizations are needed at sufficiently high combustor pressures $P_\infty \gtrsim 200$ bar over the entire range of relevant injection temperatures, since the system is always mechanically stable.

In the configuration sketched in Fig. 1, T_e is much closer to T_F than to T_O near the injection orifice. As a consequence, T_e in Fig. E.2 can be approximated as T_F plus a small temperature differential that depends on the details of the wake flow created by the orifice ring. In practice, the boundary of the mechanically unstable region in Fig. E.2 indicated by the red thick solid line provides approximately the minimum T_F necessary for warranting mechanical stability for a given P_∞. For instance, at the pressure $P_\infty = 100$ bar considered in the results presented in Section 7 for non-isothermal $C_{12}H_{26}/N_2$ systems, the mechanical spinodal surface is crossed if $T_F \lesssim 480$ K. Downstream of the injector, however, the interface temperature increases because of the heat received from the hot coflow. When $T_e > 480$ K, the system ceases to cross the mechanical spinodal surface and regularizations of β_v and $h_F - h_O$ become unnecessary. These aspects are further analyzed in Section 7.

Since the unboundedness of β_T on the mechanical spinodal surface dominates the divergent behavior of β_v, h_F, and h_O, a simple way of limiting the value of β_T is by using the regularization

$$\frac{(v-b)^2}{R^0 T v \beta_T} \approx \max(B_T, m), \tag{E.8}$$

where B_T is a dimensionless variable defined in Eq. (C.45), and m is a positive dimensionless regularization constant whose value is much smaller than unity. Figure E.3 shows the resulting regularized profiles of β_v and $h_F - h_O$.

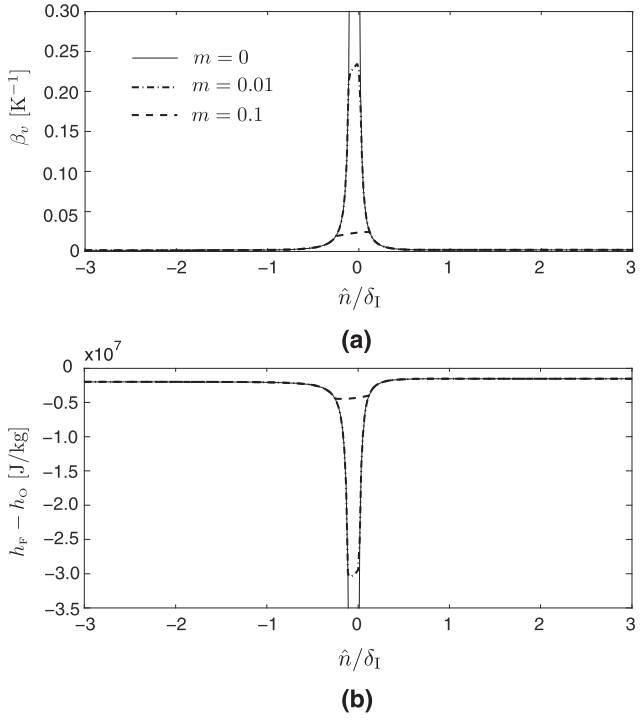

Fig. E.3. Regularized profiles of (a) volume expansivity and (b) difference of partial specific enthalpies across transcritical interfaces in $C_{12}H_{26}/N_2$ isothermal systems at $P_\infty = 50$ bar and $T_e = 500$ K. The plot includes regularized profiles with $m = 0.01$ (dot-dashed line) and $m = 0.1$ (dashed line), along with the non-regularized case $m = 0$ (solid line).

The differences in the regularized profiles of β_v and $h_F - h_O$ in Fig. E.3 have a negligible impact on the overall solution of the non-isothermal system addressed in Section 7. This is shown in Fig. E.4, which shows that distribution of σ over the transcritical region is largely independent of the regularization constant m used in Eq. (E.8). The reason for the lack of sensitivity of the solution to m is that the terms multiplying β_v and $h_F - h_O$ in the fluxes of heat and species become increasingly smaller as mechanical and transport equilibrium are approached, a condition that is always satisfied for a long portion of the interface, as discussed in Sections 5.7 and 7.2.

The singularities observed above at the limit of mechanical stability are not unique to the Peng-Robinson equation of state (14). They also occur when employing other cubic equations such as the van der Waals [51] or Redlich-Kwong [96,97] equations of state.

E2. Negative thermodynamic pressures

The thermodynamic pressure P is always a positive quantity in ideal gases, in which the intermolecular forces are negligible. In contrast, P can attain negative values in liquids since the molecules are closer and therefore exert a non-negligible attractive force on each other. Negative pressures in liquids are well-documented in the literature and are always associated with fully tensile mechanical states such as those participating in cavitation, nucleation, or capillary flows [104,127,128]. These processes are thermodynamically metastable or unstable, thereby suggesting that negative pressures often correspond to transient states in which the fluid is transitioning to a different phase. Negative pressures may also arise in fluids at high pressures, when the density is large and cohesive forces become important, as represented by the second term on the right-hand side of Eq. (14), or by equivalent terms in other equations of state [99].

The combustor pressure P_∞ and interface temperature T_e leading to locally negative pressures within the interface in $C_{12}H_{26}/N_2$ mixtures are associated with near or full transgression of the mechanical-stability limit, and are denoted in Fig. E.2 as the region hatched with dashed lines. It should be emphasized that negative pressures do not lead to any transcendental behavior in the conservation equations, neither do they induce any singularities in the thermodynamic variables discussed in Appendix E.1. They do, however, influence the calculation of transport coefficients in the following manner.

The dynamic viscosity μ, thermal conductivity λ, binary diffusion coefficient $\mathcal{D}_{F,O}$, and thermal-diffusion ratio $k_{F,T}$ are generally functions of the thermodynamic pressure and participate in the conservation equations (44)–(47) through the viscous stress tensor and the fluxes of heat and species. In particular, λ, $\mathcal{D}_{F,O}$, and $k_{F,T}$ are required for the calculation of the Onsager coefficients (144)–(146). Whereas models for these coefficients are well-established in the literature for ideal and real gases, including fully supercritical fluids, relatively much less is known about their behavior within the mechanically unstable region of the thermodynamic phase diagram, since homogeneous mixtures of phases or fluids of fundamentally different nature are untenable there. The standard models for μ, λ, $\mathcal{D}_{F,O}$, and $k_{F,T}$ in fluids at high pressures, employed in Appendices B.4 and F, cease to have physical significance at negative pressures where, for instance, $\mathcal{D}_{F,O}$ becomes undefined because of Eq. (F.41). However, note that the mechanical and transport equilibrium conditions (107) and (177) [or their equivalent forms (193) and (194) in terms of chemical potentials] are independent of viscosity and of the Onsager coefficients, and therefore are not influenced by the locally erroneous behavior of any of the transport coefficients under conditions leading to negative pressures.

The considerations above suggest that, in isothermal systems such as the ones treated in Section 6, the structure of the interface is completely insensitive to the specific manner in which λ, $\mathcal{D}_{F,O}$, and $k_{F,T}$ are modeled. In contrast, in non-isothermal systems such as the one in Fig. 1, the mechanical and transport equilibrium conditions are only satisfied asymptotically to leading order in the limit of small thermal Cahn numbers, $\epsilon_T \ll 1$. Second-order effects lead to departures from equilibrium and require consideration of transport induced by temperature gradients. This involves evaluation of λ, $\mathcal{D}_{F,O}$, and $k_{F,T}$ across the interface, and gives rise to small fluxes of heat and species. In absence of improved models for transport coefficients at mechanically unstable conditions, the approximations

$$\begin{aligned} \lambda(P, X_F, T) &\approx \lambda(P_\infty, X_F, T), \\ \mathcal{D}_{F,O}(P, X_F, T) &\approx \mathcal{D}_{F,O}(P_\infty, X_F, T), \\ k_{F,T}(P, X_F, T) &\approx k_{F,T}(P_\infty, X_F, T), \end{aligned} \tag{E.9}$$

are used in this study, where the transport coefficients are evaluated at the combustor pressure P_∞, the latter being representative of the thermodynamic pressure everywhere away from the interface in flows at small Mach numbers.

Appendix F. Supplementary expressions for molecular transport coefficients at high pressures

This appendix reviews models for the calculation of the viscosity, thermal conductivity, diffusion coefficient, and thermal-diffusion ratio at high pressures.

F1. Dynamic viscosity

The dynamic viscosity η of the mixture can be modeled as [155,156]

$$\eta = 10^{-7}\eta^* \frac{36.344\left(W' T_c\right)^{1/2}}{v_c^{2/3}} \quad [\text{Pa}\cdot\text{s}], \tag{F.1}$$

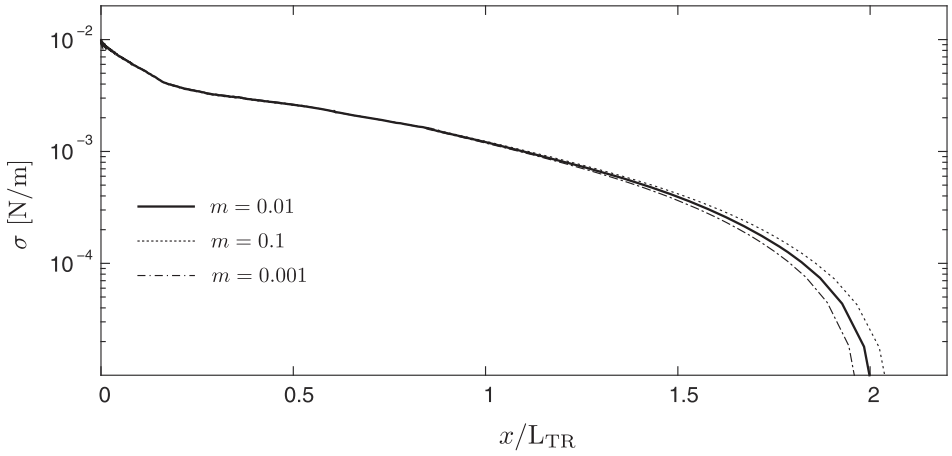

Fig. E.4. Surface-tension coefficient in the $C_{12}H_{26}/N_2$ non-isothermal system analyzed in Section 7 as a function of downstream distance (or time), including the baseline case with regularization constant $m = 0.01$ (solid line), along with two supplementary calculations with $m = 0.1$ (dotted line) and $m = 0.001$ (dot-dashed line), all other parameters being the same.

where T_c [K], v_c [cm^3/mol], and W' [g/mol] are, respectively, representative values of the critical temperature, critical molar volume, and molecular weight of the mixture given by the expressions

$$W' = \left\{ \left[\sum_{i=1}^{N} \sum_{j=1}^{N} X_i X_j \epsilon_{i,j} \sigma_{i,j}^2 W_{i,j}^{1/2} \right] \Big/ \left(\varepsilon \sigma^2 \right) \right\}^2, \quad W_{i,j} = \frac{2 W_i W_j}{W_i + W_j},$$

$$T_c = 1.2593 \varepsilon, \quad v_c = (\sigma / 0.809)^3. \tag{F.2}$$

In Eq. (F.2), ε [K] is the minimum of the pair-potential energy divided by the Boltzmann constant, and σ [Å] is the hard-sphere diameter. Both of these quantities are obtained by the empirical mixing rules

$$\varepsilon = \sum_{i=1}^{N} \sum_{j=1}^{N} X_i X_j \varepsilon_{i,j} \sigma_{i,j}^3 / \sigma^3, \quad \sigma^3 = \sum_{i=1}^{N} \sum_{j=1}^{N} X_i X_j \sigma_{i,j}^3, \tag{F.3}$$

where $\epsilon_{i,j}$ and $\sigma_{i,j}$ are obtained from

$$\varepsilon_{i,j} = \left(\varepsilon_{i,i} \varepsilon_{j,j} \right)^{1/2}, \quad \sigma_{i,j} = \xi_{i,j} \left(\sigma_i \sigma_j \right)^{1/2}, \tag{F.4}$$

with the corresponding quantities for the individual components being given by $\varepsilon_{i,i} = T_{c,i}/1.2593$ and $\sigma_{i,i} = 0.809 v_{c,i}^{1/3}$. Using the Peng-Robinson equation of state (14), the critical molar volume of the species i can be computed as $v_{c,i} = Z_c \mathrm{R}^0 T_{c,i} / P_{c,i}$, with $Z_c = 0.307$ [92], thereby yielding $v_{c,\mathrm{F}} = 932.5$ cm^3/mol for $C_{12}H_{26}$, and $v_{c,\mathrm{O}} = 94.5$ cm^3/mol for N_2. Note, however, that these values do not match the experimentally measured ones $v_{c,\mathrm{F}} = 750.4$ cm^3/mol and $v_{c,\mathrm{O}} = 89.4$ cm^3/mol [40], since the Peng-Robinson equation of state has only two coefficients, and therefore cannot be forced to simultaneously satisfy measured critical values of pressure, temperature and molar volume.

In Eq. (F.1) the prefactor η^* is given by

$$\eta^* = \frac{(T^*)^{1/2} F_c}{\Omega_v} \left(\frac{1}{G_2} + E_6 y \right) + \eta^{**}, \tag{F.5}$$

where $T^* = T/\varepsilon$ and $y = v_c/(6v)$. The remaining parameters are computed using the relations

$$\Omega_v = 1.161 (T^*)^{-0.149} + 0.525 \mathrm{e}^{-0.773 \mathrm{T}^*} + 2.162 \mathrm{e}^{-2.438 \mathrm{T}^*}, \tag{F.6}$$

$$F_c = 1 - 0.276\omega + 0.059 \mathcal{M}_r^4 + k_a, \tag{F.7}$$

$$G_1 = (1 - 0.5y)/(1 - y)^3, \tag{F.8}$$

Table F.1
Coefficients for E_k in Eq. (F.11) [155].

k	$w_{1,k}$	$w_{2,k}$	$w_{3,k}$	$w_{4,k}$
1	6.324	50.412	−51.680	1189.0
2	1.210×10^{-3}	-1.154×10^{-3}	-6.257×10^{-3}	0.03728
3	5.283	254.209	−168.48	3898.0
4	6.623	38.096	−8.464	31.42
5	19.745	7.630	−14.354	31.53
6	−1.900	−12.537	4.985	−18.15
7	24.275	3.450	−11.291	69.35
8	0.7972	1.117	0.01235	−4.117
9	−0.2382	0.06770	−0.8163	4.025
10	0.06863	0.3479	0.5926	−0.727

$$G_2 = \frac{E_1 \left(1 - \mathrm{e}^{-\mathrm{E}_4 \mathrm{y}} \right)/y + E_2 G_1 \mathrm{e}^{\mathrm{E}_5 \mathrm{y}} + \mathrm{E}_3 \mathrm{G}_1}{E_1 E_4 + E_2 + E_3}, \tag{F.9}$$

$$\eta^{**} = E_7 y^2 G_2 \exp\left[E_8 + E_9 (T^*)^{-1} + E_{10} (T^*)^{-2} \right], \tag{F.10}$$

$$E_k = w_{1,k} + w_{2,k}\omega + w_{3,k} \mathcal{M}_r^4 + w_{4,k} k_a, \quad k = 1, 2, \ldots 10, \tag{F.11}$$

where the coefficients $w_{1,k}, \ldots w_{4,k}$ are provided in Table F.1. In this formulation, ω is an acentric factor of the mixture defined as

$$\omega = \sum_{i=1}^{N} \sum_{j=1}^{N} X_i X_j \omega_{i,j} \sigma_{i,j}^3 / \sigma^3, \tag{F.12}$$

with $\omega_{i,j} = \left(\omega_i + \omega_j \right)/2$. The reduced dipole moment $\mathcal{M}_r$ and the association factor of the mixture k_a can be obtained from tables [54] and are set to zero for $C_{12}H_{26}/N_2$ mixtures.

F2. Thermal conductivity

In this study, the thermal conductivity λ of the mixture is modeled as [155,156]

$$\lambda = \frac{31.2 \times 10^3 \eta^0 \Psi}{W'} \left(G_3^{-1} + B_6 y \right) + q B_7 y^2 (T/T_c)^{1/2} G_3 \quad \left[\frac{\mathrm{W}}{\mathrm{m \cdot K}} \right], \tag{F.13}$$

where W' and T_c are given in (F.2). The rest of the parameters in Eq. (F.13) are

$$\eta^0 = 40.785 \times 10^{-7} F_c \left(W' T \right)^{1/2} / (v_c^{2/3} \Omega_v),$$

Table F.2
Coefficients for B_k in Eq. (F.17) [155].

k	$z_{1,k}$	$z_{1,k}$	$z_{1,k}$	$z_{1,k}$
1	2.417	0.748	−0.919	121.720
2	−0.509	−1.509	−49.991	69.983
3	6.611	5.621	64.760	27.039
4	14.543	−8.914	−5.638	74.344
5	0.793	0.820	−0.694	6.317
6	−5.863	12.801	9.589	65.529
7	91.089	128.110	−54.217	523.810

$$q = 3.586 \times 10^{-3/2}\left(T_c/W'\right)^{1/2}/v_c^{2/3}, \tag{F.14}$$

$$\Psi = 1 + \frac{\alpha(0.215 + 0.283\alpha - 1.061\beta + 0.267\gamma)}{0.637 + \beta\gamma + 1.061\alpha\beta}, \tag{F.15}$$

$$G_3 = \left(\frac{B_1}{y}\right)\left(\frac{1 - \mathrm{e}^{-\mathrm{B}_4 y} + \mathrm{B}_2\mathrm{G}_1\mathrm{e}^{\mathrm{B}_5 y} + \mathrm{B}_3\mathrm{G}_1}{B_1B_4 + B_2 + B_3}\right), \tag{F.16}$$

$$B_k = z_{1,k} + z_{2,k}\omega + z_{3,k}\mathcal{M}_r^4 + z_{4,k}k_a, \quad k = 1, \ldots 7, \tag{F.17}$$

where

$$\alpha = \left(\bar{c}_p^{\mathrm{IG}}/\mathrm{R}^0 - 1\right) - 1.5, \quad \beta = 0.786 - 0.711\omega + 1.317\omega^2,$$
$$\gamma = 2 + 10.5(T/T_c)^2, \tag{F.18}$$

with T_c and ω given in (F.2) and (F.12), respectively. The parameters $z_{1,k}, \ldots z_{4,k}$ are calculated based on Table F.2.

F3. Stefan-Maxwell forms of the standard fluxes of heat and species

The expressions (136) and (137) for the standard diffusion fluxes of heat and species can be recast in more physically insightful forms that involve gradients of temperature, pressure and composition. Because of the functional dependence of the molar chemical potential on pressure, temperature and composition, $\bar{\mu}_k = \bar{\mu}_k(P, T, X_1, \ldots X_{N-1})$, given explicitly by Eqs. (B.22), (B.23), and (C.47), the differential form

$$\nabla_T \bar{\mu}_k = \left(\frac{\partial \bar{\mu}_k}{\partial P}\right)_{T,X_{j|j=1,\ldots N-1}} \nabla P + \sum_{j=1}^{N-1}\left(\frac{\partial \bar{\mu}_k}{\partial X_j}\right)_{\substack{P,T,X_{i|i=1,\ldots N-1} \\ (i\neq j)}} \nabla X_j \tag{F.19}$$

is satisfied. In addition, the Gibbs-Duhem relation (C.9) can be rewritten on a molar basis at constant temperature as

$$\sum_{i=1}^{N} X_i d\bar{\mu}_i = v dP, \tag{F.20}$$

which can be spatially differentiated yielding

$$\nabla_T \bar{\mu}_N = \frac{1}{X_N}\left(v\nabla P - \sum_{j=1}^{N-1} X_j \nabla_T \bar{\mu}_j\right). \tag{F.21}$$

Upon dividing Eq. (F.19) by W_k and subtracting it from Eq. (F.21) divided by W_N, the relation

$$\nabla_T(\mu_k - \mu_N) = \left(\frac{\bar{\mathcal{V}}_k}{W_k} - \frac{v}{W_N X_N} + \sum_{m=1}^{N-1}\frac{X_m\bar{\mathcal{V}}_m}{W_N X_N}\right)\nabla P + \sum_{m=1}^{N-1}\left(\frac{X_m}{W_N X_N} + \frac{\delta_{m,k}}{W_k}\right)\sum_{j=1}^{N-1}\mathrm{R}^0 T\left(\frac{\partial \ln \mathrm{f_m}}{\partial X_j}\right)_{\substack{P,T,X_{i|i=1,\ldots N-1} \\ (i\neq j)}} \nabla X_j \tag{F.22}$$

is obtained, which connects the constant-temperature gradients of the specific chemical potential with the gradients of pressure and composition, where $\delta_{m,k}$ is the Kronecker delta and $k = 1, \ldots N-1$. In writing Eq. (F.22), use has been made of Eq. (B.17) to replace the partial derivative of the chemical potential with respect to pressure by the partial molar volume, and of Eq. (B.23) to express the partial derivative of the chemical potential with respect to the molar fraction as

$$\left(\frac{\partial \bar{\mu}_m}{\partial X_j}\right)_{\substack{P,T,X_{i|i=1,\ldots N-1} \\ (i\neq j)}} = \mathrm{R}^0 T\left(\frac{\partial \ln \mathrm{f_m}}{\partial X_j}\right)_{\substack{P,T,X_{i|i=1,\ldots N-1} \\ (i\neq j)}}, \tag{F.23}$$

where f_m is the fugacity of species m defined by the combination of Eqs. (B.22) and (C.47).

The utilization of Eq. (F.22) in Eqs. (136)-(137) for replacing the constant-temperature gradients of chemical potentials by gradients of composition and pressure leads to the Stefan-Maxwell forms

$$\boldsymbol{q} = \underbrace{-\frac{L_{q,q}}{T^2}\nabla T}_{\text{Fourier conduction}} \underbrace{+\sum_{i=1}^{N-1}(h_i - h_N)\boldsymbol{J_i}}_{\text{interdiffusion}} \underbrace{-\sum_{j=1}^{N-1}\sum_{k=1}^{N-1} L_{q,k}\mathrm{R}^0\sum_{m=1}^{N-1}\left(\frac{X_m}{W_N X_N} + \frac{\delta_{m,k}}{W_k}\right)\left(\frac{\partial \ln \mathrm{f_m}}{\partial X_j}\right)_{P,T,X_{r|r=1,\ldots N-1(r\neq j)}}\nabla X_j}_{\text{Dufour effect}} \underbrace{-\sum_{k=1}^{N-1}\frac{L_{q,k}}{T}\left(\frac{\bar{\mathcal{V}}_k}{W_k} - \frac{v}{W_N X_N} + \sum_{m=1}^{N-1}\frac{X_m\bar{\mathcal{V}}_m}{W_N X_N}\right)\nabla P}_{\text{Dufour effect (cont.)}} \tag{F.24}$$

and

$$\boldsymbol{J_i} = \underbrace{-\sum_{j=1}^{N-1}\rho D_{i,j}\nabla X_j}_{\text{Fickian diffusion}} \underbrace{-\frac{L_{q,i}}{T^2}\nabla T}_{\substack{\text{Soret effect} \\ \text{(thermal diffusion)}}} \underbrace{-\sum_{k=1}^{N-1}\frac{L_{i,k}}{T}\left(\frac{\bar{\mathcal{V}}_k}{W_k} - \frac{v}{W_N X_N} + \sum_{m=1}^{N-1}\frac{X_m\bar{\mathcal{V}}_m}{W_N X_N}\right)\nabla P}_{\text{barodiffusion}} \tag{F.25}$$

for the standard diffusion fluxes of heat and species, respectively. In Eq. (F.25), $D_{i,j}$ is the Fickian diffusion coefficient.

F4. Fickian diffusion coefficients

The Fickian portion of the standard diffusion flux (F.25) can be expressed in matrix form as

$$\mathbf{J} = -\rho\mathbf{D}\mathbf{X}, \tag{F.26}$$

where $\mathbf{J} = [\boldsymbol{J_i}]$ and $\mathbf{X} = [\nabla X_j]$ are vectors with $N-1$ components, and $\mathbf{D} = \left[D_{i,j}\right]$ is a $(N-1)\times(N-1)$ matrix composed of the Fickian diffusion coefficients. The latter are related to the Onsager coefficients $L_{i,k}$ through Eq. (F.30), which, in matrix form, can be expressed as

$$\mathbf{D} = \boldsymbol{\mathcal{L}}'\boldsymbol{\mathcal{W}}\boldsymbol{\Gamma}. \tag{F.27}$$

In Eq. (F.27), $\boldsymbol{\mathcal{L}}' = [L_{i,k}]$ is the $(N-1)\times(N-1)$ subset of the Onsager matrix $\boldsymbol{\mathcal{L}}$ denoted by dot-dashed lines in Eq. (143). This subset contains only mass-transfer-related coefficients. In addition, $\boldsymbol{\mathcal{W}} = [\mathcal{W}_{k,m}]$ is a $(N-1)\times(N-1)$ matrix whose elements depend on the local composition and are given by

$$\mathcal{W}_{k,m} = \frac{\mathrm{R}^0}{\rho X_m}\left(\frac{X_m}{W_N X_N} + \frac{\delta_{m,k}}{W_k}\right). \tag{F.28}$$

Lastly, the $(N-1)\times(N-1)$ elements of the matrix $\mathbf{\Gamma}=[\Gamma_{m,j}]$ represent high-pressure effects and are given by

$$\Gamma_{m,j}=X_m\left(\frac{\partial \ln \mathrm{f_m}}{\partial X_j}\right)_{P,T,X_{r|r=1,\dots N-1(r\neq j)}}. \tag{F.29}$$

At low pressures, the fugacity is equal to the partial pressure, and therefore $\mathbf{\Gamma}$ becomes the identity matrix. Upon substituting Eqs. (F.29) and (F.28) into (F.27), the expression

$$D_{i,j}=\sum_{k=1}^{N-1}\frac{L_{i,k}\mathrm{R}^0}{\rho}\sum_{m=1}^{N-1}\left(\frac{X_m}{W_N X_N}+\frac{\delta_{m,k}}{W_k}\right)\left(\frac{\partial \ln \mathrm{f_m}}{\partial X_j}\right)_{P,T,X_{r|r=1,\dots N-1\atop(r\neq j)}} \tag{F.30}$$

is obtained for the effective Fickian diffusion coefficient of species i into j.

By definition, the binary diffusion coefficients $\mathcal{D}_{i,m}$ satisfy the relation

$$\mathbf{J}=-\rho\mathbf{B}^{-1}\mathbf{\Gamma}\mathbf{X}, \tag{F.31}$$

where $\mathbf{B}=[\mathrm{B_{i,m}}]$ is a $(N-1)\times(N-1)$ matrix given by [137,162]

$$\mathrm{B_{i,m}}=\frac{\mathrm{X_i}}{\mathcal{D}_{\mathrm{i,N}}}+\sum_{\mathrm{k=1}\atop\mathrm{(k\neq i)}}^{\mathrm{N}}\frac{\mathrm{X_k}}{\mathcal{D}_{\mathrm{i,k}}}\quad\text{for}\quad \mathrm{i=m}\quad\text{and}\quad \mathrm{i}=1,\dots \mathrm{N}-1, \tag{F.32}$$

and

$$\mathrm{B_{i,m}}=\mathrm{X_i}\left(\frac{1}{\mathcal{D}_{\mathrm{i,N}}}-\frac{1}{\mathcal{D}_{\mathrm{i,m}}}\right)\quad\text{for}\quad \mathrm{i\neq m}\quad\text{and}\quad \mathrm{i,m}=1,\dots \mathrm{N}-1. \tag{F.33}$$

Upon combining Eqs. (F.26), (F.27) and (F.31), the relations

$$\mathcal{L}'=\mathbf{B}^{-1}\mathcal{W}^{-1} \tag{F.34}$$

and

$$\mathbf{D}=\mathbf{B}^{-1}\mathbf{\Gamma} \tag{F.35}$$

are obtained. In particular, Eqs. (F.34) and (F.35) enable the calculation of the Onsager coefficients $L_{i,k}$ [from Eq. (F.34)] and the Fickian diffusion coefficients $D_{i,j}$ [from Eq. (F.35)] by using the binary diffusion coefficients $\mathcal{D}_{i,j}$ described in Appendix F.5.

F5. Binary diffusion coefficients

The binary diffusion coefficients $\mathcal{D}_{i,j}$ can be modeled using the expression

$$\mathcal{D}_{i,j}=(D^{\infty}_{i,j})^{X_j}(D^{\infty}_{j,i})^{X_i}\prod_{\mathrm{k=1}\atop\mathrm{k\neq i,j}}^{N}(D^{\infty}_{i,k}D^{\infty}_{j,k})^{X_k/2}\quad[\mathrm{m^2/s}], \tag{F.36}$$

which follows the formulation described in Refs[162,171,172]. for non-ideal and nonpolar multicomponent mixtures. In Eq. (F.36), $D^{\infty}_{i,j}$ ($D^{\infty}_{j,i}$) corresponds to the molecular diffusion coefficient of component i (j) infinitely diluted in component j (i). These auxiliary coefficients are given by

$$\frac{cD^{\infty}_{i,j}}{(cD)^0}=\mathcal{C}_0\left(\frac{T_{r,j}P_{r,i}}{T_{r,i}P_{r,j}}\right)^{\mathcal{C}_1}\left(\frac{\eta}{\eta^0}\right)^{\left[\mathcal{C}_2(\omega_i,\omega_j)+\mathcal{C}_3(T_r,P_r)\right]}\quad[\mathrm{m^2/s}]. \tag{F.37}$$

In this formulation, c [mol/m^3] is the molar density, $T_{r,i}=T/T_{c,i}$ and $P_{r,i}=P/P_{c,i}$ are the reduced temperature and pressure, η/η^0 is the ratio between high- and low-pressure viscosities, and $\mathcal{C}_k$ are model constants given by

$$\mathcal{C}_0=\exp\left(\mathcal{C}'_1\right), \tag{F.38}$$

$$\mathcal{C}_1=10\mathcal{C}'_2, \tag{F.39}$$

$$\mathcal{C}_2=\mathcal{C}'_3\left(1-\omega_i+10\omega_j+10\omega_i\omega_j\right), \tag{F.40}$$

$$\mathcal{C}_3=\mathcal{C}'_4\left(P_{r,j}^{3\mathcal{C}'_5}-6P_{r,i}^{\mathcal{C}'_5}+6T_{r,j}^{10\mathcal{C}'_6}\right)+\mathcal{C}'_7T_{r,i}^{-\mathcal{C}'_6}+\mathcal{C}'_2\frac{T_{r,j}P_{r,i}}{T_{r,i}P_{r,j}}, \tag{F.41}$$

with $\mathcal{C}'_1=-0.0472$, $\mathcal{C}'_2=0.0103$, $\mathcal{C}'_3=-0.0147$, $\mathcal{C}'_4=-0.0053$, $\mathcal{C}'_5=-0.3370$, $\mathcal{C}'_6=-0.1852$, and $\mathcal{C}'_7=-0.1914$. The product $(cD)^0$ [mol/(m · s)] is calculated using [173]

$$(cD)^0=1.01\times10^{-2}T^{3/4}\frac{\left(1/W_i+1/W_j\right)^{1/2}}{\mathrm{R}^0\left[(\sum_\nu)_i^{1/3}+(\sum_\nu)_j^{1/3}\right]^2}\quad\left[\frac{\mathrm{m^2}}{\mathrm{s}}\right], \tag{F.42}$$

where $(\Sigma_\nu)_i$ is the diffusion-volume increment of component i given by $(\sum_\nu)_{\mathrm{N_2}}=18.50$ cm^3 and $(\sum_\nu)_{\mathrm{C_{12}H_{26}}}=250.86$ cm^3 for nitrogen and dodecane, respectively [54].

F6. Thermal-diffusion ratios

The calculation of the Onsager coefficients $L_{q,i}$, which participate in the Soret and Dufour effects in the standard diffusion fluxes (F.24)-(F.25), is connected to the coefficients $L_{i,i}$ and the thermal-diffusion ratio $k_{i,\mathrm{T}}$ of species i by the expression [163]

$$L_{q,i}=\frac{W\mathrm{R}^0TL_{i,i}}{W_iW_NX_iX_N}k_{i,\mathrm{T}}=\sum_{k=1}^{N-1}L_{i,k}\left(\frac{Q^*_k}{W_k}-\frac{Q^*_N}{W_N}\right), \tag{F.43}$$

where Q^*_k is the amount of energy that must be absorbed per mole of component k while diffusing out that component in order to maintain the temperature and pressure of the mixture locally constant.

Following the modeling approach described in Ref. [163], the expression

$$Q^*_k=-\frac{\Delta_d\bar{e}_k}{\iota_k}+\left[\sum_{j=1}^{N}\frac{X_j\Delta_d\bar{e}_j}{\iota_j}\right]\frac{\bar{\mathcal{V}}_k}{\sum_{j=1}^{N}X_j\bar{\mathcal{V}}_j}\quad\text{for}\quad k=1,\dots N, \tag{F.44}$$

is employed here, with $\Delta_d\bar{e}_k$ the departure function of the partial molar internal energy of component k defined in Eq. (C.42). Additionally, ι is a model parameter corresponding to the ratio of vaporization and viscous flow energies. The value $\iota_k=4.5$ ($k=1,\dots N$) is employed here, which is slightly larger than the standard calibrated value $\iota_k=4.0$ used in Ref. [167]. This increase in ι is made to warrant a positive semidefinite Onsager matrix when $k_{i,\mathrm{T}}$ is employed in conjunction with the aforementioned models for λ and $\mathcal{D}_{i,j}$ in the binary mixtures considered in this study (see Fig. 19 and discussion in Section 5.5).

Appendix G. Numerical methods for the calculation of transcritical interfaces

The solver employed to integrate the formulation presented in Table 8 is based on: (a) a second-order central finite-difference method for spatial discretization on one-dimensional non-uniform grids (e.g., see Ref. [174] and Ch. 2 in Ref. [175] for details); and (b) a fully-implicit variable-step second-order backward differentiation formula (BDF2) especially suited for time integration of stiff equations [176]. The resulting nonlinear system of equations is solved through an iterative globally-convergent strategy based on

Table G.1
Dimensional formulation integrated numerically by the solver for transcritical interfaces in isothermal bicomponent systems. Pseudo-time variations are included in the solver to relax the solution to the equilibrium steady state that satisfies the formulation in Table 5. (‡) The steady solution of the problem is independent of the binary diffusion coefficient.

Conservation equations	
Mechanical equilibrium	$P_\infty - P + \rho Y_\mathrm{F}\kappa_{\mathrm{F,F}}\frac{\partial^2}{\partial\hat{n}^2}(\rho Y_\mathrm{F}) - \frac{1}{2}\kappa_{\mathrm{F,F}}\left[\frac{\partial}{\partial\hat{n}}(\rho Y_\mathrm{F})\right]^2 = 0,$
Fuel species	$\frac{\partial}{\partial t}(\rho Y_\mathrm{F}) = -\frac{\partial}{\partial\hat{n}}(J_\mathrm{F} + \mathcal{J}_\mathrm{F}).$
Transport fluxes	
Standard (species)	$J_\mathrm{F} = -\frac{\rho\mathcal{D}_{\mathrm{F,O}}W_\mathrm{F}W_\mathrm{O}X_\mathrm{F}(1-X_\mathrm{F})}{\mathrm{R}^0 T_e\overline{W}}\frac{\partial}{\partial\hat{n}}(\mu_\mathrm{F} - \mu_\mathrm{O}),$
Interfacial (species)	$\mathcal{J}_\mathrm{F} = \frac{\rho\kappa_{\mathrm{F,F}}\mathcal{D}_{\mathrm{F,O}}W_\mathrm{F}W_\mathrm{O}X_\mathrm{F}(1-X_\mathrm{F})}{\mathrm{R}^0 T_e\overline{W}}\frac{\partial^3}{\partial\hat{n}^3}(\rho Y_\mathrm{F}).$
Boundary conditions	
Phase-equilibrium composition	$\rho Y_\mathrm{F} \to \rho_e^\ell Y_{\mathrm{Fe}}^\ell$ at $\hat{n}\to-\infty$, $\rho Y_\mathrm{F} \to \rho_e^g Y_{\mathrm{Fe}}^g$ at $\hat{n}\to+\infty$.
Supplementary expressions (see Appendix B, Appendix C, and Appendix F for details)	
Equation of state	Eq. (14),
Coefficients of the equation of state	Eqs. (212), and (C.10)-(C.12),
Gradient-energy coefficient	Eqs. (23), (C.17), and (C.18),
Binary diffusion coefficient‡	Eq. (F.36),
Thermodynamic relations	Eqs. (213), (214), (B.19), (B.20), (C.43), and (C.47).

the Newton-Raphson method [177] combined with line searches along the Newton direction that are guaranteed to decrease the residual by incorporating a backtracking routine [178]. Details are provided in this appendix along with specific considerations for isothermal and non-isothermal cases.

G1. Spatial and temporal discretizations

Consider the conservation equations expressed as the coupled differential system $\dot{\mathbf{y}} = \boldsymbol{\mathcal{F}}(t,\mathbf{y})$ subject to $\mathbf{y}(t_0) = \mathbf{y_0}$, where $\mathbf{y}$ denotes the vector of independent variables, $\boldsymbol{\mathcal{F}}(t,\mathbf{y})$ represents the convection and diffusion fluxes, and $\mathbf{y_0}$ is the initial value of $\mathbf{y}$. The variable-step BDF2 scheme advances the solution in time as

$$\left(\frac{1+2\Delta_n}{1+\Delta_n}\right)\mathbf{y}_{n+1} - (1+\Delta_n)\mathbf{y}_n + \left(\frac{\Delta_n^2}{1+\Delta_n}\right)\mathbf{y}_{n-1} = \Delta t_n \boldsymbol{\mathcal{F}}(t_{n+1},\mathbf{y}_{n+1}), \tag{F.1}$$

where the subscript n indicates time level, and

$$\Delta_n = \Delta t_n/\Delta t_{n-1} \tag{F.2}$$

is the ratio of time steps.

The nonlinear implicit system of algebraic Eqs. (G.1) is iteratively solved by means of the Newton-Raphson method at each time level. Specifically, defining M as the number of independent variables multiplied by the number of spatial grid points, Eq. (G.1) can be recast into $\boldsymbol{\mathcal{R}}(\boldsymbol{\mathcal{Y}}) = \mathbf{0}$, with $\boldsymbol{\mathcal{R}} \in \mathbb{R}^M$ the vector of residuals and $\boldsymbol{\mathcal{Y}} \in \mathbb{R}^M$ the discrete representation of $\mathbf{y}$. To obtain the distribution of $\boldsymbol{\mathcal{Y}}$ at time $n+1$, minimization approaches based on Newton's method iteratively find an updated solution $\boldsymbol{\mathcal{Y}}_{\{k+1\}} = \boldsymbol{\mathcal{Y}}_{\{k\}} + \Delta\boldsymbol{\mathcal{Y}}_{\{k\}}$ from the previous state $\boldsymbol{\mathcal{Y}}_{\{k\}}$ by calculating the Newton step $\Delta\boldsymbol{\mathcal{Y}}_{\{k\}} = -\boldsymbol{\mathcal{J}}_{\{k\}}^{-1}\cdot\boldsymbol{\mathcal{R}}_{\{k\}}$, where the subscript $\{k\}$ refers to a sub-implicit iteration within the time-level advancement, and $\mathcal{J}_{i,j} = \partial\mathcal{R}_i/\partial\mathcal{Y}_j$ is the Jacobian matrix. In this way, the norm of the residuals, $r = \boldsymbol{\mathcal{R}}\cdot\boldsymbol{\mathcal{R}}^T$, is reduced in every iteration. At the beginning of each time step, $\boldsymbol{\mathcal{Y}}_{\{k\}}$ is initiated with the solution of the previous time level $\boldsymbol{\mathcal{Y}}_n$ to efficiently start the iterative process that provides $\boldsymbol{\mathcal{Y}}_{n+1}$.

Taking the full Newton step $\Delta\boldsymbol{\mathcal{Y}}_{\{k\}}$ may not decrease the residual. This is the case, for example, when the solution state is not close enough to the minimum where the quadratic convergence behavior of the Newton method is achieved. The utilization of $\boldsymbol{\mathcal{J}}$, which is constructed from local derivatives, only guarantees that r decreases at the starting point of the Newton step, but not necessarily all the way. Therefore, to ensure that the Newton iteration reduces the residual, the updating step is premultiplied by a factor $\mathcal{G}_{\{k\}}$ as $\boldsymbol{\mathcal{Y}}_{\{k+1\}} = \boldsymbol{\mathcal{Y}}_{\{k\}} + \mathcal{G}_{\{k\}}\Delta\boldsymbol{\mathcal{Y}}_{\{k\}}$, with $0 < \mathcal{G}_{\{k\}} \leq 1$. Given that $\Delta\boldsymbol{\mathcal{Y}}_{\{k\}}$ is a local direction of descent, the full Newton step, i.e., $\mathcal{G}_{\{k\}} = 1$, is tested first; this will lead to quadratic convergence when $\boldsymbol{\mathcal{Y}}$ is sufficiently close to the minimum. However, if the residual increases, i.e., $r(\boldsymbol{\mathcal{Y}}_{\{k+1\}}) > r(\boldsymbol{\mathcal{Y}}_{\{k\}})$, $\Delta\boldsymbol{\mathcal{Y}}_{\{k\}}$ is backtracked along the Newton direction testing smaller values of $\mathcal{G}_{\{k\}}$ until a local minimum is found. The details of this methodology, which is guaranteed to efficiently decrease the residual norm, are fully described in Ch. 6 of Ref. [178].

An important piece of the solution methodology is the efficient and accurate calculation of $\boldsymbol{\mathcal{J}}$ at each sub-iteration of the Newton-Raphson solver. In an ideal scenario, the best option would be to analytically derive the expressions for all the terms in the Jacobian matrix such that only analytical evaluations of functions are needed to compute $\boldsymbol{\mathcal{J}}$ at runtime. This strategy would typically provide the most accurate and computationally efficient calculation of the Jacobian, which is important since the complexity of evaluating $\boldsymbol{\mathcal{J}}$ scales with its size as M^3. However, such approach is not optimal for transcritical flows due to the complex relations between the independent variables and the residual expressions involving standard and diffuse-interface fluxes, and real-gas thermodynamic functions. Instead, a practical solution is to approximate the terms of $\boldsymbol{\mathcal{J}}$ with finite differences. Similarly to most Jacobian-based solvers [177,178], this work utilizes first-order forward finite differences [175] to approximate the terms of the Jacobian matrix as it provides a good balance between accuracy and computational cost, whereas the inverse of the Jacobian is calculated by means of a lower-upper (LU) decomposition.

G2. Numerical considerations for cases involving equilibrium isothermal bicomponent systems

In isothermal cases, the solver used in this study integrates an unsteady formulation that simplifies to that in Table 5 in steady

state. In particular, the code integrates the mechanical equilibrium condition (107) and relaxes a convectionless species conservation equation (46) to the steady state. Correspondingly, $\mathcal{R}$ corresponds to the residual versions of these two equations. The boundary conditions away from interfaces correspond to phase-equilibrium composition as given by Eqs. (109) and (110). The resulting formulation, which is summarized in Table G.1, is discretely solved on uniform 1D meshes with approximately 50–75 grid points per interface thickness. The vector $\mathcal{Y}$ is composed of the independent variables ρ and Y_F, whereas P is a dependent function of ρ and Y_F through the equation of state (14). Since the transient terms become zero at equilibrium conditions, the steady state solutions are independent from the initial distributions. However, to accelerate the convergence of the calculations, ρ and Y_F are initialized following hyperbolic-tangent profiles with width values estimated by the scalings introduced in Section 4.4. Once the system has been initialized, the discrete equations are integrated in time by means of the BDF2 scheme (G.1) until a steady state solution is obtained. This final state is defined as the distribution of ρ and Y_F for which the solution does not change in time below a user-specified threshold in the infinity-norm sense. The threshold utilized in the calculations presented in this work is $||(\mathcal{Y}_{n+1} - \mathcal{Y}_n)/\mathcal{Y}_n||_\infty < 10^{-8}$.

G3. Numerical considerations for cases involving non-isothermal bicomponent systems

The non-equilibrium formulation integrated by the solver for transcritical interfaces in non-isothermal bicomponent systems is summarized in Table 8. It involves the time evolution of ρ, v_n, P, Y_F, E, and T. However, to reduce the computational complexity, the number of variables integrated implicitly in time is reduced to ρ, Y_F, and T by noticing that P is a function of ρ, T and Y_F through the equation of state (14), and that the total energy E is a function of ρ, v_n, Y_F, and T through Eq. (48). In addition, v_n can be calculated from ρ at every time level by advancing the continuity equation from the symmetry axis, where $v_n = 0$. The vector $\mathcal{R}$ is the residuals of momentum, species, and total-energy conservation equations, whereas $\mathcal{Y}$ is the discrete vector of independent variables ρ, Y_F, and T. Once the distributions of these independent variables are initialized, the full solution state at $t = 0$ is evaluated and the discrete system of equations is advanced in time following the BDF2 scheme.

The numerical solutions are obtained by integrating the system of equations in Table 8 in the domain $0 \le \hat{n} \le 10,000 R_F$, which is discretized by 250 grid points on a stretched mesh [179]. The calculations start with time steps of order $\Delta t = 10^{-10}$ s. As the interface broadens, the solver continuously increases Δt by satisfying the stability criterion $\Delta_n < (1 + \sqrt{2})$ [180], where Δ_n is the time-step ratio defined in Eq. (G.2). However, if more than five sub-iterations of the Newton-Raphson solver are required to converge the solution at a given time level, the time-step size is frozen at the subsequent implicit iteration of the system, thereby giving $\Delta_n = 1$. This constraint optimizes the computational performance of the solver by balancing the benefits of larger Δt with the longer wall-clock times typically required to converge the solution. The resulting evolution of the time-step size is such that Δt is of order $10^{-7} - 10^{-6}$ s for most of the remainder of the calculation. Downstream of the region where the interface vanishes, the time-step size increases to values of order $\Delta t = 10^{-6} - 10^{-5}$s.

References

[1] Wieber PR. Calculated temperature histories of vaporizing droplets to the critical point. *AIAA J* 1963;**1**:2764–9.

[2] Rosner DE. Liquid droplet vaporization and combustion. In: Harrje DT, Reardon FH, editors. Liquid propellant rocket combustion instability.; 1972. NASA Tech. Rep. #NASA-SP-194.

[3] Sánchez-Tarifa C, Crespo A, Fraga E. A theoretical model for the combustion of droplets in super-critical conditions and gas pockets. *Astronaut Acta* 1972;**17**:685–92.

[4] Sirignano WA, Delplanque JP. Transcritical vaporization of liquid fuels and propellants. *J Propul Power* 1999;**15**:806–902.

[5] Chehroudi B, Talley D, Mayer W, Branam R, Smith JJ, Schik A, Oschwald M. Understanding injection into high pressure supercritical environments. In: *Fifth international symposium on liquid space propulsion, long life combustion devices technology*. Huntsville: NASA Marshall Spaceflight Center; 2003. p. 27–30.

[6] Mayer WO, Ivancic B, Schik A, Hornung U. Propellant atomization and ignition phenomena in liquid oxygen/gaseous hydrogen rocket combustors. *J Propul Power* 2001;**17**:794–9.

[7] Candel S, Schmitt T, Darabiha N. Progress in transcritical combustion: experimentation, modeling and simulation. In: In 23rd ICDERS, Irvine; 2011.

[8] Chehroudi B, Talley D, Coy E. Visual characteristics and initial growth rates of round cryogenic jets at subcritical and supercritical pressures. *Phys Fluids* 2002;**14**:850–61.

[9] Chehroudi B. Recent experimental efforts on high-pressure supercritical injection for liquid rockets and their implications. *Int J Aerosp Eng* 2012;**1**:121802.

[10] Mayer WO, Schik A, Schaffler M, Tamura H. Injection and mixing processes in high-pressure liquid oxygen/gaseous hydrogen rocket combustors. *J Propul Power* 2000;**16**:823–8.

[11] Leyva IA, Chehroudi B, Talley D. Dark core analysis of coaxial injectors at sub-, near-,and supercritical pressures in a transverse acoustic field. *AIAA Paper #2007-5456*; 2007.

[12] Muthukumaran CK, Vaidyanathan A. Initial instability of round liquid jet at subcritical and supercritical environments. *Phys Fluids* 2016;**28**:074104.

[13] Segal C, Polikhov SA. Subcritical to supercritical mixing. *Phys Fluids* 2008;**20**:052101.

[14] Oschwald M, Smith JJ, Branam R, Hussong J, Schik A, Chehroudi B, Talley D. Injection of fluids into supercritical environments. *Combust Sci Technol* 2006;**178**:49–100.

[15] Dechoz J, R Rozé J. Surface tension measurement of fuels and alkanes at high pressure under different atmospheres. *Appl Surface Sci* 2004;**229**:175–82.

[16] Jianhua T, Satherley J, Schiffrin DJ. Density and interfacial tension of nitrogen-hydrocarbon systems at elevated pressures. *Chin J Chem Eng* 1993;**1**:223–31.

[17] Dahms RN, Manin J, Pickett LM, Oefelein JC. Understanding high-pressure gas-liquid interface phenomena in diesel engines. *Proc Combust Inst* 2013;**34**:1667–75.

[18] Manin J, Bardi M, Pickett LM, Dahms RN, Oefelein JC. Microscopic investigation of the atomization and mixing processes of diesel sprays injected into high pressure and temperature environments. *Fuel* 2014;**134**:531–43.

[19] Crua C, Manin J, Pickett LM. On the transcritical mixing of fuels at diesel engine conditions. *Fuel* 2017;**208**:535–48.

[20] Falgout Z, Rahm M, Sedarsky D, Linne M. Gas/fuel jet interfaces under high pressures and temperatures. *Fuel* 2016;**168**:14–21.

[21] Klima TC, Braeuer AS. Vapor-liquid-equilibria of fuel-nitrogen systems at engine-like conditions measured with raman spectroscopy in micro capillaries. *Fuel* 2019;**238**:312–19.

[22] Steinhausen C, Lamanna G, Weigand B, Stierle R, Gross J, Preusche A, Dreizler A. Experimental investigation of droplet injections in the vicinity of the critical point: a comparison of different model approaches. In: *Ilass Europe. 28th European conference on liquid atomization and spray systems*; 2017. p. 830–7.

[23] Vieille B, Chauveau C, Gijkalp I. Studies on the breakup regimes of LOX droplets. *AIAA Paper #99-0208*; 1999.

[24] Zong N, Yang V. Cryogenic fluid jets and mixing layers in transcritical and supercritical environments. *Combust Sci Technol* 2006;**178**:193–227.

[25] Oefelein JC, Yang V. Modeling high-pressure mixing and combustion processes in liquid rocket engines. *J Propul Power* 1998;**14**:843–57.

[26] Schmitt T, Selle L, Cuenot B, Poinsot T. Large-eddy simulation of transcritical flows. *CR Mec* 2009;**337**:528–38.

[27] Hickey JP, Ma PC, Ihme M, Thakur S. Large eddy simulation of shear coaxial rocket injector: real fluid effects. *AIAA Paper #2013-4071*; 2013.

[28] Müller H, Niedermeier CA, Matheis J, Pfitzner M, Hickel S. Large-eddy simulation of nitrogen injection at trans- and supercritical conditions. *Phys Fluids* 2016;**28**:015102.

[29] Lapenna PE, Creta F. Mixing under transcritical conditions: an a-priori study using direct numerical simulation. *J Supercrit Fluid* 2017;**128**:263–78.

[30] Harvazinski ME, Lacaze G, Oefelein JC, Sardeshmukh SV, Sankaran V. Computational modeling of supercritical and transcritical flows. *AIAA Paper #2017-1104* 2017.

[31] Tani H, Teramoto S, Yamanishi N, Okamoto K. A numerical study on a temporal mixing layer under transcritical conditions. *Comput Fluids* 2013;**85**:93–104.

[32] Yang V. Modeling of supercritical vaporization, mixing, and combustion processes in liquid-fueled propulsion systems. *Proc Combust Inst* 2000;**28**:925–42.

[33] Bellan J. Supercritical (and subcritical) fluid behavior and modeling: drops, streams, shear and mixing layers, jets and sprays. *Prog Ener Combust Sci* 2000;**26**:329–66.

[34] Givler SD, Abraham J. Supercritical droplet vaporization and combustion studies. *Prog Ener Combust Sci* 1996;**22**:1–28.
[35] Qiu L, Reitz RD. An investigation of thermodynamic states during high-pressure fuel injection using equilibrium thermodynamics. *Int J Multiph Flow* 2015;**72**:24–38.
[36] Mo G, Qiao L. A molecular dynamics investigation of n-alkanes vaporizing into nitrogen: transition from subcritical to supercritical. *Combust Flame* 2017;**176**:60–71.
[37] Dahms RN, Oefelein JC. On the transition between two-phase and single-phase interface dynamics in multicomponent fluids at supercritical pressures. *Phys Fluids* 2013;**25**:092103.
[38] Gaillard P, Giovangigli V, Matuszewski L. A diffuse interface LOX/hydrogen transcritical flame model. *Combust Theor Model* 2016;**20**:486–520.
[39] Gaillard, P., Giovangigli, V., Matuszewski, L., 2018. High pressure flames with multicomponent transport. To Appear, Preprint available at: http://www.cmap.polytechnique.fr/~giovangi/hptransport.pdf.
[40] Linstrom, P. J., Mallard, W. G., 2017. NIST chemistry webbook. NIST Standard Reference Database Number 69, retrieved August 28.
[41] Yu J, Eser S. Determination of critical properties (t_c, p_c) of some jet fuels. *Ind Eng Chem Res* 1995;**34**:404–9.
[42] Huber ML, Lemmon EW, Ott LS, Bruno TJ. Preliminary surrogate mixture models for the thermophysical properties of rocket propellants RP-1 and RP-2. *Energy Fuels* 2009;**23**:3083–8.
[43] Strakey PA, Talley DG, Hutt JJ. Mixing characteristics of coaxial injectors at high gas/liquid momentum ratios. *J Propul Power* 2001;**17**:402–10.
[44] Schumaker SA, Driscoll JF. Rocket combustion properties for coaxial injectors operated at elevated pressures. *AIAA Paper #2006-4704*; 2006.
[45] Lefebvre AH. *Atomization and sprays*. Hemisphere Publishing Corporation; 1989.
[46] Herding G, Snyder R, Rolon C, Candel S. Investigation of cryogenic propellant flames using computerized tomography of emission images. *J Propul Power* 1998;**13**:146–51.
[47] Schumaker SA, Danczyk S, Lightfoot M, Kastengren A. Interpretation of core length in shear coaxial rocket injectors from x-ray radiography measurements. *AIAA Paper #2014-3790*; 2014.
[48] Lefebvre AH, Ballal DR. *Gas turbine combustion*. CRC Press; 2010.
[49] Sánchez-Sanz M. *Chorros laminares de gas con valores muy dispares de las densidades del chorro ydel ambiente*. Universidad Carlos III de Madrid; 2007. Ph.D. thesis.
[50] Joo JY. The turbulent flows of supercritical fluids with heat transfer. *Annu Rev Fluid Mech* 2013;**45**:495–525.
[51] Landau LD, Lifshitz EM. *Course of theoretical physics: statistical physics*. Pergamon Press; 1969.
[52] Oakes RS, Clifford AA, Rayner CM. The use of supercritical fluids in synthetic organic chemistry. *J Chem Soc, Perkin Trans* 2001;**1**:917–41.
[53] Rowlinson JS, Widow B. *Molecular theory of capillarity*. Dover; 2002.
[54] Poling BE, Prausnitz JM, O'Connell JP. *The properties of gases and liquids*. McGraw-Hill; 2001.
[55] Licence P, Litchfield D, Dellar MP, Poliakoff M. "Supercriticality"; a dramatic but safe demonstration of the criticalpoint. *Green Chem* 2004;**6**:352–4.
[56] Lin SP, Reitz RD. Drop and spray formation from a liquid jet. *Annu Rev Fluid Mech* 1998;**30**:85–105.
[57] Lasheras JC, Hopfinger EJ. Liquid jet instability and atomization. *Annu Rev Fluid Mech* 2000;**32**:275–308.
[58] Dumouchel C. On the experimental investigation on primary atomization of liquid streams. *Exp Fluids* 2008;**45**:371–422.
[59] Villermaux E. Fragmentation. *Annu Rev Fluid Mech* 2007;**35**:419–46.
[60] Sirignano WA. *Fluid dynamics and transport of droplets and sprays*. second ed. Cambridge University Press; 2010.
[61] Sánchez AL, Urzay J, Liñán AL. The role of separation of scales in the description of spray combustion. *Proc Combust Inst* 2015;**35**:1549–77.
[62] Brackbill JU, Kothe DB, Zemach C. A continuum method for modeling surface tension. *J Comput Phys* 1992;**100**:335–54.
[63] Gorokhovski M, Herrmann M. Modeling primary atomization. *Annu Rev Fluid Mech* 2008;**40**:343–66.
[64] Popinet S. Numerical models of surface tension. *Annu Rev Fluid Mech* 2018;**50**:49–75.
[65] Tryggvason G, Scardovelli R, Zaleski S. *Direct numerical simulations of gas-liquid multiphase flows*. Cambridge Univ. Press; 2011.
[66] Scardovelli R, Zaleski S. Direct numerical simulation of free surface and interfacial flow. *Annu Rev Fluid Mech* 1999;**31**:567–603.
[67] McMillan P, Stanley H. Going supercritical. *Nat Phys* 2010;**6**:479–80.
[68] Simeoni GG, Bryk T, Gorelli FA, Krisch M, Ruocco G, Santoro M, Scopigno T. The widom line as the crossover between liquid-like and gas-like behaviour insupercritical fluids. *Nat Phys* 2010;**6**:503–7.
[69] Banuti DT, Hannemann K. Supercritical pseudo-boiling and its relevance for transcritical injection. *AIAA Paper #2014-3571*; 2014.
[70] Gallo P, Corradini D, Rovere M. Widom line and dynamical crossovers asroutes to understand supercritical water. *Nat Comm* 2014;**5**:5806.
[71] Lemmon EW, Penocello SG. The surface tension of air and air component mixtures. In: *Advances in cryogenic engineering,*. US: Springer; 1994. p. 1927–34.
[72] Sprow FB, Prausnitz JM. Surface tensions of simple liquids. *Trans Faraday Soc* 1966;**62**:1097–104.
[73] Rossini FD, Pitzer KS, Arnett RL, Braun RM, Pimentel GC. *Selected values of physical and thermodynamic properties of hydrocarbons and related compounds*. Pittsburgh: Carnegie Press; 1953.
[74] Koller TM, Klein T, Giraudet C, Chen J, Kalantar A, van der Laan GP, Rausch MH, Fröba AP. Liquid viscosity and surface tension of n-dodecane, n-octacosane, their mixtures, and a wax between 323 and 573 k by surface light scattering. *J Chem Eng Data* 2017;**62**:3319–33.
[75] García-Córdova T, Justo-García DN, García-Flores BE, García-Sánchez F. Vapor-liquid equilibrium data for the Nitrogen + Dodecane system at temperatures from (344 to 593) k and at pressures up to 60 MPa. *J Chem Eng Data* 2011;**56**:1555–64.
[76] Jofre L, Urzay J. Interface dynamics in the transcritical flow of liquid fuels into high-pressure combustors. In: 53rd AIAA/SAE/ASEE joint propulsion conference, AIAA propulsion and energy forum, AIAA Paper #2017-4040; 2017.
[77] Hazlett RN. *Thermal oxidation stability of aviation turbine fuels*. ASTM; 1991.
[78] Gunston W. *Jane's Aero-engines*. Jane's Information Group Ltd; 1999.
[79] Dornberger W. *V-2, der Schuss ins Weltall*. Viking Press; 1958.
[80] Rocketdyne, 1967. F-1 rocket engine technical manual. Rep. R-3896, Canoga Park, CA.
[81] Levack DJH. Advanced transportation system studies. technical area 3: alternate propulsion subsystem concepts. *NASA Tech Rep CR-192545*; 1993.
[82] Ballard, R. O., Olive, T., 2000. Development status of the NASA MC-i (fastrac) engine. AIAA Paper #2000-3898.
[83] Markusic T. Spacex propulsion. In: *Proceedings of the 46th AIAA/ASME/SAE/ASEE joint propulsion conference*; 2010. p. 1–17.
[84] Wang TS, Farmer RC. Computational analysis of the SSME fuel preburner flow. *NASA Tech. Rep. CR-178803*; 1995.
[85] Boeing, 1998. Space transportation system training data: Space shuttle main engine orientation. BC98-04.
[86] Burkhardt H, Sippel M, Herbertz A, Klevanski J. Comparative study of kerosene and methane propellant engines for reusable liquid booster stages. In: In 4th Int. con. launcher tech., space launcher liquid propulsion, Belgium; 2002.
[87] Binder M, Tomsik T, Veres JP. RL10A-3-3a rocket engine modeling project. *NASA Tech Memo*; 1997.
[88] Smith JJ. *High-pressure LOX/H_2 combustion*. University of Adelaide; 2007. Ph.D. thesis.
[89] Gill GS, Nurick WH. Liquid rocket engine injectors. *NASA SP*; 1976.
[90] Edwards T. Cracking and deposition behavior of supercritical aviation fuels. *Combust Sci Tech* 2006;**178**:307–34.
[91] Manfletti C. Laser ignition of an experimental cryogenic reaction and control thruster: pre-ignition conditions. *J Propul Power* 2014;**30**:925–33.
[92] Peng DY, Robinson DB. A new two-constant equation of state. *Ind Eng Chem Fundam* 1976;**15**:59–64.
[93] Martin JJ. Cubic equations of state – which one? *Ind Eng Chem Fundam* 1979;**18**:81–97.
[94] Young AF, Pessoa FLP, Ahón VRR. Comparison of volume translation and co-volume functions applied in the peng-robinson eos for volumetric corrections. *Fluid Phase Equilib* 2017;**435**:73–87.
[95] Lopez-Echeverry JS, Reif-Acherman S, Araujo-Lopez E. Peng-Robinson equation of state: 40 years through cubics. *Fluid Phase Equilib* 2017;**447**:39–71.
[96] Redlich O, Kwong JNS. On the thermodynamics of solutions. *Chem Rev* 1949;**44**:233–44.
[97] Soave G. Equilibrium constants from a modified Redlich-Kwong equation of state. *Chem Eng Sci* 1972;**27**:1197–203.
[98] Harstad KG, Miller RS, Bellan J. Efficient high-pressure state equations. *AIChE J* 1997;**43**:1605–10.
[99] Wilhelmsen O, Aasen A, Skaugen G, Aursand P, Austegard A, Aursand E, Gjennestad MA, Lund H, Linga G, Hammer M. Thermodynamic modeling with equations of state: present challenges with established methods. *Ind Eng Chem Res* 2017;**56**:3503–15.
[100] Dahms R. Gradient theory simulations of pure fluid interfaces using a generalized expression for influence parameters and a helmholtz energy equation of state for fundamentally consistent two-phase calculations. *J Colloid Interface Sci* 2015;**445**:48–59.
[101] Gibbs JW. On the equilibrium of heterogeneous substances, part i. *Trans Conn Acad Arts Sci* 1876;**3**:108–248.
[102] Heidemann RA, Khalil AM. The calculation of critical points. *AIChE J* 1980;**26**:769–79.
[103] Firoozabadi A. *Thermodynamics and applications in hydrocarbon energy production*. McGraw-Hill; 2015.
[104] O'Connell JP, Haile JM. *Thermodynamics: fundamentals for applications*. Cambridge Univ. Press; 2005.
[105] Reynolds WC, Colonna P. *Thermodynamics: fundamentals and engineering applications*. Cambridge Univ. Press; 2018.
[106] van Konynenburg PH, Scott RL. Critical lines and phase equilibria in binary van der waals mixtures. *Philos Trans R Soc Lond A* 1980;**298**:495–540.
[107] Sengers JL. How fluids unmix: discoveries by the school of Van der waals and Kamerlingh onnes. *R Netherlands Acad Arts Sci* 2002.
[108] van der Waals JD. The thermodynamic theory of capillarity under the hypothesis of a continuous variation of density. *1893 Translated by J S Rowlinson in J Stat Phys* 1979;**20**:197–244.
[109] Cahn JW, Hilliard JE. Free energy of a nonuniform system. i. interfacial free energy. *J Chem Phys* 1958;**28**:258–67.

[110] Papatzacos P. Diffuse-interface models for two-phase flow. *Phys Scr* 2000;**61**:349–60.
[111] Anderson DM, McFadden GB, Wheeler AA. Diffuse-interface methods in fluid mechanics. *Annu Rev Fluid Mech* 1998;**30**:139–65.
[112] Guo Z, Lin PA. A thermodynamically consistent phase-field model for two-phase flows with thermocapillary effects. *J Fluid Mech* 2015;**766**:226–71.
[113] Kim J. Phase-field models for multicomponent fluid flows. *Commun Comput Phys* 2012;**12**:613–61.
[114] Kou J, Sun S. Thermodynamically consistent modeling and simulation of multicomponent two-phase flow with partial miscibility. *Comput Methods in Appl Mech Eng* 2018;**331**:623–49.
[115] Heida M, Málek J, Rajagopal KR. On the development and generalizations of Cahn-Hilliard equations within a thermodynamic framework. *Z Angew Math Phys* 2012;**63**:145–69.
[116] Miqueu C, Mendiboure B, Graciaa C, Lachaise J. Modelling of the surface tension of binary and ternary mixtures with the gradient theory of fluid interfaces. *Fluid Phase Equilib* 2004;**218**:189–203.
[117] Lin H, Duan YY, Min Q. Gradient theory modeling of surface tension for pure fluids and binary mixtures. *Fluid Phase Equilib* 2007;**254**:75–90.
[118] Liu S, Fu D, Lu J. Investigation of bulk and interfacial properties for nitrogen and light hydrocarbon binary mixtures by perturbed-chain statistical associating fluid theory combined with density-gradient theory. *Ind Eng Chem Res* 2009;**48**:10734–9.
[119] Interfacial properties of selected binary mixtures containing n-alkanes. *Fluid Phase Equilib* 2009;**282**:68–81.
[120] Miqueu C, Mendiboure B, Graciaa C, Lachaise J. Modelling of the surface tension of pure components with the gradient theory of fluid interfaces: a simple and accurate expression for the influence parameters. *Fluid Phase Equilb* 2003;**207**:225–46.
[121] Carey BS, Scriven LE, Davis HT. Semiempirical theory of surface tension of binary systems. *AIChE J* 1980;**26**:705–11.
[122] Yang AJ, Fleming PD III, Gibbs JH. Molecular theory of surface tension. *J Chem Phys* 1976;**64**:3732–47.
[123] Fleming PD III, Yang AJ, Gibbs JH. A molecular theory of interfacial phenomena in multicomponent systems. *J Chem Phys* 1976;**65**:7–17.
[124] Allen MP. Molecular simulation methods for soft matter. *AIP Conf Proc* 2009;**1091**:1–43.
[125] Cheung DL, Anton L, Allen MP, Masters AJ. Computer simulation of liquids and liquid crystals. *Comput Phys Commun* 2008;**179**:61–5.
[126] Maxwell JC. On the dynamical evidence of molecular constitution of bodies. *Nature* 1875;**11**:357–9.
[127] Caupin F, Stroock AD. The stability limit and other open questions on water at negative pressure. *Liquid Polym* 2013;**152**:51–80.
[128] Brennen C. *Cavitation and bubble dynamics*. Oxford Univ. Press; 1995.
[129] Vincenti WG, Kruger CH Jr. *Introduction to physical gas dynamics*. Krieger Publishing Co. Press; 1965.
[130] CHEMKIN tutorial manual. CHEMKIN 10112, Reaction Design: San Diego, 2011.
[131] Bongiorno V, Scriven LE, Davis HT. Molecular theory of fluid interfaces. *J Colloid Interface Sci* 1976;**57**:462–75.
[132] Dahms RN, Oefelein JC. Non-equilibrium gas-liquid interface dynamics in high-pressure liquid injection systems. *Proc Combust Inst* 2015;**35**:1587–94.
[133] Lighthill MJ. Viscosity effects in sound waves of finite amplitude. In: Surveys in mechanics; 1956. Cambridge.
[134] Dongari N, Zhang Y, Reese JM. Molecular free path distribution in rarefied gases. *J Phys D* 2011;**44**:125502.
[135] Dahms R. Understanding the breakdown of classic two-phase theory and spray atomization at engine-relevant conditions. *Phys Fluids* 2016;**28**:042108.
[136] Krishna R. Uphill diffusion in multicomponent mixtures. *Chem Soc Rev* 2015;**44**:2812–36.
[137] Bird RB, Stuart WE, Lightfoot EN. *Transport phenomena*. Wiley; 2002.
[138] Onsager L. Reciprocal relations in irreversible processes. i. *Phys Rev* 1931;**37**:405–26.
[139] Landau LD, Lifshitz EM. *Course of theoretical physics: fluid mechanics*. Pergamon Press; 1987.
[140] Hirschfelder JO, Curtiss CE, Bird RB. *Molecular theory of gases and liquids*. Wiley & Sons; 1954. Chapter 8.
[141] Curie P. Sur la symétrie des phénomènes physiques: symétrie d'un champ électrique et d'un champ magnétique. *J Phys* 1894;**3**:393–415.
[142] Korteweg DJ. Sur la forme que prennentles équations du mouvements des fluidessi l'on tient compte des forces capillairescausées par des variations de densitéconsidérables mais continues et sur la théoriede la capillarité dans l'hypothése d'une variation continue de la densité. *Arch Néerl SciExactes Nat Ser II* 1901;**6**:1–24.
[143] Magaletti F, Picano F, Chinappi M, Marino L, Casciola CM. The sharp-interface limit of the cahn-hilliard/navier-stokes model for binary fluids. *J Fluid Mech* 2013;**714**:95–126.
[144] Marmottant P, Villermaux E. On spray formation. *J Fluid Mech* 2004;**498**:73–111.
[145] Boettinger WJ, Warren JA, Beckermann C, Karma A. Phase-field simulation of solidification. *Annu Rev Mater Res* 2002;**32**:163–94.
[146] Chiu PH, Lin YT. A conservative phase field method for solving incompressible two-phase flows. *J Comput Phys* 2011;**169**:624–51.
[147] Saurel R, Pantano C. Diffuse-interface capturing methods for compressible two-phase flows. *Annu Rev Fluid Mech* 2018;**50**:105–30.
[148] Jain SS, Mani A, Moin PA. Conservative diffuse-interface method for compressible two-phase flows. *J Comput Phys* 2020;**418**:109606.
[149] Jamet D. Diffuse interface models in fluid mechanics. *Adv Water Resour* 2001;**25**:335–48.
[150] Walas SM. *Phase equilibria in chemical engineering*. Butterworth-Heinemann; 1985. Chapter 11.
[151] Burcat A, Ruscic B. *Third millennium ideal gas and condensed phase thermochemical database for combustion with updates from active thermochemical tables*. Argonne, IL: Argonne National Laboratory; 2005.
[152] Miller RS. Long time mass fraction statistics in stationary compressible isotropic turbulence at supercritical pressure. *Phys Fluids* 2000;**12**:2020–32.
[153] de la Rosa JOM, Laredo-Sánchez GC, Viveros-García T, Ochoa-Tapia JA. CEos aid in evaluation of enthalpy of reaction. *Chem Eng Proc* 2006;**45**:559–67.
[154] Raju M, Banuti DT, Ma PC, Ihme M. Widom lines in binary mixtures of supercritical fluids. *Sci Rep* 2017;**7**:3027.
[155] Chung TH, Lee LL, Starling KE. Applications of kinetic gas theories and multiparameter correlation for prediction of dilute gas viscosity and thermal conductivity. *Ind Eng Chem Fund* 1984;**23**:8–13.
[156] Chung TH, Ajlan M, Lee LL, Starling KE. Generalized multiparameter correlation for nonpolar and polar fluid transport properties. *Ind Eng Chem Fund* 1988;**27**:671–9.
[157] Masi E, Bellan J, Harstad KG, Okong'o NA. Multi-species turbulent mixing under supercritical-pressure conditions: modelling, direct numerical simulation and analysis revealing species spinodal decomposition. *J Fluid Mech* 2013;**721**:578–626.
[158] Oefelein J, Dahms R, Lacaze G. Detailed modeling and simulation of high–pressure fuel injection processes in diesel engines. *SAE Int J Eng* 2012;**5**:1258.
[159] Hakim L, Ruiz A, Schmitt T, Boileau M, Staffelbach G, Ducruix S, Cuenot B, Candel S. Large eddy simulations of multiple transcritical coaxial flames submitted to a high-frequency transverse acoustic modulation. *Proc Combust Inst* 2015;**35**:1461–8.
[160] Mayer W, Telaar J, Branam R, Schneider G, Hussong J. Raman measurements of cryogenic injection at supercritical pressure. *Heat Mass Trans* 2003;**39**:709–19.
[161] Schmitt T, Rodriguez J, Leyva IA, Candel S. Experiments and numerical simulation of mixing under supercritical conditions. *Phys Fluids* 2012;**24**:055104.
[162] Leahy-Dios A, Firoozabadi A. Unified model for nonideal multicomponent molecular diffusion coefficients. *AIChE J* 2007;**53**:2932–9.
[163] Firoozabadi A, Ghorayeb K, Shukla K. Theoretical model of thermal diffusion factors in multicomponent mixtures. *AIChE J* 2000;**46**:892–900.
[164] Li Z, Firoozabadi A. Modeling asphaltene precipitation by n-alkanes from heavy oils and bitumens using cubic-plus-association equation of state. *Energy Fuels* 2010;**24**:1106–13.
[165] Mutoru JW, Firoozabadi A. Form of multicomponent Fickian diffusion coefficients matrix. *J Chem Thermodyn* 2011;**43**:1192–203.
[166] Jindrová T, Mikyška J, Firoozabadi A. Phase behavior modeling of bitumen and light normal alkanes and CO_2 by PR-EOS and CPA-EOS. *Energy Fuels* 2016;**30**:515–25.
[167] Shukla K, Firoozabadi A. A new model of thermal diffusion coefficients in binary hydrocarbon mixtures. *Ind Eng Chem Res* 1998;**37**:3331–42.
[168] Gonzalez-Bagnoli MG, Shapiro AA, Stenby EH. Evaluation of the thermodynamic models for the thermal diffusion factor. *Philos Mag* 2003;**83**:2171–83.
[169] Jamet D, Lebaigue O, Coutris N, Delhaye JM. The second gradient method for the direct numerical simulation of liquid-vapor flows with phase change. *J Comput Phys* 2001;**169**:624–51.
[170] R F Curl J, Pitzer KS. Volumetric and thermodynamic properties of fluids - enthalpy, free energy, and entropy. *Ind Eng Chem* 1958;**50**:265–74.
[171] Vignes A. Diffusion in binary mixtures. *Ind Eng Chem Fund* 1966;**5**:189–99.
[172] Kooijman HA, Taylor R. Estimation of diffusion coefficients in multicomponent liquid systems. *Ind Eng Chem Res* 1991;**30**:1217–22.
[173] Fuller EN, Schettler PD, Giddings JC. A new method for prediction of binary gas-phase diffusion coefficients. *Ind Eng Chem* 1966;**58**:18–27.
[174] Harlow FH, Welch JE. Numerical calculation of time-dependent viscous incompressible flow of fluid with free surface. *Phys Fluids* 1965;**8**:2182.
[175] Moin P. *Fundamentals of engineering numerical analysis*. Cambridge University Press; 2010.
[176] Curtiss CF, Hirschfelder JO. Integration of stiff equations. *Proc Natl Acad Sci USA* 1952;**38**:235–43.
[177] Press WH, Teukolsky SA, Vetterling WT, Flannery BP. *Numerical recipes: the art of scientific computing*. Cambridge University Press; 2007.
[178] Dennis JE, Schnabel RB. *Numerical methods for unconstrained optimization and nonlinear equations*. Prentice Hall; 1983.
[179] Vinokur M. On one-dimensional stretching functions for finite-difference calculations. *J Comput Phys* 1983;**50**:215–34.
[180] Brenan, K. E., Campbell, S. L., Petzold, L. R., 1989. Numerical solution of initial-value problems in differential algebraic equations. North-Holland.

Dr. Lluís Jofre, Postdoctoral Fellow at the Center for Turbulence Research, Stanford University (USA). He obtained his Mechanical Engineering Degree in 2008 from the Technical University of Catalonia BarcelonaTech (Spain), jointly with the KTH Royal Institute of Technology, Sweden. In 2014, he obtained a Ph.D. in Fluid Mechanics and Thermal Engineering also from the Technical University of Catalonia BarcelonaTech, Spain. His main research areas include high-pressure transcritical flows, two-phase flows, modeling and computational studies of turbulence in multiphysics environments, uncertainty quantification, and data science in Fluid Mechanics.

Dr. Javier Urzay, Senior Research Engineer at the Center for Turbulence Research, Stanford University (USA). He obtained his B.Sc./M.Sc. degree in Mechanical Engineering in 2005 from the Carlos III University of Madrid (Spain), and his M.Sc. and Ph.D. degrees in Aerospace Engineering in 2006 and 2010 from the University of California San Diego (USA) working on theoretical aspects of combustion physics and fluid mechanics. His research interests include chemically reacting flows, multiphase turbulent flows, chemical rockets, hypersonic aerothermodynamics, supersonic combustion, and their engineering applications to aeronautics and astronautics. He currently serves in the U.S. Air Force Reserves at Travis Air Force Base, California.